



HAL
open science

Enriched continuum modelling of band-gap metamaterials : mechanical characterization and reflection/transmission properties of interfaces

Félix Erel-Demore

► **To cite this version:**

Félix Erel-Demore. Enriched continuum modelling of band-gap metamaterials: mechanical characterization and reflection/transmission properties of interfaces. Other. Ecole Centrale de Lyon, 2022. English. NNT: 2022ECDL0008 . tel-04288019

HAL Id: tel-04288019

<https://theses.hal.science/tel-04288019>

Submitted on 15 Nov 2023

HAL is a multi-disciplinary open access archive for the deposit and dissemination of scientific research documents, whether they are published or not. The documents may come from teaching and research institutions in France or abroad, or from public or private research centers.

L'archive ouverte pluridisciplinaire **HAL**, est destinée au dépôt et à la diffusion de documents scientifiques de niveau recherche, publiés ou non, émanant des établissements d'enseignement et de recherche français ou étrangers, des laboratoires publics ou privés.

THÈSE DE DOCTORAT DE L'ÉCOLE CENTRALE DE LYON
MEMBRE DE L'UNIVERSITÉ DE LYON

ÉCOLE DOCTORALE ED162
MÉCANIQUE - ÉNERGÉTIQUE - GÉNIE CIVIL - ACOUSTIQUE
SPÉCIALITÉ : GÉNIE MÉCANIQUE

Soutenue publiquement le 20/10/2022 par

FÉLIX ÉREL-DEMORE

**Enriched continuum modelling of band-gap metamaterials:
mechanical characterization and reflection/transmission
properties of interfaces**

Devant le jury composé de :

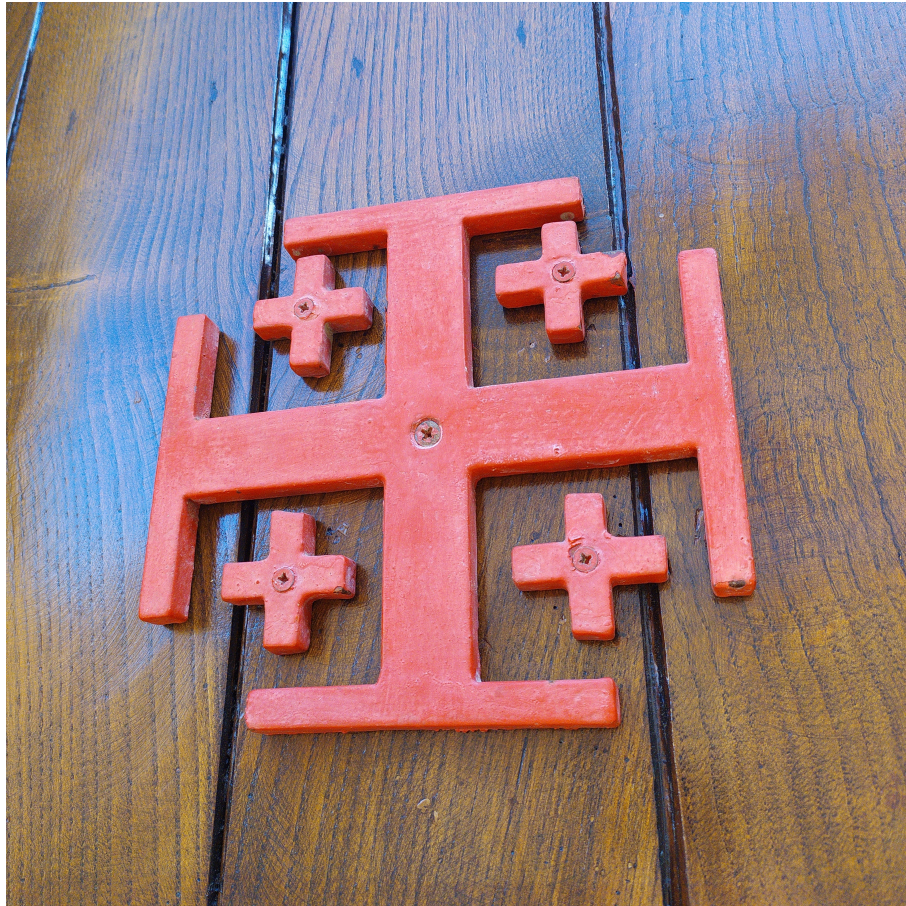
Manuel COLLET	Directeur de recherche CNRS	LTDS	<i>Directeur</i>
Marco-Valerio DAGOSTINO	Maître de Conférences	INSA Lyon	<i>Examinatrice</i>
Jean-François DEÛ	Professeur des Universités	CNAM Paris	<i>Rapporteur</i>
Louis JÉZÉQUEL	Professeur des Universités	EC Lyon	<i>Co-directeur</i>
Bruno LOMBARD	Directeur de recherche CNRS	LMA Marseille	<i>Président</i>
Angela MADEO	Professeure des Universités	TU Dortmund	<i>Co-directrice</i>
Jeanette ORLOWSKY	Professeure des Universités	TU Dortmund	<i>Examinatrice</i>
Pierre SEPPECHER	Professeur des Universités	Université de Toulon	<i>Rapporteur</i>

Die Natur baut keine Maschinen, keine Lokomotiven, Eisenbahnen, Telegraphen, Spinnautomaten etc. Sie sind Produkte der menschlichen Industrie; natürliches Material, verwandelt in Organe des menschlichen Willens über die Natur oder seiner Betätigung in der Natur. Sie sind von der menschlichen Hand geschaffene Organe des menschlichen Hirns; vergegenständlichte Wissenskraft.

La nature ne construit ni machines, ni locomotives, ni chemins de fer, ni télégraphes électriques, ni métiers à tisser automatiques, etc. Ce sont là des produits de l'industrie humaine, de la matière naturelle, transformée en instruments de la volonté et de l'activité humaines sur la nature. Ce sont des instruments du cerveau humain créés par la main humaine, la puissance objectivée du savoir.

Nature builds no machines, no locomotives, railways, electric telegraphs, self-acting mules, etc. These are products of human industry; natural material transformed into organs of the human will over nature, or of human participation in nature. They are organs of the human brain, created by the human hand ; the power of knowledge, objectified.

GRUNDRISSE DER KRITIK DER POLITISCHEN ÖKONOMIE,
KARL MARX



Detail of the Jerusalem cross of the door of the Church of San Cataldo (Palermo, Italy) visited prior and at the end of this research work. The four Greek crosses may recall the classical microstructured unit cell from which has been designed the new unit cell presented in the following pages, of which this central cross potent pattern has been an inspiration.

Remerciements

Je ne peux d'abord que remercier Louis, Manuel et Angela de leur indulgence tout au long de ces quatre années et sans qui je n'aurais pu commencer, terminer ni poursuivre mes travaux de thèse de L'École Centrale de Lyon à la *Technische Universität* à Dortmund. A défaut d'avoir été à la hauteur de leur encadrement, ce qui aurait été certes difficile, ces quatre années auront été l'opportunité de maîtriser et d'approfondir des connaissances que mon premier postdoc permettra, je l'espère, de mettre en valeur.

Je remercie également les membres du jury de thèse pour l'intérêt porté à ma présentation à travers leurs nombreuses questions, en particulier à Jean-François Deü et Pierre Seppecher pour avoir rapporté ces travaux, à Bruno Lombard pour avoir présidé le jury ainsi qu'à Jeanette Orłowsky et Marco-Valerio Dagostino pour avoir assisté à cette présentation en anglais.

Après l'annonce du résultat, j'ai d'abord eu une pensée pour mon grand père et ma grand mère, qui ont sans doute tiré à la fois plus d'inquiétude pour la soutenance et de fierté à l'annonce du résultat que moi-même.

Je remercie mes parents qui m'ont fourni tout au long de mes études, de la prépa à la soutenance de thèse, les conditions de la réussite, ainsi que ma belle-mère chez qui j'ai passé les dernières semaines de rédaction et a été la première à apprendre que mon manuscrit était terminé.

Tout travail, aussi spécialisé soit-il, étant collectif, je tiens également à remercier Sébastien Thibaud du FEMTO-ST qui a poussé l'électroérosion aux limites de fabrication, sans lequel la fabrication du démonstrateur n'aurait pas été possible, Stéphane Lemahieu côté instrumentation, ainsi que Lionel Charles et Sébastien Leone avec qui j'ai partagé la salle de pause au déjeuner.

Ces années au LTDS, malgré la pandémie, ont été aussi l'occasion, entre stagiaires, doctorant.e.s, postdoc et même maîtres de conférences, l'occasion d'organiser de nombreuses soirées, de raclettes en barbecues, qui auront été la meilleure partie de mes études, en pensant particulièrement à Alexy et Zakaria avec qui il a toujours été un plaisir de parler science, ainsi que Pradeep pour nos nombreuses discussions.

Clin d'oeil à mon frère et ma cousine, qui ont respectivement été aussi contentes de pouvoir me rejoindre durant le confinement que de me fuir pour le centre ville ;)

Enfin, mes pensées vont à Lara qui a partagé le plus difficile de mes années de thèse et qui m'a donné la motivation pour la réussir : le meilleur reste à venir.

Résumé : Ce manuscrit traite des métamatériaux pouvant empêcher la propagation des ondes élastiques dans des gammes de fréquences particulières appelées « bandes interdites ». La conception d'un nouveau métamatériau à bande interdite est présentée, de la définition des spécifications fonctionnelles de la cellule de base jusqu'au processus de fabrication de notre preuve de concept et sa caractérisation expérimentale. Il est montré que la compréhension des mécanismes de résonance locale, combinée à l'optimisation de la géométrie et au choix d'un procédé de fabrication adéquat permet d'améliorer considérablement les performances théoriques de la cellule. Compte tenu des multiples contraintes imposées à notre dispositif expérimental, en termes, par exemple, de modélisation, de temps de calcul et de fabrication et de mesures, une attention particulière a été portée à la fois au processus d'excitation et à l'acquisition des résultats expérimentaux, qui seront donc également présentés en détail. Le chapitre 3 de ce manuscrit présente dans le formalisme variationnel, en plus du milieu de Cauchy, le modèle micromorphique relaxé qui sera chargé de conduire la simplification nécessaire pour avancer vers la conception de métastructures à grande échelle dans le chapitre 4, qui présente également la comparaison entre les modèles théoriques et l'expérience, fournissant ainsi une validation de notre modèle. Le modèle micromorphique relaxé permet de décrire le comportement des métastructures (ici, les métamatériaux à bande interdite) dans le cadre simplifié de la mécanique des milieux continus avec l'introduction de seulement quelques paramètres homogénéisés en plus du module de Young et du coefficient de Poisson. Les paramètres macroscopiques constitutifs de notre modèle ont été identifiés sur la maille unitaire nouvellement conçue par une première détermination des paramètres élastiques du modèle micromorphe relaxé par approche inverse (la simulation classique étant basée sur l'analyse de Bloch-Floquet de nos structures périodiques), ouvrant la voie à la conception et à la réalisation de métastructures complexes, dont un exemple sera donné à la fin du manuscrit. Nous montrerons également que, sous certaines hypothèses, le comportement mécanique des métastructures à bande interdite peut être parfaitement reproduit par notre modèle micromorphique relaxé sur une large bande de fréquence et ce avec un gain de temps considérable.

Mots clés : métamatériaux mécaniques, modèle micromorphique, band gap, métastructures.

Abstract: This manuscript aims to deal with metamaterials that can inhibit wave propagation in particular frequency ranges which are known as “frequency band-gaps”. The conception of a new band-gap metamaterial is presented, from the definition of the functional specifications of the unit cell to the manufacturing process of our proof of concept and its experimental characterization. We will show that the comprehension of local resonance mechanisms, combined with the optimization of the geometry and the choice of an adequate manufacturing process allows to considerably improve the theoretical performances of the unit cell. Given the multiple constraints imposed to our experimental set-up, in terms, e.g., of modelling, computing time, manufacturing and measurements, a special attention was paid to both the excitation process and the acquisition of the experimental results, which will therefore also be presented in detail. Chapter 3 of this manuscript presents, in addition to the classical Cauchy continuum, the relaxed micromorphic model which will be in charge of leading the required simplification to proceed towards the design of large-scale metastructures in Chapter 4, which also presents the comparison between the theoretical models and the experiment, thus providing a solid validation of our model to be used as a basis for metastructural design. The “relaxed micromorphic” model allows to describe the behavior of metastructures (here, band-gap metamaterials) in the simplified framework of continuum mechanics with the introduction of only few homogenized parameters additionally to the classical Young modulus and Poisson ratio. The constitutive macroscopic parameters of our model have been identified on the newly designed unit cell by a first determination of the elastic parameters of the relaxed micromorphic model by inverse approach (the classical simulation being based on the Bloch-Floquet analysis of our periodic structures), this opens the way to the efficient design and realization of engineering metastructures, an example of which will be given at the end of the manuscript. We will also show that, under certain assumptions, the mechanical behavior of band-gap metastructures can be perfectly reproduced by our relaxed micromorphic model over a wide frequency band and with considerable time savings.

Keywords: Mechanical metamaterials, micromorphic models, Band gaps, meta-structures.

Contents

1	Introduction	1
2	Design & experimental characterization of the <i>proof-of-concept</i>	7
2.1	Functional specifications of the unit cell	8
2.2	Dimensioning criteria of the unit cell	9
2.2.1	Dimensioning the band-gap	11
2.2.2	Mechanical dimensioning	17
2.3	Determination of cell and plate parameters	18
2.3.1	Geometry of the cell	19
2.3.2	Geometry of the plate	21
2.4	Validation of the functional specifications	22
2.4.1	For the band-gap	22
2.4.2	For the microstructured plate	22
2.5	Manufacturing the microstructured plate	22
2.6	Instrumentation and measurements	23
2.6.1	Design of the actuator	23
2.6.2	Experimental measurements	27
3	From Cauchy to micromorphic modelling	31
3.1	The classical Cauchy model	32
3.1.1	The Mandel-Voigt notation	38
3.1.2	The isotropic Cauchy material	39
3.2	The relaxed micromorphic model	43
3.2.1	The axl mapping	47
3.2.2	Application to our microstructured cell	48
3.3	The equivalent macroscopic Cauchy model	52
3.4	The piezoelectric model	53
3.5	Symmetries	57
3.5.1	A first case: plane \mathcal{P} of normal \mathbf{n}	58
3.5.2	Using the Curie's Principle	59
3.6	Boundary conditions at interfaces	61
3.6.1	Between two Cauchy continua	61
3.6.2	Between a Cauchy medium and a relaxed micromorphic medium	62
3.7	Solving	64
3.7.1	Discretization of the geometry	65
3.7.2	Damping of the structures	75
3.8	Convergence of the microstructured and relaxed micromorphic models	81
3.8.1	The long-wave limit: statics	84
3.8.2	Broadband dynamics of the metamaterial's plate	89

Contents

4	Confronting our models to the experiment	93
4.1	Writing of the 3D model	95
4.1.1	For the classical Cauchy model	95
4.1.2	For the relaxed micromorphic model	98
4.2	Recalibrating the model	101
4.2.1	For the microstructured system	102
4.2.2	For the micromorphic system	107
4.3	Perturbating the model	114
4.4	Comparison with the experiment	122
4.4.1	Point-to-point displacement comparison	123
4.4.2	2D response of the plate	126
4.5	Enabling meta-structural engineering design	128
5	Conclusion and perspectives	135
	Annexes	139
A	Variation of the action of the relaxed micromorphic medium	141
B	Comparison of the FRFs	143
C	Discrete model	151
C.1	The rigid body model	151
C.2	The Euler-Bernoulli beam	151
C.3	The Guyan static reduction	152
C.4	Parametrization	152
C.5	Parameters identification	154
C.6	Pendulum's parameters	155
C.7	Writing the equations	156
C.8	Linearization	157
	Bibliography	173

Introduction

From the ancient greek μετά “beyond”, a “meta”material is an architected material showing exotic properties, *i.e.* mechanical characteristics that cannot be found in nature [Dell’Isola 2016b]. If metamaterials were first elaborated for optics (metamaterials presenting a negative refraction index by [Veselago 1968]), the first experimental realization was not carried out until the 2000s [Veselago 2006]. More recently, the idea of metamaterials was also translated to mechanics, allowing the manipulation of elastic waves, *e.g.*

- twist in response to being pushed or pulled [Frenzel 2017, Rizzi 2019]
- cloaking [Bückmann 2015, Misseroni 2016]
- focusing [Guenneau 2007, Bacigalupo 2014]
- channeling [Kaina 2017, Tallarico 2017]

This wave approach allows to see under the same angle extremely different phenomena as presented in Figure 1.1.

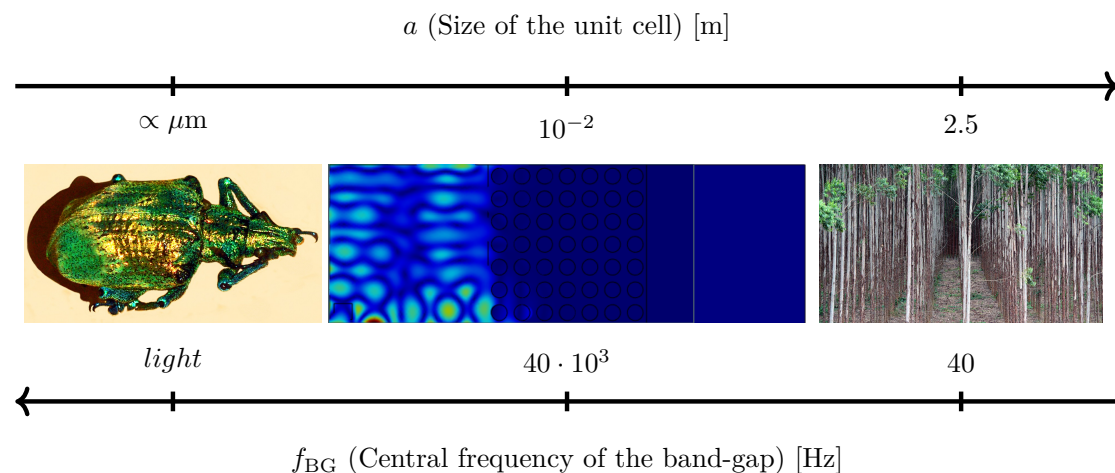


Figure 1.1: (left to right) (a) *Lamprocyphus augustus*, whose iridescent scales contain a photonic crystal structure with directional band-gaps [Galusha 2008]. (b) Frequency response in a temperature-dependent band-gap phononic crystal slab based on the combination of metallic parts and highly dissipative polymers [Billon 2019]. (c) Resonances in trees may result in forests acting as a natural seismic metamaterial for Rayleigh surface waves [Colombi 2016].

Chapter 1. Introduction

In the effort of modeling mechanical metamaterials' properties, many exotic features have been unveiled, such as:

- negative refraction [Zhu 2014, Kaina 2015, Willis 2016, Li 2004, Bordiga 2019]
- negative longitudinal and volume compressibility [Nicolaou 2012]
- negative effective bulk modulus [Lee 2009]
- negative effective mass density [Lee 2008]
- negative Poisson's ratio (auxetic materials) [Lakes 1987]

This manuscript aims to deal with metamaterials that can inhibit wave propagation in particular frequency ranges which are known as “frequency band-gaps” [Liu 2018, Wang 2014, O.R. Bilal 2018, Celli 2019]. The characteristics of the band-gap strongly depend on the metamaterial microstructure and such an effect may be obtained by two different phenomena:

- local resonance, where an element at the local scale comes into resonance independently of the whole structure, concentrating energy around the stressed surfaces.
- Bragg scattering [Bragg 1915], where the wavelength of the waves propagating in the structure coincides with the characteristic length of the period array, making the reflection and transmission phenomena occurring at the local scale inhibit the global wave propagation.

In Chapter 2 of this manuscript, we will present the conception of a new band-gap metamaterial, from the definition of the functional specifications of the unit cell to the manufacturing process of our *proof of concept* and its experimental characterization. We will show that the comprehension of local resonance mechanisms, combined with the optimization of the geometry and the choice of an adequate manufacturing process allows to considerably improve the theoretical performances of the unit cell. Given the multiple constraints imposed to our experimental set-up, in terms, *e.g.*, of modelling, computing time, manufacturing and measurements, a special attention was paid to both the excitation process and the acquisition of the experimental results, which will therefore also be presented in detail.

Very classically, the experimental results of such a prototype could have been compared to the numerical results obtained by solving a full microstructured model, *e.g.*, by the Finite Element Method. Such theoretical models accounting for any single element of the considered structure rapidly show their limits both in terms of complexity and computational performances. Indeed, the metastructures studied in this manuscript present two scales of interest:

- the macro scale, at which the physical phenomenons that we aim to control occur and which is often of interest for Engineers
- the micro scale, which is the scale of the unit cell

While the specific features of the unit cell are of primary importance when seeking for specific band-gap characteristics, they become secondary when one aims to design a large-scale metastructure for wave control. With this central idea in mind, we introduce a homogenized model (Relaxed Micromorphic) that encompass the main wanted metamaterial' characteristics, while keeping simple enough to allow the design of complex large-scale metastructures with significantly reduced computational time.

The denomination “macro” and “micro” does not refer to deal with the characteristic length of the structure or respectively of the unit cell but rather of their relative proportion [Barchiesi 2019]. The meshing of such small elements on a large-scale structures coupled with the use of the classical Cauchy model would inevitably lead to an enormous increase in computation time and would not allow the design of real, large-scale engineering structures which are able to resist to vibrations and shocks in a large range of frequencies. Therefore, new modelling tools are required to overcome these problems.

We present in Chapter 3 of this manuscript the so-called relaxed micromorphic model which will be in charge of leading the required simplification to proceed towards the design of large-scale metastructures in Chapter 4, which also presents the comparison between the theoretical models and the experiment, thus providing a solid validation of our model to be used as a basis for metastructural design.

The “relaxed micromorphic” model allows to describe the behavior of metastructures (here, band-gap metamaterials) in the simplified framework of continuum mechanics with the introduction of only few homogenized parameters additionally to the classical Young modulus and Poisson ratio. The constitutive macroscopic parameters of our model have been identified on the newly designed unit cell by a first determination of the elastic parameters of the relaxed micromorphic model by inverse approach (the classical simulation being based on the Bloch-Floquet analysis of our periodic structures), this opens the way to the efficient design and realization of engineering metastructures, an example of which will be given at the end of the manuscript. We will also show that, under certain assumptions, the mechanical behavior of band-gap metastructures can be perfectly reproduced by our relaxed micromorphic model over a wide frequency band and with considerable time savings.

The general progression of the work presented here and the three chapters composing this manuscript (in addition to the present introduction and general conclusion) has been designed following the “engineer’s approach” as represented in Figure 1.2.

Chapter 1. Introduction

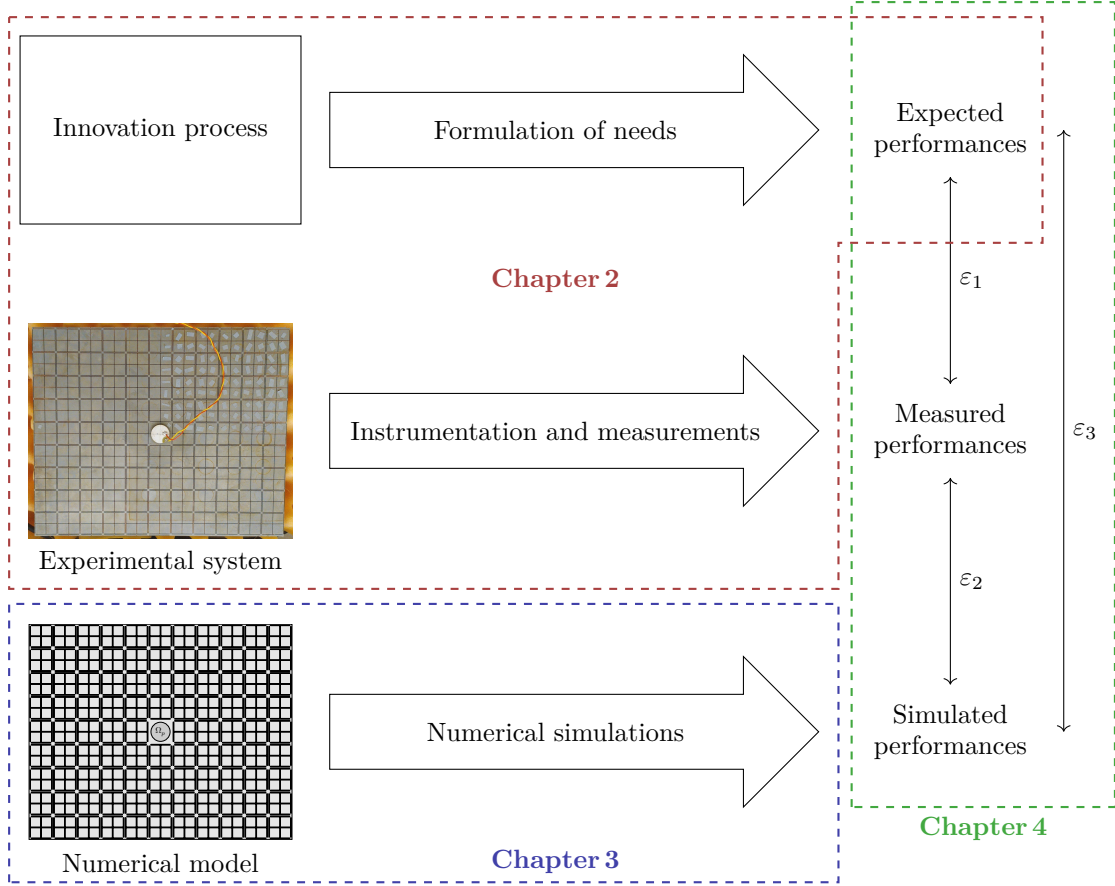


Figure 1.2: Plan of the manuscript seen by the engineer's approach.

Notations

Vectors (elements of \mathbb{R}^3) and second order tensors ("elements of $\mathbb{R}^{3 \times 3}$ ") will be written using bold letters, *e.g.* \mathbf{u} and \mathbf{P} , while higher orders tensors will be written, unless otherwise stated, \mathbb{M} , \mathbb{C} , \mathbb{K} , *etc.* As we will work through this manuscript only in Cartesian coordinates, considerably simplifying our tensorial computations, the partial derivative with respect to the space variable X_i will be written

$$\cdot_{,i} = \frac{\partial \cdot}{\partial X_i} \quad (1.1)$$

We denote the scalar products on \mathbb{R}^3 and $\mathbb{R}^{3 \times 3}$ (of associated norm $\langle \cdot, \cdot \rangle = \|\cdot\|^2$):

$$\langle \mathbf{x}, \mathbf{y} \rangle_{\mathbb{R}^3} = x_i y_i \quad \text{and} \quad \langle \mathbf{X}, \mathbf{Y} \rangle_{\mathbb{R}^{3 \times 3}} = X_{ij} Y_{ij} \quad (1.2)$$

that will be indifferently written $\langle \cdot, \cdot \rangle$ in the absence of ambiguity. We define the following first or second order differential operators for scalars $x \in \mathbb{R}$, vectors $\mathbf{x} \in \mathbb{R}^3$ and second-order tensors $\mathbf{X} \in \mathbb{R}^{3 \times 3}$:¹

¹the Einstein notation of summation over repeated indices is used if not differently specified.

– Divergence:

$$\operatorname{div} \mathbf{x} = x_{i,i} \quad \text{and} \quad (\operatorname{div} \mathbf{X})_i = X_{ij,j} \quad (1.3)$$

– Gradient:

$$(\nabla x)_i = x_{,i} \quad \text{and} \quad (\nabla \mathbf{x})_{ij} = x_{i,i,j} \quad (1.4)$$

– Laplacian:

$$\Delta x = x_{,ii} \quad \text{and} \quad (\Delta \mathbf{x})_j = x_{i,i,j} \quad (1.5)$$

– Curl (ε being the Levi-Civita operator):

$$(\operatorname{curl} \mathbf{x})_i = \varepsilon_{ijk} x_{k,j} \quad (1.6)$$

We will denote by Ω the volume occupied by our continuum body in its reference configuration and by $\partial\Omega$ its boundary, which will eventually be divided into $\partial\Omega_{\mathcal{D}}$ and $\partial\Omega_{\mathcal{N}}$, where are respectively applied Dirichlet or Neumann boundary conditions.

The Lebesgue space of square integrable functions on $\Omega \subset \mathbb{R}^3$ with values in \mathbb{R} , \mathbb{R}^3 or $\mathbb{R}^{3 \times 3}$ will be classically denoted $L^2(\Omega)$. Given the expressions of our action functionals presented in this manuscript, we also introduce the Sobolev space

$$H^1(\Omega) = \{\mathbf{u} \in L^2(\Omega) \mid \nabla \mathbf{u} \in L^2(\Omega)\} \quad (1.7)$$

of norm

$$\|\mathbf{u}\|_{H^1(\Omega)}^2 = \|\mathbf{u}\|_{L^2(\Omega)}^2 + \|\nabla \mathbf{u}\|_{L^2(\Omega)}^2 \quad (1.8)$$

We also introduce $H_0^1(\Omega)$ as “the subspace of functions $H^1(\Omega)$ being zero on $\partial\Omega$ ”. We will see that, our problems being numerically solved by the Finite-Element Method, such spaces are the most appropriate to integrate our partial differential equations.

The constitutive laws used in this manuscript require the manipulation of second order tensors. For this purpose, we will write:

– $\mathfrak{s}(\mathbb{R}^3)$ the vector space of second order symmetric tensors, *i.e.* who verify

$$\mathbf{X}^T = \mathbf{X} \quad \text{i.e.} \quad X_{ij} = X_{ji} \quad (1.9)$$

– $\mathfrak{so}(\mathbb{R}^3)$ the Lie-algebra of second order skew-symmetric tensors, *i.e.* who verify

$$\mathbf{X}^T = -\mathbf{X} \quad \text{i.e.} \quad X_{ij} = -X_{ji} \quad (1.10)$$

Given this, one can decompose every element of $\mathbb{R}^{3 \times 3}$ into their symmetric and skew-symmetric parts, in formulas

$$\operatorname{sym} \mathbf{X} = \frac{\mathbf{X} + \mathbf{X}^T}{2} \in \mathfrak{s}(\mathbb{R}^3) \quad \text{and} \quad \operatorname{skew} \mathbf{X} = \frac{\mathbf{X} - \mathbf{X}^T}{2} \in \mathfrak{so}(\mathbb{R}^3) \quad (1.11)$$

One can also recall that, given a fourth order tensor \mathbb{C} and a second order tensor \mathbf{X} then $\mathbb{C} \mathbf{X}$ is a second order tensor of components

$$(\mathbb{C} \mathbf{X})_{ij} = \mathbb{C}_{ijkl} X_{kl} \quad (1.12)$$

Design & experimental characterization of the *proof-of-concept*

Contents

2.1	Functional specifications of the unit cell	8
2.2	Dimensioning criteria of the unit cell	9
2.2.1	Dimensioning the band-gap	11
2.2.2	Mechanical dimensioning	17
2.3	Determination of cell and plate parameters	18
2.3.1	Geometry of the cell	19
2.3.2	Geometry of the plate	21
2.4	Validation of the functional specifications	22
2.4.1	For the band-gap	22
2.4.2	For the microstructured plate	22
2.5	Manufacturing the microstructured plate	22
2.6	Instrumentation and measurements	23
2.6.1	Design of the actuator	23
2.6.2	Experimental measurements	27

2.1 Functional specifications of the unit cell

We will see in Chapter 3 that the modelling of linear mechanical problems described by a displacement field \mathbf{u} under load(s) \mathbf{f} can be represented, under some hypothesis, as a linear set of equations. Considering the system to occupy a material domain Ω and to be composed of Cauchy materials of mass density ρ , Young modulus E and Poisson ratio ν , one can write

$$\mathbb{D}(\rho(\mathbf{x}), E(\mathbf{x}), \nu(\mathbf{x}), \mathbf{x}, \Omega)\mathbf{u}(\mathbf{x}) = \mathbf{f}(\mathbf{x}) \quad (2.1)$$

Under that form, mechanical problems can be split into two main categories:

- Direct problems, *i.e.*

$$\text{Determine } \mathbf{u} \text{ and/or } \mathbf{f} \text{ such as } \mathbb{D}(\rho(\mathbf{x}), E(\mathbf{x}), \nu(\mathbf{x}), \mathbf{x}, \Omega)\mathbf{u} = \mathbf{f} \quad (2.2)$$

- Inverse problems

$$\text{Determine } \Omega, \rho, E \text{ and } \nu \text{ such as } \mathbb{D}(\rho(\mathbf{x}), E(\mathbf{x}), \nu(\mathbf{x}), \mathbf{x}, \Omega)\mathbf{u}_0(\mathbf{x}) = \mathbf{f}_0(\mathbf{x}) \quad (2.3)$$

The first category can be seen as characterization of a given system: one checks if the considered system satisfies the required performances, which may be of very different natures, even by the quantities considered: displacement and its successive derivatives, stress, etc. In the case of inverse problems, one seeks, for a given set of performances (in terms of displacements, body forces, energy dissipated, loads, *etc*) to determine the geometry and/or mechanical properties of the considered structure: our microstructured cell belonging to the second category, which we wanted to verify the functional specifications presented in Table 2.1.

Name	Function	Level
PF1	To have a band gap at audible frequencies	$f_{\text{BG}} < 15$ [kHz]
PF2	To have a wide enough band-gap	$\Delta f \sim 1$ [kHz]

Table 2.1: Main functions performed by the metamaterial cell

where $f_{\text{BG}} = \frac{f_{\text{max}} + f_{\text{min}}}{2}$ and $\Delta f = f_{\text{max}} - f_{\text{min}}$, where f_{max} and f_{min} are respectively the upper and lower limit of the band gap, *i.e.* for which the dispersion equation $\omega = \omega(\mathbf{k})$ admits no solution $\in \mathbb{R}$. To this first part of the triptych “Product-Material-Process” are added the constraints of the material and of the chosen process of fabrication. While, from a theoretical point of view, the choice of material and process of fabrication has to be made after a first conception of the geometry realising the main functions given previously, practically numerous constraints considerably reduces the couples “Material-Process” available before the design of the unit cell. These will then, in turn, induce constraints on the geometry, manufacturing constraints whose dimensioning characteristics are given in Table 2.2.

Name	Function	Level
MC1	To be realized <i>via</i> an available process	Wire EDM
MC2	To be realized in an available material	TA6V
MC3	To have a machinable thickness	$e < e_{\max}$
MC4	To resist machining forces	$e > 0.5$ [mm]
MC5	To allow passage of the machining tool	$e_{\text{hole}} > 0.35$ [mm]
MC6	To have no sharp interior angles	$r_{\text{hole}} > e_{\text{hole}}/2$ [mm]
MC7	To stand in the machining area	$S < 250$ [mm] \times 250 [mm]
MC8	To be achievable in a “reasonable” time	$t_{\text{manufacturing}} < 1$ week

Table 2.2: Manufacturing constraints for the microstructured plate

where EDM stands for Electrical Discharge Machining (which will be presented in the following sections), TA6V is the usual titanium alloy used, e is the out-of-plane thickness of bulk plate, e_{hole} is the minimum width of the holes drilled in the plate and r_{hole} their radiuses and S the plate’s size. Finally, despite the fact that the manufactured experimental set-up will only be solicited in a characterization phase, *i.e.* under a very low load, it still has to satisfy the additional conditions given in Table 2.3.

Name	Function	Level
CF1	To be transported at the lab	$s > 2$
CF2	To resist to its own weight in experimental conditions	$s > 2$

Table 2.3: Static design constraints for the microstructured plate

where s is the factor of safety whose computation will be presented in the following sections. The design cases will be detailed in the following parts.

2.2 Dimensioning criteria of the unit cell

As topology optimization has successfully shown [Sigmund 2001], the design of mechanical components leaves no room for imagination. Indeed, from a theoretical point of view, the mechanician should consider:

- the functional surfaces fulfilling the main functions of the mechanical part
- thicknesses associated to the aforementioned surfaces to fulfill the constraints functions (*e.g.* resist to loads and/or displacements imposed to the structure)

How to link these volumes together can be determined considering the chosen manufacturing process, the nature of the loads applied on the structure, *etc.* Such procedure

Design & experimental characterization of the *proof-of-concept*

is precisely the one considered for topology optimization, with has been made possible through, *e.g.*, additive manufacturing. Such design procedure would be particularly advantageous for the metamaterial conception, where the characteristics of the band-gap are particularly difficult to predict with respect to the architected cell geometry. This procedure could have been written

$$\text{Find } \rho_c : \Omega_c \mapsto \{0, 1\} : \max \Delta f \quad (2.4)$$

$$\text{subject to } f_{\text{BG}} \leq 15 \text{ [Hz]} \quad (2.5)$$

where ρ_c denotes the (eventual) presence of matter in Ω_c . To our knowledge, no topology optimization software consider such procedure, the identification of the band gap characteristics requiring to plot the dispersion curves, making such optimization expensive in terms of computational time, in addition to the difficulty of solving inverse problems. Instead of developing this procedure, we very classically propose

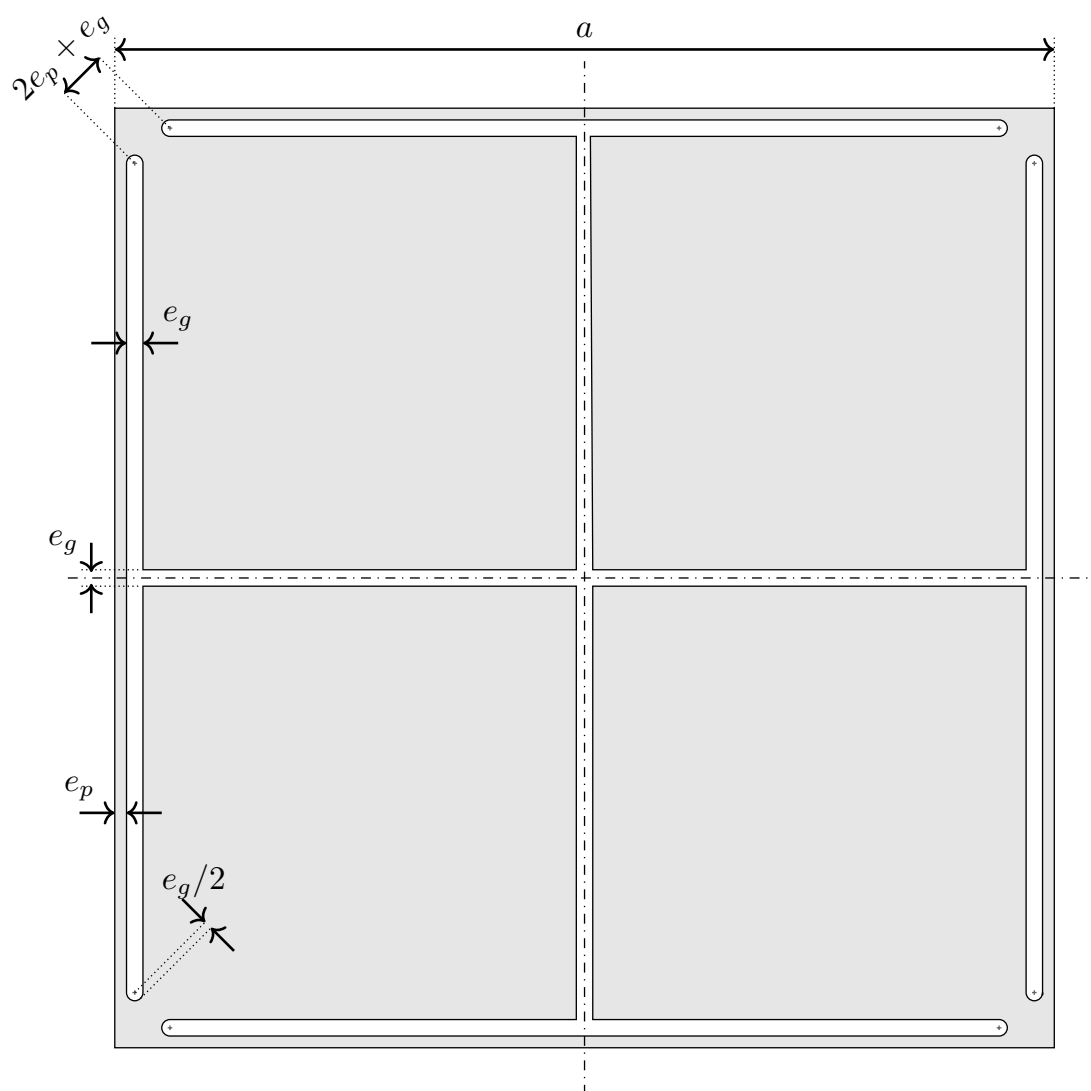


Figure 2.1: Definitive geometry of the architected cell with its parametrization.

a is the side of the cell, e_p and e_g are respectively the minimum in-plane thickness and hole width. We will show in the following sections that this specific geometry allows e_p and e_g to be limited only by manufacturing constraints. From this unit cell has been designed what we will call in the rest of this manuscript the “microstructured plate”, presented in Figure 2.2.

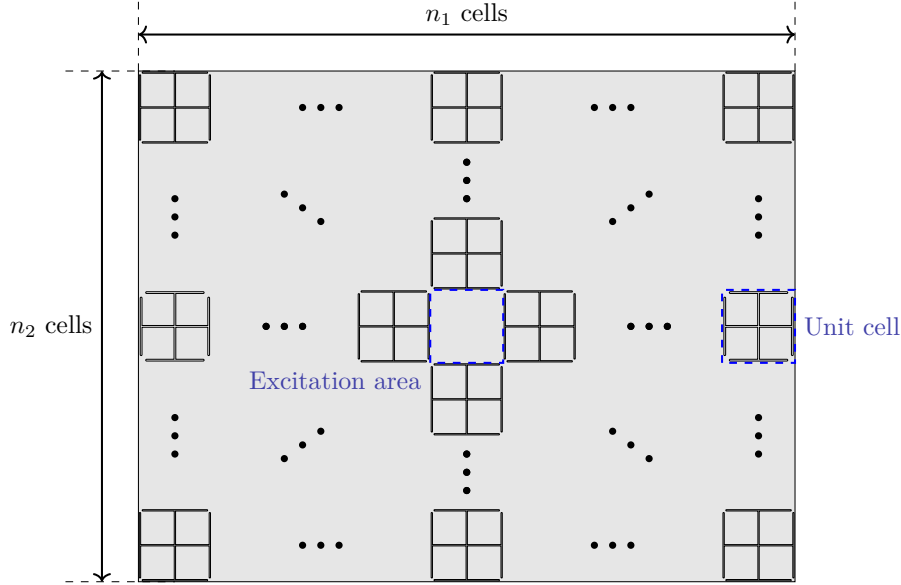


Figure 2.2: Geometry of the architected plate consisting in a bidimensionnal paving of the unit cell given in 2.1, with, in the center, the excitation zone.

Given this, the design of our *proof of concept* is reduced, in addition to the unit cell parameters, to the determination of the following parameters:

- e , the thickness of the plate
- (n_1, n_2) , the number of cells in the two directions of space of the plate.

By introducing the geometries of the unit cell and the plate, we very classically switched from an inverse problem to the determination of only a few parameters, which will be determined by checking the conformity of the structures to constraints given in Tables 2.1, 2.2 and 2.3. We will, however, expose in the following sections how this technological solution imposed itself.

2.2.1 Dimensioning the band-gap

The conformity of the proposed cell to functions PF1 and PF2 of the functional specifications has been verified *via* the multiphysic finite-element (see Chapter 3) software *Comsol Multiphysics*[®]. Given the small damping of the considered material, the computation of the band gap characteristics, the Bloch-Floquet method is used to compute the dispersion curves ($\omega = \omega(\mathbf{k})$ method) of our unit cell. If such method does not allow to characterize, *e.g.*, the attenuation of mechanical waves in our media, allows to easily identify

the band-gap frequency range. It will also allow, as presented in Chapter 3, to compute the relaxed micromorphic parameters. Let us now present the mathematical tools used for designing our architected unit cell. The Floquet theorem [Floquet 1883], states that for the ordinary differential equation

$$\frac{\partial \mathbf{u}}{\partial \mathbf{x}}(\mathbf{x}) = \mathbf{A}(\mathbf{x})\mathbf{u}(\mathbf{x}) \quad \text{in } \mathbb{R}^2 \quad (2.6)$$

where $\mathbf{A} : (\mathbf{u}, \mathbf{x}) \mapsto \mathbf{A}(\mathbf{x})\mathbf{u}(\mathbf{x})$ is $(\mathbf{r}_1, \mathbf{r}_2)$ -periodic, *i.e.*

$$\forall (m_1, m_2) \in \mathbb{Z}^2, \mathbf{A}(\mathbf{x} + m_1\mathbf{r}_1 + m_2\mathbf{r}_2) = \mathbf{A}(\mathbf{x}) \quad (2.7)$$

the solution \mathbf{u} can be expressed as the linear combination of

$$\mathbf{v}(\mathbf{x})e^{i\langle \mathbf{k}, \mathbf{x} \rangle} \quad (2.8)$$

where \mathbf{v}_i is $(\mathbf{r}_1, \mathbf{r}_2)$ -periodic and $\mathbf{k} \in \mathbb{C}^2$. The structures considered in this manuscript, consisting of two-dimensional paving of our unit cell verify such periodicity condition upon its geometry \mathcal{G}

$$\mathcal{G}(\mathbf{x} + m_1\mathbf{r}_1 + m_2\mathbf{r}_2) = \mathcal{G}(\mathbf{x}) \quad (2.9)$$

where \mathbf{r}_1 and \mathbf{r}_2 are the lattice vectors, $(m_1, m_2) \in \mathbb{Z}^2$. Our primitive cell is a square of side a denoted as Ω_c . The reciprocal unit cell Ω_r , corresponding to the first Brillouin zone, is defined by the reciprocal lattice vector basis $(\mathbf{g}_1, \mathbf{g}_2)$ such as

$$\langle \mathbf{r}_i, \mathbf{g}_j \rangle = 2\pi\delta_{ij} \quad (2.10)$$

The primitive and reciprocal lattice are given in Figure 2.3.

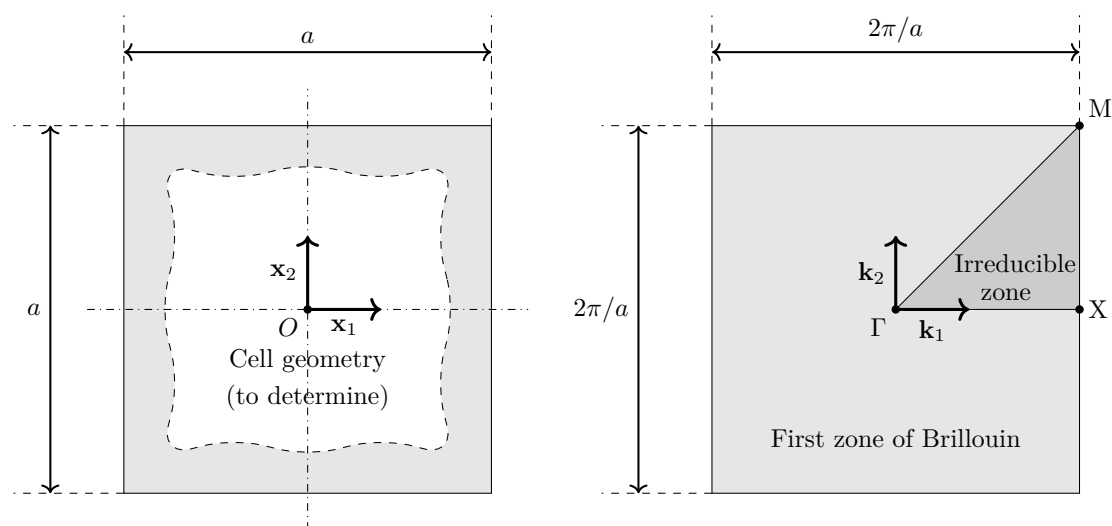


Figure 2.3: (left) Geometry of the cell in the physical space (right) Dual space, the first zone of Brillouin and the irreducible zone.

The Bloch theorem [Bloch 1929] states that $\forall \mathbf{u} \in \mathcal{L}^2(\mathbb{R}^2, \mathbb{C}^2)$ can be represented as

$$\mathbf{u}(\mathbf{x}) = \int_{\Omega_r} \mathbf{U}(\mathbf{x}, \mathbf{k})e^{i\langle \mathbf{k}, \mathbf{x} \rangle} d\mathbf{k} \quad (2.11)$$

where \mathbf{U} , Ω_r -periodic with respect to \mathbf{k} , can be expressed as

$$\mathbf{U}(\mathbf{x}, \mathbf{k}) = \sum_{(m_1, m_2) \in \mathbb{Z}^2} \mathcal{F}(\mathbf{u})(\mathbf{k} + m_1 \mathbf{g}_1 + m_2 \mathbf{g}_2) e^{i(m_1 \mathbf{g}_1 + m_2 \mathbf{g}_2, \mathbf{x})} \quad (2.12)$$

where $\mathcal{F}(\mathbf{u})$ is the Fourier transform of \mathbf{u} . For our architected unit cell, we have to solve the eigenvalues problem [Mace 2008] defined by the local Cauchy equilibrium

$$\omega^2 \rho \mathbf{u} + \nabla \cdot \mathbb{C} \text{sym} \nabla \mathbf{u} = \mathbf{0} \quad \text{in } \Omega_c \quad (2.13)$$

with the boundary conditions

$$\begin{cases} \mathbf{u}_r = e^{-ik_1 a} \mathbf{u}_l \\ \mathbf{u}_t = e^{-ik_2 a} \mathbf{u}_b \end{cases} \quad (2.14)$$

where \mathbf{u}_l , \mathbf{u}_r , \mathbf{u}_t and \mathbf{u}_b are the respective displacements of the left, right, top and bottom borders of the unit cell and $(k_1, k_2) \in [-\pi/a, \pi/a]^2$. The values of the parameters of the TA6V titanium alloy considered are given in Table 2.4. This usual titanium alloy has been considered with respect to the manufacturing process considered (Wire EDM requires metal alloys) and its well-known performances:

ρ_c	E	ν
[kg/m ³]	[GPa]	-
4400	112	0.34

Table 2.4: Mechanical parameters used for the computation of dispersion curves of our unit cell.

Given the tetragonal symmetry imposed to our unit cell, the characterisation of the band gap through the computation of the dispersion curves has been made [Joannopoulos 2011, Maurin 2018] upon the contour of the irreducible Brillouin zone [Brillouin 1953] instead of the whole Brillouin zone, allowing to slightly reduce the computational time of this eigenvalue problem, reducing the computation of Equation 2.13 on

$$(k_1, k_2) \in \left[-\frac{\pi}{a}, \frac{\pi}{a} \right]^2 \quad (2.15)$$

to its computation along the contour of the irreducible Brillouin zone

$$(k_1, k_2) \in \Gamma X \cup \Gamma M \quad (2.16)$$

corresponding respectively to the propagation at 0 and 45°. Such assumption, although not being proved, allows to quickly characterize the band-gap and calibrate the relaxed micromorphic parameters. The computation of the dispersion over the entire irreducible Brillouin zone has been made, to check the conformity of the cell to constraints given in Tables 2.2 and 2.3, at the end of the design procedure.

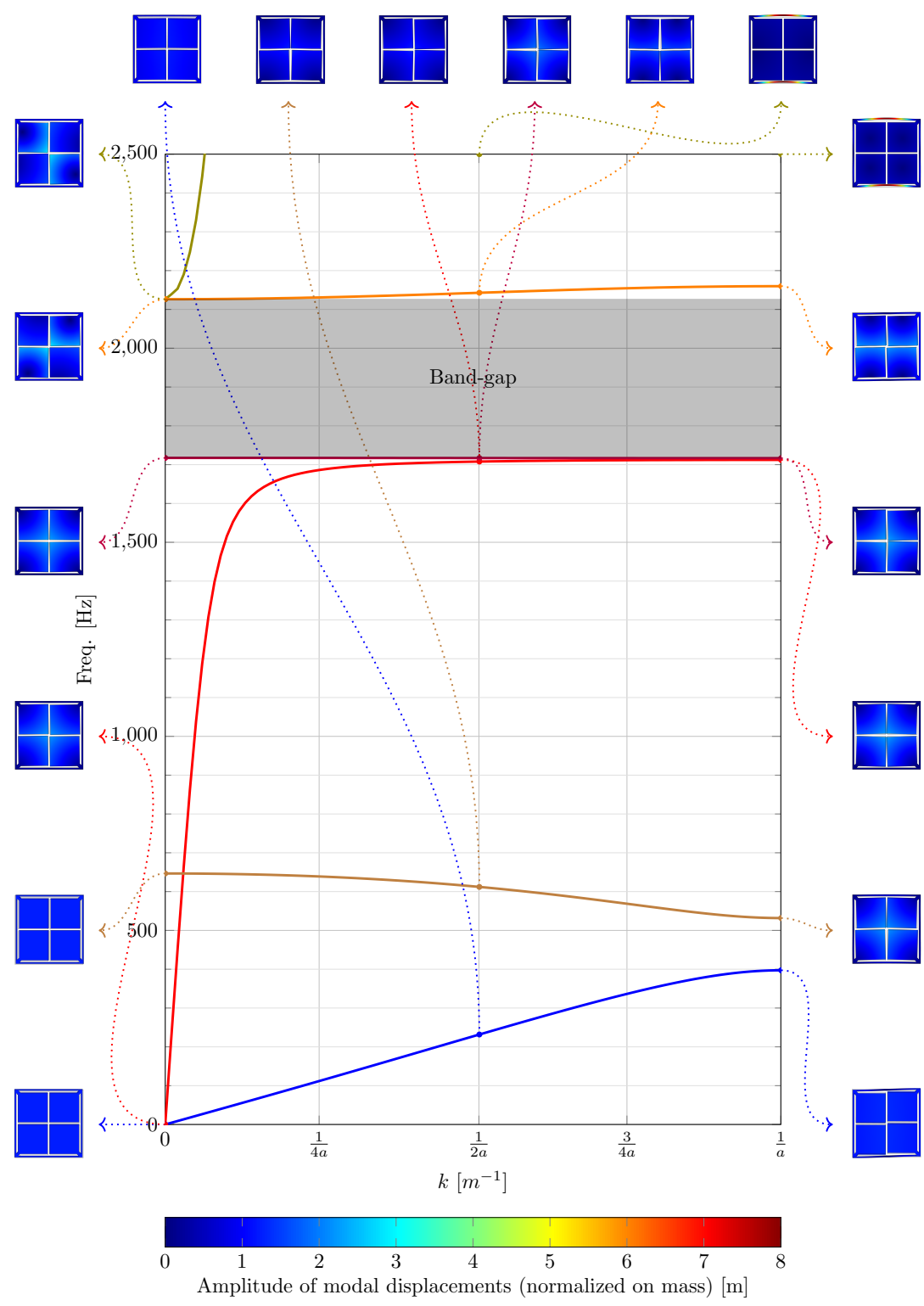
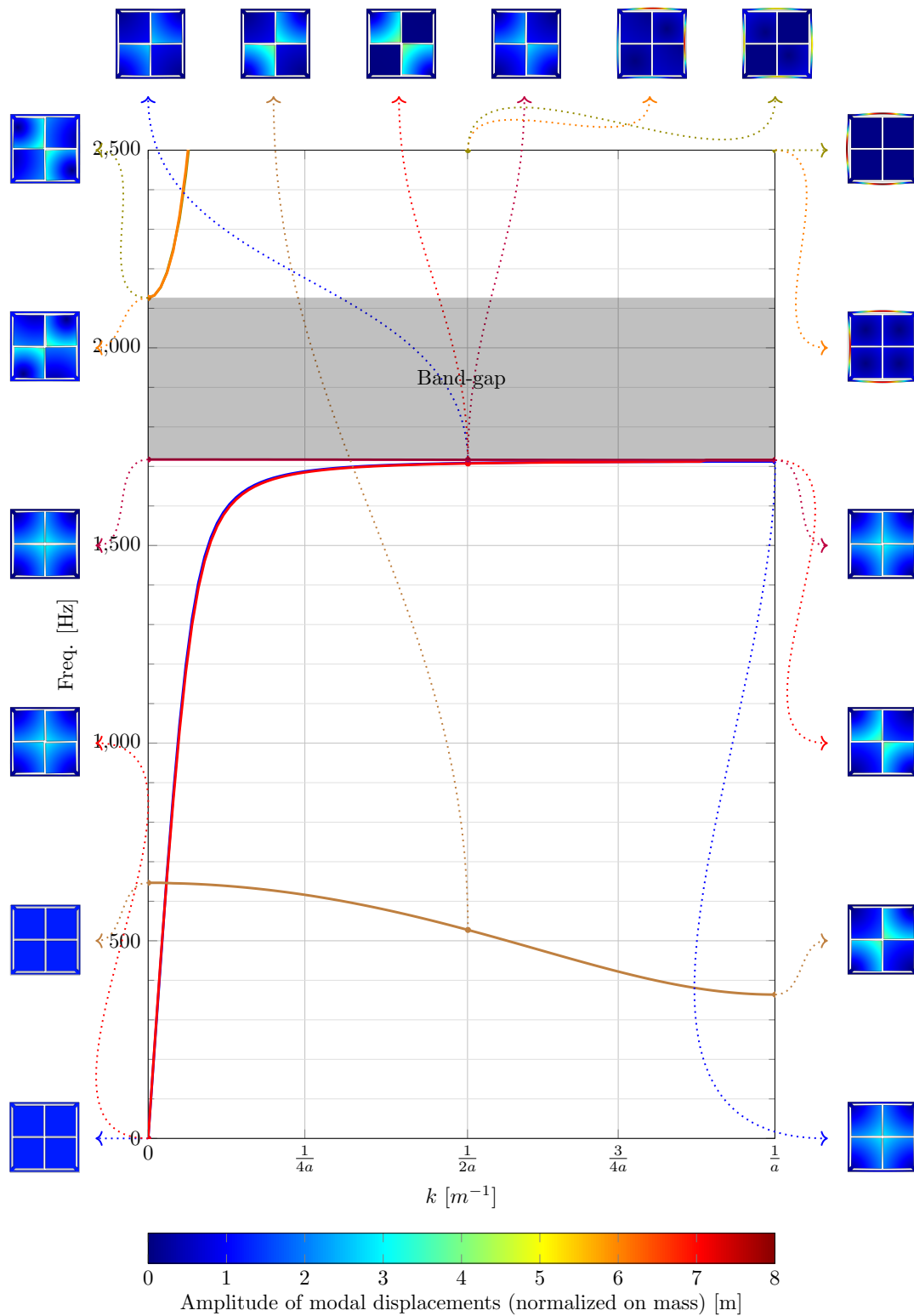


Figure 2.4: Dispersion curves along ΓX for the considered microstructured cell and their respective modeshapes.

Figure 2.5: Dispersion curves along ΓM for the considered microstructured cell

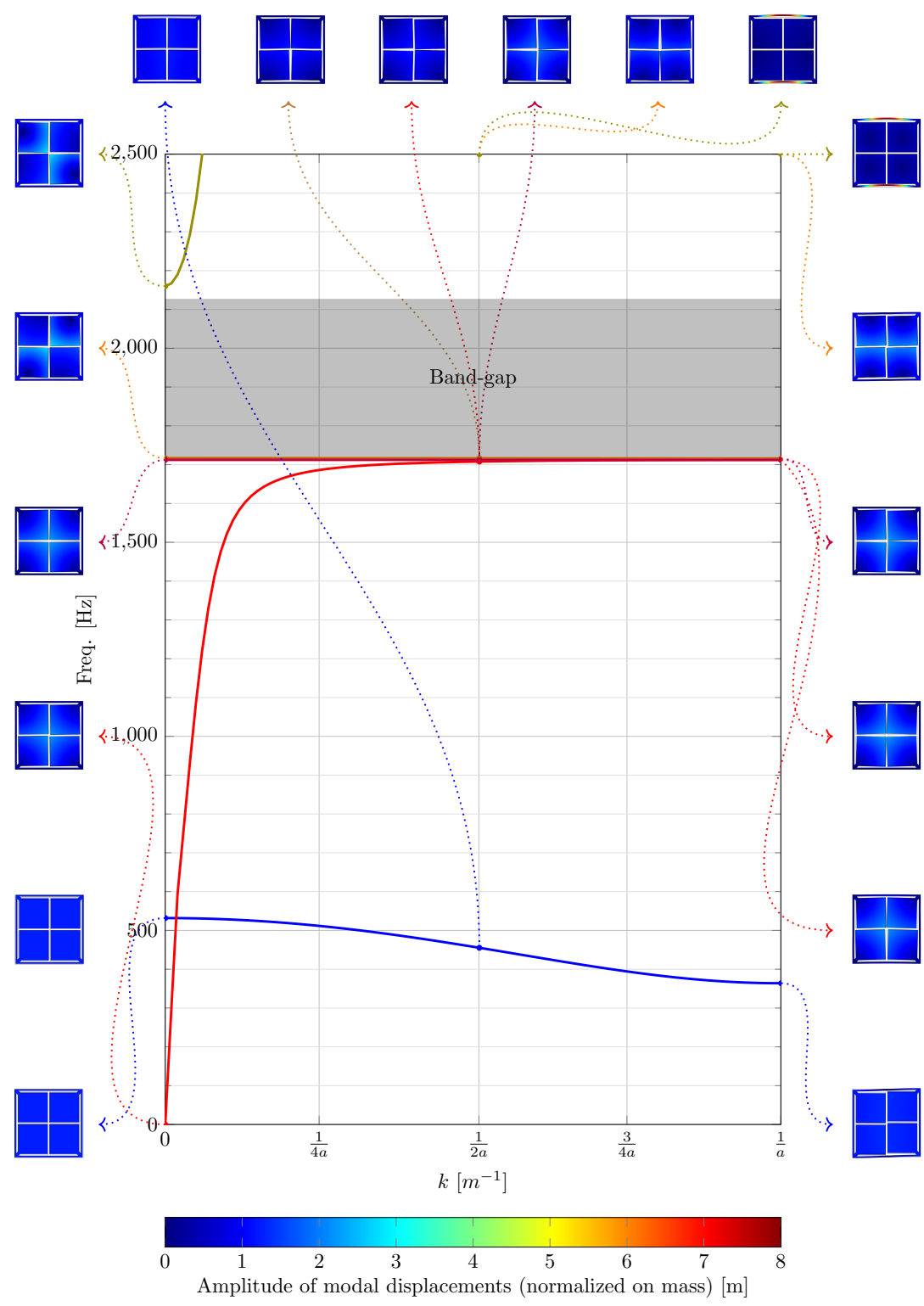


Figure 2.6: Dispersion curves along XM for the considered microstructured cell

2.2.2 Mechanical dimensioning

To verify the ability of the microstructured plate to verify constraints presented in Table 2.3, corresponding to the phase of transport and manipulation at the lab, a static test has been realized. The body forces introduced is of ten times the gravity in the plate's most unfavorable case, *i.e.* in a horizontal position resting on the centers of each of its corners. This situation is presented in Figure 2.7.

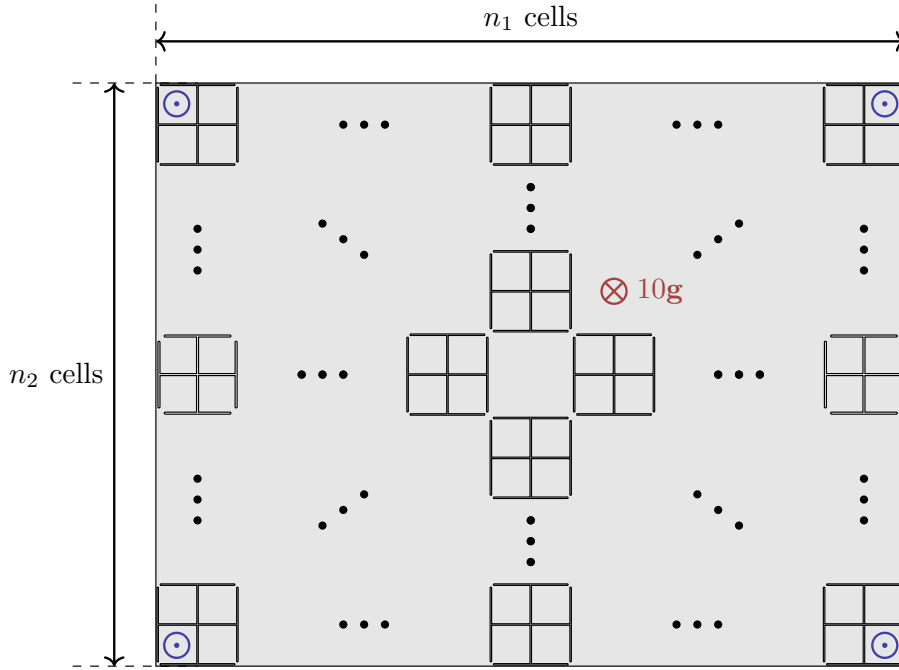


Figure 2.7: Top view of the full microstructured plate with (*blue*) the boundary conditions consisting of 4 flat supports at the corners of the plate and (*red*) the load ($10g$).

We consider the plate under ten times the gravity, the latter being orthogonal to the microstructured plate, put on 4, at the center of the resonators at the corners of the plate as presented in Figure 2.7. One now have to solve

$$\nabla \cdot \mathbb{C} \operatorname{sym} \nabla \mathbf{u} + 10\rho_c \mathbf{g} = \mathbf{0} \quad \text{in } \Omega \quad (2.17)$$

where $\mathbf{g} = -g\mathbf{x}_3 \approx -9.81\mathbf{x}_3$ [$\text{m}\cdot\text{s}^{-2}$]. By symmetry (see Chapter 3), one can consider only 1/4 of the plate by adding on the symmetry planes created, also allowing to have a well-posed problem (in-plane rigid body moves being deleted) as given in Figure 2.8.

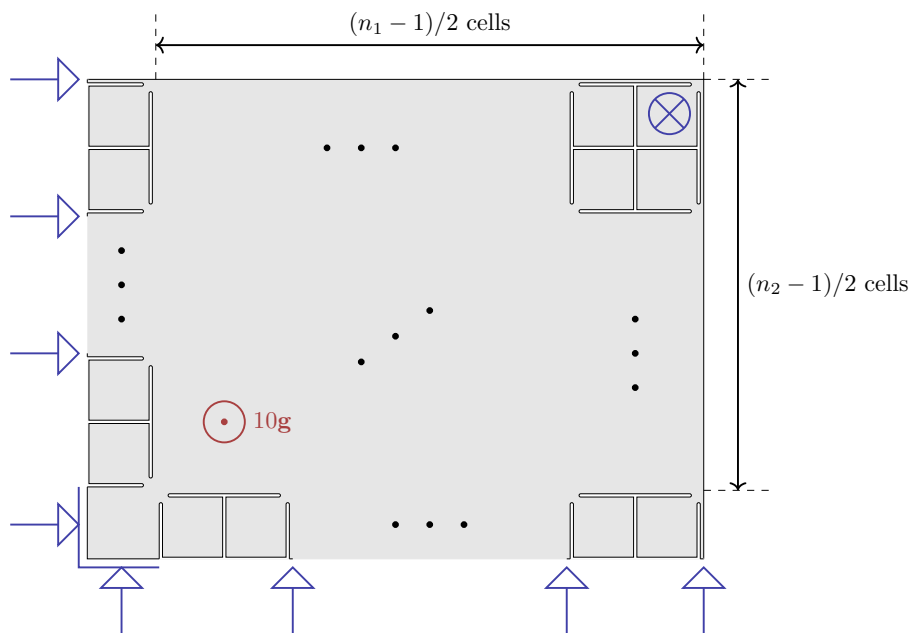


Figure 2.8: Top view of the symmetrized microstructured plate with (blue) the boundary conditions consisting of a flat support at the corner of the plate and (red) the load (10g).

The boundary conditions are

$$\begin{cases} \langle \mathbf{u}, \mathbf{n} \rangle = 0 & \text{for the symmetry planes of normal } \mathbf{n} \\ \langle \mathbf{u}, \mathbf{x}_3 \rangle = 0 & \text{for the ponctual contact} \end{cases} \quad (2.18)$$

where s is the safety coefficient for the considered case, defined as

$$s = \frac{\sigma_0}{\sigma_{VM}} \quad (2.19)$$

where σ_{VM} is the Von Mises yield criterion (maximum distortion criterion), defined as

$$\sigma_{VM} = \sqrt{\frac{3}{2} \text{Tr}(\boldsymbol{\sigma} \cdot \boldsymbol{\sigma})} \quad (2.20)$$

2.3 Determination of cell and plate parameters

We have presented the mathematical tools to check if our unit cell was able to meet the manufacturing constraints (given in Tables 2.2 and 2.3) and more specifically the band gap characteristics (see Table 2.1). We saw that the dimensionning of our structure, at the difference of “classical” dimensionning, was made in two different parts, to know:

- the band-gap characteristics, through the computation of the Bloch-Floquet analysis
- a more “classical” dimensionning on the full structure

We directly presented, in Figures 2.1 and 2.2 the respective geometries and parametrization of the unit cell and the full structure, considerably simplifying the design of the cell to the choice of parameters:

- the size of the unit cell a
- (half) the minimum in-plane thickness e_p
- the with of the holes e_g
- the out-of-plane thickness e
- (n_1, n_2) the number of cells in the two directions of space

If, for the sake of simplicity, we directly presented the final geometry of the unit cell, we will now present how the comprehension of the mechanisms of the band-gap effect eventually allowed to propose a new geometry which, coupled to the adequate manufacturing process, tremendously lowering the position of the band-gap with respect to the size of the unit cell.

2.3.1 Geometry of the cell

The increasing complexity of mechanical systems going and the deepening of knowledge make the innovation process more and more difficult. Despite the *slow* transformation of design process into Design Science [Cross 2001], the so-called “conception” of mechanical components is rather a “reconception” process.

In this spirit, *nanos gigantum umeris insidentes* [Dell’Isola 2016a], we based our thinking on the unit cell given in [Madeo 2018b], whose exploration of the mechanisms of local resonance has allowed us to eventually propose a unit cell with a considerably lower band-gap given with respect to its size. Figure 2.9 presents the “classical” unit cell and our new architected cell.

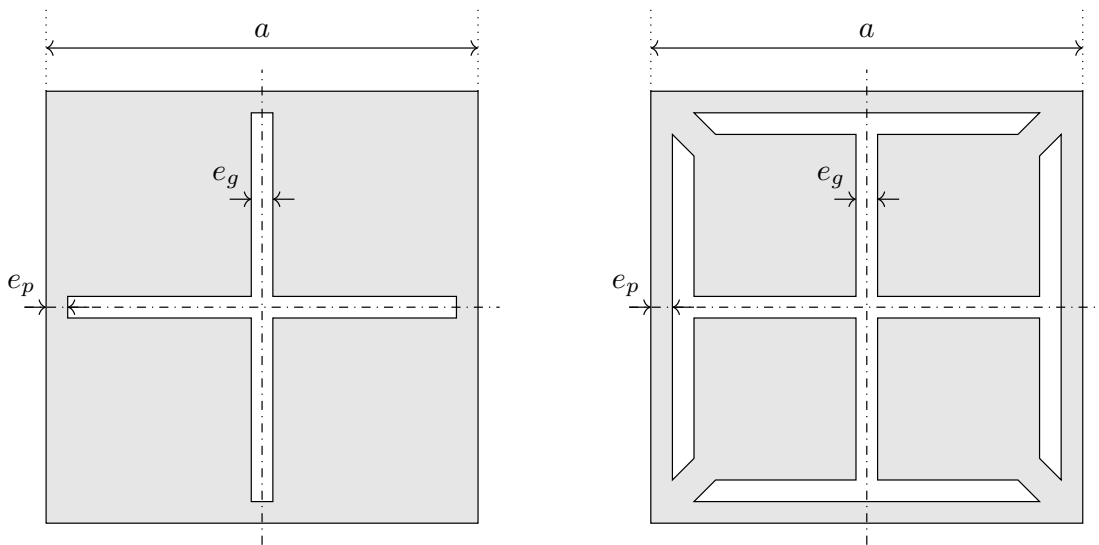


Figure 2.9: (left) classical architected cell and (right) novel geometry.

Design & experimental characterization of the *proof-of-concept*

The parametrization of the geometry of the unit cell has not been left to chance: the triptych Product-Process-Material determining the conception of systems, we chose to highlight the manufacturing and static design constraints by the parameters

- e_g is the minimum width of the holes
- e_p as the minimum in-plane thickness

to completely determine, in addition to the unit cell size a , the geometry of the cell. For a given cell of parameters (a, e_p, e_g) of band-gap characteristics $(f_{\text{BG}}, \Delta f)$, the cell of parameters (ra, re_p, re_g) of band-gap characteristics $(f_{\text{BG}}^r, \Delta^r f)$ will verify

$$f_{\text{BG}}^r = \frac{f_{\text{BG}}}{r} \quad \text{and} \quad \Delta^r f = \frac{\Delta f}{r} \quad (2.21)$$

We can therefore introduce, in the spirit of Buckingham's π theorem,

$$\pi_p = \frac{e_p}{a} \quad \text{and} \quad \pi_g = \frac{e_g}{a} \quad (2.22)$$

to parameterize our cell geometry by (a, π_p, π_g) . One can remember that the band-gap effect is obtained, in our case, by local resonance. To lower this resonant frequency, one can:

- increase the mass of the resonating element
- decrease the stiffness of the “beam” and “spring” like elements

Given the symmetries the unit cell should verify, one can consider only a 1/8 of cell. The identification of the resonant and spring-like elements can then be done as given in Figure 2.10, and the “new” microstructured unit cell can be understood as a repositioning of the resonating element along the first bisector.

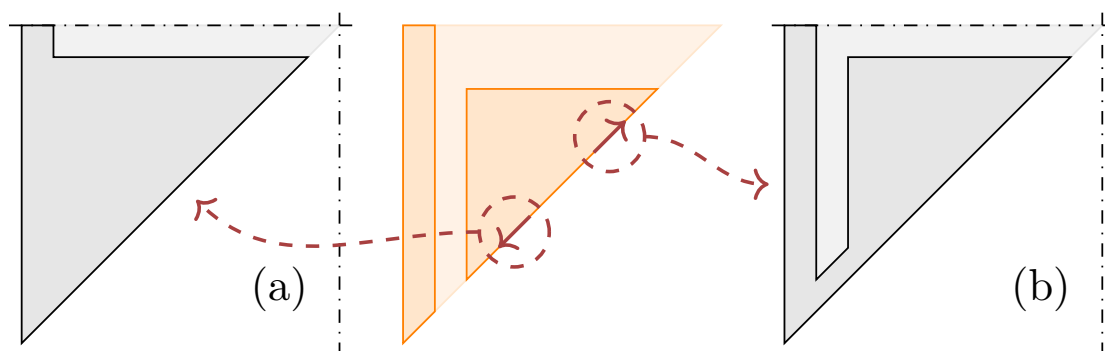


Figure 2.10: Configurations available for the positioning of the resonator. (*center*) side of the cell and resonator, whose position generates two different unit cell geometry.

For both cells, the minimization of f_{BG} is obtained by the minimization of the “beam” stiffness, *i.e.* the minimization of π_p , as confirmed by a parametric study. The minimum value of e_p is set by the manufacturing constraints. A second parametric study upon e_g gives, for the “classical” unit cell

$$f_{\text{BG}} = \min f_{\text{BG}} \quad \text{for} \quad \pi_g = 0.8 \quad (2.23)$$

Such a result should not be surprising: indeed, for this geometry, the stiffness and the resonator's mass of the system cannot be simultaneously optimized, having

$$\frac{a_r}{a} + \frac{l_p}{a} = 1 \quad \text{and} \quad \frac{l_p}{a} = \pi_g \quad (2.24)$$

where a_r is the size of one square resonator and l_p the length of a "beam" element linking them. We can see here a classical limitation of the "performances" of the design of mechanical structures: the value of π_g minimizing f_{BG} is not given by manufacturing constraints, but by the cell geometry itself. The novel geometry does not have this disadvantage, having

$$1 = 2\pi_p + 3\pi_g + 2\frac{a_r}{a} \quad \text{and} \quad 1 = 2\pi_p + 2\pi_g + \frac{l_p}{a} \quad (2.25)$$

allowing to simultaneously minimize the stiffness and maximize the resonator's mass. Therefore, the values of e_p and e_g , corresponding to the limitations imposed by the manufacturing process, according to Table 2.2, are

$$\boxed{e_p = 0.25 \text{ [mm]} \quad \text{and} \quad e_g = 0.35 \text{ [mm]}} \quad (2.26)$$

2.3.2 Geometry of the plate

The determination of a , n_1 , n_2 and e is made respecting constraints given in Tables 2.2 and 2.3. For a proper visualization of the band-gap effect, it is usually considered that one should have

$$\frac{n_1 - n_c}{2}, \frac{n_2 - n_c}{2} \geq 4 \quad (2.27)$$

On the other hand, as it has been mentioned before, the manufacturing time is heavily determined by the number of holes in the plate, a manual intervention being required for each cell. As the machining area is limited (see Table 2.2), after several tests, we eventually set

$$\boxed{a = 2 \text{ [cm]}} \quad (2.28)$$

Test made on the side of the plate limited the available zone to architecture the plate, leading to

$$\boxed{n_1 = 11 \quad \text{and} \quad n_2 = 9} \quad (2.29)$$

We will see in Chapters 3 and 4 that these values occasioned a degradation of the performances of our *proof of concept* and were also of significant importance for the relaxed micromorphic modelling, which will be discussed in Chapter 5. The out-of-plane thickness e of the plate has to be:

- small enough to maximize the response of the structure
- big enough to verify static design constraints given in Table 2.3

Due to the restrictions of available plates, we eventually set

$$\boxed{e = 1 \text{ [mm]}} \quad (2.30)$$

We will show in the following sections such value allows to measure the displacement in the plate, it is not adapted to the plane strain hypothesis. This inadequate hypothesis will be treated in Chapter 4.

2.4 Validation of the functional specifications

2.4.1 For the band-gap

Figures 2.4, 2.5 and 2.6 present the dispersion curves and the respective acoustic/optic modes of the cell along the contour of the irreducible Brillouin zone for $a = 2$ [cm], which is the value retained for manufacturing. From these plots, one can deduce the characteristics of the band-gap for the considered cell, which are given in Table 2.5.

Central frequency of the band-gap	Width of the band-gap
1920 [Hz]	409 [Hz]

Table 2.5: Characteristics of the final cell

2.4.2 For the microstructured plate

Despite the fact that the static response does not present the same difficulties that the resolution for a large frequential range, one can note the necessary thinness of the elements at the corners of the cell and along the borders of each cell, contrasting with the ones of the resonant elements, assuring the convergence of the results with respect to the mesh.

The maximum Von Mises stress is reached in the corner of plate, close the punctual support. The safety coefficient, having $\sigma_0 = 50$ [MPa], we have

$$s = \frac{\sigma_0}{\max \sigma_{VM}} = 4.4 \quad (2.31)$$

which satisfies the constraints given in Table 2.3.

2.5 Manufacturing the microstructured plate

The manufacturing process should theoretically be chosen with respect to the functions and constraints the considered mechanical is supposed to verify (which have been given in Tables 2.1 and 2.3). However, in practice, the opposite approach is considered, given:

- the available manufacturing processes
- the laboratory culture
- the cost

which therefore limit our manufacturing possibilities. The titanium alloy bulk plate has eventually been microstructured at the FEMTO-ST in Besançon, under the supervision of Pr. Sébastien Thibaud by Electrical Discharge Machining wire erosion (EDM wire erosion). Figure 2.11 presents the cutting of the holes in the plate.

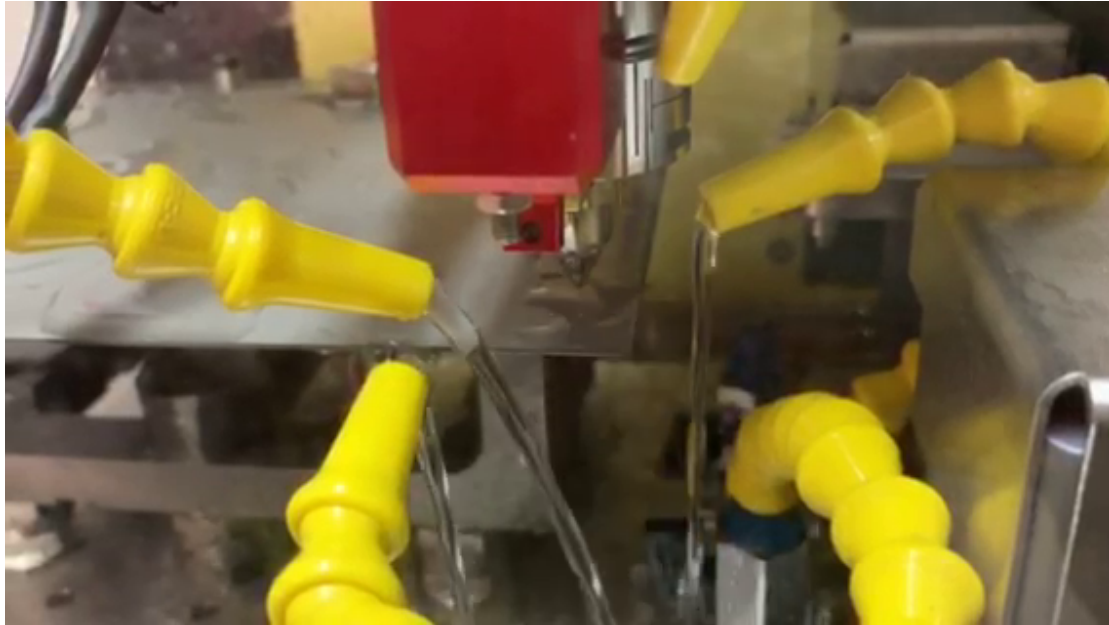


Figure 2.11: Manufacturing of the microstructured plate.

2.6 Instrumentation and measurements

2.6.1 Design of the actuator

Given the bidimensionnal aspect of the microstructured plate on one hand and its relatively low mechanical resistance, we considered solliciting the plate by a piezoelectric excitation by patches at the center of the plate. If the modelling of such elements will be presented in Chapter 3, we explain here how these elements allowed the characterization of our *proof of concept*. Figure 2.12 presents the positioning and different implementations of the patches and their electrical supply with initial (dashed) and deformed (displacements, extremely exaggerated, are not represented at the “right scale”) of the plate. For an easier readability, only the central part of the microstructured plate is represented. The sides of the patches glued to the plate are linked to the electrical ground while the exterior sides of the patches are under the same electrical potential.

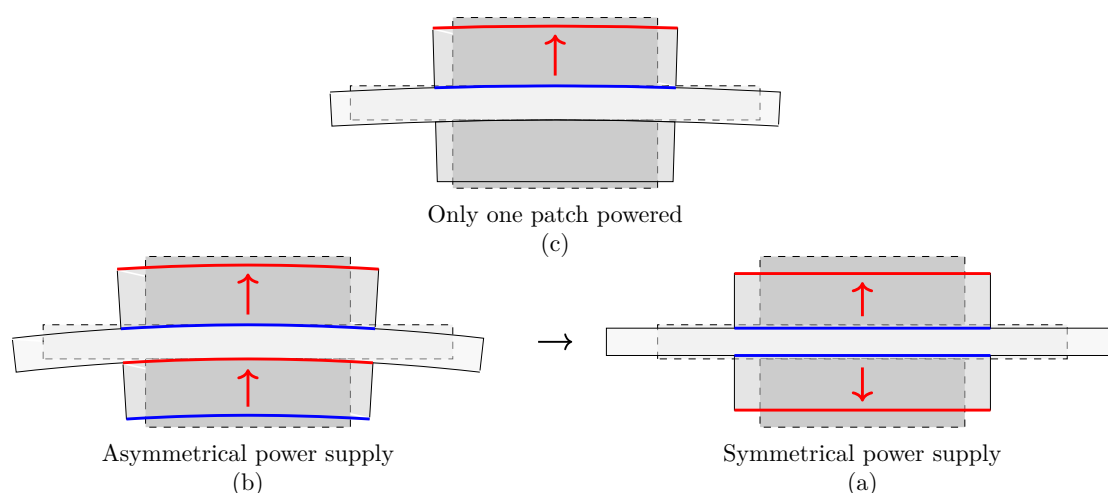


Figure 2.12: Considered power supplies with the piezoelectric patches. Elements in dashed lines represent the non-powered piezoelectric patches and undistorted center of the plate while elements in continuous lines represent the powered piezoelectric patches deforming the microstructured plate. In particular, blues lines represent the side of the piezoelectric patches connected to the ground while red lines represent the powered side of the piezoelectric patches, the red arrows the polarization. For the sake of simplicity and symmetry reasons, the same electric potential is applied on both red areas.

The power supply of the piezoelectric patches is designed to avoid flexural vibration modes in the plate at the considered frequencies, so that the applied load is a pure in-plane expansion as shown in Figure 2.12 (a). Such a setup, in addition to preserving the symmetry of the system along the medium plane of the microstructured plate, characteristic that will be used during the numerical simulations of the system for the comparison with the experiments. As the titanium alloy plate has to be connected to the ground, configuration shown in Figure 2.12 (b) is discarded, while configuration Figure 2.12 (c), mainly solliciting the bending modes of the plate, is not adapted to the relaxed micromorphic modelling. The chosen electric supply with its wiring is presented in Figure 2.13.

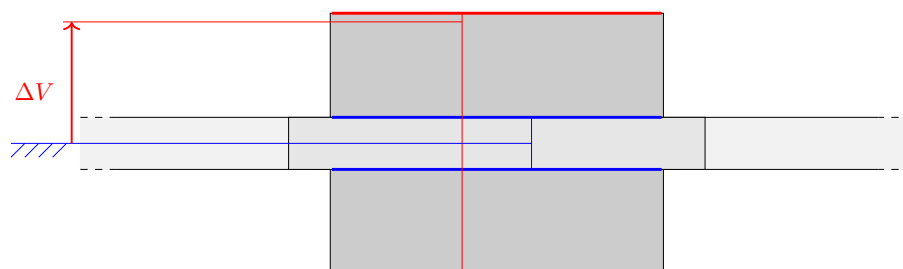


Figure 2.13: Chosen electric supply of the piezoelectric patches

Two piezoelectric patches (MEGGIT PZ 21, $\varnothing 16[\text{mm}]$ $2[\text{mm}]$ -thick) are used as actuators to generate in-plane extension pulse waves in the plate (see Figure 2.14). Ex-

citation signals are generated by a function generator and then amplified to power the piezoelectric patches.

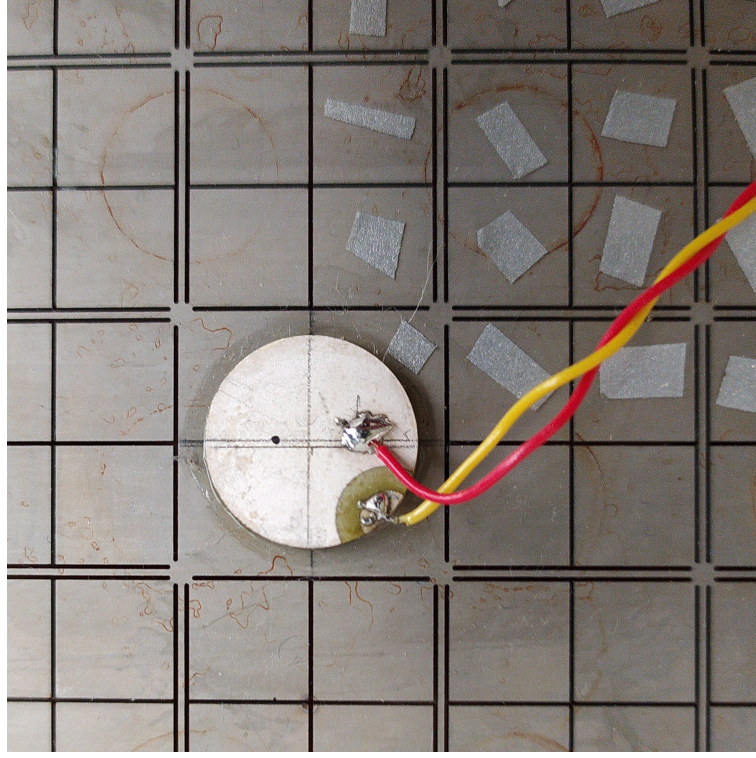


Figure 2.14: Upper piezoelectric patch *in situ* with its electric supply, glued to the architected plate.

A proper way to visualize the band-gap for our *proof of concept* would have, as it has been done *via* numerical simulations in [Barbagallo 2019a], to send expansion pulses with the piezoelectric patches which, with the adequate frequency parameters, would have allowed to “see the waves vanishing” as propagating into the microstructured plate. Given the relative narrowness of our band gap, an appropriate excitation signal V would have been a burst signal centered in the band gap, of spectrum

$$\mathcal{F}(V)(\omega) = \frac{2}{\Delta\omega} \exp \left[-2 \left(\frac{\omega - \omega_0}{\Delta\omega} \right)^2 \right] \quad (2.32)$$

where $\mathcal{F}(V)$ is the Fourier transform of V , $\omega_0 = 2\pi \cdot 1900$ [rad.s⁻¹] and $\Delta\omega = 50$ [rad.s⁻¹]. We then have

$$V(t) = \exp \left(-i\omega_0 t - \frac{1}{8} \Delta\omega^2 t^2 \right) \quad (2.33)$$

Unfortunately, the small size of the plate combined to the titanium alloy used for manufacturing does not allow such temporal approach: indeed, anticipating Chapter 3, the wavelength λ_c of to the central component of the spectrum $\mathcal{F}(V)$ for the titanium alloy

considered is

$$\lambda_c = \frac{2\pi c_l}{\omega_0} = \frac{2\pi}{\omega_0} \sqrt{\frac{\lambda}{\rho}} = 10.2 \text{ [m]} \gg 25 \text{ [cm]} \quad (2.34)$$

way bigger than the plate's size (25 [cm]). Consequently, the small size of the plate does not allow to see the (non-)propagation of waves in the band-gap as, the multiple reflections of the emitted waves on the traction-free boundaries preventing the proper identification of the vanishing waves. Given this, we then consider the classical computation of the frequency response function (FRF) of the system, defined by

$$\text{FRF}(\mathbf{x}) = \frac{\mathcal{F}(\dot{\mathbf{u}})(\mathbf{x})}{\mathcal{F}(V)} \quad (2.35)$$

which, in the approximation of linearity, does not depend of V . We could argue for a long time about the validity of such an hypothesis by considering each component of the energy chain as presented in Figure 2.15. The analysis of the experimental results in Chapter 4 will largely justify this hypothesis.

The experimental characterization of a linear system is usually made by one of the three following processes:

- white noise
- sine sweeps
- impulse response

Given the small amplitudes measured and the piezoelectric excitation, the technique of the impulse response is considered, *i.e.*

$$V(t) = V_0 \sin(2\pi \frac{f_0 t}{t_0}) \quad (2.36)$$

where V_0 (in [V]), f_0 (in [Hz]) and t_0 (in [s]) are respectively the amplitude, the maximum frequency and the duration of the input signal. As the theoretical band-gap lays between 1700 and 2100 [Hz], sine sweeps are chosen to impose the external load and the signal's frequency is swept from 0 to 2500 [Hz], therefore

$$f_0 = 2500 \text{ [Hz]} \quad (2.37)$$

The amplitude of the excitation must be chosen respecting the conditions:

- be lower than the breakdown voltage of the piezoelectric patches
- be high enough to have measurable output signals
- be low enough to have a linear response

As the last condition has already been evoked, several tests allow us to set

$$V_0 = 100 \text{ [V]} \quad (2.38)$$

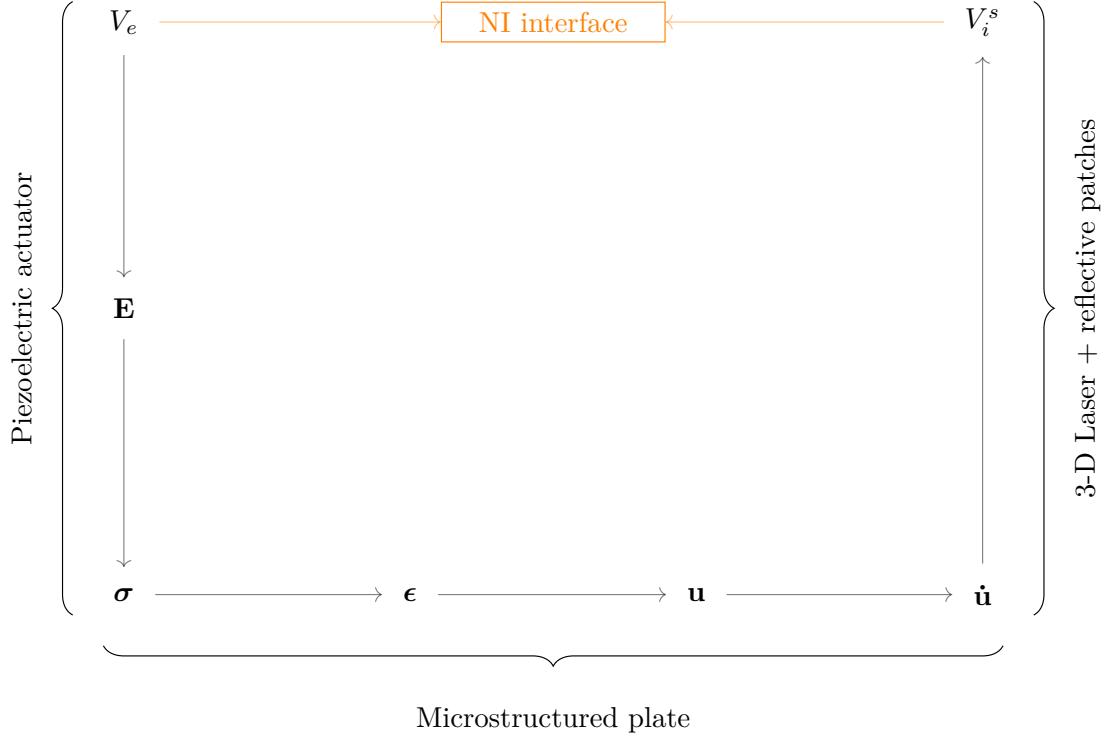


Figure 2.15: Energy and acquisition chain for the experimental set-up.

The duration of the excitation is given by the desired frequency resolution for the comparison with our experimental models. Indeed, by duality, we have

$$\Delta f = \frac{1}{t_0} \implies t_0 = \frac{1}{\Delta f} \quad (2.39)$$

Requiring $f_r = 0.1$ [Hz], we deduce

$$t_0 = 10 \text{ [s]} \quad (2.40)$$

2.6.2 Experimental measurements

Given the low amplitude of the displacements in the plate, the 3-D laser Polytec CLV-3D has been chosen to measure speeds at the surface of the microstructured plate. The instrumentation of the plate is presented in Figure 2.16.

As the microstructured plate had to be re-positioned for each point measured, only 1/4 of the plate is instrumented, *i.e.* reflector patches are glued on each resonator of the upper right part of the plate. For the sake of simplicity, we consider each measure to correspond at the center of the resonator instrumented, *i.e.*

$$\dot{\mathbf{u}}(\mathbf{x}_{\text{measured}}^i) = \dot{\mathbf{u}}((n_1^i a \pm a/2)\mathbf{x}_1 + (n_2^i a \pm a/2)\mathbf{x}_2) \quad (2.41)$$

where $(n_1^i, n_2^i) \in \mathbb{N}^2$. In Chapter 4, we will show that such an assumption, taking into account the frequency range and the titanium alloy used, is particularly suitable for the comparison with the theoretical models.

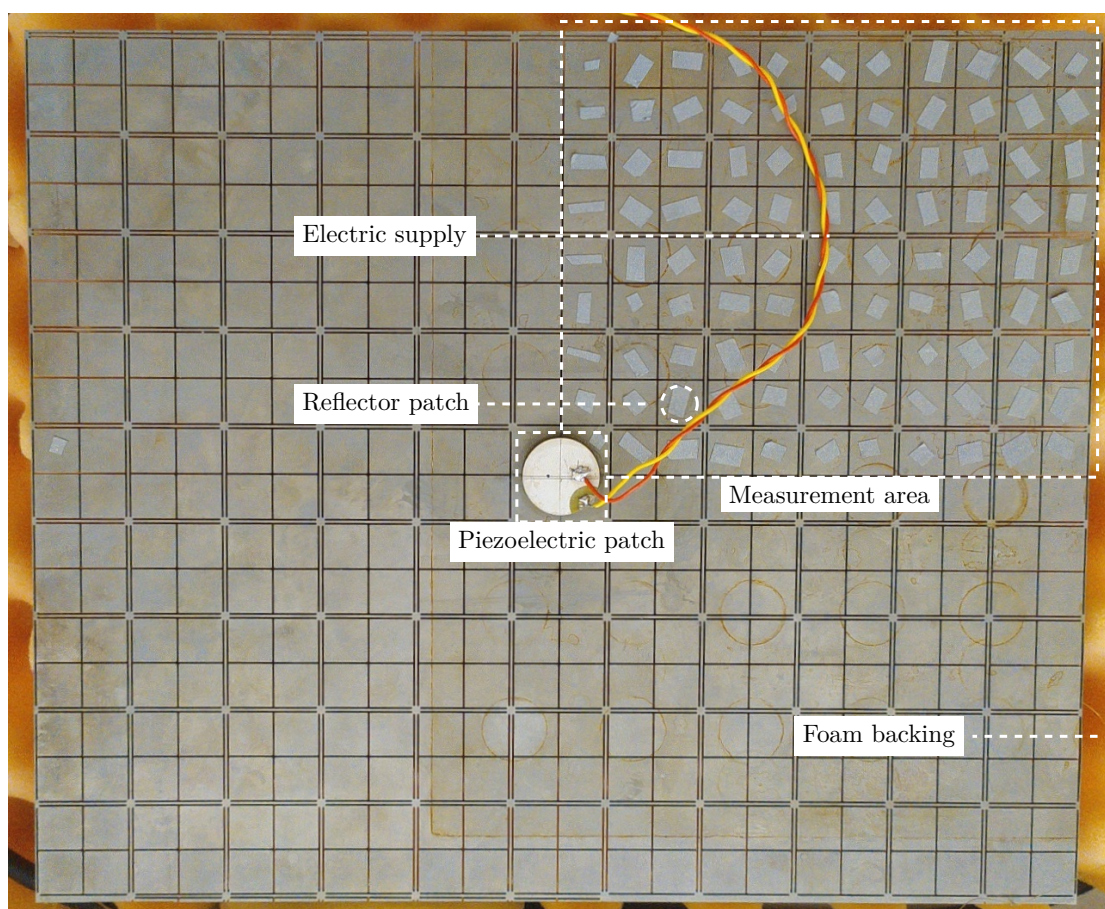


Figure 2.16: Experimental set-up: glued in the center of the metamaterial's plate there is the top piezoelectric patch (another one being placed on the other side of the plate) that has been used as an actuator for the external excitation. The tapes placed on the top-right quarter of the plate can reflect a laser's beam for speed measurements.

To both record the excitation signal and the measured speeds in the three directions of space, an interface under MATLAB has been designed, allowing to easily choose the main parameters for each test, namely the required frequency range, the resolution and coordinates of the considered measurement points. This interface is given in Figure 2.17.

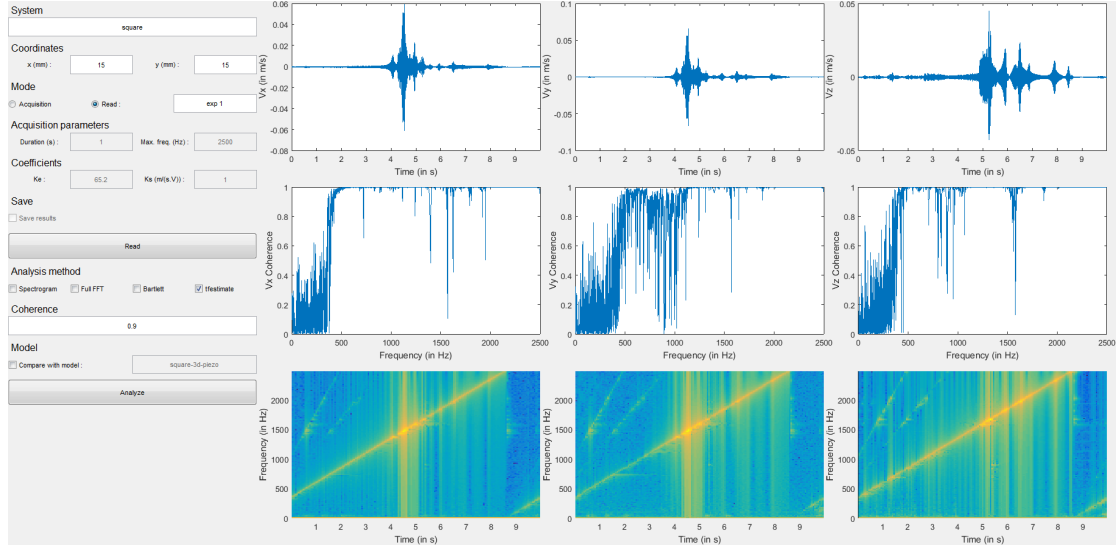


Figure 2.17: Overview of the interface developed under MATLAB. (left) Parameters of the acquisition/reading. (right, top to bottom) Temporal response in the three directions of space with their respective coherence and spectrogram.

One can quickly notice, although it has not been investigated, on the plotting of the spectrogram, higher-order non-linear components of velocity spectrum, revealed by the presence of, in addition to the linear response signaled by the main yellow line, of two small lines of respective double and triple slope. Eventually, the analogical signals are sampled and sent to the computer *via* a NATIONAL INSTRUMENTS interface as presented in Figure 2.18.

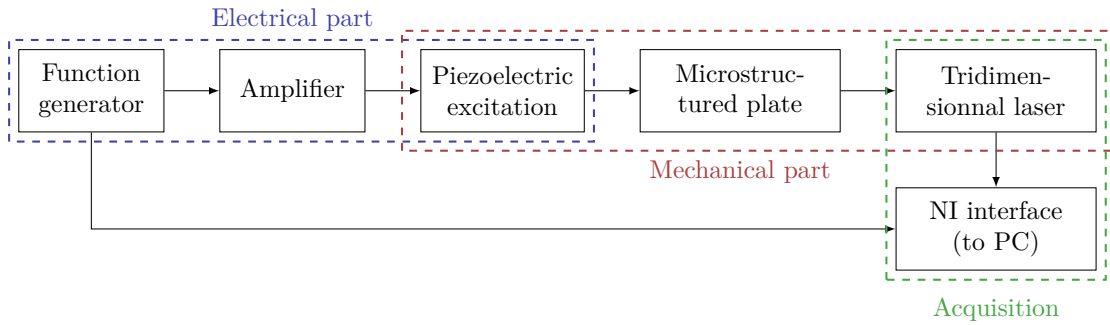


Figure 2.18: Energy and information chain of the instrumented microstructured plate.

Very classically, one now has to determine the sampling parameter Δt for our measurements. Given the position of the theoretical band gap, we set the frequency range investigated Δf to be

$$\Delta f = [0, 2500] \text{ [Hz]} \quad (2.42)$$

According to the Shannon-Nyquist sample theorem, in order to correctly sample a sig-

nal of maximum frequency f_0 , the sampling period Δt must verify

$$\Delta t \geq \frac{1}{f_{\mathcal{N}}} \quad \text{with} \quad f_{\mathcal{N}} = 2f_0 \quad (2.43)$$

where $f_{\mathcal{N}}$ is the Nyquist frequency. We therefore chose

$$\Delta t = 2 \cdot 10^{-4} \text{ [s]} \quad (2.44)$$

Given this, the only theoretical hypothesis introduced in the experimental results is the linearity, justifying the inverse Fourier transform of the measured signals. Such hypothesis, allowing the computation of the theoretical response in the frequency domain instead of the of time domain as presented in Figure 2.19, considerably simplifies the comparison. More generally, we chose not to add any additional hypothesis on the experimental results, despite the numerous experimental defects: as we will present in Chapter 4, our theoretical models will endorse every inadequate hypothesis and experimental error.

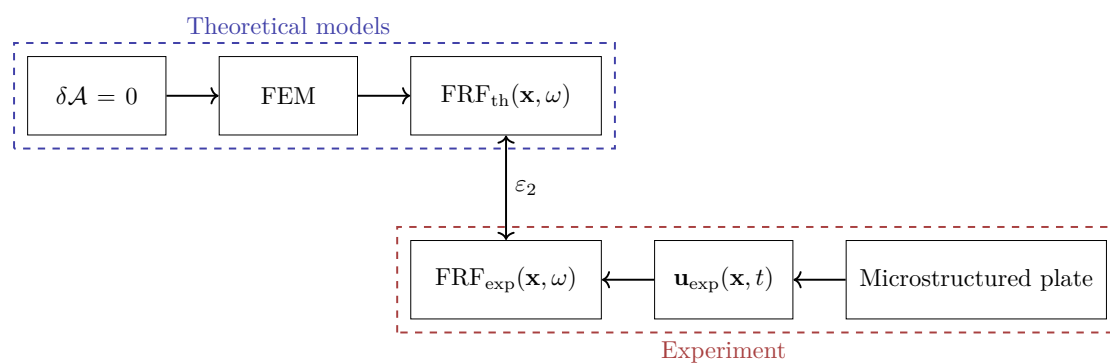


Figure 2.19: Comparison in the frequency domain between the experimental system and the theoretical models as presented in Figure 1.2.

From Cauchy to micromorphic modelling

Contents

3.1	The classical Cauchy model	32
3.1.1	The Mandel-Voigt notation	38
3.1.2	The isotropic Cauchy material	39
3.2	The relaxed micromorphic model	43
3.2.1	The axl mapping	47
3.2.2	Application to our microstructured cell	48
3.3	The equivalent macroscopic Cauchy model	52
3.4	The piezoelectric model	53
3.5	Symmetries	57
3.5.1	A first case: plane \mathcal{P} of normal \mathbf{n}	58
3.5.2	Using the Curie's Principle	59
3.6	Boundary conditions at interfaces	61
3.6.1	Between two Cauchy continua	61
3.6.2	Between a Cauchy medium and a relaxed micromorphic medium	62
3.7	Solving	64
3.7.1	Discretization of the geometry	65
3.7.2	Damping of the structures	75
3.8	Convergence of the microstructured and relaxed micromorphic models	81
3.8.1	The long-wave limit: statics	84
3.8.2	Broadband dynamics of the metamaterial's plate	89

3.1 The classical Cauchy model

The classical Cauchy modelling of a continuous medium considers the displacement field $\mathbf{u} : \Omega \times [t_1, t_2] \rightarrow \mathbb{R}^3$ to be the only kinematic field. Moreover, the Cauchy postulate [Cauchy 1828a, Cauchy 1828b, Piola 1825] supposes that the forces applied on Ω are of two types:

- Body forces given $\forall \mathbf{x} \in \Omega$ by their density (such a hypothesis allowed him to simplify the local equilibrium by ρ_c):

$$\mathbf{f}(\mathbf{x})dm = \rho_c(\mathbf{x})\mathbf{f}(\mathbf{x})d\Omega \quad (3.1)$$

- Contact forces \mathbf{t} characterized by a surface density of force depending only of the considered point \mathbf{x} and the normal \mathbf{n} [Dell’Isola 2016] to $\partial\Omega$ at \mathbf{x} :

$$\mathbf{t}(\mathbf{x}, \mathbf{n})d\Gamma \quad (3.2)$$

Given these hypotheses, the transformation φ of the considered structure corresponding to its deformation under the aforementioned forces (and/or prescribed displacements) is represented in Figure 3.1.

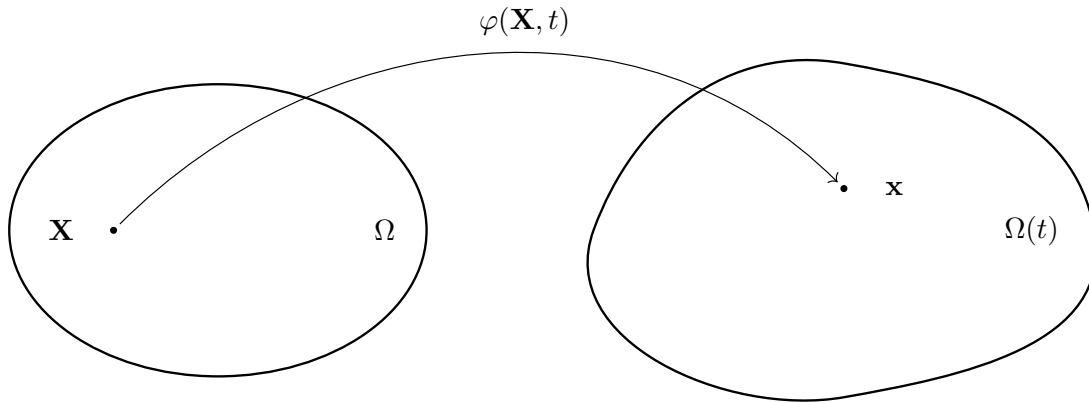


Figure 3.1: Transformation of a Cauchy medium

where \mathbf{X} is the position of the considered particle in a configuration (reached or not by our structure) chosen as reference and \mathbf{x} its current position: this is the Lagrangian description. The structures studied in this manuscript, given the loading cases considered, will deviate little from their initial reference configuration, that will allow us to write

$$\forall t \in [t_1, t_2] : \Omega(t) = \Omega = \Omega(t_1) = \Omega(t_2) \quad (3.3)$$

and

$$\mathbf{x} = \mathbf{X} + \mathbf{u}(\mathbf{X}, t) \quad (3.4)$$

Such a hypothesis allows to indifferently use \mathbf{x} or \mathbf{X} in our formulas:

- the Lagrangian variable to compute time derivatives, allowing to “forget” the subtleties linked *e.g* to the notion of particle derivative.
- the Eulerian variable when it will come to write constitutive laws, equilibriums, *etc.*

This hypothesis will be kept for the rest of the manuscript and, for the sake of simplicity, \mathbf{x} will be used in the following chapters. Given this, the kinetic k_c and strain w_c energy densities of the classical Cauchy continuum are defined as

$$\begin{aligned} k_c(\dot{\mathbf{u}}) &= \frac{1}{2} \langle \dot{\mathbf{u}}, \rho_c \dot{\mathbf{u}} \rangle \\ w_c(\text{sym } \nabla \mathbf{u}) &= \frac{1}{2} \langle \text{sym } \nabla \mathbf{u}, \mathbb{C} \text{sym } \nabla \mathbf{u} \rangle \end{aligned} \quad (3.5)$$

where $\dot{\mathbf{u}} = \frac{d\mathbf{u}}{dt}$, $\rho_c : \Omega \rightarrow \mathbb{R}^+$ the mass density and $\mathbb{C} : \mathfrak{s}(\mathbb{R}^3) \rightarrow \mathfrak{s}(\mathbb{R}^3)$ a 4th order tensor, which is:

- symmetric, *i.e.*

$$\forall (\mathbf{X}, \mathbf{Y}) \in \mathfrak{s}(\mathbb{R}^3)^2 : \langle \mathbf{X}, \mathbb{C}\mathbf{Y} \rangle = \langle \mathbf{Y}, \mathbb{C}\mathbf{X} \rangle \quad (3.6)$$

- positive, *i.e.*

$$\forall \mathbf{X} \in \mathfrak{s}(\mathbb{R}^3) : \langle \mathbf{X}, \mathbb{C}\mathbf{X} \rangle \geq 0 \quad (3.7)$$

- definite, *i.e.*

$$\langle \mathbf{X}, \mathbb{C}\mathbf{X} \rangle = 0 \quad \Rightarrow \quad \mathbf{X} = \mathbf{0} \quad (3.8)$$

Two important remarks can be made here:

- To choose $\mathbb{C} \text{sym } \nabla \mathbf{u} \in \mathfrak{s}(\mathbb{R}^3)$ ($= \boldsymbol{\sigma}$, which will be introduced later) is the Boltzmann’s axiom of symmetry [Boltzmann 1905], so called by Hamel [Hamel 1912]. The possible asymmetry of such a tensor has been mentioned by Cauchy at the end of his life, Saint-Venant, Poisson, Kelvin and Voigt through the XIXth century until the Cosserats’ [Cosserat 1909] works, which will briefly be evoked in the following section.
- $\mathbb{C} \in \mathfrak{s}(\mathbb{R}^{3 \times 3})$ is not an additional hypothesis here, in the sense that, w_c being a quadratic form, \mathbb{C} is necessarily symmetric. Such an assumption makes the number of its independent coefficients automatically fall to at most 21, to compare to the 81 in the most general case.

The Lagrangian density ℓ_c of the Cauchy continuum is defined, as it is for any mechanical system, by

$$\ell_c(\dot{\mathbf{u}}, \nabla \mathbf{u}) = k_c(\dot{\mathbf{u}}) - w_c(\text{sym } \nabla \mathbf{u}) \quad (3.9)$$

The action functional \mathcal{A}_c of a Cauchy medium occupying a bounded domain $\Omega \subset \mathbb{R}^3$ is

$$\mathcal{A}_c = \mathcal{A}_{\text{ext}}^c + \mathcal{A}_{\text{int}}^c \quad \text{where} \quad \begin{cases} \mathcal{A}_{\text{int}}^c[\mathbf{u}] = \int_{t_1}^{t_2} \int_{\Omega} \ell_c d\Omega dt = \int_{t_1}^{t_2} \int_{\Omega} (k_c - w_c) d\Omega dt \\ \mathcal{A}_{\text{ext}}^c[\mathbf{u}] = \int_{t_1}^{t_2} \int_{\partial\Omega_N} \langle \mathbf{t}, \mathbf{u} \rangle d\Gamma dt + \int_{t_1}^{t_2} \int_{\Omega} \langle \mathbf{f}, \mathbf{u} \rangle d\Omega dt \end{cases} \quad (3.10)$$

Chapter 3. From Cauchy to micromorphic modelling

where $\mathbf{f} : \Omega \rightarrow \mathbb{R}^3$ and $\mathbf{t} : \partial\Omega_{\mathcal{N}} \rightarrow \mathbb{R}^3$ are known, being modeled by the mechanician. Usually, the modelling of mechanical systems, in addition to body and contact forces, requires the imposition of displacement upon some of its boundaries, corresponding to kinematic links with other parts of the considered structure: \mathbf{u} has to verify the Dirichlet boundary condition

$$\forall t \in [t_1, t_2], \mathbf{u} = \mathbf{u}_0 \quad \text{on } \partial\Omega_{\mathcal{D}} \quad (3.11)$$

A well-posed (mechanical) problem requires

$$\partial\Omega = \partial\Omega_{\mathcal{D}} \cup \partial\Omega_{\mathcal{N}} \quad \text{and} \quad \partial\Omega_{\mathcal{D}} \cap \partial\Omega_{\mathcal{N}} = \emptyset \quad (3.12)$$

To close our Cauchy-Kowalewski problem, we set the initial conditions

$$\begin{cases} \mathbf{u}(t = t_1) = \mathbf{u}_i \\ \dot{\mathbf{u}}(t = t_1) = \mathbf{v}_i \end{cases} \quad \text{in } \Omega. \quad (3.13)$$

Through this manuscript, we will always consider our media to verify Heaviside (homogeneous) initial conditions, *i.e.*

$$\begin{cases} \mathbf{u}(t = t_1) = \mathbf{0} \\ \dot{\mathbf{u}}(t = t_1) = \mathbf{0} \end{cases} \quad (3.14)$$

The order of derivation of the initial conditions necessary for the well-posedness can be inferred from, as we will see later, the strong form of the problem under the state-space representation. As we chose to describe our mechanical structures through the Principle of Least Action, *i.e.*, in the case of continua, giving the Lagrangian density of our system, the usual hypothesis of small deformation, *i.e.*

$$\frac{\partial u_i}{\partial x_j} \ll 1 \quad \forall \{i, j\} \in \{1, 2, 3\}^2 \quad (3.15)$$

has not be explicitly made. Such assumptions must not, despite their apparent similarity, be confused with Equation 3.3, and both should be explicitly mentioned if used. We can quickly mention the Euler's critical load, well known result of buckling, obtained in a linear framework (*i.e.* with hypothesis 3.15) but without Equation 3.3 (internal forces and torques are computed on the distorted configuration).

The Principle of Least Action [Dell'Isola 2012b] states that the trajectory followed by the system $\mathbf{u} : (\mathbf{x}, t) \in \Omega \times [t_1, t_2] \mapsto \mathbf{u}(\mathbf{x}, t)$ is the one for which the action functional is stationary (the Hamilton Principle, as we introduced a Lagrangian density), *i.e.* verifies

$$\{\delta\mathcal{A}_c[\mathbf{u}] = 0 \text{ where } \mathbf{u} \text{ verifies 3.11 and 3.13}\} \quad (3.16)$$

Given the kinetic and strain energy densities introduced in (3.9), we can define the space of configuration \mathcal{Q} to which \mathbf{u} should belong

$$\mathcal{Q} = \{\mathbf{u} : \mathbf{u} \text{ verifies 3.11 and 3.13}\} \quad (3.17)$$

Figure 3.2 represents the actual evolution of the system in the space of configuration, $\mathbf{u}(t_1)$ and $\mathbf{u}(t_2)$ being given.

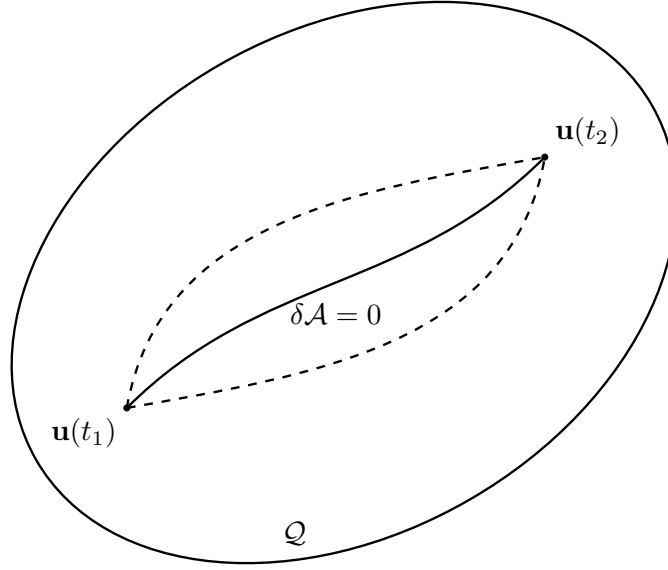


Figure 3.2: Evolution of the system in the space of configurations \mathcal{Q} : two admissible trajectories (dashed lines) and the actual trajectory (thick line) verifying the Principle of Least Action.

The computation of the stationarity of the action \mathcal{A}_c and therefore of its first variation $\delta\mathcal{A}$ can be seen, through $\delta\mathbf{u}$, in two different ways:

- a small perturbation around the actual trajectory \mathbf{u}_0 :

$$\mathbf{u} = \mathbf{u}_0 + \delta\mathbf{u} \quad (3.18)$$

- the difference between two admissible trajectories \mathbf{u}_1 and \mathbf{u}_2 of the system:

$$\Delta\mathbf{u} = \mathbf{u}_2 - \mathbf{u}_1 \quad (3.19)$$

Under this second form, one can derive the boundary and initial conditions for $\delta\mathbf{u}$:

$$\begin{cases} \delta\mathbf{u}(t_1) = \mathbf{0} = \delta\mathbf{u}(t_2) & \text{in } \Omega \\ \forall t \in [t_1, t_2], \delta\mathbf{u}(t) = \mathbf{0} & \text{on } \partial\Omega_{\mathcal{D}} \end{cases} \quad (3.20)$$

Before computing the first variation of \mathcal{A} , one can notice that

$$\forall (\mathbf{S}, \mathbf{X}) \in \mathfrak{s}(\mathbb{R}^3) \times \mathbb{R}^{3 \times 3}, \langle \mathbf{X}, \mathbf{S} \rangle = \langle \text{sym } \mathbf{X}, \mathbf{S} \rangle \quad (3.21)$$

Let us begin with the strain energy density:

$$\begin{aligned} \delta \int_{t_1}^{t_2} \int_{\Omega} w_c(\nabla\mathbf{u}) d\Omega dt &= \delta \int_{t_1}^{t_2} \int_{\Omega} \frac{1}{2} \langle \text{sym } \nabla\mathbf{u}, \mathbb{C} \text{sym } \nabla\mathbf{u} \rangle d\Omega dt \\ &= \int_{t_1}^{t_2} \int_{\Omega} \langle \nabla\delta\mathbf{u}, \mathbb{C} \text{sym } \nabla\mathbf{u} \rangle d\Omega dt \\ &= \int_{t_1}^{t_2} \int_{\Omega} \text{div}(\mathbb{C} \text{sym } \nabla\mathbf{u} \cdot \delta\mathbf{u}) d\Omega dt - \int_{t_1}^{t_2} \int_{\Omega} \langle \text{div}(\mathbb{C} \text{sym } \nabla\mathbf{u}), \delta\mathbf{u} \rangle d\Omega dt \end{aligned} \quad (3.22)$$

Chapter 3. From Cauchy to micromorphic modelling

Gauss theorem

$$\int_{\Omega} \operatorname{div} \mathbf{X} \, d\Omega = \int_{\partial\Omega} \mathbf{X} \cdot d\Gamma = \int_{\partial\Omega} \langle \mathbf{X}, \mathbf{n} \rangle d\Gamma \quad (3.23)$$

where \mathbf{n} is the normal of $\partial\Omega$ at the considered point and $d\Gamma$ the elementary surface gives

$$\delta \int_{t_1}^{t_2} \int_{\Omega} w_c(\nabla \mathbf{u}) \, d\Omega dt = \int_{t_1}^{t_2} \int_{\partial\Omega} \langle (\mathbb{C} \operatorname{sym} \nabla \mathbf{u}) \cdot \mathbf{n}, \delta \mathbf{u} \rangle d\Gamma dt - \int_{t_1}^{t_2} \int_{\Omega} \langle \operatorname{div}(\mathbb{C} \operatorname{sym} \nabla \mathbf{u}), \delta \mathbf{u} \rangle d\Omega dt \quad (3.24)$$

The stationarity of the kinetic energy is easier, having

$$\begin{aligned} \delta \int_{t_1}^{t_2} \int_{\Omega} k_c(\dot{\mathbf{u}}) \, d\Omega dt &= \delta \int_{t_1}^{t_2} \int_{\Omega} \frac{1}{2} \langle \dot{\mathbf{u}}, \rho_c \dot{\mathbf{u}} \rangle \, d\Omega dt \\ &= \int_{t_1}^{t_2} \int_{\Omega} \langle \delta \dot{\mathbf{u}}, \rho_c \dot{\mathbf{u}} \rangle \, d\Omega dt \\ &= \int_{t_1}^{t_2} \int_{\Omega} \left[\frac{d}{dt} \langle \delta \mathbf{u}, \rho_c \dot{\mathbf{u}} \rangle - \langle \delta \mathbf{u}, \rho_c \ddot{\mathbf{u}} \rangle \right] \, d\Omega dt \\ &= \int_{\Omega} \int_{t_1}^{t_2} \frac{d}{dt} \langle \delta \mathbf{u}, \rho_c \dot{\mathbf{u}} \rangle \, d\Omega dt - \int_{t_1}^{t_2} \int_{\Omega} \langle \delta \mathbf{u}, \rho_c \ddot{\mathbf{u}} \rangle \, d\Omega dt \quad (3.25) \\ &\quad \text{(integration by parts)} \\ &= \int_{\Omega} [\langle \delta \mathbf{u}, \rho_c \dot{\mathbf{u}} \rangle]_{t_1}^{t_2} \, d\Omega - \int_{t_1}^{t_2} \int_{\Omega} \langle \delta \mathbf{u}, \rho_c \ddot{\mathbf{u}} \rangle \, d\Omega dt \\ &\quad \text{=0 by Equation 3.20} \\ &= - \int_{t_1}^{t_2} \int_{\Omega} \langle \delta \mathbf{u}, \rho_c \ddot{\mathbf{u}} \rangle \, d\Omega dt \end{aligned}$$

Eventually, we get

$$\begin{cases} \delta \mathcal{A}_{\text{int}}^c &= \int_{t_1}^{t_2} \int_{\Omega} \langle \delta \mathbf{u}, -\rho_c \ddot{\mathbf{u}} + \operatorname{div}(\mathbb{C} \operatorname{sym} \nabla \mathbf{u}) \rangle \, d\Omega dt - \int_{t_1}^{t_2} \int_{\partial\Omega} \langle \delta \mathbf{u}, (\mathbb{C} \operatorname{sym} \nabla \mathbf{u}) \cdot \mathbf{n} \rangle \, d\Gamma dt \\ \delta \mathcal{A}_{\text{ext}}^c &= \int_{t_1}^{t_2} \int_{\Omega} \langle \delta \mathbf{u}, \mathbf{f} \rangle \, d\Omega dt + \int_{t_1}^{t_2} \int_{\partial\Omega_N} \langle \delta \mathbf{u}, \mathbf{t} \rangle \, d\Gamma dt \end{cases} \quad (3.26)$$

The volume and the surface integrals being necessarily strictly equal to zero, we have

$$\begin{cases} \int_{t_1}^{t_2} \int_{\Omega} \langle \delta \mathbf{u}, \rho_c \ddot{\mathbf{u}} - \operatorname{div}(\mathbb{C} \operatorname{sym} \nabla \mathbf{u}) - \mathbf{f} \rangle \, d\Omega dt = 0 \\ \int_{t_1}^{t_2} \int_{\partial\Omega} \langle (\mathbb{C} \operatorname{sym} \nabla \mathbf{u}) \cdot \mathbf{n}, \delta \mathbf{u} \rangle \, d\Gamma dt - \int_{t_1}^{t_2} \int_{\partial\Omega_N} \langle \mathbf{t}_0, \delta \mathbf{u} \rangle \, d\Gamma dt = 0 \end{cases} \quad (3.27)$$

Having $\partial\Omega = \partial\Omega_{\mathcal{D}} \cup \partial\Omega_{\mathcal{N}}$, we have

$$\begin{aligned}
\int_{t_1}^{t_2} \int_{\partial\Omega} \langle (\mathbb{C} \operatorname{sym} \nabla \mathbf{u}) \cdot \mathbf{n}, \delta \mathbf{u} \rangle d\Gamma dt &= \int_{t_1}^{t_2} \int_{\partial\Omega_{\mathcal{D}}} \langle (\mathbb{C} \operatorname{sym} \nabla \mathbf{u}) \cdot \mathbf{n}, \delta \mathbf{u} \rangle d\Gamma dt + \int_{t_1}^{t_2} \int_{\partial\Omega_{\mathcal{N}}} \langle (\mathbb{C} \operatorname{sym} \nabla \mathbf{u}) \cdot \mathbf{n}, \delta \mathbf{u} \rangle d\Gamma dt \\
&\stackrel{=0 \text{ by Equation 3.20}}{=} \int_{t_1}^{t_2} \int_{\partial\Omega_{\mathcal{N}}} \langle (\mathbb{C} \operatorname{sym} \nabla \mathbf{u}) \cdot \mathbf{n}, \delta \mathbf{u} \rangle d\Gamma dt \\
&= \int_{t_1}^{t_2} \int_{\partial\Omega_{\mathcal{N}}} \langle \mathbf{t}, \delta \mathbf{u} \rangle d\Gamma dt
\end{aligned} \tag{3.28}$$

Given this, the traction-free boundary condition is said to be “natural”, *i.e.* automatically verified if the generalized work of the boundary forces is not included. Otherwise,

$$(\mathbb{C} \operatorname{sym} \nabla \mathbf{u}) \cdot \mathbf{n} = \mathbf{t} \quad \text{on } \partial\Omega_{\mathcal{N}} \tag{3.29}$$

In the same way, if $\mathbf{u} = \mathbf{u}_0$ on $\partial\Omega_{\mathcal{D}}$ was imposed *via* a Lagrange multiplier, replacing the action \mathcal{A} by \mathcal{A}'

$$\mathcal{A}'_c[\mathbf{u}, \boldsymbol{\lambda}] = \mathcal{A}_c[\mathbf{u}] - \int_{t_1}^{t_2} \int_{\partial\Omega_{\mathcal{D}}} \langle \boldsymbol{\lambda}, \mathbf{u} - \mathbf{u}_0 \rangle d\Gamma dt \tag{3.30}$$

one can easily derive from this

$$\int_{t_1}^{t_2} \int_{\partial\Omega_{\mathcal{D}}} \langle (\mathbb{C} \operatorname{sym} \nabla \mathbf{u}) \cdot \mathbf{n} - \boldsymbol{\lambda}, \delta \mathbf{u} \rangle d\Gamma dt = 0 \tag{3.31}$$

making the Lagrange multiplier $\boldsymbol{\lambda}$ correspond to the traction forces at the boundary $\partial\Omega_{\mathcal{D}}$ of the prescribed displacement (such a result is well-known for rigid solid mechanics). Given this, we get the classical equilibrium equation of the Cauchy continuum under its strong form

$$\rho_c \ddot{\mathbf{u}} = \operatorname{div} \boldsymbol{\sigma} + \mathbf{f} \tag{3.32}$$

where $\boldsymbol{\sigma}$ is the Cauchy stress tensor given by the constitutive law (stress-strain relation)

$$\boldsymbol{\sigma} = \mathbb{C} \operatorname{sym} \nabla \mathbf{u} \tag{3.33}$$

The associated boundary conditions are

$$\begin{cases} \mathbf{u} = \mathbf{u}_0 & \text{on } \partial\Omega_{\mathcal{D}} & \text{(Dirichlet)} \\ \boldsymbol{\sigma} \cdot \mathbf{n} = \mathbf{t} & \text{on } \partial\Omega_{\mathcal{N}} & \text{(Neumann)} \end{cases} \tag{3.34}$$

With the formalism of the Principle of Least Action, we deduced from the stationarity of the Action:

- the equilibrium equations in Ω
- the boundary conditions on $\partial\Omega$ *via* integration by parts

We are now going, thanks to some additional hypothesis, to simplify the expression of \mathbb{C} : for now, \mathbb{C} has 21 independent coefficient, which would be quite difficult to identify experimentally. The manipulation of second and fourth order tensors necessary for such simplifications commonly used for the materials considered in this manuscript and therefore requires specific mathematical tools.

3.1.1 The Mandel-Voigt notation

We deduced, through the Principle of Least Action, differential equations verified by \mathbf{u} in vector form: to facilitate the computation of the equilibrium, we are going to introduce the Mandel-Voigt notation, allowing to easily “replace” the second and fourth order tensors as, respectively, vectors and matrices. We consider a linear mapping $\mathbf{m} : \mathfrak{s}(\mathbb{R}^3) \rightarrow \mathbb{R}^6$ ([Voigt 1887, Voigt 1889, Mandel 1962]): the 6 independent components of $\mathbf{x} \in \mathfrak{s}(\mathbb{R}^3)$ are isomorphically mapped in a corresponding vector $\bar{\mathbf{x}}$ such as

$$\bar{\mathbf{x}}_\alpha = \mathbf{m}_{\alpha ij} \mathbf{x}_{ij} \quad \text{and} \quad \bar{\mathbf{x}} = \begin{pmatrix} \mathbf{x}_{11} & \mathbf{x}_{22} & \mathbf{x}_{33} & c\mathbf{x}_{23} & c\mathbf{x}_{13} & c\mathbf{x}_{12} \end{pmatrix}^T \quad (3.35)$$

where $c = 2$ in the Voigt notation, and $c = \sqrt{2}$ for the Mandel notation. The components of the defined mapping \mathbf{m} can be represented as 3×3 matrices, $\alpha \in \llbracket 1, 6 \rrbracket$, we have

$$\begin{aligned} \mathbf{m}_{1ij} &= \begin{pmatrix} 1 & 0 & 0 \\ 0 & 0 & 0 \\ 0 & 0 & 0 \end{pmatrix}, \mathbf{m}_{2ij} = \begin{pmatrix} 0 & 0 & 0 \\ 0 & 1 & 0 \\ 0 & 0 & 0 \end{pmatrix}, \mathbf{m}_{3ij} = \begin{pmatrix} 0 & 0 & 0 \\ 0 & 0 & 0 \\ 0 & 0 & 1 \end{pmatrix} \\ \mathbf{m}_{4ij} &= \begin{pmatrix} 0 & 0 & 0 \\ 0 & 0 & \frac{c}{2} \\ 0 & \frac{c}{2} & 0 \end{pmatrix}, \mathbf{m}_{5ij} = \begin{pmatrix} 0 & 0 & \frac{c}{2} \\ 0 & 0 & 0 \\ \frac{c}{2} & 0 & 0 \end{pmatrix}, \mathbf{m}_{6ij} = \begin{pmatrix} 0 & \frac{c}{2} & 0 \\ \frac{c}{2} & 0 & 0 \\ 0 & 0 & 0 \end{pmatrix} \end{aligned} \quad (3.36)$$

Reciprocally, we define the reverse mapping $\mathbf{m}^{-1} : \mathbb{R}^6 \rightarrow \mathfrak{s}(\mathbb{R}^3)$ by

$$\mathbf{x}_{ij} = \mathbf{m}_{ij\alpha}^{-1} \bar{\mathbf{x}}_\alpha \quad (3.37)$$

Where

$$\begin{aligned} \mathbf{m}_{ij1}^{-1} &= \begin{pmatrix} 1 & 0 & 0 \\ 0 & 0 & 0 \\ 0 & 0 & 0 \end{pmatrix}, \mathbf{m}_{ij2}^{-1} = \begin{pmatrix} 0 & 0 & 0 \\ 0 & 1 & 0 \\ 0 & 0 & 0 \end{pmatrix}, \mathbf{m}_{ij3}^{-1} = \begin{pmatrix} 0 & 0 & 0 \\ 0 & 0 & 0 \\ 0 & 0 & 1 \end{pmatrix} \\ \mathbf{m}_{ij4}^{-1} &= \begin{pmatrix} 0 & 0 & 0 \\ 0 & 0 & \frac{1}{c} \\ 0 & \frac{1}{c} & 0 \end{pmatrix}, \mathbf{m}_{ij5}^{-1} = \begin{pmatrix} 0 & 0 & \frac{1}{c} \\ 0 & 0 & 0 \\ \frac{1}{c} & 0 & 0 \end{pmatrix}, \mathbf{m}_{ij6}^{-1} = \begin{pmatrix} 0 & \frac{1}{c} & 0 \\ \frac{1}{c} & 0 & 0 \\ 0 & 0 & 0 \end{pmatrix} \end{aligned} \quad (3.38)$$

Every other component of the mapping being strictly equal to zero, and requiring

$$\mathbf{m}_{\alpha ij} \mathbf{m}_{ij\beta}^{-1} = \delta_{\alpha\beta} \quad (3.39)$$

where $\delta_{\alpha\beta}$ is the Kronecker symbol, we deduce

$$\begin{aligned} \bar{\boldsymbol{\sigma}}_\alpha &= \mathbf{m}_{\alpha ij} \boldsymbol{\sigma}_{ij} \\ &= \mathbf{m}_{\alpha ij} [\mathbb{C}]_{ijkl} \mathbf{m}_{kl\beta}^{-1} [\text{sym } \nabla \mathbf{u}]_\beta \\ &= \bar{\mathbb{C}}_{\alpha\beta} \bar{\boldsymbol{\varepsilon}}_\beta \end{aligned} \quad (3.40)$$

where

$$\bar{\mathbb{C}}_{\alpha\beta} = \mathbf{m}_{\alpha ij} \mathbb{C}_{ijkl} \mathbf{m}_{kl\beta}^{-1} \quad (3.41)$$

Given the symmetry of \mathbb{C} , we have

$$\bar{\mathbb{C}} = \begin{pmatrix} \mathbb{C}_{1111} & \mathbb{C}_{1122} & \mathbb{C}_{1133} & \frac{2}{c} \mathbb{C}_{1123} & \frac{2}{c} \mathbb{C}_{1123} & \frac{2}{c} \mathbb{C}_{1112} \\ * & \mathbb{C}_{2222} & \mathbb{C}_{2233} & \frac{c}{2} \mathbb{C}_{2223} & \frac{c}{2} \mathbb{C}_{2223} & \frac{c}{2} \mathbb{C}_{2212} \\ * & * & \mathbb{C}_{3333} & \frac{c}{2} \mathbb{C}_{3323} & \frac{c}{2} \mathbb{C}_{3323} & \frac{c}{2} \mathbb{C}_{3312} \\ * & * & * & \frac{c}{4} \mathbb{C}_{2323} & \frac{c}{4} \mathbb{C}_{2323} & \frac{c}{4} \mathbb{C}_{2312} \\ * & * & * & * & \frac{c}{2} \mathbb{C}_{1323} & \frac{c}{4} \mathbb{C}_{1312} \\ * & * & * & * & * & \frac{c}{4} \mathbb{C}_{1212} \end{pmatrix} \quad (3.42)$$

We can now easily compute constitutive laws involving second and fourth order symmetric tensors. Moreover, it will allow us simplify, in the case of material symmetries, the expression of \mathbb{C} , *i.e.* the number of its independent coefficients.

3.1.2 The isotropic Cauchy material

The materials modeled by the classical Cauchy continuum often presents several material symmetries, *i.e.* any transformation \mathcal{T} in the symmetry group of the considered material leaves its constitutive laws untouched. As we introduced the classical Cauchy continuum *via* its kinetic and strain energy densities, writing $\mathcal{T} : \mathbf{u} \mapsto \mathbf{u}'$, one could easily rather verify that

$$\begin{cases} k_c(\dot{\mathbf{u}}') = k_c(\dot{\mathbf{u}}) \\ w_c(\mathbf{u}') = w_c(\mathbf{u}) \end{cases} \quad (3.43)$$

Such relations, eventually giving relations between the coefficients of \mathbb{C} , will considerably simplify its expression and the number of independent coefficients. Let us consider here the case of an isotropic material, *i.e.* that the behaviour of our continuum are independent of the direction of sollicitation. One can easily verify that

$$\begin{aligned} k_c(\dot{\mathbf{u}}) &= \frac{1}{2} \langle \dot{\mathbf{u}}, \rho_c \dot{\mathbf{u}} \rangle = \frac{1}{2} \rho_c \dot{\mathbf{u}}^T \dot{\mathbf{u}} \quad (\text{on one hand}) \\ &= \frac{1}{2} \langle \dot{\mathbf{u}}', \rho_c \dot{\mathbf{u}}' \rangle \quad (\text{on the other hand}) \\ &= \frac{1}{2} \langle \mathbf{Q} \dot{\mathbf{u}}, \rho_c \mathbf{Q} \dot{\mathbf{u}} \rangle \\ &= \frac{1}{2} (\mathbf{Q} \dot{\mathbf{u}})^T \rho_c \mathbf{Q} \dot{\mathbf{u}} \\ &= \frac{1}{2} \rho_c \dot{\mathbf{u}}^T \mathbf{Q}^T \mathbf{Q} \dot{\mathbf{u}} \\ &= \frac{1}{2} \rho_c \dot{\mathbf{u}}^T \dot{\mathbf{u}} \quad \text{as } \mathbf{Q} \in \mathbb{O}(\mathbb{R}^3) \end{aligned} \quad (3.44)$$

Chapter 3. From Cauchy to micromorphic modelling

where $\mathbb{O}(\mathbb{R}^3)$ is the orthogonal group of \mathbb{R}^3 . That was much to prove that $\|\dot{\mathbf{u}}\|$ is a scalar (and so ρ_c). Anyway, this is the general method to get relations between the parameters of our constitutive laws (here, we get no such a relation for density). Things become more involved when it comes to the strain energy density. First, we have

$$\mathbf{x}' = \mathbf{Q}\mathbf{x}, \mathbf{u}' = \mathbf{Q}\mathbf{u} \text{ and } \nabla_{\mathbf{x}'}\mathbf{u}'(\mathbf{x}') = \mathbf{Q}^T[\nabla_{\mathbf{x}}\mathbf{u}(\mathbf{Q}\mathbf{x})]\mathbf{Q} \quad (3.45)$$

Then \mathbb{C} have to verify, for an isotropic continuum,

$$\forall \mathbf{Q} \in \mathbb{O}(\mathbb{R}^3), \langle \text{sym } \mathbf{Q}^T[\nabla_{\mathbf{x}}\mathbf{u}(\mathbf{Q}\mathbf{x})]\mathbf{Q}, \mathbb{C} \text{sym } \mathbf{Q}^T[\nabla_{\mathbf{x}}\mathbf{u}(\mathbf{Q}\mathbf{x})]\mathbf{Q} \rangle = \langle \text{sym } \nabla\mathbf{u}, \mathbb{C} \text{sym } \nabla\mathbf{u} \rangle \quad (3.46)$$

where $\mathbb{O}(\mathbb{R}^3)$, for a material of a lower class of symmetry, would have to be replaced to the corresponding symmetry group of the considered material. Thanks to the Mandel-Voigt notation that have just been introduced, these quantities can be easily computed. If the computation of 3.46, being tedious, will not be presented in this manuscript, one can briefly give the transformations \mathbf{Q} used to simplify \mathbb{C} :

- permutations, *e.g.*, in the case of tetragonal symmetry,

$$\mathbf{Q} = \begin{pmatrix} 0 & 1 & 0 \\ 1 & 0 & 0 \\ 0 & 0 & 1 \end{pmatrix} \quad (3.47)$$

- rotations of angle θ around \mathbf{n} , that can be computed by the Euler-Rodrigues formula

$$\mathcal{Q}(\mathbf{u}) = \mathbf{u} + \sin \theta \mathbf{n} \wedge \mathbf{u} + (1 - \cos \theta)(\mathbf{n} \wedge (\mathbf{n} \wedge \mathbf{u})) \quad (3.48)$$

Eventually, for an isotropic material considered here, the number of independent coefficients is reduced to two, λ and μ , called the Lamé coefficients and homogeneous to a stress, shaping \mathbb{C} like

$$\mathbb{C} = \begin{pmatrix} 2\mu + \lambda & \lambda & \lambda & 0 & 0 & 0 \\ * & 2\mu + \lambda & \lambda & 0 & 0 & 0 \\ * & * & 2\mu + \lambda & 0 & 0 & 0 \\ 0 & 0 & 0 & \mu & 0 & 0 \\ 0 & 0 & 0 & 0 & \mu & 0 \\ 0 & 0 & 0 & 0 & 0 & \mu \end{pmatrix} \quad (3.49)$$

That can be put under the form

$$\boldsymbol{\sigma} = \mathbb{C} \text{sym } \nabla\mathbf{u} = 2\mu \text{sym } \nabla\mathbf{u} + \lambda \mathbf{1} \text{Tr } \nabla\mathbf{u} \quad \text{i.e.} \quad \sigma_{ij} = \mu(u_{i,j} + u_{j,i}) + \lambda \delta_{ij} u_{k,k} \quad (3.50)$$

Usually, rather than the Lamé coefficients [Lamé 1852], materials are known through their Young modulus E (in Pa) and the Poisson coefficient ν (dimensionless), defined, for an axial tensile load along \mathbf{x}_1 , by

$$E = \frac{\sigma_{11}}{u_{1,1}} \quad \text{and} \quad \nu = -\frac{u_{2,2}}{u_{1,1}} = -\frac{u_{3,3}}{u_{1,1}} \quad (3.51)$$

Using the principle of superposition, one can get

$$\frac{1}{2}(u_{i,j} + u_{j,i}) = \frac{1+\nu}{E}\sigma_{ij} - \frac{\nu}{E}\sigma_{kk}\delta_{ij} \quad \text{i.e.} \quad \text{sym } \nabla \mathbf{u} = \frac{1+\nu}{E}\boldsymbol{\sigma} + \frac{\nu}{E}\mathbb{1} \text{Tr } \boldsymbol{\sigma} \quad (3.52)$$

That would lead to

$$\mu = \frac{E}{2(1+\nu)} \quad \text{and} \quad \lambda = \frac{\nu E}{(1+\nu)(1-2\nu)} \quad (3.53)$$

As the manufacturer of the plate used as *proof of concept* provided the mechanical parameters E and ν , such relations will be useful to write easily the strain energy density of our classical Cauchy model. To study the dispersion relations in this continuum, let us use indicial notations for an easier manipulation of the operators, and consider a medium free from volume forces, *i.e.* $\mathbf{f} = \mathbf{0}$:

$$\begin{aligned} \rho_c \ddot{u}_i &= \sigma_{ij,j} = \mu(u_{i,j} + u_{j,i})_{,j} + \lambda(\delta_{ij} u_{k,k})_{,j} \\ &= \mu u_{i,jj} + \mu u_{j,ij} + \lambda u_{j,ij} \\ &= (\lambda + \mu)u_{j,ij} + \mu u_{i,jj} \end{aligned} \quad (3.54)$$

Under that form, one can notice that

$$\begin{cases} [\nabla(\text{div } \mathbf{u})]_i = u_{j,ij} \\ [\Delta \mathbf{u}]_i = \Delta u_i = u_{i,jj} \end{cases} \quad (3.55)$$

Given this and 3.54, we get the Lamé-Navier equation

$$\rho_c \ddot{\mathbf{u}} = (\lambda + \mu)\nabla(\text{div } \mathbf{u}) + \mu\Delta \mathbf{u} \quad (3.56)$$

Let us use the Helmholtz decomposition for \mathbf{u} :

$$\exists(\phi, \mathbf{A}) \in \mathcal{C}^2(\mathbb{R}^3, \mathbb{R}) \times \mathcal{C}^2(\mathbb{R}^3, \mathbb{R}^3) : \mathbf{u} = \text{curl } \mathbf{A} - \nabla\phi \quad (3.57)$$

Where ϕ is the scalar potential and \mathbf{A} the vector potential. ϕ and \mathbf{A} being defined respectively up to a constant and a gradient (gauge-invariance of the potentials), one can choose \mathbf{A} to verify

$$\text{div } \mathbf{A} = \mathbf{0} \quad (3.58)$$

Given this choice, substituting in 3.56, we have

$$\rho_c(\text{curl } \ddot{\mathbf{A}} - \ddot{\nabla}\phi) = (\lambda + \mu)\nabla(\text{div}(\text{curl } \mathbf{A} - \nabla\phi)) + \mu\Delta(\text{curl } \mathbf{A} - \nabla\phi) \quad (3.59)$$

Having

$$\begin{cases} \text{div } \text{curl } \mathbf{A} = \mathbf{0} \\ \text{div}(\nabla\phi) = \Delta\phi \\ \Delta \mathbf{A} = \text{curl } \text{curl } \mathbf{A} + \nabla(\text{div } \mathbf{A}) \end{cases} \quad (3.60)$$

Chapter 3. From Cauchy to micromorphic modelling

We deduce

$$\begin{aligned}
 \rho_c(\operatorname{curl} \ddot{\mathbf{A}} - \nabla \ddot{\phi}) &= -(\lambda + \mu)\nabla(\Delta\phi) + \mu\Delta(\operatorname{curl} \mathbf{A} - \nabla\phi) \\
 &= -(\lambda + \mu)\nabla(\Delta\phi) + \mu\Delta(\operatorname{curl} \mathbf{A} - \nabla\phi) \\
 &= -(\lambda + \mu)\nabla(\Delta\phi) + \mu(\operatorname{curl} \operatorname{curl} \operatorname{curl} \mathbf{A} - \nabla\Delta\phi) \\
 &= -(\lambda + 2\mu)\nabla(\Delta\phi) + \mu\operatorname{curl} \Delta\mathbf{A}
 \end{aligned} \tag{3.61}$$

Given the orthogonality of the decomposition for $\Omega = \mathbb{R}^3$, one has

$$\begin{cases} \rho_c \ddot{\phi} = (2\mu + \lambda)\Delta\phi \\ \rho_c \ddot{\mathbf{A}} = \mu\Delta\mathbf{A} \end{cases} \tag{3.62}$$

which are two D'Alembert equations. One can introduce the speed of propagation of longitudinal and shear waves, respectively c_l and c_s :

$$c_l = \sqrt{\frac{2\mu + \lambda}{\rho_c}} > c_s = \sqrt{\frac{\mu}{\rho_c}} \tag{3.63}$$

Given these relations, an isotropic Cauchy material can be equivalently defined by its Lamé coefficients λ and μ or its longitudinal and shear velocities c_l and c_s . Such properties will be explored in Chapter 4. At last, let us give the analytical expressions of the kinetic and strain densities of energy for such medium:

$$\begin{cases} k_c = \frac{1}{2}\rho_c(\dot{u}_1^2 + \dot{u}_2^2) \\ w_c = \frac{1}{2} [2\mu(u_{1,1}^2 + u_{2,2}^2) + \lambda(u_{1,1} + u_{2,2})^2 + \mu(u_{2,1} + u_{1,2})^2] \end{cases} \tag{3.64}$$

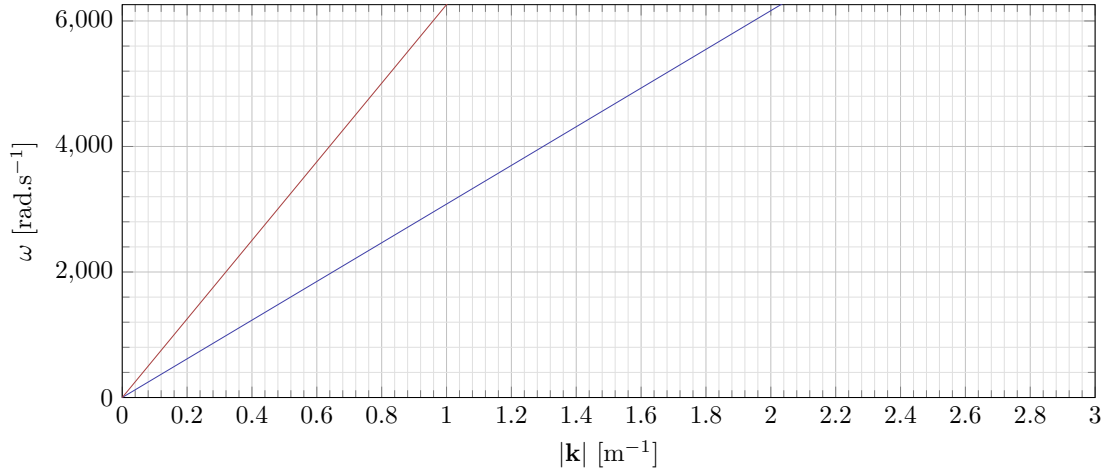


Figure 3.3: Dispersion curves for the Cauchy continuum for longitudinal (*red*) and shear waves (*blue*), of respective equations $\omega = c_l|\mathbf{k}|$ and $\omega = c_s|\mathbf{k}|$ in an isotropic plate.

One can see, despite the ability of such a model to predict many mechanical behaviors (*e.g.* deformations, transmitted forces, maximum load, *etc*), the classical Cauchy model reveals itself unable to describe dispersive behaviors of structures.

3.2 The relaxed micromorphic model

The classical Cauchy continuum “simplified” the material behaviour considering the representative volume element, thus neglecting the heterogeneity of matter at a lower scale, which is generally of no particular interest for Engineering Sciences. In the same way, enriched continua aim to “simplify” the architected unit cell, taking into account its dispersive properties by the introduction of a new Lagrangian density adapted to our media.

As we chose to describe our continua through the Principle of Least Action, *i.e.* by introducing a local action [Truesdell 1960, Toupin 1962], two strategies may be considered to model dispersion and more precisely band-gaps at a bigger scale, by introducing:

- higher order operators (medium of order n)

- additional kinematic fields (medium of grade n)

These strategies are presented in Figure 3.4 [Maugin 1980, Cosserat 1909, Mindlin 1964, Mindlin 1965, Cosserat 1909, Eringen 1968, Eringen 1999, Cauchy 1828a].

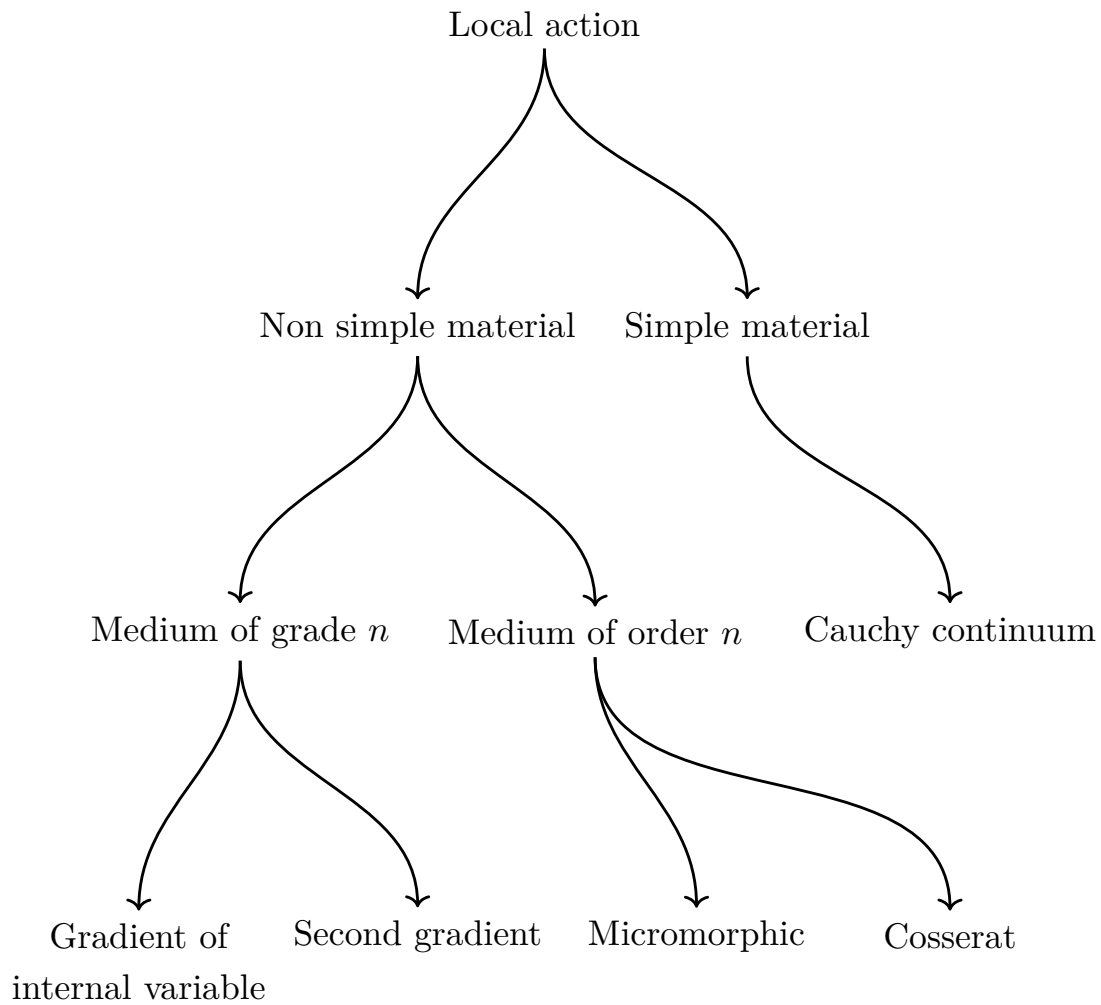


Figure 3.4: Classical and generalized continuum mechanics.

Second and higher order gradient theories, despite their ability to describe, *e.g.* dispersion of acoustic modes [Dell'Isola 2012a, Placidi 2014], fail when it comes to consider metamaterial considered in this manuscript, that can inhibit wave propagation in a given frequency range.

Such a complex phenomenon requires the introduction of additional kinematic variables to our continuum [Madeo 2014, Madeo 2015, Madeo 2016a, Madeo 2017]. In the relaxed micromorphic model, the non-symmetric micro-distortion second-order tensor $\mathbf{P}(\in \mathbb{R}^{3 \times 3})$ completes the kinematic description of our continuum, describing the deformation of the microstructure at the microscopic scale. The transformation of such a medium is presented in Figure 3.5.

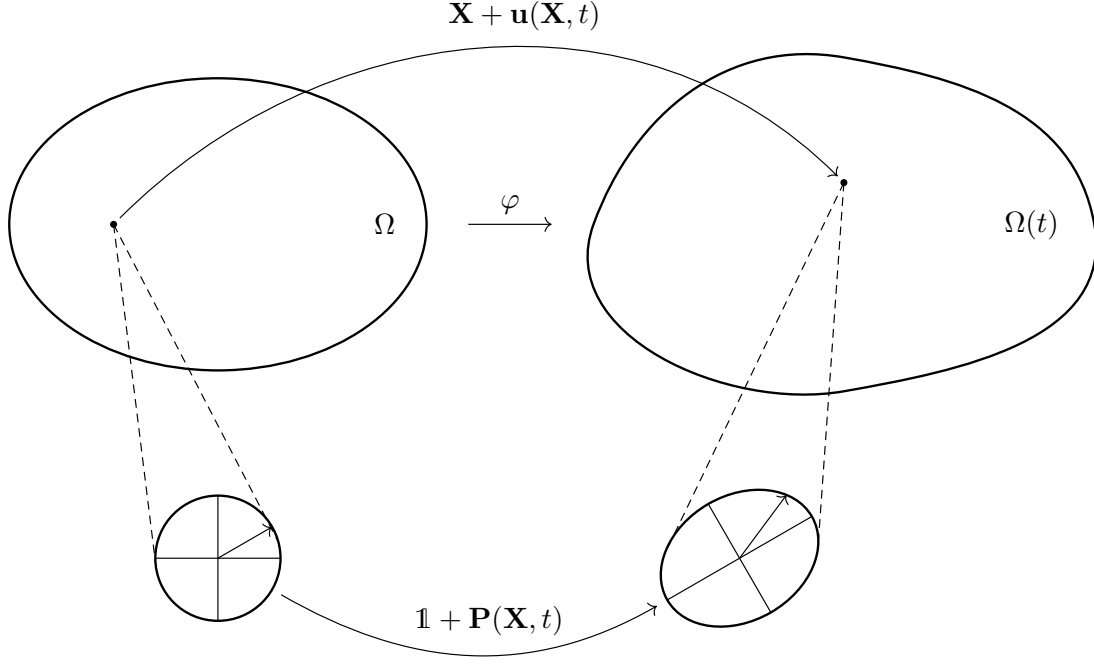


Figure 3.5: Transformation for an enriched micromorphic medium

Local density of kinetic k_m and potential w_m energy in the relaxed micromorphic medium are defined as [Madeo 2018a, d'Agostino 2020]¹

$$\begin{aligned}
 k_m(\dot{\mathbf{u}}, \nabla \dot{\mathbf{u}}, \dot{\mathbf{P}}) &= \frac{1}{2} \langle \dot{\mathbf{u}}, \rho_m \dot{\mathbf{u}} \rangle \text{ (Cauchy inertia)} \\
 &+ \frac{1}{2} \langle \text{sym } \dot{\mathbf{P}}, \mathbb{J}_m \text{sym } \dot{\mathbf{P}} \rangle + \frac{1}{2} \langle \text{skew } \dot{\mathbf{P}}, \mathbb{J}_c \text{skew } \dot{\mathbf{P}} \rangle \text{ (free micro-inertia)} \\
 &+ \frac{1}{2} \langle \text{sym } \nabla \dot{\mathbf{u}}, \mathbb{T}_e \text{sym } \nabla \dot{\mathbf{u}} \rangle + \frac{1}{2} \langle \text{skew } \nabla \dot{\mathbf{u}}, \mathbb{T}_c \text{skew } \nabla \dot{\mathbf{u}} \rangle \text{ (gradient micro-inertia)} \\
 w_m(\nabla \mathbf{u}, \mathbf{P}) &= \frac{1}{2} \langle \text{sym}(\nabla \mathbf{u} - \mathbf{P}), \mathbb{C}_e \text{sym}(\nabla \mathbf{u} - \mathbf{P}) \rangle \text{ (elastic energy)} \\
 &+ \frac{1}{2} \langle \text{sym } \mathbf{P}, \mathbb{C}_m \text{sym } \mathbf{P} \rangle \text{ (micro self energy)} \\
 &+ \frac{1}{2} \langle \text{skew}(\nabla \mathbf{u} - \mathbf{P}), \mathbb{C}_c \text{skew}(\nabla \mathbf{u} - \mathbf{P}) \rangle \text{ (local rotational elastic coupling)}
 \end{aligned} \tag{3.65}$$

where $\mathbb{J}_m : \mathfrak{s}(\mathbb{R}^3) \rightarrow \mathfrak{s}(\mathbb{R}^3)$, $\mathbb{J}_c : \mathfrak{so}(\mathbb{R}^3) \rightarrow \mathfrak{so}(\mathbb{R}^3)$, $\mathbb{T}_e : \mathfrak{s}(\mathbb{R}^3) \rightarrow \mathfrak{s}(\mathbb{R}^3)$, $\mathbb{T}_c : \mathfrak{so}(\mathbb{R}^3) \rightarrow \mathfrak{so}(\mathbb{R}^3)$, $\mathbb{C}_c : \mathfrak{so}(\mathbb{R}^3) \rightarrow \mathfrak{so}(\mathbb{R}^3)$, $\mathbb{C}_m : \mathfrak{s}(\mathbb{R}^3) \rightarrow \mathfrak{s}(\mathbb{R}^3)$, $\mathbb{C}_e : \mathfrak{s}(\mathbb{R}^3) \rightarrow \mathfrak{s}(\mathbb{R}^3)$ which are all symmetric, defining quadratic forms, like it did for the classical Cauchy medium, *i.e.*

$$\begin{aligned}
 [\mathbb{J}_m, \mathbb{T}_e, \mathbb{C}_e, \mathbb{C}_m]_{ijkl} &= [\mathbb{J}_m, \mathbb{T}_e, \mathbb{C}_e, \mathbb{C}_m]_{klij} \quad \forall (i, j, k, l) \in \{1, 2, 3\}^4 \\
 [\mathbb{J}_c, \mathbb{T}_c, \mathbb{C}_c]_{ij} &= [\mathbb{J}_c, \mathbb{T}_c, \mathbb{C}_c]_{ji} \quad \forall (i, j) \in \{1, 2, 3\}^2
 \end{aligned} \tag{3.66}$$

¹The relaxed micromorphic model classically requires curvature terms $L_c^2 \text{curl } \mathbf{P} \dots$. However, while important for the static case, these terms give little correction to the dynamics of our metamaterials and are hence neglected in the remainder of this manuscript.

Chapter 3. From Cauchy to micromorphic modelling

The Lagrangian density ℓ_m of the relaxed micromorphic continuum is

$$\ell_m(\dot{\mathbf{u}}, \nabla \mathbf{u}, \nabla \dot{\mathbf{u}}, \mathbf{P}, \dot{\mathbf{P}}) = k_m(\dot{\mathbf{u}}, \nabla \dot{\mathbf{u}}, \dot{\mathbf{P}}) - w_m(\nabla \mathbf{u}, \mathbf{P}) \quad (3.67)$$

The action functional \mathcal{A}_m for the micromorphic medium occupying Ω is defined as:

$$\mathcal{A}_m = \mathcal{A}_{\text{int}}^m + \mathcal{A}_{\text{ext}}^m \text{ where } \begin{cases} \mathcal{A}_{\text{int}}^m[\mathbf{u}, \mathbf{P}] = \int_{t_1}^{t_2} \int_{\Omega} \ell_m d\Omega dt = \int_0^T \int_{\Omega} (k_m - w_m) d\Omega dt \\ \mathcal{A}_{\text{ext}}^m[\mathbf{u}] = \int_{t_1}^{t_2} \int_{\partial\Omega_N} \langle \mathbf{t}, \mathbf{u} \rangle d\Gamma dt + \int_{t_1}^{t_2} \int_{\Omega} \langle \mathbf{f}, \mathbf{u} \rangle d\Omega dt \end{cases} \quad (3.68)$$

One can notice, in the absence of space derivatives upon \mathbf{P} , the absence of additional generalized forces in $\mathcal{A}_{\text{ext}}^m[\mathbf{u}]$. The Dirichlet boundary condition are written

$$\begin{cases} \mathbf{u} = \mathbf{u}_0 \\ \mathbf{P} = \mathbf{P}_0 \end{cases} \quad \text{on } \partial\Omega_D \quad (3.69)$$

And the initial conditions are

$$\begin{cases} \mathbf{u}(t = t_1) = \mathbf{u}_i \\ \dot{\mathbf{u}}(t = t_1) = \mathbf{v}_i \end{cases} \quad \text{and} \quad \begin{cases} \mathbf{P}(t = t_1) = \mathbf{U}_i \\ \dot{\mathbf{P}}(t = t_1) = \mathbf{V}_i \end{cases} \quad \text{in } \Omega \quad (3.70)$$

The Principle of Least Action states that the trajectory followed by the system $(\mathbf{u}, \mathbf{P}) : (\mathbf{x}, t) \in \Omega \times [t_1, t_2] \mapsto (\mathbf{u}(\mathbf{x}, t), \mathbf{P}(\mathbf{x}, t))$ is the one for which the action functional is stationary, *i.e.* verifies

$$\{\delta \mathcal{A}_m[\mathbf{u}, \mathbf{P}] = 0 \text{ where } (\mathbf{u}, \mathbf{P}) \text{ verifies } 3.69 \text{ and } 3.70\} \quad (3.71)$$

Given the kinetic and strain energy densities introduced in 3.67, we can define the space of configuration \mathcal{Q}_m to which (\mathbf{u}, \mathbf{P}) should belong

$$\mathcal{Q}_m = \{(\mathbf{u}, \mathbf{P}) : (\mathbf{u}, \mathbf{P}) \text{ verify } 3.69 \text{ and } 3.70\} \quad (3.72)$$

Like for the Cauchy medium, $(\delta \mathbf{u}, \delta \mathbf{P})$ verifies

$$\begin{cases} \delta \mathbf{u}(t_1) = \mathbf{0} = \delta \mathbf{u}(t_2) \\ \delta \mathbf{P}(t_1) = \mathbf{0} = \delta \mathbf{P}(t_2) \end{cases} \quad \text{in } \Omega \quad \text{and} \quad \begin{cases} \forall t \in [t_1, t_2], \delta \mathbf{u} = \mathbf{0} \\ \forall t \in [t_1, t_2], \delta \mathbf{P} = \mathbf{0} \end{cases} \quad \text{on } \partial\Omega_D \quad (3.73)$$

We can now compute the stationarity of \mathcal{A}_m . Let us begin with the Cauchy inertia term:

$$\delta \int_{t_1}^{t_2} \int_{\Omega} \frac{1}{2} \langle \dot{\mathbf{u}}, \rho_m \dot{\mathbf{u}} \rangle d\Omega dt = - \int_{t_1}^{t_2} \int_{\Omega} \langle \rho_m \ddot{\mathbf{u}}, \delta \mathbf{u} \rangle d\Omega dt \quad (3.74)$$

as seen in 3.25. To deal with skew-symmetric terms, one can notice that

$$\forall (\mathbf{A}, \mathbf{X}) \in \mathfrak{so}(\mathbb{R}^3) \times \mathbb{R}^{3 \times 3}, \langle \mathbf{X}, \mathbf{A} \rangle = \langle \text{skew } \mathbf{X}, \mathbf{A} \rangle \quad (3.75)$$

allowing us, *e.g.*, to compute the free micro-inertia term:

$$\delta \int_{t_1}^{t_2} \int_{\Omega} \frac{1}{2} \left[\langle \text{sym } \dot{\mathbf{P}}, \mathbb{J}_m \text{sym } \dot{\mathbf{P}} \rangle + \langle \text{skew } \dot{\mathbf{P}}, \mathbb{J}_c \text{skew } \dot{\mathbf{P}} \rangle \right] d\Omega dt = - \int_{t_1}^{t_2} \int_{\Omega} \langle \delta \mathbf{P}, \mathbb{J}_m \text{sym } \ddot{\mathbf{P}} + \mathbb{J}_c \text{skew } \ddot{\mathbf{P}} \rangle d\Omega dt \quad (3.76)$$

Given the complexity of the computation of the first variation of this action functional, the expression of the other terms is detailed in Annex A. We can give here the Euler-Lagrange equations for the relaxed micromorphic medium:

$$\left\{ \begin{array}{l} \frac{d}{dt} \left(\frac{\partial \ell_m}{\partial \dot{u}_i} + \left[\frac{\partial \ell_m}{\partial \dot{u}_{i,j}} \right]_{,j} \right) + \left[\frac{\partial \ell_m}{\partial u_{i,j}} \right]_{,j} = f_i \\ \frac{d}{dt} \frac{\partial \ell_m}{\partial \dot{P}_{ij}} - \frac{\partial \ell_m}{\partial P_{ij}} = 0 \end{array} \right. \quad i.e. \quad \left\{ \begin{array}{l} \frac{d}{dt} \left[\frac{\partial \ell_m}{\partial \dot{\mathbf{u}}} - \operatorname{div} \frac{\partial \ell_m}{\partial \nabla \dot{\mathbf{u}}} \right] + \operatorname{div} \frac{\partial \ell_m}{\partial \nabla \mathbf{u}} = \mathbf{f} \\ \frac{d}{dt} \frac{\partial \ell_m}{\partial \dot{\mathbf{P}}} - \frac{\partial \ell_m}{\partial \mathbf{P}} = \mathbf{0} \end{array} \right. \quad (3.77)$$

Given this, the equilibrium equations of the relaxed micromorphic medium are

$$\left\{ \begin{array}{l} \rho_m \ddot{\mathbf{u}} - \operatorname{div} \hat{\boldsymbol{\sigma}} = \operatorname{div} \tilde{\boldsymbol{\sigma}} + \mathbf{f} \\ \mathbb{J}_m \operatorname{sym} \ddot{\mathbf{P}} + \mathbb{J}_c \operatorname{skew} \ddot{\mathbf{P}} = \tilde{\mathbf{s}} - \mathbf{s} \end{array} \right. \quad \text{in } \Omega \quad (3.78)$$

with the (generalized) boundary condition

$$(\tilde{\boldsymbol{\sigma}} + \hat{\boldsymbol{\sigma}}) \cdot \mathbf{n} = \mathbf{t} \quad \text{on } \partial\Omega_{\mathcal{N}} \quad (3.79)$$

where \mathbf{n} is the normal to the boundary $\partial\Omega$, \mathbf{t} is the traction corresponding to the externally applied load, and the following (generalized) stress-strain relations

$$\left\{ \begin{array}{l} \tilde{\boldsymbol{\sigma}} = \mathbb{C}_e \operatorname{sym} (\nabla \mathbf{u} - \mathbf{P}) + \mathbb{C}_c \operatorname{skew} (\nabla \mathbf{u} - \mathbf{P}) \\ \hat{\boldsymbol{\sigma}} = \mathbb{T}_e \operatorname{sym} \nabla \ddot{\mathbf{u}} + \mathbb{T}_c \operatorname{skew} \nabla \ddot{\mathbf{u}} \\ \mathbf{s} = \mathbb{C}_m \operatorname{sym} \mathbf{P} \end{array} \right. \quad (3.80)$$

We can notice, in the absence of terms of the form $\operatorname{curl} \mathbf{P}$ in the Lagrangian density of the relaxed micromorphic continuum, no extra natural boundary condition arises from the application of the Principle of Least Action. Therefore, a special attention must be brought to the boundary conditions upon \mathbf{P} to guarantee the convergence of the modelling with respect to the classical Cauchy medium.

3.2.1 The axl mapping

We already introduced the Voigt notation for second and fourth order symmetric tensors, allowing to represent \mathbb{C}_c , \mathbb{C}_m , \mathbb{J}_m , \mathbb{T}_e in a suitable way. However, we introduced in our formulation the skew-symmetric part of $\nabla \mathbf{u}$ and \mathbf{P} and the associated operators \mathbb{C}_c , \mathbb{J}_c and \mathbb{T}_c , requiring a new mapping to represent them more easily. Like we did for symmetric tensors, we define, for $\mathbf{X} \in \mathfrak{so}(\mathbb{R}^3)$,

$$[\operatorname{axl} \mathbf{X}]_k = \frac{1}{2} \varepsilon_{kij} X_{ji} \quad (3.81)$$

where ε_{ijk} is the Levi-Civita operator, defined by

$$\varepsilon_{ijk} = \begin{vmatrix} \delta_{i1} & \delta_{i2} & \delta_{i3} \\ \delta_{j1} & \delta_{j2} & \delta_{j3} \\ \delta_{k1} & \delta_{k2} & \delta_{k3} \end{vmatrix} = \varepsilon_{kij} \quad (\text{using circular permutation}) \quad (3.82)$$

Chapter 3. From Cauchy to micromorphic modelling

allowing to represent second order skew-symmetric tensors as elements of \mathbb{R}^3 :

$$\mathbf{X} = \begin{pmatrix} 0 & -X_{21} & -X_{31} \\ X_{21} & 0 & -X_{32} \\ X_{31} & X_{32} & 0 \end{pmatrix} \quad \text{then} \quad \text{axl } \mathbf{X} = \begin{pmatrix} X_{21} \\ X_{32} \\ X_{31} \end{pmatrix} \quad (3.83)$$

Using such mapping for $\tilde{\boldsymbol{\sigma}}, \hat{\boldsymbol{\sigma}}$, skew \mathbf{P} and skew $\nabla \mathbf{u}$ allow us to represent, as we did for fourth order symmetric tensors, $\mathbb{C}_c, \mathbb{J}_c$ and \mathbb{T}_c as symmetric (defining quadratic forms) matrices, respectively $\bar{\mathbb{C}}_c, \bar{\mathbb{J}}_c$ and $\bar{\mathbb{T}}_c : \mathbb{R}^3 \rightarrow \mathbb{R}^3$ of only 3 independent components.

3.2.2 Application to our microstructured cell

The unit cell has already been introduced in Chapter 2, one can synthesize here the geometrical and mechanical parameters used throughout this manuscript in Figure 3.6 and Table 3.1, from which we will compute the relaxed micromorphic coefficients.

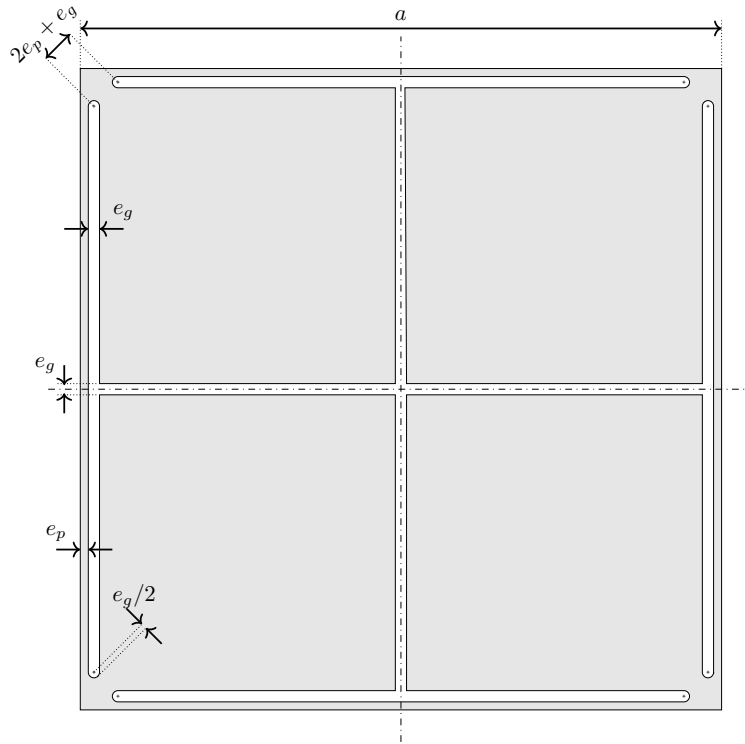


Figure 3.6: Definitive geometry of the architected cell with its parametrization.

The values of the geometrical parameters a (side of the cell), e_p (half of the minimal thickness) e_g (width of the holes) and the mechanical parameters, corresponding to an usual titanium alloy are given in Table 3.1.

The $e_g/2$ dimension corresponds to the hole's radius while the $2e_p + e_g$ dimension allows to guarantee a minimal in-plane thickness of e_p in the plate.

a	e_g	e_p	ρ_{Ti}	E_{Ti}	ν_{Ti}
[mm]	[mm]	[mm]	[kg/m ³]	[GPa]	-
20	0.35	0.25	4400	112	0.34

Table 3.1: Geometrical and mechanical properties of the unit cell given in Figure 3.6.

To simplify the computation of the relaxed micromorphic model coefficients, one can invoke the Neumann's Principle, stating that every lattice symmetry of the crystal must also be a symmetry of the constitutive law supposed to describe the physics of our system at the macroscopic scale. The unit cell geometry presenting a tetragonal symmetry, for which the symmetry group associated is the Dihedral group \mathbb{D}_4 , the elastic and the micro-inertia tensors of the considered micromorphic medium may be written as

$$\begin{aligned}
\mathbb{C}_e &= \begin{pmatrix} \lambda_e + 2\mu_e & \lambda_e & \star & 0 & 0 & 0 \\ \lambda_e & \lambda_e + 2\mu_e & \star & 0 & 0 & 0 \\ \star & \star & \star & 0 & 0 & 0 \\ 0 & 0 & 0 & \star & 0 & 0 \\ 0 & 0 & 0 & 0 & \star & 0 \\ 0 & 0 & 0 & 0 & 0 & \mu_e^* \end{pmatrix}, \mathbb{C}_m = \begin{pmatrix} \lambda_m + 2\mu_m & \lambda_m & \star & 0 & 0 & 0 \\ \lambda_m & \lambda_m + 2\mu_m & \star & 0 & 0 & 0 \\ \star & \star & \star & 0 & 0 & 0 \\ 0 & 0 & 0 & \star & 0 & 0 \\ 0 & 0 & 0 & 0 & \star & 0 \\ 0 & 0 & 0 & 0 & 0 & \mu_m^* \end{pmatrix}, \\
\mathbb{J}_m &= \begin{pmatrix} \eta_3 + 2\eta_1 & \eta_3 & \star & 0 & 0 & 0 \\ \eta_3 & \eta_3 + 2\eta_1 & \star & 0 & 0 & 0 \\ \star & \star & \star & 0 & 0 & 0 \\ 0 & 0 & 0 & \star & 0 & 0 \\ 0 & 0 & 0 & 0 & \star & 0 \\ 0 & 0 & 0 & 0 & 0 & \eta_1^* \end{pmatrix}, \mathbb{T}_e = \begin{pmatrix} \bar{\eta}_3 + 2\bar{\eta}_1 & \bar{\eta}_3 & \star & 0 & 0 & 0 \\ \bar{\eta}_3 & \bar{\eta}_3 + 2\bar{\eta}_1 & \star & 0 & 0 & 0 \\ \star & \star & \star & 0 & 0 & 0 \\ 0 & 0 & 0 & \star & 0 & 0 \\ 0 & 0 & 0 & 0 & \star & 0 \\ 0 & 0 & 0 & 0 & 0 & \bar{\eta}_1^* \end{pmatrix}, \\
\mathbb{C}_c &= \begin{pmatrix} \star & 0 & 0 \\ 0 & \star & 0 \\ 0 & 0 & 4\mu_c \end{pmatrix}, \quad \mathbb{J}_c = \begin{pmatrix} \star & 0 & 0 \\ 0 & \star & 0 \\ 0 & 0 & 4\eta_2 \end{pmatrix} \text{ and } \mathbb{T}_c = \begin{pmatrix} \star & 0 & 0 \\ 0 & \star & 0 \\ 0 & 0 & 4\bar{\eta}_2 \end{pmatrix}.
\end{aligned} \tag{3.84}$$

Such a hypothesis reduces the number of relaxed micromorphic coefficients to 16 (counting the density). If the specific calibration procedure used to determine the values of the relaxed micromorphic parameters of the unit cell has not been developed in this thesis, we can briefly say that it consists of:

- the computation of the coefficients of strain energy density

Chapter 3. From Cauchy to micromorphic modelling

- the comparison of the dispersion curves of the two models

Indeed, the computation of the generalized stress-strain relations can be made in the static regime. Such a method largely relies on the KUBC method (Kinetic Uniform Boundary Conditions) [Hill 1963, Hill 1967, Mandel 1972], *e.g.* for \mathbb{C}_m

$$\frac{1}{2} \langle \mathbf{E}, \mathbb{C}_m \mathbf{E} \rangle = \frac{1}{\Omega_c} \inf \left\{ \int_{\Omega_c} \frac{1}{2} \langle \text{sym}(\nabla \mathbf{u} + \mathbf{E}), \mathbb{C} \text{sym}(\nabla \mathbf{u} + \mathbf{E}) \rangle d\Omega \mid \mathbf{u} \in \mathcal{C}_0^\infty(\Omega_c, \mathbb{R}^3) \right\} \quad (3.85)$$

implying that \mathbb{C}_m depends on the size and shape of unit cell. Using Neumann's Principle, the computation of these coefficients is restricted to tetragonal unit cells, *e.g.* Figure 3.6, which is the solution finally adopted given the microstructured plate manufactured presented in 2. Figure 3.7 presents several possible identifications of the unit cell.

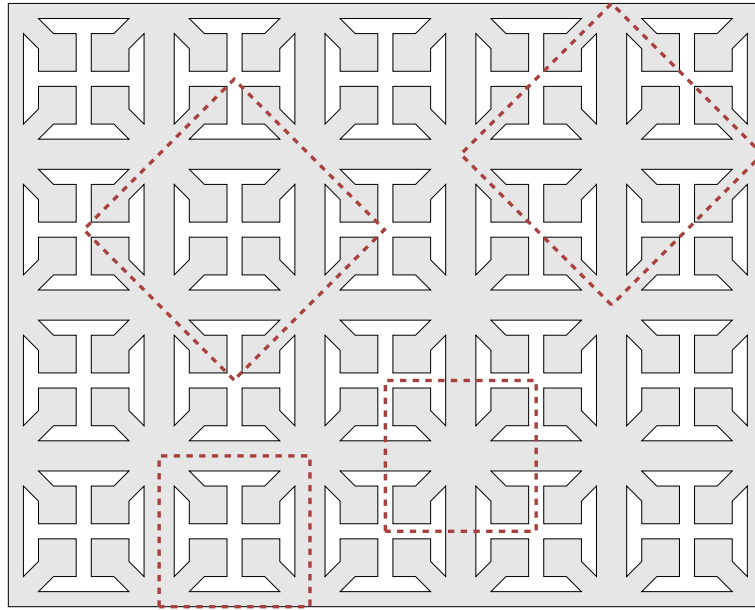


Figure 3.7: (red) Different identifications of the unit cell from a microstructured plate.

The computation of inertial parameters is based on the comparison of the relaxed micromorphic dispersion curves with those obtained *via* a classic Bloch-Floquet analysis (see Chapter 2) [Aivaliotis 2020, d'Agostino 2020]. Thanks to the homogenization, the computation of the dispersion curves for the relaxed micromorphic model can be made analytically, reducing the partial differential equation system (*i.e.* our constitutive laws) into the algebraic system

$$\text{Det } \mathbb{D}(\mathbf{k}, w) = 0 \quad (3.86)$$

where \mathbb{D} is a 6×6 matrix obtained *via* "injecting" in our local equilibrium equations the monochromatic plane wave

$$\mathbf{u}(\mathbf{x}, t) = \hat{\mathbf{U}} \exp(\langle \mathbf{k}, \mathbf{x} \rangle - \omega t), \mathbf{P}(\mathbf{x}, t) = \hat{\mathbf{P}} \exp(\langle \mathbf{k}, \mathbf{x} \rangle - \omega t) \quad \text{and} \quad \mathbf{k} = k \hat{\mathbf{k}} \quad (3.87)$$

where $\hat{\mathbf{U}}$ is the polarization vector, $\|\hat{\mathbf{k}}\| = 1$ is the direction of wave propagation and k the wave number. The dispersion curves along ΓX and ΓM of the architected unit cell and the relaxed micromorphic model are given in 3.8.

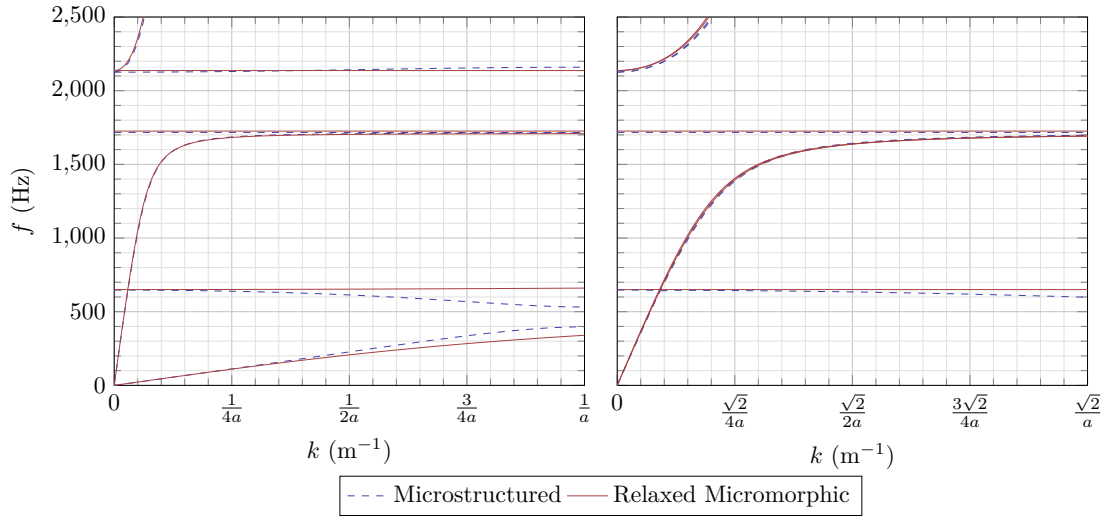


Figure 3.8: (*left*) Dispersion curves of the microstructured and the relaxed micromorphic systems along ΓX (propagation at 0°). (*right*) Dispersion curves of the microstructured and the relaxed micromorphic systems along ΓM (propagation at 45°).

The calibrated values of the relaxed micromorphic parameters relative to the metamaterial in Figure 3.6 and used for the simulations are presented in Table 3.2.

ρ	μ_e	λ_e	μ_e^*
[kg/m ³]	[Pa]	[Pa]	[Pa]
3841	$2.53 \cdot 10^9$	$1.01 \cdot 10^8$	$1.26 \cdot 10^6$
μ_m	λ_m	μ_m^*	μ_c
[Pa]	[Pa]	[Pa]	[Pa]
$4.51 \cdot 10^9$	$1.83 \cdot 10^8$	$2.70 \cdot 10^8$	10^5
η_1	η_2	η_3	η_1^*
[kg/m]	[kg/m]	[kg/m]	[kg/m]
38.99	$5.99 \cdot 10^{-3}$	1.58	2.31
$\bar{\eta}_1$	$\bar{\eta}_2$	$\bar{\eta}_3$	$\bar{\eta}_1^*$
[kg/m]	[kg/m]	[kg/m]	[kg/m]
$8 \cdot 10^{-4}$	0.02	0.008	0.09

Table 3.2: Values of the elastic and micro-inertia relaxed micromorphic parameters calibrated on the metamaterial whose unit cell is reported in Figure 3.6.

Chapter 3. From Cauchy to micromorphic modelling

By enriching the description of our structures with additional kinematic fields, in our case micro-distorsion tensor \mathbf{P} , the equilibrium and constitutive laws of our media have been complexified. On the other hand, the domain on which our variational principles hold are considerably simplified, as presented in Figure 3.9.

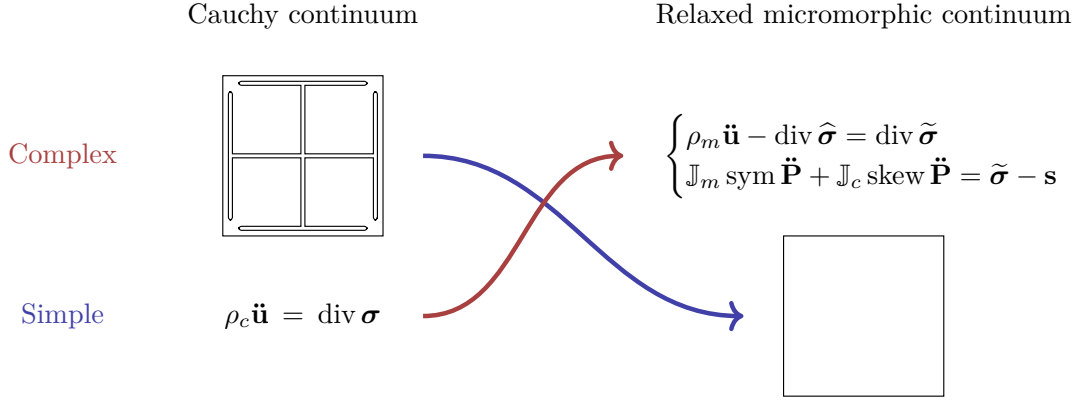


Figure 3.9: Respective domains and constitutive laws of the classical Cauchy and the relaxed micromorphic medium.

If, at first sight, it may seem like we left one evil for another, one shall remember that the resolution of systems in Engineering Sciences heavily relies on the Finite-Element Method (that will be presented in the following sections), for which neither the nature nor the physical significance of the problem's variables matter, to the difference of the number of nodes, shape functions and weak formulation considered.

3.3 The equivalent macroscopic Cauchy model

Considering a very large sample of our microstructured material, the effect of the microstructure can be considered as negligible. Under that hypothesis, the relaxed micromorphic model is equivalent to a classical Cauchy model of elastic stiffness tensor \mathbb{C}_M . Its strain density energy w_e is then defined by [Barbagallo 2017, Barbagallo 2019b]

$$w_e(\nabla \mathbf{u}) = \frac{1}{2} \langle \text{sym } \nabla \mathbf{u}, \mathbb{C}_M \text{sym } \nabla \mathbf{u} \rangle \quad (3.88)$$

Its identification can be made by a harmonic tensor mean of the constitutive tensors $\mathbb{C}_{\text{micro}}$ and \mathbb{C}_e :

$$\mathbb{C}_M = \mathbb{C}_m (\mathbb{C}_m + \mathbb{C}_e)^{-1} \mathbb{C}_e \quad (3.89)$$

Thanks to the ‘‘Cartan-like’’ decomposition of the constitutive laws (sym and skew split), the computation of \mathbb{C}_e can be made *via* the ‘‘Reuss-like’’ homogenization formula

$$\mathbb{C}_e = \mathbb{C}_m (\mathbb{C}_m - \mathbb{C}_M)^{-1} \mathbb{C}_M \quad (3.90)$$

\mathbb{C}_M , in the Voigt-Mandel notation, is

$$\mathbb{C}_M = \begin{pmatrix} \lambda_M + 2\mu_M & \lambda_M & * & 0 & 0 & 0 \\ \lambda_M & \lambda_M + 2\mu_M & * & 0 & 0 & 0 \\ * & * & * & 0 & 0 & 0 \\ 0 & 0 & 0 & * & 0 & 0 \\ 0 & 0 & 0 & 0 & * & 0 \\ 0 & 0 & 0 & 0 & 0 & \mu_M^* \end{pmatrix} \quad (3.91)$$

The values of λ_M , μ_M and μ_M^* given in Table 3.3, are obtained by periodic homogenization, boundary conditions mimicking an infinite number of unit cells, in formulas

$$\frac{1}{2} \langle \mathbf{E}, \mathbb{C}_M \mathbf{E} \rangle = \frac{1}{\Omega_c} \inf \left\{ \int_{\Omega_c} \frac{1}{2} \langle \text{sym}(\nabla \mathbf{u} + \mathbf{E}), \mathbb{C} \text{sym}(\nabla \mathbf{u} + \mathbf{E}) \rangle d\Omega \mid \mathbf{u} \in \mathcal{C}^\infty(\Omega_c, \mathbb{R}^3) \text{ is periodic} \right\} \quad (3.92)$$

making these coefficients independent of the size and shape of the unit cell. The values of the mechanical parameters of this equivalent macroscopic Cauchy model are given in Table 3.3.

λ_M	μ_M	μ_M^*
[Pa]	[Pa]	[Pa]
6.51×10^7	1.62×10^9	1.25×10^6

Table 3.3: Values of the elastic the corresponding long-wave limit Cauchy material parameters calibrated on the metamaterial whose unit cell is reported in Figure 3.6.

The kinetic energy density remaining untouched, *i.e.*

$$k_e = \frac{1}{2} \langle \dot{\mathbf{u}}, \rho_m \dot{\mathbf{u}} \rangle \quad (3.93)$$

Plotting the dispersion diagrams of such a medium would asymptotically give the dispersion curves at $f = 0$, at least for the acoustic ones, of the architected cell. If such a continuum does not allow to describe the band-gap effect of the microstructured unit cell given in 3.6, we will show that it still allows to represent, under some hypothesis, the static response of our microstructured plates.

3.4 The piezoelectric model

We presented in Chapter 2 the piezoelectric excitation used to characterize our *proof of concept*: given the strong coupling between the microstructured plate and these patches, its modelling was required to solve this multiphysics problem.

Chapter 3. From Cauchy to micromorphic modelling

Piezoelectricity refers to the ability of certain materials to be polarized under the application of mechanical stress [Curie 1881] and reciprocally to generate a mechanical strain when a electric potential is applied. Figure 3.10 presents the interactions between Electrostatics and Mechanics.

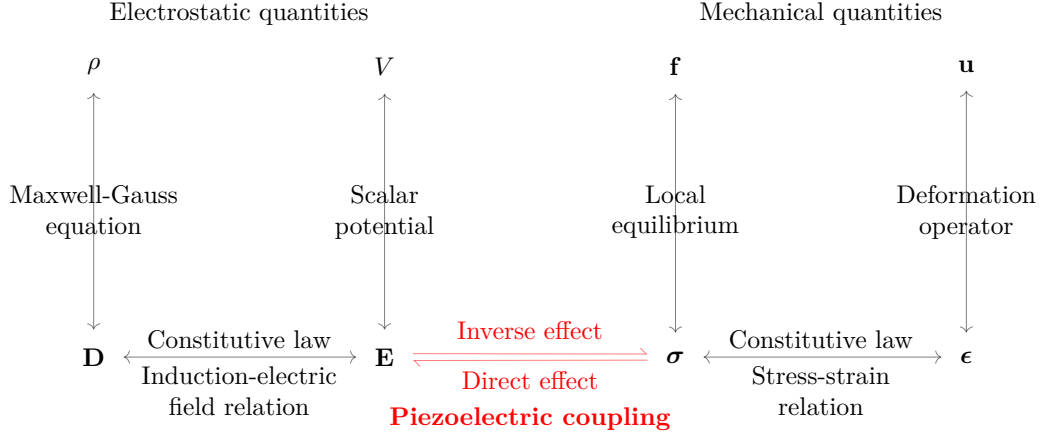


Figure 3.10: Between mechanic and electrostatic: the piezoelectric effect.

The modelling of such a coupled system can, once again, be made through the Principle of Least Action. In our case, the action functional \mathcal{A}_p introduced is

$$\mathcal{A}_p = \mathcal{A}_{\text{int}}^p + \mathcal{A}_{\text{ext}}^p \quad \text{where} \quad \mathcal{A}_{\text{int}}^p [\mathbf{u}, V] = \int_{t_1}^{t_2} \int_{\Omega_p} \ell_p d\Omega dt = \int_{t_1}^{t_2} \int_{\Omega_p} (k_p - w_p - q) d\Omega dt \quad (3.94)$$

where ℓ_p is the Lagrangian density of the piezoelectric medium, k_p , w_p and q being respectively the kinetic, strain and electric potential energy density of the piezoelectric patch. Their respective expressions are respectively given by:

$$\begin{aligned} k_p &= \frac{1}{2} \langle \dot{\mathbf{u}}, \rho_p \dot{\mathbf{u}} \rangle \\ w_p &= \frac{1}{2} \langle \text{sym } \nabla \mathbf{u}, \mathbb{C}_p \text{sym } \nabla \mathbf{u} + \boldsymbol{\xi}^T \mathbf{E} \rangle \\ q &= \frac{1}{2} \langle \mathbf{E}, \varepsilon_0 \boldsymbol{\varepsilon} \mathbf{E} + \boldsymbol{\xi} \text{sym } \nabla \mathbf{u} \rangle \end{aligned} \quad (3.95)$$

where $\rho_p : \Omega \rightarrow \mathbb{R}^+$ is the mass density, $\varepsilon_0 = 8.86 \cdot 10^{-12} [\text{F/m}]$ is the vacuum permittivity, $\mathbf{E} : \Omega \rightarrow \mathbb{R}^3$ is the electric vector field (in V/m), $\boldsymbol{\varepsilon} : \mathbb{R}^3 \rightarrow \mathbb{R}^3$ and $\boldsymbol{\xi} : \mathfrak{s}(\mathbb{R}^3) \rightarrow \mathbb{R}^3$ is the piezoelectric tensor. In the approximation of the electrostatic, \mathbf{E} derives from the electric potential $V : \Omega \rightarrow \mathbb{R}$, *i.e.*

$$\mathbf{E} = -\nabla V \quad (3.96)$$

For the work of external forces and charges, we have

$$\mathcal{A}_{\text{ext}}^p[\mathbf{u}, V] = \mathcal{A}_{\text{ext}}^{\text{meca}}[\mathbf{u}] + \mathcal{A}_{\text{ext}}^{\text{elec}}[V] \text{ where } \begin{cases} \mathcal{A}_{\text{ext}}^{\text{meca}}[\mathbf{u}] = \int_{t_1}^{t_2} \left[\int_{\Omega} \langle \mathbf{f}, \mathbf{u} \rangle d\Omega + \int_{\partial\Omega_{\mathcal{N}}^{\mathbf{u}}} \langle \mathbf{t}_0, \mathbf{u} \rangle d\Gamma \right] dt \\ \mathcal{A}_{\text{ext}}^{\text{elec}}[V] = \int_{t_1}^{t_2} \left[\int_{\Omega} \rho_v V d\Omega + \int_{\partial\Omega_{\mathcal{N}}^V} \rho_s V d\Gamma \right] dt \end{cases} \quad (3.97)$$

where $\rho_v : \Omega \rightarrow \mathbb{R}$ and $\rho_s : \partial\Omega_{\mathcal{N}}^V \rightarrow \mathbb{R}$ are respectively the volumic and surfacic densities of electrical charges, in $[\text{C.m}^{-3}]$ and $[\text{C.m}^{-2}]$. The Dirichlet boundaries conditions are

$$\begin{cases} \mathbf{u} = \mathbf{u}_0 & \text{on } \partial\Omega_{\mathcal{D}}^{\mathbf{u}} \\ V = V_0 & \text{on } \partial\Omega_{\mathcal{D}}^V \end{cases} \quad (3.98)$$

We also have

$$\partial\Omega = \begin{cases} \partial\Omega_{\mathcal{D}}^{\mathbf{u}} \cup \Omega_{\mathcal{N}}^{\mathbf{u}} & \text{with } \partial\Omega_{\mathcal{D}}^{\mathbf{u}} \cap \Omega_{\mathcal{N}}^{\mathbf{u}} = \emptyset \\ \partial\Omega_{\mathcal{D}}^V \cup \Omega_{\mathcal{N}}^V & \text{with } \partial\Omega_{\mathcal{D}}^V \cap \Omega_{\mathcal{N}}^V = \emptyset \end{cases} \quad (3.99)$$

At last, the initial conditions are

$$\begin{cases} \mathbf{u}(t = t_1) = \mathbf{u}_i \\ \dot{\mathbf{u}}(t = t_1) = \mathbf{v}_i \\ V(t = t_1) = V_i \end{cases} \quad \text{in } \Omega \quad (3.100)$$

The Principle of Least Action states that the trajectory followed by the system $(\mathbf{u}, V) : (\mathbf{x}, t) \in \Omega \times [t_1, t_2] \mapsto (\mathbf{u}(\mathbf{x}, t), V(\mathbf{x}, t))$ is the one for which the action functional is stationary, *i.e.* verifies

$$\{\delta\mathcal{A}_p[\mathbf{u}, V] = 0 \text{ where } (\mathbf{u}, V) \text{ verifies 3.98 and 3.100}\} \quad (3.101)$$

Given the kinetic and strain energy densities introduced in (3.95), we can define the space of configuration \mathcal{Q}_p to which \mathbf{u} should belong

$$\mathcal{Q}_p = \{(\mathbf{u}, V) : (\mathbf{u}, V) \text{ verifies 3.98 and 3.100}\} \quad (3.102)$$

To properly compute the variation of Action, $(\delta\mathbf{u}, \delta V)$ shall verify

$$\begin{cases} \delta\mathbf{u}(t_1) = \mathbf{0} = \delta\mathbf{u}(t_2) \\ \delta V(t_1) = 0 = \delta V(t_2) \end{cases} \quad \text{in } \Omega \quad \text{and} \quad \begin{cases} \forall t \in [t_1, t_2], \delta\mathbf{u} = \mathbf{0} & \text{on } \partial\Omega_{\mathcal{D}}^{\mathbf{u}} \\ \forall t \in [t_1, t_2], \delta V = 0 & \text{on } \partial\Omega_{\mathcal{D}}^V \end{cases} \quad (3.103)$$

As the kinetic and strain energy densities are very close to the ones introduced for the classical Cauchy medium, the local equilibriums deduced from the Least Action Principle can be quickly computed. Let us just notice that

$$\begin{aligned} \langle \text{sym } \nabla \mathbf{u}, \boldsymbol{\xi}^T \mathbf{E} \rangle &= \text{Tr}([\text{sym } \nabla \mathbf{u}]^T \cdot \boldsymbol{\xi}^T \mathbf{E}) \\ &= \text{Tr}[\mathbf{E}^T \cdot ([\text{sym } \nabla \mathbf{u}]^T \cdot \boldsymbol{\xi}^T)^T] \\ &= \mathbf{E}^T \cdot (\boldsymbol{\xi} \text{sym } \nabla \mathbf{u}) \\ &= \langle \mathbf{E}, \boldsymbol{\xi} \text{sym } \nabla \mathbf{u} \rangle \end{aligned} \quad (3.104)$$

Chapter 3. From Cauchy to micromorphic modelling

One can notice that such computation does not rely on the symmetry of $\boldsymbol{\varepsilon} = \text{sym } \nabla \mathbf{u}$, *i.e.* would still hold without the small displacement hypothesis. Given this, we have

$$\begin{aligned} \delta \mathcal{A}_p &= \int_{t_1}^{t_2} \int_{\Omega} [\dots + \delta V [\text{div}(\varepsilon_0 \boldsymbol{\varepsilon} \mathbf{E} + \boldsymbol{\xi} \text{sym } \nabla \mathbf{u}) - \rho_v] + \dots] d\Omega dt \\ &+ \int_{t_1}^{t_2} \int_{\partial \Omega_{\mathcal{N}}^u} \delta V (\langle \mathbf{D}, \mathbf{n} \rangle - \rho_s) d\Gamma dt \\ &+ \int_{t_1}^{t_2} \int_{\partial \Omega_{\mathcal{N}}^V} \dots d\Gamma dt \end{aligned} \quad (3.105)$$

the “dotted” terms being already known. We eventually get the equilibrium laws

$$\begin{cases} \rho_p \ddot{\mathbf{u}} = \text{div } \boldsymbol{\sigma} + \mathbf{f} & \text{(Cauchy equilibrium)} \\ \text{div } \mathbf{D} = \rho_v & \text{(Maxwell-Gauss law)} \end{cases} \quad (3.106)$$

where the Cauchy stress tensor $\boldsymbol{\sigma}$ and the electric induction \mathbf{D} are given by the constitutive laws

$$\begin{cases} \boldsymbol{\sigma} = \mathbb{C}_p \text{sym } \nabla \mathbf{u} + \boldsymbol{\xi}^T \mathbf{E} \\ \mathbf{D} = \varepsilon_0 \boldsymbol{\varepsilon} \mathbf{E} + \boldsymbol{\xi} \text{sym } \nabla \mathbf{u} \end{cases} \quad (3.107)$$

The Neumann boundary conditions associated are

$$\begin{cases} \boldsymbol{\sigma} \cdot \mathbf{n} = \mathbf{t} & \text{on } \partial \Omega_{\mathcal{N}}^u \\ \langle \mathbf{D}, \mathbf{n} \rangle = \rho_s & \text{on } \partial \Omega_{\mathcal{N}}^V \end{cases} \quad (3.108)$$

The elastic tensor \mathbb{C}_p , the piezoelectric tensor $\boldsymbol{\xi}$, and the relative permittivity tensor $\boldsymbol{\varepsilon}$ are here presented in Voigt notation for the considered 3D case. Given the cylindrical symmetry of the piezoelectric patches presented in Chapter 2, these tensors take the form:

$$\begin{aligned} \mathbb{C}_p &= \begin{pmatrix} C_{11} & C_{12} & C_{13} & 0 & 0 & 0 \\ C_{12} & C_{11} & C_{13} & 0 & 0 & 0 \\ C_{13} & C_{13} & C_{33} & 0 & 0 & 0 \\ 0 & 0 & 0 & C_{44} & 0 & 0 \\ 0 & 0 & 0 & 0 & C_{44} & 0 \\ 0 & 0 & 0 & 0 & 0 & C_{66} \end{pmatrix}, \\ \boldsymbol{\xi} &= \begin{pmatrix} 0 & 0 & 0 & 0 & \xi_{15} & 0 \\ 0 & 0 & 0 & \xi_{15} & 0 & 0 \\ \xi_{31} & \xi_{31} & \xi_{33} & 0 & 0 & 0 \end{pmatrix}, \quad \boldsymbol{\varepsilon} = \begin{pmatrix} \varepsilon_{11} & 0 & 0 \\ 0 & \varepsilon_{11} & 0 \\ 0 & 0 & \varepsilon_{33} \end{pmatrix}. \end{aligned} \quad (3.109)$$

The values of the parameters used for the numerical simulations of the piezoelectric patches introduced in Chapter 2 are presented in Table 3.4.

C_{11}	C_{12}	C_{13}	C_{33}	C_{44}	C_{66}
[GPa]	[GPa]	[GPa]	[GPa]	[GPa]	[GPa]
1140	757	724	1110	263	403
ρ_p	ε_{11}	ε_{33}	ξ_{31}	ξ_{33}	ξ_{15}
[kg /m ³]	-	-	[C/m ²]	[C/m ²]	[C/m ²]
7780	$3.24 \cdot 10^3$	$3.98 \cdot 10^3$	-2.92	23.4	16.2

Table 3.4: Mechanical, coupling and electrical parameters parameters of the piezoelectric patches.

3.5 Symmetries

Given the relative complexity of the considered problems, it can be advantageous to consider the eventual symmetries of the models to solve. The symmetry of a problem occurs when are reunited:

- the symmetry of geometry
- the symmetry of boundary conditions
- the symmetry of load(s)
- the symmetry of constitutive laws

Such a situation is presented in Figure 3.11.

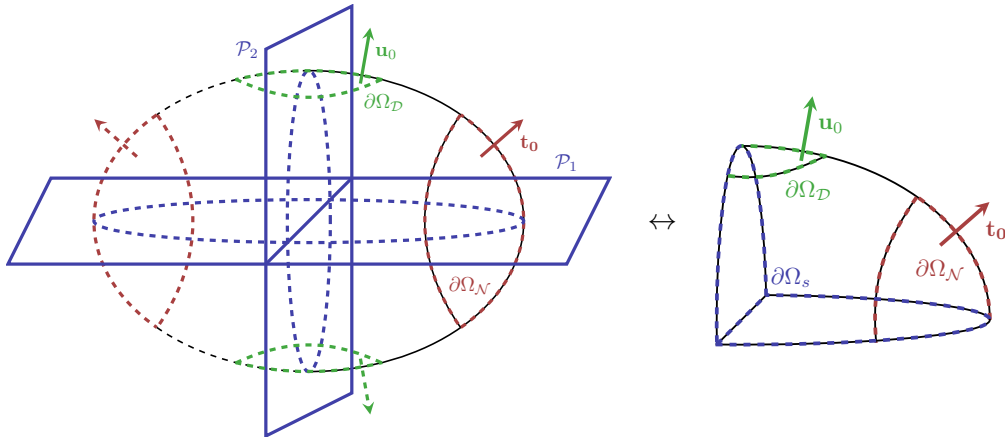


Figure 3.11: (left) Unsymmetrized system with its load and symmetry planes. (right) Reduced system with the created symmetry boundary $\partial\Omega_s$.

Under these conditions, one can compute the response of the full system by considering only the smallest part of it allowing to recreate the whole system. Given the nature of the considered metamaterial and the general context of this manuscript, this first proof is reduced in the case of Cartesian coordinates, for symmetries along planes (O, \mathbf{x}_1) and (O, \mathbf{x}_2) , which is precisely the case of this framework.

3.5.1 A first case: plane \mathcal{P} of normal \mathbf{n}

In a first time, we will show that the structure of the constitutive laws of the relaxed micromorphic medium implies, considering that the symmetries of the displacement \mathbf{u} are conserved, certain symmetries upon the microdistorsion \mathbf{P} . Having $(\mathbf{t}_1, \mathbf{t}_2)$ such as $\mathbf{t}_1 \wedge \mathbf{t}_2 = \mathbf{n}$, then $(\mathbf{t}_1, \mathbf{t}_2, \mathbf{n})$ forms an orthonormal basis, therefore

$$\exists!(u_1, u_2, u_3) \in \mathcal{C}^1(\mathbb{R}^3 \times [t_1, t_2], \mathbb{R}^3) : \mathbf{u} = u_1 \mathbf{t}_1 + u_2 \mathbf{t}_2 + u_3 \mathbf{n} \quad (3.110)$$

The relations of symmetry for \mathbf{u} allow to write

$$\forall(\mathbf{x}, x_3) \in \mathcal{P} \times \mathbb{R}, \begin{cases} u_1(\mathbf{x} + x_3 \mathbf{n}) = u_1(\mathbf{x} - x_3 \mathbf{n}) \\ u_2(\mathbf{x} + x_3 \mathbf{n}) = u_2(\mathbf{x} - x_3 \mathbf{n}) \\ u_3(\mathbf{x} + x_1 \mathbf{t}_1 + x_2 \mathbf{t}_2) = 0 \end{cases} \quad (3.111)$$

One can compute $\nabla \mathbf{u}$ in the symmetry plane in the base $(\mathbf{t}_1, \mathbf{t}_2, \mathbf{n})$ by

$$\forall \mathbf{v}, ((\nabla \mathbf{u}) \cdot \mathbf{v})(\mathbf{x}) = \lim_{\varepsilon \rightarrow 0} \frac{1}{2} \frac{\mathbf{u}(\mathbf{x} + \varepsilon \mathbf{v}) - \mathbf{u}(\mathbf{x} - \varepsilon \mathbf{v})}{\varepsilon} \quad (3.112)$$

With the symmetry relations, one can deduce

$$\forall \mathbf{x} \in \mathcal{P}, ((\nabla \mathbf{u}) \cdot \mathbf{t}_1)(\mathbf{x}) = \begin{pmatrix} \star \\ \star \\ 0 \end{pmatrix} \quad (3.113)$$

By the same way, one can deduce

$$\forall \mathbf{x} \in \mathcal{P}, ((\nabla \mathbf{u}) \cdot \mathbf{t}_2)(\mathbf{x}) = \begin{pmatrix} \star \\ \star \\ 0 \end{pmatrix} \text{ and } ((\nabla \mathbf{u}) \cdot \mathbf{n})(\mathbf{x}) = \begin{pmatrix} 0 \\ 0 \\ \star \end{pmatrix} \quad (3.114)$$

In the symmetry plane, one has

$$\forall \mathbf{x} \in \mathcal{P}, (\nabla \mathbf{u})_{[\mathbf{t}_1, \mathbf{t}_2, \mathbf{n}]}(\mathbf{x}) = \begin{pmatrix} \star & \star & 0 \\ \star & \star & 0 \\ 0 & 0 & \star \end{pmatrix} \quad (3.115)$$

The equilibrium equations for \mathbf{P} being

$$\mathbb{J}_m \text{sym } \ddot{\mathbf{P}} + \mathbb{J}_c \text{skew } \ddot{\mathbf{P}} = \mathbb{C}_e \text{sym } (\nabla \mathbf{u} - \mathbf{P}) + \mathbb{C}_c \text{skew } (\nabla \mathbf{u} - \mathbf{P}) - \mathbb{C}_m \text{sym } \mathbf{P} \quad (3.116)$$

Can be rewritten under the form

$$\left[\frac{d^2}{dt^2} \mathbb{J}_m + \mathbb{C}_e + \mathbb{C}_m \right] \text{sym } \mathbf{P} + \left[\frac{d^2}{dt^2} \mathbb{J}_c + \mathbb{C}_c \right] \text{skew } \mathbf{P} = \mathbb{C}_e \text{sym } \nabla \mathbf{u} + \mathbb{C}_c \text{skew } \nabla \mathbf{u} \quad (3.117)$$

Supposing moreover that the inertial and stiffness operators of the material considered have the following shape along the symmetry plane in the considered base (which is the case for our considered metamaterial)

$$\mathbb{J}_m = \begin{pmatrix} \star & \star & \star & 0 & 0 & 0 \\ \star & \star & \star & 0 & 0 & 0 \\ \star & \star & \star & 0 & 0 & 0 \\ 0 & 0 & 0 & \star & 0 & 0 \\ 0 & 0 & 0 & 0 & \star & 0 \\ 0 & 0 & 0 & 0 & 0 & \star \end{pmatrix}, \mathbb{C}_e = \begin{pmatrix} \star & \star & \star & 0 & 0 & 0 \\ \star & \star & \star & 0 & 0 & 0 \\ \star & \star & \star & 0 & 0 & 0 \\ 0 & 0 & 0 & \star & 0 & 0 \\ 0 & 0 & 0 & 0 & \star & 0 \\ 0 & 0 & 0 & 0 & 0 & \star \end{pmatrix}, \mathbb{C}_m = \begin{pmatrix} \star & \star & \star & 0 & 0 & 0 \\ \star & \star & \star & 0 & 0 & 0 \\ \star & \star & \star & 0 & 0 & 0 \\ 0 & 0 & 0 & \star & 0 & 0 \\ 0 & 0 & 0 & 0 & \star & 0 \\ 0 & 0 & 0 & 0 & 0 & \star \end{pmatrix},$$

$$\mathbb{C}_c = \begin{pmatrix} \star & 0 & 0 \\ 0 & \star & 0 \\ 0 & 0 & \star \end{pmatrix}, \quad \mathbb{J}_c = \begin{pmatrix} \star & 0 & 0 \\ 0 & \star & 0 \\ 0 & 0 & \star \end{pmatrix}$$
(3.118)

The structures of \mathbf{u} and \mathbf{P} being conserved, one can deduce

$$\forall \mathbf{x} \in \mathcal{P}, \mathbf{P}_{[t_1, t_2, \mathbf{n}]}(\mathbf{x}) = \begin{pmatrix} \star & \star & 0 \\ \star & \star & 0 \\ 0 & 0 & \star \end{pmatrix}$$
(3.119)

In fact, we are going to prove that those properties of symmetry are independent of the constitutive laws of the considered relaxed micromorphic medium, but on the opposite that the shape of these constitutive laws have to satisfy such symmetry relations.

3.5.2 Using the Curie's Principle

\mathbf{u} and \mathbf{P} not depending on the orientation of space, supposing our problem to have a symmetry with respect to the plane \mathcal{P} of normal \mathbf{n} , one can apply Curie's Symmetry Principle, which gives

$$\begin{cases} \mathbf{u}(\mathbf{x}^*) = \mathbf{u}^*(\mathbf{x}) \\ \mathbf{P}(\mathbf{x}^*) = \mathbf{P}^*(\mathbf{x}) \end{cases}$$
(3.120)

χ^* being the symmetric of χ with respect to \mathcal{P} . Let us define \mathbf{t}_1 and \mathbf{t}_2 so that $(\mathbf{t}_1, \mathbf{t}_2, \mathbf{t}_3 = \mathbf{n})$ forms an orthonormal basis, thus

$$\mathbf{t}_1^* = \mathbf{t}_1, \mathbf{t}_2^* = \mathbf{t}_2 \text{ and } \mathbf{n}^* = -\mathbf{n}$$
(3.121)

And

$$\begin{aligned} (\mathbf{t}_1 \otimes \mathbf{t}_1)^* &= \mathbf{t}_1 \otimes \mathbf{t}_1, (\mathbf{t}_1 \otimes \mathbf{t}_2)^* = \mathbf{t}_1 \otimes \mathbf{t}_2, (\mathbf{t}_1 \otimes \mathbf{n})^* = -\mathbf{t}_1 \otimes \mathbf{n} \\ (\mathbf{t}_2 \otimes \mathbf{t}_1)^* &= \mathbf{t}_2 \otimes \mathbf{t}_1, (\mathbf{t}_2 \otimes \mathbf{t}_2)^* = \mathbf{t}_2 \otimes \mathbf{t}_2, (\mathbf{t}_2 \otimes \mathbf{n})^* = -\mathbf{t}_2 \otimes \mathbf{n} \\ (\mathbf{n} \otimes \mathbf{t}_1)^* &= -\mathbf{n} \otimes \mathbf{t}_1, (\mathbf{n} \otimes \mathbf{t}_2)^* = -\mathbf{n} \otimes \mathbf{t}_2 \text{ and } (\mathbf{n} \otimes \mathbf{n})^* = \mathbf{n} \otimes \mathbf{n} \end{aligned}$$
(3.122)

Chapter 3. From Cauchy to micromorphic modelling

Let us write \mathbf{u} and \mathbf{P} in this base:

$$\begin{cases} \exists!(u_1, u_2, u_3) \in \mathcal{C}^0(\mathbb{R}^3, \mathbb{R}^3) : \mathbf{u} = u_i \mathbf{t}_i \\ \exists!(P_{11}, P_{22}, P_{33}, P_{12}, P_{13}, P_{21}, P_{31}, P_{32}, P_{23}) \in \mathcal{C}^0(\mathbb{R}^3, \mathbb{R}^9) : \mathbf{P} = P_{ij} \mathbf{t}_i \otimes \mathbf{t}_j \end{cases} \quad (3.123)$$

Let us also write \mathbf{x} as

$$\exists!(\mathbf{x}_0, \varepsilon) \in \mathcal{P} \times \mathbb{R} : \mathbf{x} = \mathbf{x}_0 + \varepsilon \mathbf{n} \quad (3.124)$$

Then

$$\mathbf{x}^* = \mathbf{x}_0 - \varepsilon \mathbf{n} \quad (3.125)$$

For \mathbf{u} , substituting in 3.120, one can get

$$u_1(\mathbf{x}_0 - \varepsilon \mathbf{n}) \mathbf{t}_1 + u_2(\mathbf{x}_0 - \varepsilon \mathbf{n}) \mathbf{t}_2 + u_3(\mathbf{x}_0 - \varepsilon \mathbf{n}) \mathbf{n} = u_1(\mathbf{x}_0 + \varepsilon \mathbf{n}) \mathbf{t}_1 + u_2(\mathbf{x}_0 + \varepsilon \mathbf{n}) \mathbf{t}_2 - u_3(\mathbf{x}_0 + \varepsilon \mathbf{n}) \mathbf{n} \quad (3.126)$$

By identification

$$\forall \mathbf{x}_0 \in \mathcal{P}, \forall \varepsilon \in \mathbb{R} \begin{cases} u_1(\mathbf{x}_0 - \varepsilon \mathbf{n}) = u_1(\mathbf{x}_0 + \varepsilon \mathbf{n}) \\ u_2(\mathbf{x}_0 - \varepsilon \mathbf{n}) = u_2(\mathbf{x}_0 + \varepsilon \mathbf{n}) \\ u_3(\mathbf{x}_0 - \varepsilon \mathbf{n}) = -u_3(\mathbf{x}_0 + \varepsilon \mathbf{n}) \end{cases} \quad (3.127)$$

In the same way, we have for \mathbf{P}

$$\forall \mathbf{x}_0 \in \mathcal{P}, \forall \varepsilon \in \mathbb{R} \begin{cases} P_{11}(\mathbf{x}_0 - \varepsilon \mathbf{n}) = P_{11}(\mathbf{x}_0 + \varepsilon \mathbf{n}) \\ P_{12}(\mathbf{x}_0 - \varepsilon \mathbf{n}) = P_{12}(\mathbf{x}_0 + \varepsilon \mathbf{n}) \\ P_{13}(\mathbf{x}_0 - \varepsilon \mathbf{n}) = -P_{13}(\mathbf{x}_0 + \varepsilon \mathbf{n}) \\ P_{21}(\mathbf{x}_0 - \varepsilon \mathbf{n}) = P_{21}(\mathbf{x}_0 + \varepsilon \mathbf{n}) \\ P_{22}(\mathbf{x}_0 - \varepsilon \mathbf{n}) = P_{22}(\mathbf{x}_0 + \varepsilon \mathbf{n}) \\ P_{23}(\mathbf{x}_0 - \varepsilon \mathbf{n}) = -P_{23}(\mathbf{x}_0 + \varepsilon \mathbf{n}) \\ P_{31}(\mathbf{x}_0 - \varepsilon \mathbf{n}) = -P_{31}(\mathbf{x}_0 + \varepsilon \mathbf{n}) \\ P_{32}(\mathbf{x}_0 - \varepsilon \mathbf{n}) = -P_{32}(\mathbf{x}_0 + \varepsilon \mathbf{n}) \\ P_{33}(\mathbf{x}_0 - \varepsilon \mathbf{n}) = P_{33}(\mathbf{x}_0 + \varepsilon \mathbf{n}) \end{cases} \quad (3.128)$$

These conditions allow to reconstruct the displacement and microdistorsion fields in the whole plate, when knowing them in one fourth of the plate. For consistency reasons, when considering the symmetry planes, these conditions imply:

$$\forall \mathbf{x} \in \mathcal{N}, \begin{cases} \langle \mathbf{u}, \mathbf{n} \rangle = 0 \\ \langle \mathbf{P}, n \otimes \mathbf{t}_1 \rangle = 0 \\ \langle \mathbf{P}, n \otimes \mathbf{t}_2 \rangle = 0 \\ \langle \mathbf{P}, \mathbf{t}_1 \otimes \mathbf{n} \rangle = 0 \\ \langle \mathbf{P}, \mathbf{t}_2 \otimes \mathbf{n} \rangle = 0 \end{cases} \quad \text{i.e. } \forall \mathbf{x} \in \mathcal{P}, \mathbf{u}_{[\mathbf{t}_1, \mathbf{t}_2, \mathbf{n}]}(\mathbf{x}) = \begin{pmatrix} \star \\ \star \\ 0 \end{pmatrix} \quad \text{and} \quad \mathbf{P}_{[\mathbf{t}_1, \mathbf{t}_2, \mathbf{n}]}(\mathbf{x}) = \begin{pmatrix} \star & \star & 0 \\ \star & \star & 0 \\ 0 & 0 & \star \end{pmatrix} \quad (3.129)$$

This can be written, using Einstein's convention, as

$$\forall \mathbf{x} \in \mathcal{P}, \begin{cases} u_i n_i = 0 \\ (\delta_{ki} - n_k n_i) (P_{ij} n_j) = 0 \quad \forall k = \{1, 2, 3\} \end{cases} \quad (3.130)$$

3.6 Boundary conditions at interfaces

The structures considered in this manuscript consisting of an assembly of different continua, *e.g.*, as we introduced before, Cauchy, relaxed micromorphic or piezoelectric medium, one should consider the conditions of continuity at the interfaces between those media. We will show that the introduction of additional kinematic field (\mathbf{P} in our case) needs the imposition of additional boundary conditions [Madeo 2016b].

3.6.1 Between two Cauchy continua

Let us consider two Cauchy media Ω_1 and Ω_2 and respective Lagrangian densities ℓ_1 and ℓ_2 having a common boundary $\partial\Omega_i$ of normal \mathbf{n} as presented in Figure 3.12.

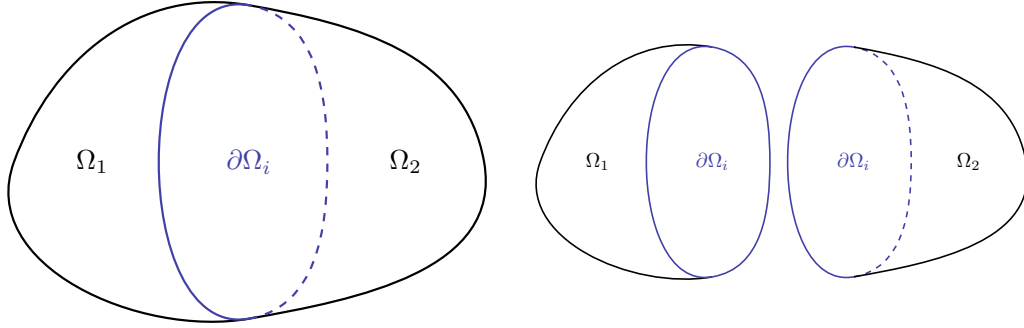


Figure 3.12: Interface between two Cauchy media

Let us fictively split the two media with their respective displacements \mathbf{u}_1 and \mathbf{u}_2 . The continuity of displacement

$$\mathbf{u}_1 = \mathbf{u}_2 \quad \text{on } \partial\Omega_i \quad (3.131)$$

Is imposed *via* the Lagrange multiplier $\boldsymbol{\lambda}$, modifying the action of the system \mathcal{A} by

$$\mathcal{A}'[\mathbf{u}_1, \mathbf{u}_2, \boldsymbol{\lambda}] = \mathcal{A}[\mathbf{u}_1, \mathbf{u}_2] - \int_{\partial\Omega_i} \langle \boldsymbol{\lambda}, \mathbf{u}_2 - \mathbf{u}_1 \rangle d\Gamma dt \quad (3.132)$$

Classically, the Lagrange equation \mathcal{L}_λ associated to λ gives the continuity of displacement (the constrain imposed):

$$\int_{\partial\Omega_i} \langle \delta\boldsymbol{\lambda}, \mathbf{u}_2 - \mathbf{u}_1 \rangle d\Gamma dt = 0 \quad (3.133)$$

Let us detail the Euler-Lagrange equations for \mathbf{u}_1 and \mathbf{u}_2 . The action of the system is

$$\mathcal{A}[\mathbf{u}_1, \mathbf{u}_2, \boldsymbol{\lambda}] = \int_{t_1}^{t_2} \left[\int_{\Omega_1} \ell_1[\dot{\mathbf{u}}_1, \boldsymbol{\nabla}\mathbf{u}_1, \mathbf{u}_1] d\Omega + \int_{\Omega_2} \ell_2[\dot{\mathbf{u}}_2, \boldsymbol{\nabla}\mathbf{u}_2, \mathbf{u}_2] d\Omega - \int_{\partial\Omega_i} \langle \boldsymbol{\lambda}, \mathbf{u}_2 - \mathbf{u}_1 \rangle d\Gamma \right] dt \quad (3.134)$$

As we did before, the stationarity of the boundary term for \mathcal{L}_{u_1} gives

$$\int_{t_1}^{t_2} \int_{\partial\Omega_i} \left\langle \delta\mathbf{u}_1, \frac{\partial\ell_1}{\partial\boldsymbol{\nabla}\mathbf{u}_1} \cdot \mathbf{n}_1 + \boldsymbol{\lambda} \right\rangle d\Gamma dt = 0 \quad (3.135)$$

Chapter 3. From Cauchy to micromorphic modelling

The stationarity of the boundary term for \mathcal{L}_{u_2} gives

$$\int_{t_1}^{t_2} \int_{\partial\Omega_i} \left\langle \delta \mathbf{u}_2, \frac{\partial \ell_2}{\partial \nabla \mathbf{u}_2} \cdot \mathbf{n}_2 - \boldsymbol{\lambda} \right\rangle d\Gamma dt = 0 \quad (3.136)$$

Under this form, one can see that $\boldsymbol{\lambda}$ is the traction force exerted by Ω_1 on Ω_2 on the boundary $\partial\Omega_i$. Having

$$\mathbf{n}_1 = -\mathbf{n}_2 = \mathbf{n} \quad (3.137)$$

And

$$\boldsymbol{\sigma}_1 = -\frac{\partial \ell_1}{\partial \nabla \mathbf{u}_1} \quad \text{and} \quad \boldsymbol{\sigma}_2 = -\frac{\partial \ell_2}{\partial \nabla \mathbf{u}_2} \quad (3.138)$$

We have

$$\boldsymbol{\sigma}_1 \cdot \mathbf{n} = \boldsymbol{\sigma}_2 \cdot \mathbf{n} \quad \text{on } \partial\Omega_i \quad (3.139)$$

i.e. the continuity of traction forces at the interface $\partial\Omega_i$. As we considered the action functional $\mathcal{A}[\mathbf{u}_1, \mathbf{u}_2, \boldsymbol{\lambda}]$, such an approach can be considered as a mixed formulation, allowing to compute the interfaces forces between the two continua.

3.6.2 Between a Cauchy medium and a relaxed micromorphic medium

Let us consider a Cauchy medium Ω_c and a relaxed micromorphic medium Ω_m of respective Lagrangians density ℓ_c and ℓ_m having a common boundary $\partial\Omega_i$ of normal \mathbf{n} directed from Ω_1 towards Ω_2 as presented in Figure 3.13.

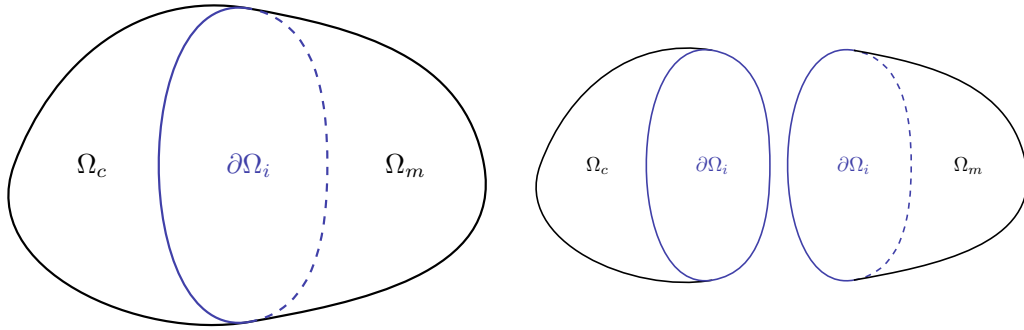


Figure 3.13: (left) Interface between a Cauchy and a relaxed micromorphic medium. (right) Fictive split between a Cauchy and a relaxed micromorphic medium.

Let us fictively split the two media with their respective displacements \mathbf{u}_c and \mathbf{u}_m . The continuity of displacement

$$\mathbf{u}_c = \mathbf{u}_m \quad \text{on } \partial\Omega_i \quad (3.140)$$

Is imposed *via* the Lagrange multiplier $\boldsymbol{\lambda}$, modifying the action of the system \mathcal{A} by

$$\mathcal{A}'[\mathbf{u}_c, \mathbf{u}_m, \mathbf{P}, \boldsymbol{\lambda}] = \mathcal{A}[\mathbf{u}_c, \mathbf{u}_m, \mathbf{P}] - \int_{\partial\Omega_i} \langle \boldsymbol{\lambda}, \mathbf{u}_m - \mathbf{u}_c \rangle d\Gamma dt \quad (3.141)$$

Classically, the Lagrange equation \mathcal{L}_λ associated to λ gives the continuity of displacement (the constrain imposed):

$$\int_{\partial\Omega_i} \langle \delta\lambda, \mathbf{u}_m - \mathbf{u}_c \rangle d\Gamma dt = 0 \quad (3.142)$$

Let us detail the Euler-Lagrange equations for \mathbf{u}_c , \mathbf{u}_m and \mathbf{P} . The action of the system is

$$\mathcal{A}_{\text{int}}[\mathbf{u}_c, \mathbf{u}_m, \mathbf{P}, \lambda] = \int_{t_1}^{t_2} \left[\int_{\Omega_c} \ell_c[\dot{\mathbf{u}}_c, \nabla \mathbf{u}_c, \mathbf{u}_c] d\Omega + \int_{\Omega_m} \ell_m(\dot{\mathbf{u}}_m, \nabla \mathbf{u}_m, \nabla \dot{\mathbf{u}}_m, \mathbf{P}, \dot{\mathbf{P}}) d\Omega - \int_{\partial\Omega_i} \langle \lambda, \mathbf{u}_m - \mathbf{u}_c \rangle d\Gamma \right] dt \quad (3.143)$$

As we did before, the stationarity of the boundary term for \mathcal{L}_{u_c} gives

$$\int_{t_1}^{t_2} \int_{\partial\Omega_i} \left\langle \delta\mathbf{u}_c, \frac{\partial \ell_c}{\partial \nabla \mathbf{u}_c} \cdot \mathbf{n}_c + \lambda \right\rangle d\Gamma dt = 0 \quad (3.144)$$

The stationarity of the boundary term for \mathcal{L}_{u_m} gives

$$\int_{t_1}^{t_2} \int_{\partial\Omega_i} \left\langle \delta\mathbf{u}_m, \left[\frac{\partial \ell_m}{\partial \nabla \mathbf{u}_m} - \frac{d}{dt} \frac{\partial \ell_m}{\partial \nabla \dot{\mathbf{u}}_m} \right] \cdot \mathbf{n}_m - \lambda \right\rangle d\Gamma dt = 0 \quad (3.145)$$

Under this form, one can see that λ is the traction force exerted by Ω_c on Ω_m on the boundary $\partial\Omega_i$. Having

$$\mathbf{n}_c = -\mathbf{n}_m = \mathbf{n} \quad (3.146)$$

and

$$\boldsymbol{\sigma} = -\frac{\partial \ell_c}{\partial \nabla \mathbf{u}_c}, \quad \hat{\boldsymbol{\sigma}}_m = -\frac{\partial \ell_m}{\partial \nabla \mathbf{u}_m} \quad \text{and} \quad \tilde{\boldsymbol{\sigma}}_m = \frac{d}{dt} \frac{\partial \ell_m}{\partial \nabla \dot{\mathbf{u}}_m} \quad (3.147)$$

we have

$$\boldsymbol{\sigma} \cdot \mathbf{n} = (\hat{\boldsymbol{\sigma}} + \tilde{\boldsymbol{\sigma}}) \cdot \mathbf{n} \quad \text{on } \partial\Omega_i \quad (3.148)$$

One can precise the column-wise expression of $\tilde{\boldsymbol{\sigma}} + \hat{\boldsymbol{\sigma}}$:

$$\begin{aligned} (\tilde{\boldsymbol{\sigma}} + \hat{\boldsymbol{\sigma}})_{*1} &= \begin{pmatrix} 2\mu_e(-P_{11} + u_{1,1}) + \lambda_e(-P_{11} - P_{22} + u_x + v_y) - \omega^2(2\bar{\eta}_1 u_{1,1} + \bar{\eta}_3(u_{1,1} + u_{2,2})) \\ \mu_c(-p_{12} + p_{21} + u_{1,2} - u_{2,1}) + \mu_e^*(-P_{12} - P_{21} + u_{1,2} + u_{2,1}) - \omega^2(\bar{\eta}_2(u_{1,2} - u_{2,1}) + \bar{\eta}_1^*(u_{1,2} + u_{2,1})) \end{pmatrix} \\ &\quad \star \\ (\tilde{\boldsymbol{\sigma}} + \hat{\boldsymbol{\sigma}})_{*2} &= \begin{pmatrix} \mu_c(P_{12} - P_{21} - u_{1,2} + u_{2,1}) + \mu_e^*(-P_{12} - P_{21} + u_{1,2} + u_{2,1}) + \omega^2((\bar{\eta}_2 - \bar{\eta}_1^*)u_{1,2} - (\bar{\eta}_2 + \bar{\eta}_1^*)u_{2,1}) \\ 2\mu_e(-P_{22} + u_{2,2}) + \lambda_e(-P_{11} - P_{22} + u_{1,1} + u_{2,2}) - \omega^2(2\bar{\eta}_1 u_{2,2} + \bar{\eta}_3(u_{1,1} + u_{2,2})) \end{pmatrix} \\ &\quad \star \end{aligned} \quad (3.149)$$

For a generalized vertical traction-free border, the relaxed micromorphic medium verifies

$$\begin{cases} 2\mu_e(-P_{11} + u_{1,1}) + \lambda_e(-P_{11} - P_{22} + u_x + v_y) - \omega^2(2\bar{\eta}_1 u_{1,1} + \bar{\eta}_3(u_{1,1} + u_{2,2})) & = 0 \\ \mu_c(-p_{12} + p_{21} + u_{1,2} - u_{2,1}) + \mu_e^*(-P_{12} - P_{21} + u_{1,2} + u_{2,1}) - \omega^2(\bar{\eta}_2(u_{1,2} - u_{2,1}) + \bar{\eta}_1^*(u_{1,2} + u_{2,1})) & = 0 \end{cases} \quad (3.150)$$

Chapter 3. From Cauchy to micromorphic modelling

For a horizontal generalized traction-free border, the relaxed micromorphic medium verifies

$$\begin{cases} \mu_c(P_{12} - P_{21} - u_{1,2} + u_{2,1}) + \mu_e^*(-P_{12} - P_{21} + u_{1,2} + u_{2,1}) + \omega^2((\bar{\eta}_2 - \bar{\eta}_1^*)u_{1,2} - (\bar{\eta}_2 + \bar{\eta}_1^*)u_{2,1}) & = 0 \\ 2\mu_e(-P_{22} + u_{2,2}) + \lambda_e(-P_{11} - P_{22} + u_{1,1} + u_{2,2}) - \omega^2(2\bar{\eta}_1 u_{2,2} + \bar{\eta}_3(u_{1,1} + u_{2,2})) & = 0 \end{cases} \quad (3.151)$$

The continuity of the traction forces at a vertical border is

$$\begin{cases} 2\mu_e(-P_{11} + u_{1,1}) + \lambda_e(-P_{11} - P_{22} + u_x + v_y) - \omega^2(2\bar{\eta}_1 u_{1,1} + \bar{\eta}_3(u_{1,1} + u_{2,2})) = 2\mu u_{1,1} + \lambda(u_{1,1} + u_{2,2}) \\ \mu_c(-p_{12} + p_{21} + u_{1,2} - u_{2,1}) + \mu_e^*(-P_{12} - P_{21} + u_{1,2} + u_{2,1}) - \omega^2(\bar{\eta}_2(u_{1,2} - u_{2,1}) + \bar{\eta}_1^*(u_{1,2} + u_{2,1})) = \mu(u_{1,2} + u_{2,1}) \end{cases} \quad (3.152)$$

The continuity of the traction forces at a horizontal border is

$$\begin{cases} \mu_c(P_{12} - P_{21} - u_{1,2} + u_{2,1}) + \mu_e^*(-P_{12} - P_{21} + u_{1,2} + u_{2,1}) + \omega^2((\bar{\eta}_2 - \bar{\eta}_1^*)u_{1,2} - (\bar{\eta}_2 + \bar{\eta}_1^*)u_{2,1}) = \mu(u_{1,2} + u_{2,1}) \\ 2\mu_e(-P_{22} + u_{2,2}) + \lambda_e(-P_{11} - P_{22} + u_{1,1} + u_{2,2}) - \omega^2(2\bar{\eta}_1 u_{2,2} + \bar{\eta}_3(u_{1,1} + u_{2,2})) = 2\mu u_{2,2} + \lambda(u_{1,1} + u_{2,2}) \end{cases} \quad (3.153)$$

3.7 Solving

We presented, in the previous sections of this chapter, the models that will allow us to describe, *e.g.*, the microstructured plate presented in 2. With the powerful Principle of Least Action, we showed that, through the Calculus of Variation, the movement of mechanical systems \mathbf{u} could be represented by a set of differential equations, called the *strong form of the problem*:

$$\text{Find } \mathbf{u} : \quad \mathbf{A}\mathbf{u} = \mathbf{f} \quad \text{in } \Omega \quad (3.154)$$

where \mathbf{A} is a differential operator: for the isotropic linear classical Cauchy model, the dynamic stiffness operator

$$\mathbf{A}\mathbf{u} = \rho_p \ddot{\mathbf{u}} - (\lambda + \mu) \nabla(\text{div}\mathbf{u}) - \mu \Delta \mathbf{u} \quad (3.155)$$

and \mathbf{f} a function defined on Ω (corresponding, in our case, to body forces in our medium). Such a solution \mathbf{u} equivalently verifies what is called the *weak form of the problem*

$$\text{Find } \mathbf{u} : \quad \int_{\Omega} \langle \mathbf{u}^*, \mathbf{A}\mathbf{u} \rangle d\Omega = \int_{\Omega} \langle \mathbf{u}^*, \mathbf{f} \rangle d\Omega \quad \forall \mathbf{u}^* \quad (3.156)$$

where \mathbf{u}^* is the test function associated to \mathbf{u} verifying

$$\mathbf{u}^* = \mathbf{0} \quad \text{on } \partial\Omega_{\mathcal{D}} \quad (3.157)$$

While the complexity of the considered problems forbids us to find any analytical solution and the nature of the differential operator requires an important regularity of the solutions \mathbf{u} , the weak formulation allows, through skillfully integrating by parts, to lower the derivation order applied on \mathbf{u} (and necessarily raise those upon \mathbf{u}^*) and

therefore the conditions of regularity of the solution sought. As we used the formalism of variational methods to introduce our models, it seems more appropriate to present the Lax-Milgram theorem under its “variational form”, *i.e.* having a bilinear form a ($a = \langle \mathbf{A}\mathbf{u}, \mathbf{u}^* \rangle$ satisfies such conditions) upon the adequate Hilbert space \mathcal{H} being:

– continuous:

$$\exists c > 0 : \forall(\mathbf{u}, \mathbf{u}^*) \in \mathcal{H}^2, |a(\mathbf{u}, \mathbf{u}^*)| \leq c \|\mathbf{u}\| \|\mathbf{u}^*\| \quad (3.158)$$

– coercive:

$$\exists \alpha > 0 : \forall(\mathbf{u}, \mathbf{u}^*) \in \mathcal{H}^2, |a(\mathbf{u}, \mathbf{u}^*)| \geq \alpha \|\mathbf{u}\| \|\mathbf{u}^*\| \quad (3.159)$$

– symmetric:

$$\forall(\mathbf{u}, \mathbf{u}^*) \in \mathcal{H}^2, a(\mathbf{u}, \mathbf{u}^*) = a(\mathbf{u}^*, \mathbf{u}) \quad (3.160)$$

And f a continuous linear form ($f = \langle \mathbf{f}, \mathbf{u}^* \rangle$ is a such one), then

Problem 3.156 has a unique solution, which minimize $\frac{1}{2}a(\mathbf{u}^*, \mathbf{u}^*) - f(\mathbf{u}^*)$

The parity of the orders of derivation and the symmetry of every operator we introduced make problem involving classical Cauchy medium verify such conditions. For a classical Cauchy medium in the frequency domain, the weak formulation is

$$\int_{\Omega} [\langle \text{sym } \nabla \mathbf{u}^*, \mathbb{C} \text{sym } \nabla \mathbf{u} \rangle - \omega^2 \langle \mathbf{u}^*, \rho_c \mathbf{u} \rangle] d\Omega = \int_{\Omega} \langle \mathbf{u}^*, \mathbf{f} \rangle d\Omega + \int_{\partial\Omega_N} \langle \mathbf{u}^*, \mathbf{t}_0 \rangle d\Gamma \quad (3.161)$$

For the relaxed micromorphic model, things are a bit more tricky, as we have

$$\begin{aligned} & \int_{\Omega} \langle \text{sym}(\nabla \mathbf{u}^* - \mathbf{P}^*), \mathbb{C}_e \text{sym}(\nabla \mathbf{u} - \mathbf{P}) \rangle + \langle \text{sym } \mathbf{P}^*, \mathbb{C}_m \text{sym } \mathbf{P} \rangle + \langle \text{skew}(\nabla \mathbf{u}^* - \mathbf{P}^*), \mathbb{C}_c \text{skew}(\nabla \mathbf{u} - \mathbf{P}) \rangle d\Omega \\ & - \omega^2 \int_{\Omega} \langle \mathbf{u}^*, \rho_m \mathbf{u} \rangle + \langle \text{sym } \mathbf{P}^*, \mathbb{J}_m \text{sym } \mathbf{P} \rangle + \langle \text{skew } \mathbf{P}^*, \mathbb{J}_c \text{skew } \mathbf{P} \rangle d\Omega \\ & - \omega^2 \int_{\Omega} \langle \text{sym } \nabla \mathbf{u}^*, \mathbb{T}_e \text{sym } \nabla \mathbf{u} \rangle + \langle \text{skew } \nabla \mathbf{u}^*, \mathbb{T}_c \text{skew } \nabla \mathbf{u} \rangle d\Omega = 0 \end{aligned} \quad (3.162)$$

Unfortunately, the relaxed micromorphic model we presented introduced the second-order tensor \mathbf{P} , necessitating more powerful mathematical tools to solve our problems. One can refer to [Ghiba 2015] for a study of the well-posedness of the relaxed micromorphic continuum model.

3.7.1 Discretization of the geometry

Finite element method seeks to find a numerical solution to 3.161 where \mathbf{u} is approximated by, *e.g.*, low-degree polynomial functions. To choose the appropriate function form becoming very tricky for complex structures, the finite elements method proceeds in two steps:

– Divide the domain Ω into simple elements Ω_e

Chapter 3. From Cauchy to micromorphic modelling

- Choose an appropriate interpolation function for both \mathbf{u} and \mathbf{u}^* for each domain Ω_i

Let us approximate our domain Ω by $\Omega_{\text{F.E.}}$ paved by elements Ω_i , *i.e.*

$$\Omega_{\text{F.E.}} = \bigcup_i \Omega_i \quad \text{with} \quad \Omega_i \cap \Omega_j = \emptyset \quad \text{for} \quad i \neq j \quad (3.163)$$

In the case of Bubnov-Galerkin method, \mathbf{u} and \mathbf{u}^* are interpolated by the same shape functions \mathbf{e}_i :

$$\mathbf{u}(\mathbf{x}) = \mathbf{e}_i(\mathbf{x})\mathbf{q}_i \quad \text{and} \quad \mathbf{u}^*(\mathbf{x}) = \mathbf{e}_i(\mathbf{x})\mathbf{q}_i^* \quad (3.164)$$

where, for example, \mathbf{q}_i can represent the displacement at the vertices of each element, called the nodes of the meshing (other choices are possible, which still have to respect the unisolvency principle). Injecting these relations in Equation 3.156, by linearity, we get

$$q_j^* a(\mathbf{e}_i, \mathbf{e}_j) q_i = q_j^* f(\mathbf{e}_j) \quad (3.165)$$

For the classical Cauchy problem presented in Equation 3.161, we have:

$$\mathbf{q}^{*\text{T}} [\mathbb{K} - \omega^2 \mathbb{M}] \mathbf{q} = \mathbf{q}^{*\text{T}} \mathbf{F} \quad (3.166)$$

where

$$\mathbf{K}_{ij} = \int_{\Omega_{\text{F.E.}}} \langle \text{sym } \nabla \mathbf{e}_i, \mathbb{C} \text{sym } \nabla \mathbf{e}_j \rangle d\Omega, \quad \mathbf{M}_{ij} = \int_{\Omega_{\text{F.E.}}} \langle \mathbf{e}_i, \rho_c \mathbf{e}_j \rangle d\Omega \quad \text{and} \quad \mathbf{F}_i = \int_{\Omega_{\text{F.E.}}} \langle \mathbf{e}_i, \mathbf{f} \rangle d\Omega + \int_{\partial\Omega_{\text{F.E.}}} \langle \mathbf{e}_i, \mathbf{t}_0 \rangle d\Gamma \quad (3.167)$$

The explicit expressions of \mathbb{K} and \mathbb{M} will be given at the end of this subsection. At first sight, one could make two remarks:

- A numerical integration has to be done over the whole domain Ω
- Such integration has to be done “many times” ($n(n+1)/2$ times, n being the number of degrees of freedom of the discretized system, *i.e.* the size of \mathbf{q}_i , using the symmetry of \mathbb{K} and \mathbb{M})

The Finite Element Method shows here its strength: the \mathbf{e}_i are chosen to be of small support, making most of these integrations directly equal to zero (eventually simplifying considerably the inversion of the system), and the rest of them reduced to, as we will see, reduce to the elements around the considered nodes. One could detail here the assembling procedure for each element, the transformation of the reference element, the numeric integration leading to 3.166, *etc.* We are rather going to focus on the implementation of such a method in the case of our microstructured cell and more specifically the relaxed micromorphic model. The finite element method reduces discretization of the problem to the choice of:

- the meshing of the geometry (h-adaptativity, r-adaptivity for the nodes)
- the shape functions (p-adaptivity)

The choice of these parameters can be made by answering to the question: “Is the chosen interpolation able to describe the response of the system in each element?”. To guarantee the continuity of both the displacement and stress, we choose \mathbf{u} and its components to be interpolated by quadratic Lagrange polynomials over each element, while \mathbf{P} is interpolated, necessarily, by linear Lagrange polynomials: such a choice guarantees the continuity of generalized stresses over the whole structure. Such a polynomial is given in Figure 3.14.

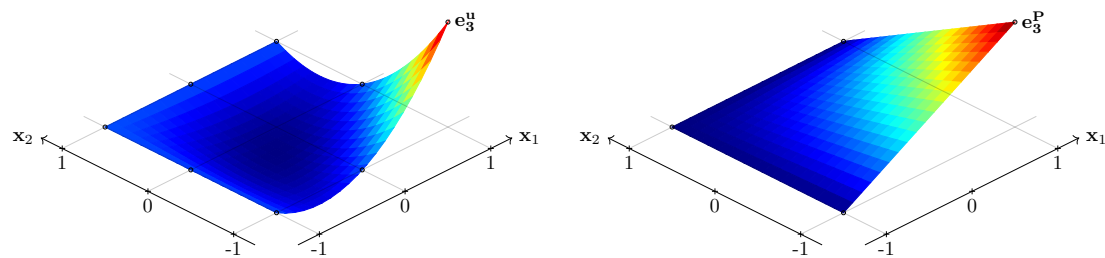


Figure 3.14: (*left*) Shape function $e_3^{\mathbf{u}}$ chosen for \mathbf{u} . The black dots represents the nodes where \mathbf{u} is interpolated. (*right*) Shape function $e_3^{\mathbf{P}}$ chosen for \mathbf{P} . The black dots represents the nodes where \mathbf{P} is interpolated.

Such a polynomial e_i verifies, given a set of n different nodes \mathbf{x}_j ,

$$e_i(\mathbf{x}_j) = \delta_{ij} \quad (3.168)$$

Given this, one instantly has

$$u_i(\mathbf{x}) = u_i(\mathbf{x}_j)e_j^{\mathbf{u}}(\mathbf{x}) \quad \text{and} \quad P_{ij}(\mathbf{x}) = P_{ij}(\mathbf{x}_k)e_k^{\mathbf{P}}(\mathbf{x}) \quad (3.169)$$

As it has been mentioned before, as we essentially work in two dimensions, triangular and rectangular elements are used where the geometry allows it. Inevitably, such elements can not perfectly describe the microstructure designed, especially in round corners, as represented in Figure 3.15.

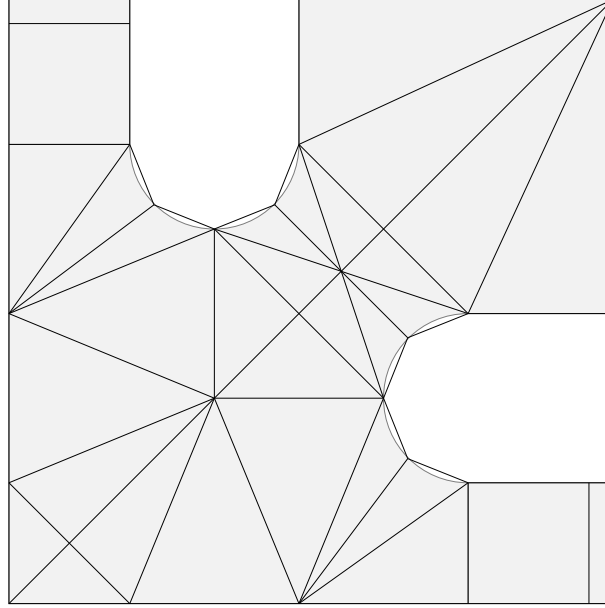


Figure 3.15: Unrefined mesh for the corner of the microstructured cell, the exact geometry of the cell is represented in gray, one can notice the difference between the mesh and the geometry at the bottom of the holes.

Given the importance of this zone for the correct description of the band-gap effect, a really thin mesh is necessary, increasing drastically the size of the problem. Such an assumption can be proven, all things equal otherwise, *via* the the Cea's Lemma:

$$\forall \mathbf{u}_1^* \in \mathcal{H}_1 \subset \mathcal{H}, \|\mathbf{u} - \mathbf{u}^*\| \leq \frac{c}{\alpha} \|\mathbf{u} - \mathbf{u}_1^*\| \forall \mathbf{u}^* \in \mathcal{H} \quad (3.170)$$

where c and α have already been introduced giving the Lax-Milgram theorem. Given our geometry and our considered elements, we won't be able to perfectly pave our microstructured cell (such a mesh is therefore called *non-conforming mesh*):

$$\Omega \neq \Omega_{\text{FE}} \quad (3.171)$$

Such considerations would, on a theoretical level, be very technical to deal with: as it is not the case for the relaxed micromorphic model, it will not be presented here and the meshing will be considered as conforming for the microstructured plate. In practice, the "right size" of the mesh has to be found *via* iterations, all thing equal otherwise, refining the meshing of the structure. A compromise between the size of the mesh and the regularity (and nature) of the shape functions can be profitable for a faster computation of the response of the system: this has not been considered in this manuscript. As the order of our shape functions have been chosen with respect to the constitutive laws of our problem, the size of the mesh is the only parameter remaining to converge to the "exact" solution. To answer to "Is the chosen interpolation able to describe the response of the system in each element?", one can see the structure alternatively from an structural and from an ondulatory point of view. We are going to justify this on the mesh used for the microstructured cell and the equivalent relaxed micromorphic one presented in Figure 3.16.

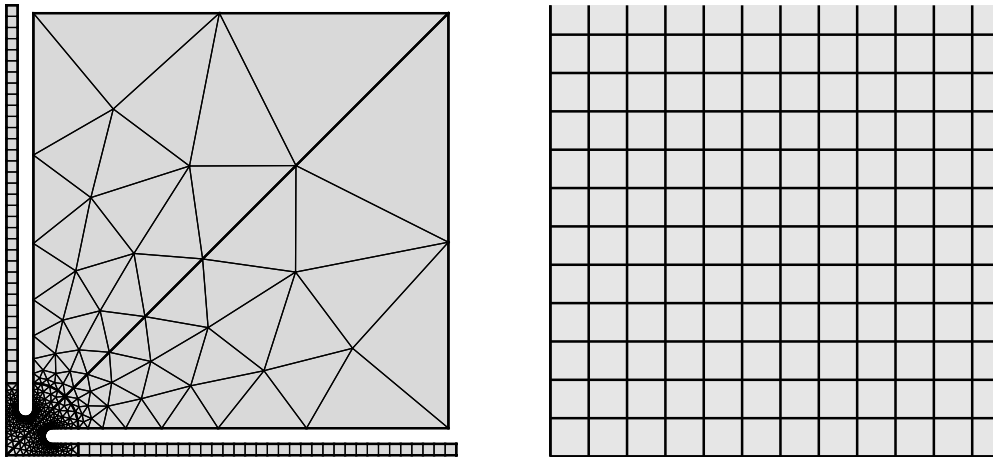


Figure 3.16: (*left*) Mesh for a quarter unit cell of the microstructured model: the portions of domain with coarse mesh allows a reduction of the total number of degrees of freedom, while a finer mesh is needed in the slender portions of the domain in order to be able to properly describe the behaviour of the microstructure in the band-gap frequency range. (*right*) Mesh for the equivalent relaxed micromorphic model.

One can identify on Figure 3.16 (*left*) three zones corresponding to three different meshes:

- the resonating square
- the “beams”
- the “corner” of the unit cell

One has to choose the size of the mesh with respect to the considered frequency range upon which the response is computed: we saw, in section 2.1, that the displacement in a isotropic Cauchy material could be written, through Helmholtz decomposition, as the sum of two functions, solutions of D’Alembert equations of propagation speeds c_l and c_s . For a given frequency f , one can introduce the wavelength λ as

$$c = \lambda \cdot f \quad \Rightarrow \quad \lambda = \frac{c}{f} \quad (3.172)$$

Writing, as it is classically done, $h(K)$ as the greatest dimension of a given element K composing the mesh as presented in Figure 3.17, one should have

$$h(K) < \lambda \quad i.e. \quad h(K) < \frac{c}{f} \quad (3.173)$$

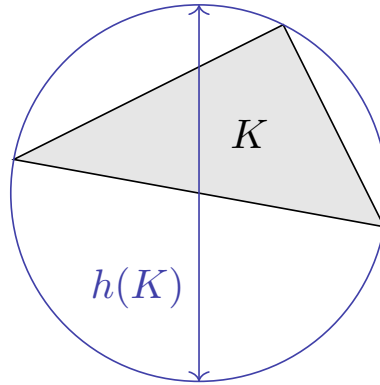


Figure 3.17: Element K of a Finite Element model with its greatest dimension $h(K)$.

With inequality 3.173, the mesh used in the Finite Element Method has to be refined as the computed frequency increases. Such a hypothesis can be verified on the beam under axial tensile load presented in Figure 3.18: for the first mode (*left*) a coarser mesh allows the good description of the mode, while, for the 5th mode a refined mesh is needed.

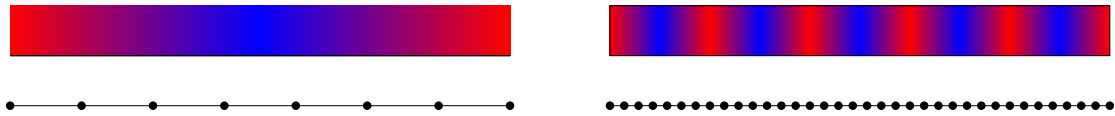


Figure 3.18: (*top*) Scaled displacement for the first (*left*) and 5th (*right*) tensile mode of the beam with their respective (*bottom*) mesh necessary for convergence.

Given this, one can explain why the resonating square has been so coarsely meshed: for the considered frequencies, such element can be considered as a rigid body, and therefore behaves like one. At the opposite, a way thinner mesh has to be implemented for the corner of the unit cell, as well as the beams constituting its sides.

The optimization of the meshing of the relaxed micromorphic domain, given the simplicity of its geometry, that can be paved by quadrangular elements, is reduced to the choice of the elements' size d . As it has been made for the classical Cauchy model, a parametric analysis upon the size of the mesh leads to

$$d = 0.85 \cdot 10^{-3} \text{ [m]} \tag{3.174}$$

As no transformation is necessary for the relaxed micromorphic model, we present the elementary matrix for the relaxed micromorphic model.

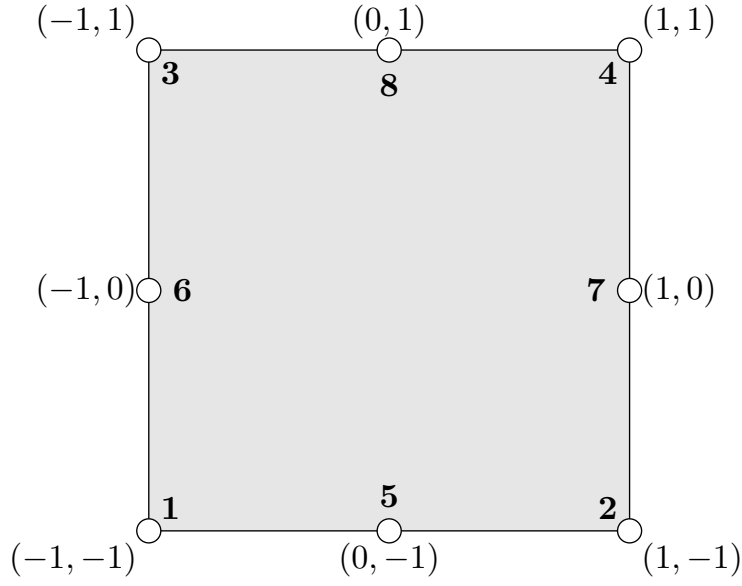


Figure 3.19: Elementary unit of the relaxed micromorphic model

Our polynomial basis is, for u_i :

$$(1, x_1, x_1x_2, x_2, x_1^2, x_1^2x_2, x_1x_2^2, x_2^2) \quad (3.175)$$

From this, one can define the shape functions

$$\begin{aligned} e_1^{\mathbf{u}} &= \frac{1}{4}(1-x_1)(1-x_2)(1+x_1+x_2), & e_2^{\mathbf{u}} &= \frac{1}{4}(1+x_1)(1-x_2)(1-x_1+x_2), \\ e_3^{\mathbf{u}} &= \frac{1}{4}(1-x_1)(1+x_2)(1+x_1-x_2), & e_4^{\mathbf{u}} &= \frac{1}{4}(1+x_1)(1+x_2)(1-x_1-x_2), \\ e_5^{\mathbf{u}} &= \frac{1}{2}(1-x_1)(1-x_2)(1+x_1), & e_6^{\mathbf{u}} &= \frac{1}{2}(1-x_1)(1-x_2)(1+x_2), \\ e_7^{\mathbf{u}} &= \frac{1}{2}(1+x_1)(1-x_2)(1+x_2), & e_8^{\mathbf{u}} &= \frac{1}{2}(1-x_1)(1+x_1)(1+x_2) \end{aligned} \quad (3.176)$$

For P_{ij} , interpolated by linear Lagrange polynomials, the basis is:

$$(1, x_1, x_1x_2, x_2) \quad (3.177)$$

Given this, the shape functions for \mathbf{P} are

$$e_1^{\mathbf{P}} = \frac{1}{4}(1-x_1)(1-x_2), \quad e_2^{\mathbf{P}} = \frac{1}{4}(1+x_1)(1-x_2), \quad e_3^{\mathbf{P}} = \frac{1}{4}(1-x_1)(1+x_2), \quad e_4^{\mathbf{P}} = \frac{1}{4}(1+x_1)(1+x_2) \quad (3.178)$$

Chapter 3. From Cauchy to micromorphic modelling

For u_i , we have

$$u_i(\mathbf{x}) = \begin{pmatrix} e_1^{\mathbf{u}} & e_2^{\mathbf{u}} & e_3^{\mathbf{u}} & e_4^{\mathbf{u}} & e_5^{\mathbf{u}} & e_6^{\mathbf{u}} & e_7^{\mathbf{u}} & e_8^{\mathbf{u}} \end{pmatrix} \begin{pmatrix} \mathbf{u}_i(1) \\ \mathbf{u}_i(2) \\ \mathbf{u}_i(3) \\ \mathbf{u}_i(4) \\ \mathbf{u}_i(5) \\ \mathbf{u}_i(6) \\ \mathbf{u}_i(7) \\ \mathbf{u}_i(8) \end{pmatrix} = \mathbf{e}_{\mathbf{u}}^{\mathbf{T}} \mathbf{q}_{\mathbf{u}}^i \quad (3.179)$$

For P_{ij} , we have

$$P_{ij}(\mathbf{x}) = \begin{pmatrix} e_1^{\mathbf{P}} & e_2^{\mathbf{P}} & e_3^{\mathbf{P}} & e_4^{\mathbf{P}} \end{pmatrix} \begin{pmatrix} P_{ij}(1) \\ P_{ij}(2) \\ P_{ij}(3) \\ P_{ij}(4) \end{pmatrix} = \mathbf{e}_{\mathbf{P}}^{\mathbf{T}} \mathbf{q}_{\mathbf{P}}^{ij} \quad (3.180)$$

Classically, the Cauchy inertial contribution is

$$-\omega^2 \begin{pmatrix} \mathbf{q}_{\mathbf{u}}^1 & \mathbf{q}_{\mathbf{u}}^2 \end{pmatrix}^* \begin{pmatrix} \rho_m \mathbb{M}^{\mathbf{u}} & \mathbb{O} \\ \star & \rho_m \mathbb{M}^{\mathbf{u}} \end{pmatrix} \begin{pmatrix} \mathbf{q}_{\mathbf{u}}^1 \\ \mathbf{q}_{\mathbf{u}}^2 \end{pmatrix} \quad (3.181)$$

The free micro-inertia contribution is

$$-\omega^2 \begin{pmatrix} \mathbf{q}_{\mathbf{P}}^{11} & \mathbf{q}_{\mathbf{P}}^{12} & \mathbf{q}_{\mathbf{P}}^{21} & \mathbf{q}_{\mathbf{P}}^{22} \end{pmatrix}^* \begin{pmatrix} (2\eta_1 + \eta_3) \mathbb{M}^{\mathbf{P}} & \mathbb{O} & \mathbb{O} & \eta_3 \mathbb{M}^{\mathbf{P}} \\ \star & (\eta_1^* + \eta_2) \mathbb{M}^{\mathbf{P}} & (\eta_1^* - \eta_2) \mathbb{M}^{\mathbf{P}} & \mathbb{O} \\ \star & \star & (\eta_1^* + \eta_2) \mathbb{M}^{\mathbf{P}} & \mathbb{O} \\ \star & \star & \star & (2\eta_1 + \eta_3) \mathbb{M}^{\mathbf{P}} \end{pmatrix} \begin{pmatrix} \mathbf{q}_{\mathbf{P}}^{11} \\ \mathbf{q}_{\mathbf{P}}^{12} \\ \mathbf{q}_{\mathbf{P}}^{21} \\ \mathbf{q}_{\mathbf{P}}^{22} \end{pmatrix} \quad (3.182)$$

The gradient micro-inertia contribution is

$$-\omega^2 \begin{pmatrix} \mathbf{q}_{\mathbf{u}}^1 & \mathbf{q}_{\mathbf{u}}^2 \end{pmatrix}^* \begin{pmatrix} (2\bar{\eta}_1 + \bar{\eta}_3) \mathbb{K}_1 + (\bar{\eta}_1^* + \bar{\eta}_2) \mathbb{K}_2 & \bar{\eta}_3 \mathbb{K}_0 + (\bar{\eta}_1^* - \bar{\eta}_2) \mathbb{K}_0^{\mathbf{T}} \\ \star & (2\bar{\eta}_1 + \bar{\eta}_3) \mathbb{K}_2 + (\bar{\eta}_1^* + \bar{\eta}_2) \mathbb{K}_1 \end{pmatrix} \begin{pmatrix} \mathbf{q}_{\mathbf{u}}^1 \\ \mathbf{q}_{\mathbf{u}}^2 \end{pmatrix} \quad (3.183)$$

The elastic energy contribution is

$$\begin{pmatrix} \mathbf{q}_{\mathbf{u}}^1 \\ \mathbf{q}_{\mathbf{u}}^2 \\ \mathbf{q}_{\mathbf{P}}^{11} \\ \mathbf{q}_{\mathbf{P}}^{12} \\ \mathbf{q}_{\mathbf{P}}^{21} \\ \mathbf{q}_{\mathbf{P}}^{22} \end{pmatrix}^{\star \mathbf{T}} \begin{pmatrix} (2\mu_e + \lambda_e) \mathbb{K}_1 + \mu_e^* \mathbb{K}_2 & \lambda_e \mathbb{K}_0 + \mu_e^* \mathbb{K}_0^{\mathbf{T}} & -2(\mu_e + \lambda_e) \mathbb{H}_1 & -\mu_e^* \mathbb{H}_2 & -\mu_e^* \mathbb{H}_2 & -\lambda_e \mathbb{H}_1 \\ \star & (2\mu_e + \lambda_e) \mathbb{K}_2 + \mu_e^* \mathbb{K}_1 & -\lambda_e \mathbb{H}_2 & -\mu_e^* \mathbb{H}_1 & -\mu_e^* \mathbb{H}_1 & -(2\mu_e + \lambda_e) \mathbb{H}_2 \\ \star & \star & (2\mu_e + \lambda_e) \mathbb{M}^{\mathbf{P}} & \mathbb{O} & \mathbb{O} & \lambda_e \mathbb{M}^{\mathbf{P}} \\ \star & \star & \star & \mu_e^* \mathbb{M}^{\mathbf{P}} & \mu_e^* \mathbb{M}^{\mathbf{P}} & \mathbb{O} \\ \star & \star & \star & \star & \mu_e^* \mathbb{M}^{\mathbf{P}} & \mathbb{O} \\ \star & \star & \star & \star & \star & (2\mu_e + \lambda_e) \mathbb{M}^{\mathbf{P}} \end{pmatrix} \begin{pmatrix} \mathbf{q}_{\mathbf{u}}^1 \\ \mathbf{q}_{\mathbf{u}}^2 \\ \mathbf{q}_{\mathbf{P}}^{11} \\ \mathbf{q}_{\mathbf{P}}^{12} \\ \mathbf{q}_{\mathbf{P}}^{21} \\ \mathbf{q}_{\mathbf{P}}^{22} \end{pmatrix} \quad (3.184)$$

The micro self energy contribution is

$$\begin{pmatrix} \mathbf{q}_P^{11} & \mathbf{q}_P^{12} & \mathbf{q}_P^{21} & \mathbf{q}_P^{22} \end{pmatrix}^* \begin{pmatrix} (2\mu_m + \lambda_m)\mathbb{M}^P & \mathbb{O} & \mathbb{O} & \lambda_m\mathbb{M}^P \\ \star & \mu_m^*\mathbb{M}^P & \mu_m^*\mathbb{M}^P & \mathbb{O} \\ \star & \star & \mu_m^*\mathbb{M}^P & \mathbb{O} \\ \star & \star & \star & (2\mu_m + \lambda_m)\mathbb{M}^P \end{pmatrix} \begin{pmatrix} \mathbf{q}_P^{11} \\ \mathbf{q}_P^{12} \\ \mathbf{q}_P^{21} \\ \mathbf{q}_P^{22} \end{pmatrix} \quad (3.185)$$

And the local rotational elastic energy contribution is

$$\begin{pmatrix} \mathbf{q}_u^1 & \mathbf{q}_u^2 & \mathbf{q}_P^{12} & \mathbf{q}_P^{21} \end{pmatrix}^* \begin{pmatrix} \mu_c\mathbb{K}_1 & \mu_c\mathbb{K}_0^T & -\mu_c\mathbb{H}_2 & -\mu_c\mathbb{H}_2 \\ \star & \mu_c\mathbb{K}_2 & -\mu_c\mathbb{H}_1 & -\mu_c\mathbb{H}_1 \\ \star & \star & \mu_c\mathbb{M}^P & \mu_c\mathbb{M}^P \\ \star & \star & \star & \mu_c\mathbb{M}^P \end{pmatrix} \begin{pmatrix} \mathbf{q}_u^1 \\ \mathbf{q}_u^2 \\ \mathbf{q}_P^{12} \\ \mathbf{q}_P^{21} \end{pmatrix} \quad (3.186)$$

where the square (given the shape functions chosen for \mathbf{u} and \mathbf{P}) matrices \mathbb{M}^u , \mathbb{M}^P , \mathbb{K}_1 , \mathbb{K}_2 , \mathbb{K}_0 , \mathbb{H}_1 and \mathbb{H}_2 are given by

$$\begin{aligned} [\mathbb{M}^u]_{ij} &= d^2 \int_{-1}^1 \int_{-1}^1 e_i^u e_j^u dx_1 dx_2 & \text{and} & & [\mathbb{M}^P]_{ij} &= d^2 \int_{-1}^1 \int_{-1}^1 e_i^P e_j^P dx_1 dx_2 \\ [\mathbb{K}_1]_{ij} &= d^2 \int_{-1}^1 \int_{-1}^1 e_{i,1}^u e_{j,1}^u dx_1 dx_2, & [\mathbb{K}_2]_{ij} &= d^2 \int_{-1}^1 \int_{-1}^1 e_{i,2}^u e_{j,2}^u dx_1 dx_2 & \text{and} & & [\mathbb{K}_0]_{ij} &= d^2 \int_{-1}^1 \int_{-1}^1 e_{i,1}^u e_{j,2}^u dx_1 dx_2 \\ [\mathbb{H}_1]_{ij} &= d^2 \int_{-1}^1 \int_{-1}^1 e_{i,1}^u e_j^P dx_1 dx_2 & \text{and} & & [\mathbb{H}_2]_{ij} &= d^2 \int_{-1}^1 \int_{-1}^1 e_{i,2}^u e_j^P dx_1 dx_2 \end{aligned} \quad (3.187)$$

Choosing to sort the degrees of freedom by

$$\mathbf{q} = \left(\mathbf{q}_u^1 \quad \mathbf{q}_u^2 \quad \mathbf{q}_P^{11} \quad \mathbf{q}_P^{12} \quad \mathbf{q}_P^{21} \quad \mathbf{q}_P^{22} \right)^T \quad (3.188)$$

The generalized mass and stiffness matrices \mathbb{M}_m and \mathbb{K}_m of the relaxed micromorphic model can be written as

$$\mathbb{M}_m = \begin{pmatrix} \mathbb{M}_1 & \mathbb{O} \\ \star & \mathbb{M}_2 \end{pmatrix} \quad \text{and} \quad \mathbb{K}_m = \begin{pmatrix} \bar{\mathbb{K}} & \mathbb{H} \\ \star & \mathbb{K}_P \end{pmatrix} \quad (3.189)$$

Chapter 3. From Cauchy to micromorphic modelling

where

$$\begin{aligned}
 \mathbb{M}_1 &= \begin{pmatrix} \rho_m \mathbb{M}^u + (2\bar{\eta}_1 + \bar{\eta}_3)\mathbb{K}_1 + (\bar{\eta}_1^* + \bar{\eta}_2)\mathbb{K}_2 & \bar{\eta}_3\mathbb{K}_0 + (\bar{\eta}_1^* - \bar{\eta}_2)\mathbb{K}_0^T \\ \star & \rho_m \mathbb{M}^u + (2\bar{\eta}_1 + \bar{\eta}_3)\mathbb{K}_2 + (\bar{\eta}_1^* + \bar{\eta}_2)\mathbb{K}_1 \end{pmatrix} \\
 \mathbb{M}_2 &= \begin{pmatrix} (2\eta_1 + \eta_3)\mathbb{M}^P & \mathbb{O} & \mathbb{O} & \eta_3\mathbb{M}^P \\ \star & (\eta_1^* + \eta_2)\mathbb{M}^P & (\eta_1^* - \eta_2)\mathbb{M}^P & \mathbb{O} \\ \star & \star & (\eta_1^* + \eta_2)\mathbb{M}^P & \mathbb{O} \\ \star & \star & \star & (2\eta_1 + \eta_3)\mathbb{M}^P \end{pmatrix} \\
 \bar{\mathbb{K}} &= \begin{pmatrix} (2\mu_e + \lambda_e + \mu_c)\mathbb{K}_1 + \mu_e^*\mathbb{K}_2 & \lambda_e\mathbb{K}_0 + (\mu_e^* + \mu_c)\mathbb{K}_0^T \\ \star & (2\mu_e + \lambda_e)\mathbb{K}_2 + \mu_e^*\mathbb{K}_1 + \mu_c\mathbb{K}_2 \end{pmatrix} \\
 \mathbb{H} &= \begin{pmatrix} -2(\mu_e + \lambda_e)\mathbb{H}_1 & -(\mu_e^* + \mu_c)\mathbb{H}_2 & -(\mu_e^* + \mu_c)\mathbb{H}_2 & -\lambda_e\mathbb{H}_1 \\ -\lambda_e\mathbb{H}_2 & -(\mu_e^* + \mu_c)\mathbb{H}_1 & -(\mu_e^* + \mu_c)\mathbb{H}_1 & -(2\mu_e + \lambda_e)\mathbb{H}_2 \end{pmatrix} \\
 \mathbb{K}_P &= \begin{pmatrix} (2\mu_e + \lambda_e + 2\mu_m + \lambda_m)\mathbb{M}^P & \mathbb{O} & \mathbb{O} & (\lambda_e + \lambda_m)\mathbb{M}^P \\ \star & (\mu_e^* + \mu_m^* + \mu_c)\mathbb{M}^P & (\mu_e^* + \mu_m^* + \mu_c)\mathbb{M}^P & \mathbb{O} \\ \star & \star & (\mu_e^* + \mu_m^* + \mu_c)\mathbb{M}^P & \mathbb{O} \\ \star & \star & \star & (2\mu_e + \lambda_e + 2\mu_m + \lambda_m)\mathbb{M}^P \end{pmatrix} \quad (3.190)
 \end{aligned}$$

the Finite Element Method applied to the relaxed micromorphic model gives the following

$$\mathbf{q}^{*T} \left(\mathbb{K}_m - \omega^2 \mathbb{M}_m \right) \mathbf{q} = \mathbf{q}^{*T} \mathbf{F}_m \quad (3.191)$$

where \mathbf{F}_m is the generalized force vector defined by

$$\mathbf{F}_m = \left(\mathbf{F}^T \quad \mathbf{0} \quad \mathbf{0} \quad \mathbf{0} \quad \mathbf{0} \right)^T \quad (3.192)$$

Which has to be compared to the elementary mass and stiffness matrices of a classical Cauchy medium

$$\begin{aligned}
 \mathbb{K}_c &= \begin{pmatrix} (2\mu_e + \lambda_e)\mathbb{K}_1 + \mu_e^*\mathbb{K}_2 & \lambda_e\mathbb{K}_0 + \mu_e^*\mathbb{K}_0^T \\ \star & (2\mu_e + \lambda_e)\mathbb{K}_2 + \mu_e^*\mathbb{K}_1 \end{pmatrix} \\
 \mathbb{M}_c &= \begin{pmatrix} \rho_c \mathbb{M}^u & \mathbb{O} \\ \star & \rho_c \mathbb{M}^u \end{pmatrix} \quad (3.193)
 \end{aligned}$$

the contribution of one element being

$$\left(\mathbf{q}_u^1 \quad \mathbf{q}_u^2 \right)^* \left(\mathbb{K}_c - \omega^2 \mathbb{M}_c \right) \begin{pmatrix} \mathbf{q}_u^1 \\ \mathbf{q}_u^2 \end{pmatrix} = \left(\mathbf{q}_u^1 \quad \mathbf{q}_u^2 \right)^* \begin{pmatrix} \mathbf{F}_1 \\ \mathbf{F}_2 \end{pmatrix} \quad (3.194)$$

The expressions of \mathbf{F}_1 and \mathbf{F}_2 has not been mentioned yet, we have

$$\mathbf{F}_i = d^2 \int_{-1}^1 \int_{-1}^1 f_i \mathbf{e}_u dx_1 dx_2 \quad (3.195)$$

These computations may seem a little bit tedious, but one should keep in mind that, being done only once numerically, the complexity of the Finite Element Method is reduced to the assembly of the elementary matrices (almost negligible in terms of computational time) and the inversion of a – sometime huge – matrix system. The tremendous decrease of number in the nodes through the homogenization largely compensates the complexification of the elementary matrices and (generalized) displacement field of the relaxed micromorphic model.

3.7.2 Damping of the structures

We chose to describe our mechanical systems *via* the Principle of Least Action, allowing to deduce elegantly the equilibrium equations and the constitutive laws of our media from the Lagrangian density: in return, such systems were necessarily conservative, *i.e.*

$$\frac{dE_c}{dt} = 0 \quad \text{where} \quad E_c = K_c + W_c \quad \text{and} \quad \begin{cases} K_c = \int_{\Omega} k_c d\Omega \\ W_c = \int_{\Omega} w_c d\Omega \end{cases} \quad (3.196)$$

Indeed, having (the first equality uses, in some way, Euler's identity on homogeneous functions)

$$\frac{dk_c}{dt} = \frac{1}{2} \frac{d\dot{u}_i \rho_c \dot{u}_i}{dt} = \dot{u}_i \rho_c \ddot{u}_i = \dot{u}_i \frac{d\rho_c \dot{u}_i}{dt} = \left\langle \dot{\mathbf{u}}, \frac{d}{dt} \frac{\partial k_c}{\partial \dot{\mathbf{u}}} \right\rangle \quad \text{and} \quad \frac{dw_c}{dt} = \left\langle \nabla \dot{\mathbf{u}}, \frac{\partial w_c}{\partial \nabla \dot{\mathbf{u}}} \right\rangle \quad (3.197)$$

one can deduce

$$\frac{d}{dt} \int_{\Omega} (k + w) d\Omega = \int_{\Omega} \left\langle \dot{\mathbf{u}}, \frac{\partial k_c}{\partial \dot{\mathbf{u}}} - \operatorname{div} \frac{\partial w_c}{\partial \nabla \dot{\mathbf{u}}} \right\rangle d\Omega - \int_{\partial\Omega} \left\langle \dot{\mathbf{u}}, \frac{\partial w_c}{\partial \nabla \dot{\mathbf{u}}} \cdot \mathbf{n} \right\rangle d\Gamma \quad (3.198)$$

As k_c and w_c are independent from, respectively, $\nabla \dot{\mathbf{u}}$ and $\dot{\mathbf{u}}$, we have

$$\frac{\partial k_c}{\partial \dot{\mathbf{u}}} = \frac{\partial \ell_c}{\partial \dot{\mathbf{u}}} \quad \text{and} \quad \frac{\partial w_c}{\partial \nabla \dot{\mathbf{u}}} = - \frac{\partial \ell_c}{\partial \nabla \dot{\mathbf{u}}} \quad (3.199)$$

The last term $\int_{\partial\Omega} \left\langle \dot{\mathbf{u}}, \frac{\partial w_c}{\partial \nabla \dot{\mathbf{u}}} \right\rangle d\Gamma$ corresponds to the power of contact forces: to be rigorous, we should have:

– included the conservative forces in the expression of the mechanical energy, *i.e.*

$$\begin{cases} \exists U : \mathbf{f} = - \frac{\partial U}{\partial \dot{\mathbf{u}}} & \text{in } \Omega \\ \exists V : \mathbf{t} = - \frac{\partial V}{\partial \dot{\mathbf{u}}} & \text{on } \partial\Omega \end{cases} \quad \text{then} \quad W_c = \int_{\Omega} (w_c + U) d\Omega + \int_{\partial\Omega} V d\Gamma \quad (3.200)$$

– considered a system free from external (contact) forces, *i.e.* verifying

$$\boldsymbol{\sigma} \cdot \mathbf{n} = \mathbf{0} \quad (3.201)$$

Chapter 3. From Cauchy to micromorphic modelling

In both cases, this last term vanishes. The local equilibrium in a Cauchy continuum, *via* the Euler-Lagrange equations, is

$$\frac{d}{dt} \frac{\partial \ell_c}{\partial \dot{\mathbf{u}}} + \operatorname{div} \frac{\partial \ell_c}{\partial \nabla \mathbf{u}} = \mathbf{0} \quad (3.202)$$

Allowing us to conclude. Such a proof can be repeated for the relaxed micromorphic model, having

$$\begin{aligned} \frac{d}{dt} \int_{\Omega} (k_m + w_m) d\Omega &= \int_{\Omega} \left\langle \dot{\mathbf{u}}, \frac{d}{dt} \left[\frac{\partial k_m}{\partial \dot{\mathbf{u}}} - \operatorname{div} \frac{\partial k_m}{\partial \nabla \dot{\mathbf{u}}} \right] + \operatorname{div} \frac{\partial w_m}{\partial \nabla \mathbf{u}} \right\rangle d\Omega \\ &+ \int_{\Omega} \left\langle \dot{\mathbf{P}}, \frac{d}{dt} \frac{\partial k_m}{\partial \dot{\mathbf{P}}} - \frac{\partial w_m}{\partial \mathbf{P}} \right\rangle d\Omega \\ &+ \int_{\partial\Omega} \left\langle \dot{\mathbf{u}}, \left[\frac{d}{dt} \frac{\partial k_m}{\partial \nabla \dot{\mathbf{u}}} + \frac{\partial w_m}{\partial \nabla \mathbf{u}_m} \right] \cdot \mathbf{n} \right\rangle d\Gamma \end{aligned} \quad (3.203)$$

As we have

$$\frac{dk_m}{dt} = \left\langle \dot{\mathbf{u}}, \frac{d}{dt} \frac{\partial k_m}{\partial \dot{\mathbf{u}}} \right\rangle + \left\langle \dot{\mathbf{P}}, \frac{d}{dt} \frac{\partial k_m}{\partial \dot{\mathbf{P}}} \right\rangle + \left\langle \nabla \dot{\mathbf{u}}, \frac{d}{dt} \frac{\partial k_m}{\partial \nabla \dot{\mathbf{u}}} \right\rangle \quad (3.204)$$

Replacing, with consideration to the respective forms of kinetic and strain energy densities, k_m and w_m by, respectively, ℓ_m and $-\ell_m$, the two first terms, corresponding to the Euler-Lagrange equations of the relaxed micromorphic medium, equal zero. The last one being the generalized power of contact forces, the argument we gave for the classical Cauchy medium still holds, which ends the proof.

The conservativity of our systems, when it comes to their numerical resolution, causes great difficulties in terms of numerical resolution, and the relaxed micromorphic model, instead of escaping such problems, rather sinks in those complexities. We saw, in the previous subsection, that our set of differential equations modelling our continua could be, in a good approximation, represented by a matrix system of the form

$$\mathbf{q}^{*\top} [\mathbb{K} - \omega^2 \mathbb{M}] \mathbf{q} = \mathbf{q}^{*\top} \mathbf{F} \quad (3.205)$$

We can classically split \mathbf{q} upon the nodes at prescribed displacement ($\in \partial\Omega_{\mathcal{D}}$ in the case of a conforming mesh and $\partial\Omega_s$ if symmetries are considered) and those at prescribed force (body or contact forces). Having $\partial\Omega_{\mathcal{D}} \cup \partial\Omega_{\mathcal{N}} = \emptyset$, we have

$$\begin{pmatrix} \mathbf{0} & \mathbf{q}_i^{*\top} \end{pmatrix} \begin{pmatrix} \mathbb{K}_{00} - \omega^2 \mathbb{M}_{00} & \mathbb{K}_{0i} - \omega^2 \mathbb{M}_{0i} \\ \star & \mathbb{K}_{ii} - \omega^2 \mathbb{M}_{ii} \end{pmatrix} \begin{pmatrix} \mathbf{q}_0 \\ \mathbf{q}_i \end{pmatrix} = \begin{pmatrix} \mathbf{0} & \mathbf{q}_i^{*\top} \end{pmatrix} \begin{pmatrix} \mathbf{F}_i \\ \mathbf{F}_0 \end{pmatrix} \quad (3.206)$$

As $\mathbf{q}^* = \mathbf{0}$ on $\partial\Omega_{\mathcal{D}}$, which does not allow to compute the corresponding forces allowing to verify $\mathbf{u} = \mathbf{u}_0$. We saw that the use of a Lagrange multiplier λ allowed to compute them, the associated system is

$$\begin{pmatrix} \mathbf{q}_0^{*\top} & \mathbf{q}_i^{*\top} & \mathbf{q}_\lambda^{*\top} \end{pmatrix} \begin{pmatrix} \mathbb{K}_{00} - \omega^2 \mathbb{M}_{00} & \mathbb{K}_{0i} - \omega^2 \mathbb{M}_{0i} & -\mathbf{1} \\ \mathbb{K}_{0i}^{\top} - \omega^2 \mathbb{M}_{0i}^{\top} & \mathbb{K}_{ii} - \omega^2 \mathbb{M}_{ii} & \mathbb{O} \\ \mathbf{1} & \mathbb{O} & \mathbb{O} \end{pmatrix} \begin{pmatrix} \mathbf{q}'_0 \\ \mathbf{q}_i \\ \lambda \end{pmatrix} = \begin{pmatrix} \mathbf{q}_0^{*\top} & \mathbf{q}_i^{*\top} & \mathbf{q}_\lambda^{*\top} \end{pmatrix} \begin{pmatrix} \mathbf{F}_i \\ \mathbf{F}_0 \\ \mathbf{q}_0 \end{pmatrix} \quad (3.207)$$

Let us go back to equation 3.206. \mathbf{q}_i is easily given by

$$\mathbf{q}_i = [\mathbb{K}_{ii} - \omega^2 \mathbb{M}_{ii}]^{-1} [\mathbf{F}_0 - (\mathbb{K}_{0i} - \omega^2 \mathbb{M}_{0i}) \mathbf{q}_0] \quad (3.208)$$

Requiring the reversibility of $\mathbb{K}_{ii}^T - \omega^2 \mathbb{M}_{ii}^T$: such a matrix, corresponding to the dynamic stiffness of the structure with the boundary conditions $\mathbf{u} = \mathbf{0}$ on $\partial\Omega_{\mathcal{D}}$, is therefore symmetric. The term $(\mathbb{K}_{0i} - \omega^2 \mathbb{M}_{0i}) \mathbf{q}_0$ corresponds to the (generalized) forces induced by the prescribed displacement on $\partial\Omega_{\mathcal{D}}$. For the sake of simplicity, let us go back to the classical

$$[\mathbb{K} - \omega^2 \mathbb{M}] \mathbf{q} = \mathbf{F} \quad (3.209)$$

We will not develop here any method of modal synthesis, but just say, using spectral theorem, that

$$\exists \Phi \in \mathbb{O}(\mathbb{R}^3) : \begin{cases} \Phi^T \mathbb{K} \Phi = \Omega^2 \\ \Phi^T \mathbb{M} \Phi = \mathbf{1} \end{cases} \quad \text{where} \quad \Omega_{ij} = \begin{cases} \omega_i & \text{if } i = j \\ 0 & \text{otherwise} \end{cases} \quad (3.210)$$

where the i^{th} column of Φ is the modeshape of our structure associated with the eigenfrequency ω_i . Given this, the response of linear systems, including continua through the Finite Element Method, may be seen as a linear combination of one degree of freedom resonators. Such a reduction allows to compute \mathbf{q} by

$$\mathbf{q}_i = \Phi_{ji} \frac{\Phi_{ij} \mathbf{F}_j}{\omega_i^2 - \omega^2} \quad (3.211)$$

which, having $\omega_i \in \mathbb{R}^+$, clearly shows the divergence of the frequency response function ($\mathbf{q} : \omega \mapsto \mathbf{q}(\omega)$, FRF) at each eigenfrequency of the structure ω_i . With that formulation, modal synthesis can be seen as an intermediary between the resolution of mechanical problems in the physical space (\mathbf{x}, t) and the dual space (\mathbf{k}, ω) as presented in Figure 3.20.

Chapter 3. From Cauchy to micromorphic modelling

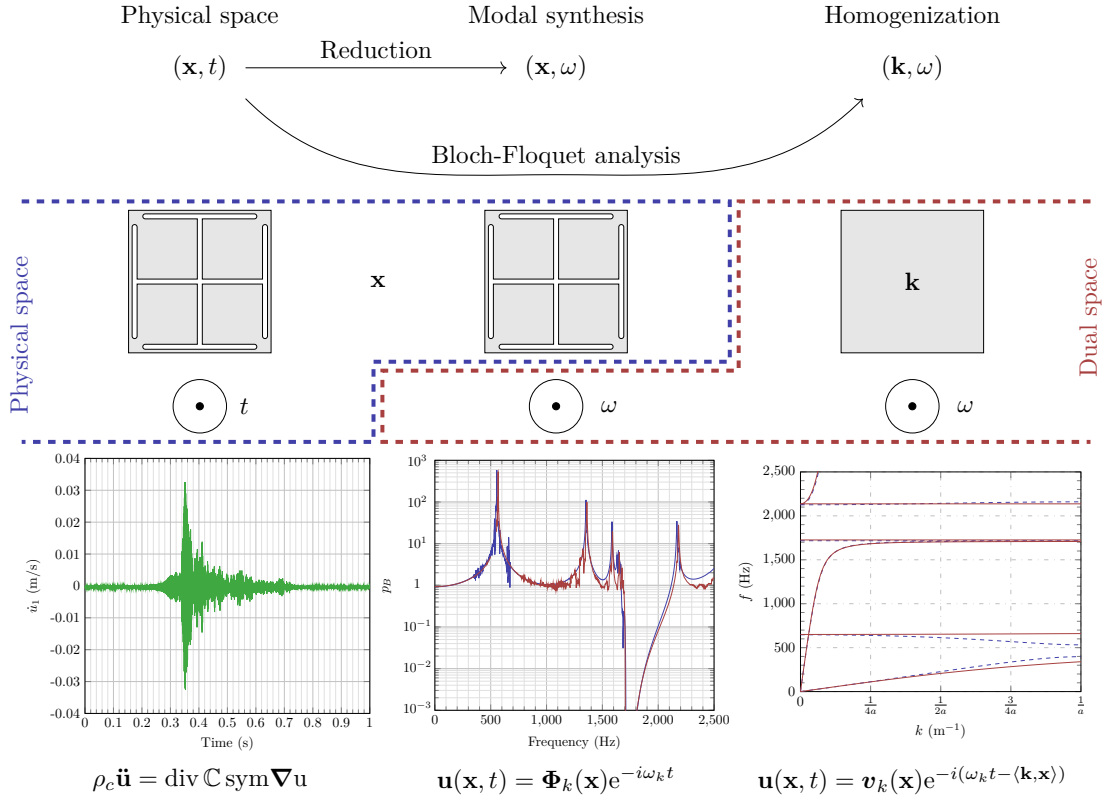


Figure 3.20: Integration of linear systems using modal synthesis or homogenization techniques.

Microstructured plates studied in the following sections and chapters of this manuscript, due to their particular geometry, present a great number of modes in the frequency range considered: the inversion of such models, given the considerable variation of amplitude on a narrow range of frequencies, is made difficult for solvers. Such a statement is all the more verified for the relaxed micromorphic where, given the presence of micro-distortion \mathbf{P} , the number of (generalized) modes of the structure tremendously increases. For now, we presented the divergence of the response of our structure from a structural point of view: before going any further, Let us present how these resonance occurs from a wave point of view. *Via* the Bloch-Floquet analysis, we saw that the dispersion curves of the unit cell took the form

$$\omega = \omega(\mathbf{k}) \quad (3.212)$$

In the absence of damping, which would considerably complexify the computation of dispersion curves (requiring, *e.g.*, the use of the Shift-cell operator), one has

$$\forall \mathbf{k} \in \mathbb{R}^2, \text{Re}(\omega(\mathbf{k})) \cdot \text{Im}(\omega(\mathbf{k})) = 0 \quad (3.213)$$

i.e. ω is either real, either a pure imaginary number (in the band-gap). Reciprocally, for a given $\omega \in \mathbb{R}$ and writing $\mathbf{k} = k\hat{\mathbf{k}}$ where $\|\hat{\mathbf{k}}\| = 1$, we necessarily have

$$\forall \omega \in \mathbb{R}, \text{Re}(k) \cdot \text{Im}(k) = 0 \quad (3.214)$$

i.e. that propagation (eventually) occurs in the considered medium without attenuation. Such considerations allows to understand, from the wave point of view, how the resonance occurs: it is well known, since Fourier, that the frequency response of a (linear) system corresponds to the stationary response of the system to a sinusoidal excitation. Once again, we can take a glance at a finite beam under an axial tensile load, as presented in Figure 3.21.

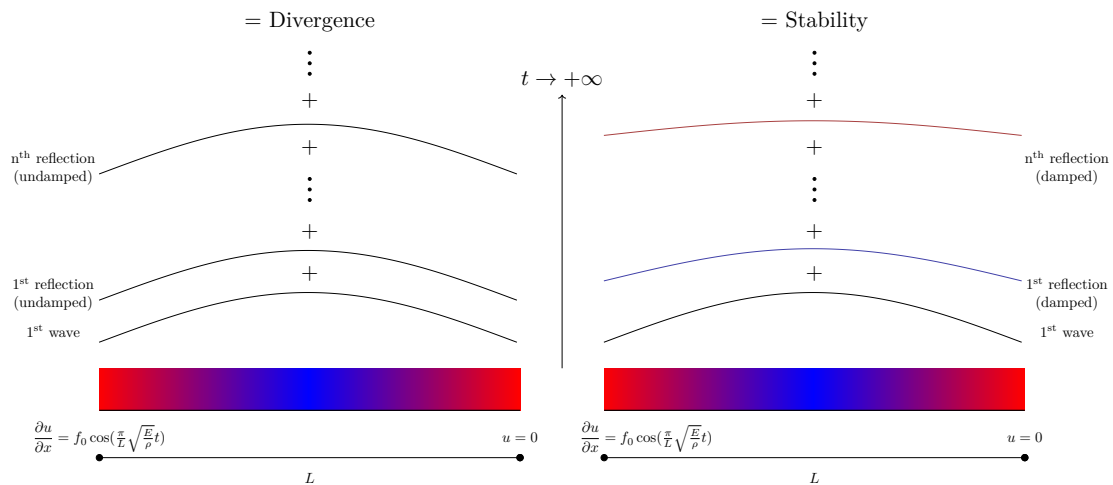


Figure 3.21: (*left*) First mode of a beam under a axial tensile load with the divergence of its response in the absence of damping. (*right*) First mode of a damped beam under a axial tensile load with the emitted and reflected waves eventually converging to its stationary response as $t \rightarrow +\infty$.

In the absence of dissipation in the material, each wave sent by the excitation propagates through the beam at constant amplitude, and so do its multiple reflections: as $t \rightarrow +\infty$, the response of the beam, *i.e.* the sum of every wave (those emitted by the excitation, their reflections, the reflections of their reflections, *etc*), of constant amplitude eventually diverges, as presented in Figure 3.22.

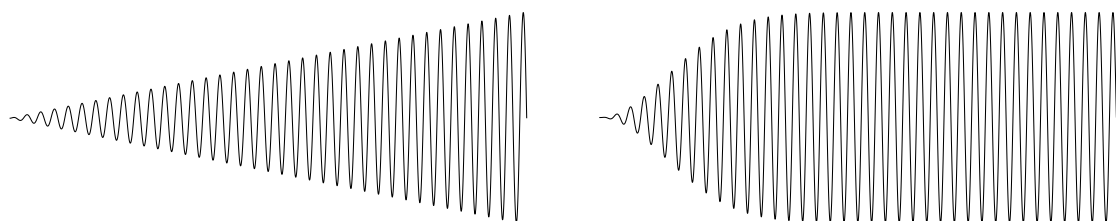


Figure 3.22: (*left*) Co-localized response of the beam for the undamped system. (*right*) Co-localized response of the beam for the damped system.

The impossibility to compute the response of systems at a given set of frequencies, can therefore be understood through two different points of view:

- the non-invertibility of the dynamic stiffness operator $\mathbb{K} - \omega^2\mathbb{M}$

Chapter 3. From Cauchy to micromorphic modelling

- the undamped propagation of waves in the considered medium

To overcome such a difficulty, two approaches are possible:

- introduce some dissipative terms in our constitutive laws
- modify our dynamic stiffness operator, making it invertible $\forall \omega$

Both techniques have been, for long, known for the classical Cauchy continuum. In the first one, we can mention the viscous damping, where an additional stress is introduced, proportional to the strain rate:

$$\boldsymbol{\sigma} = \mathbb{C} \text{sym } \nabla \mathbf{u} + \mathbb{C}_v \text{sym } \nabla \dot{\mathbf{u}} \quad (3.215)$$

Given the difficulty to experimentally determine the parameters (21 in the most general case) of \mathbb{C}_v , viscous damping is usually considered as isotropic, allowing to reduce to 2 the numbers of damping parameters. Applying such a method to the relaxed micromorphic model would have led to introduce a great number of damping coefficients, despite the tetragonal symmetry considered. Let us quickly write what could have been our generalized stresses in such a case:

$$\begin{cases} \tilde{\boldsymbol{\sigma}} = \mathbb{C}_e \text{sym } (\nabla \mathbf{u} - \mathbf{P}) + \mathbb{C}_c \text{skew}(\nabla \mathbf{u} - \mathbf{P}) + \mathbb{C}_e^v \text{sym } (\nabla \dot{\mathbf{u}} - \dot{\mathbf{P}}) + \mathbb{C}_c^v \text{skew}(\nabla \dot{\mathbf{u}} - \dot{\mathbf{P}}) \\ \mathbf{s} = \mathbb{C}_m \text{sym } \mathbf{P} + \mathbb{C}_m^v \text{sym } \dot{\mathbf{P}} \end{cases} \quad (3.216)$$

Once again, we insist that such expressions of the generalized stresses are not compatible with the Principle of Least Action to which should be preferred, *e.g.*, the Virtual work Principle. Such an approach would eventually allow, among others, to identify clearly the influence of each parameter of the relaxed micromorphic model in the creation of the band-gap effect. Unfortunately, the identification procedure of the relaxed micromorphic parameters is not compatible with such an approach: indeed, the Bloch-Floquet analysis, allowing to plot the dispersion curves for $\mathbf{k} \in \mathbb{R}^2$, should be abandoned in favor of the “Shift Cell Operator” method [Collet 2011]: the identification of the band-gap, among others, would be considerably harder (having to compare real and imaginary parts of f or \mathbf{k} , *etc*). The other approach, known as “structural damping”, is usual implemented on the Finite Element model of the structures. We can mention:

- the modal damping, where each mode Φ_k is damped with its own damping ratio η_k , such as

$$\mathbf{q}_j = \Phi_{jk} \frac{\Phi_{kj} \mathbf{F}_k}{\omega_k^2 + i\eta_k \omega_k \omega - \omega^2} \quad (3.217)$$

Such an approach has not even been considered for the relaxed micromorphic model, as it requires to diagonalize the undamped Finite Element model, which would be, at last, tedious for our modelling.

- the Rayleigh damping, where the Finite Element Model is modified by

$$\mathbf{q}^{*T} [\mathbb{K} + i\omega(\alpha\mathbb{M} + \beta\mathbb{K}) - \omega^2\mathbb{M}] \mathbf{q} = \mathbf{q}^{*T} \mathbf{F} \quad (3.218)$$

- the loss factor damping, which is half-way between the the structural damping and the “physical” approach, where the Young Modulus is modified by introducing an imaginary part, *i.e.*

$$E_{\text{damped}} = (1 + i\eta)E \quad (3.219)$$

Such a non-causal approach is only valid in the frequency domain, which is precisely the case of our framework. This model can easily be transposed to the relaxed micromorphic model, having

$$w_c \propto E \quad (3.220)$$

then

$$w_c^{\text{damped}} = (1 + i\eta)w_c \quad (3.221)$$

In the same manner, whenever the relaxed micromorphic model needs to be damped, we will modify the generalized strain density energy by

$$w_m^{\text{damped}} = (1 + i\eta)w_m \quad (3.222)$$

More generally, the choice of an adapted damping in our framework should be led by two different considerations:

- The possibility to adapt them for relaxed micromorphic modelling
- The materials used for our experimental set-up

The “limitations” induced by the relaxed micromorphic medium have just been investigated: doing this, we reduced the available choices of our damping: at the other hand, we shall consider if our remaining damping model can be adapted for the materials we used. Fortunately, for the experimental set-up used as a *proof of concept* of our work we presented in Chapter 2 made of titanium alloy, the damping is usually really low. For that reason, we set

$$\eta_c = 0.002 = \eta_m \quad (3.223)$$

The loss factor damping can easily being introduced in *Comsol Multiphysics*[®]: if it is already implemented for the Cauchy continuum, for the relaxed micromorphic one, the weak formulation had to be modified as given for every model considered in the following chapters.

3.8 Convergence of the microstructured and relaxed micromorphic models

The main challenge for metamaterials’ modelling consists in the description of their broadband mechanical response. More particularly, a suitable model must be able to describe metamaterials’ response for the larger possible set of frequencies. We will show in the following sections that the RMM is able to correctly describe the metamaterial’s response for a very wide side set of frequencies going well beyond the first band-gap.

Chapter 3. From Cauchy to micromorphic modelling

Nevertheless, specific attention must be paid to the so-called long-wave or static limit which can be recovered from the dynamic model when considering very small frequencies, in the limit $\omega \rightarrow 0$.

In this section, we explicitly point out this static limit both for the microstructured and the relaxed micromorphic model. We show that, since internal lengths are neglected, the relaxed micromorphic static limit coincides with an equivalent Cauchy medium. We remark that for the experimental metamaterial's specimen's size (9×11 cells), this equivalent Cauchy medium slightly deviates from the static response of the full microstructured metamaterial. However, this difference remains smaller than 10 % (see Figure 3.26) and becomes even smaller as soon as higher frequencies are considered.

To improve the relaxed micromorphic response of these small samples for the static limit, internal lengths should be introduced. This would lead, on the other hand, to a more complex identification procedure for the dynamic regime. We thus limit ourselves to the case of negligible internal lengths, knowing that this leads to a controlled inaccuracy in the static limit for small specimens.

In summary, we have shown that our hypothesis of neglecting static internal lengths may produce a small and controlled inaccuracy for the static limiting case when considering a specimen of the size considered in our experiment (9×11 cells) and an external load applied on a unique unit cell ($c = 1$).

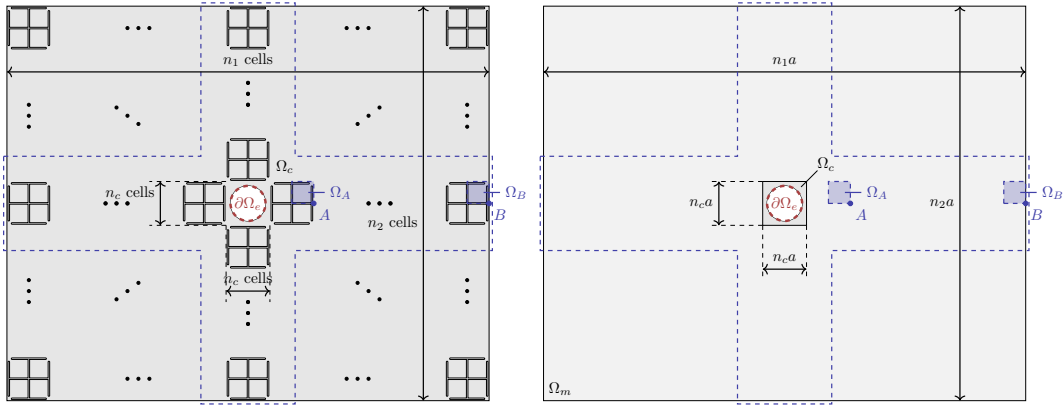


Figure 3.23: (left) Top view of the full microstructured plate and identification of points A and B. (right) Top view of the full relaxed micromorphic plate and identification of the corresponding volumes Ω_A and Ω_B . Given the strong directivity of the plate we do not consider other points outside the dashed domain to show the simulation's results.

The action functional associated to the microstructured plate presented in Figure 3.23 (left) is

$$\mathcal{A} = \mathcal{A}_{\text{int}}[\mathbf{u}] = \int_{t_1}^{t_2} \int_{\Omega_c} (k_c - w_c) dx_1 dx_2 \quad (3.224)$$

The action functional associated to the plate consisting of Cauchy and relaxed micro-

morphic media presented in Figure 3.23 (*right*) is

$$\mathcal{A}_{\text{int}}[\mathbf{u}, \mathbf{P}] = \int_0^T \left[\int_{\Omega_c} (k_c - w_c) dx_1 dx_2 + \int_{\Omega_m} (k_m - w_m) dx_1 dx_2 \right] dt \quad (3.225)$$

The plane strain hypothesis for the relaxed micromorphic model is

$$\mathbf{u} = \begin{pmatrix} u_1 \\ u_2 \\ 0 \end{pmatrix} \quad \text{in } \Omega_c, \quad \mathbf{u} = \begin{pmatrix} u_1 \\ u_2 \\ 0 \end{pmatrix} \quad \text{and} \quad \mathbf{P} = \begin{pmatrix} P_{11} & P_{12} & 0 \\ P_{21} & P_{22} & 0 \\ 0 & 0 & 0 \end{pmatrix} \quad \text{in } \Omega_m. \quad (3.226)$$

With such a modelling, the continuity of displacement being automatically verified, the perfect contact conditions between the Cauchy material and the relaxed micromorphic material at the interfaces $\partial\Omega_c$ and the traction-free conditions on $\partial\tilde{\Omega}_f$ are

$$(\hat{\boldsymbol{\sigma}} + \tilde{\boldsymbol{\sigma}}) \cdot \mathbf{n} = \boldsymbol{\sigma} \cdot \mathbf{n} \quad \text{on } \partial\Omega_c \quad \text{and} \quad (\hat{\boldsymbol{\sigma}} + \tilde{\boldsymbol{\sigma}}) \cdot \mathbf{n} = \mathbf{0} \quad \text{on } \partial\tilde{\Omega}_f \quad (3.227)$$

The applied load is given as an imposed displacement on the boundary $\partial\Omega_v$ (see Figure 3.23) in the form:

$$\mathbf{u} = \psi \mathbf{n} \quad (\text{expansion load}) \quad (3.228)$$

where \mathbf{n} is the unit normal to each surface and $\psi = 10^{-3}$ [m], this value being of no particular importance, as a linear system is considered here. As the considered structure verifies the symmetries presented in Section 2.4, one can consider only a fourth of the microstructured plate, *e.g.* defined by $(x_1 > 0, x_2 > 0)$. Such a configuration is presented in Figure 3.24.

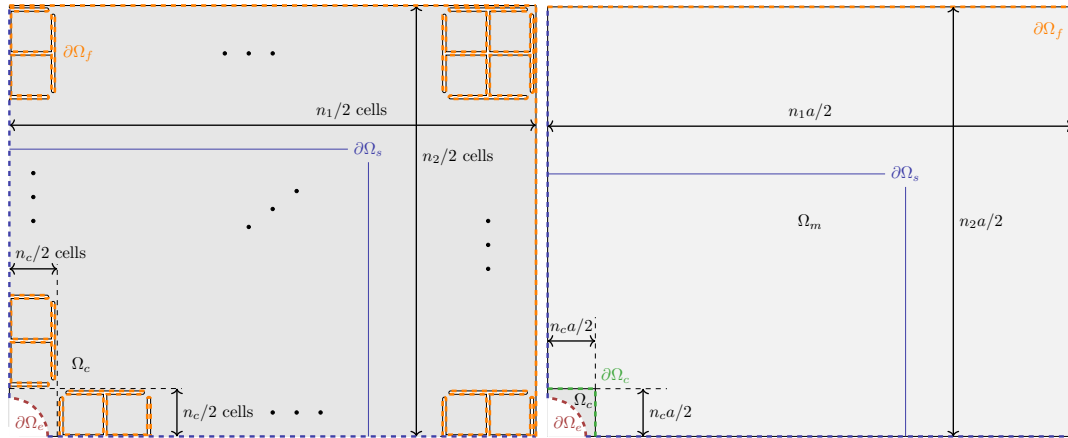


Figure 3.24: (*left*) Top view of the symmetrized microstructured plate, denomination of the traction-free boundaries $\partial\Omega_f$ and the symmetry boundaries $\partial\Omega_s$. (*right*) Top view of the symmetrized relaxed micromorphic plate, denomination of the traction-free boundaries $\partial\Omega_f$ and the symmetry boundaries $\partial\Omega_s$.

On the boundary of the newly created symmetry lines $\partial\Omega_s$ we have to impose the following boundary conditions:

$$\begin{cases} u_i n_i = 0 \\ (\delta_{ki} - n_k n_i)(P_{ij} n_j) = 0 \end{cases} \quad (3.229)$$

Chapter 3. From Cauchy to micromorphic modelling

where again, n_i are the components of the unit normal to the each surface and δ_{ij} is the Kronecker delta operator. The symmetry condition for \mathbf{u} being well-known, one can detail the effective condition applied on \mathbf{P} . It is for both symmetry planes

$$P_{12} = 0 = P_{21} \quad (3.230)$$

Since the relaxed micromorphic model is a homogenized model, it is not always worth comparing the solution displacement field pointwise with the one issued *via* the microstructured simulations. A consistent difference between these pointwise fields may be expected. To provide a more stable comparison, an average displacement field over a representative portion of the unit cell can be considered. To this aim we start identifying the points A and B in the considered structure as (see also Fig. 3.23):

$$\left\{ \begin{array}{l} A = (n_c a/2 + a, 0)^T \\ B = (n_1 a/2, 0)^T \end{array} \right. \quad \text{and surfaces} \quad \left\{ \begin{array}{l} \Omega_A = [n_c a/2, n_c a/2 + a] \times [0, a/2] \\ \Omega_B = [(n_1 - 1)a/2, n_1 a/2] \times [0, a/2] \end{array} \right. \quad (3.231)$$

where n_1 is the number of cells of the plate on its main axis (see Fig. 3.23). We then introduce a pointwise measure of displacement p and a mean measure of displacement m as:

$$\left\{ \begin{array}{l} p_X = \frac{1}{\psi} \sqrt{\langle \mathbf{u}(\mathbf{x}), \bar{\mathbf{u}}(\mathbf{x}) \rangle} \\ m_X = \frac{4}{\psi a^2} \int_{\Omega_X} \sqrt{\langle \mathbf{u}(\mathbf{x}), \bar{\mathbf{u}}(\mathbf{x}) \rangle} d\Omega \end{array} \right. \quad \text{for } X = \{A, B\} \quad (3.232)$$

where a superposed bar indicate the complex conjugate operation. The Hermitian norm used here, not necessary for the static response of the system, where the displacement stays real despite the hysteretic damping, finds its use computing the dynamic response of the plate. With these indicators, we are ready to study the convergence between the microstructured and the relaxed micromorphic model.

3.8.1 The long-wave limit: statics

In a first and intuitive approach, increasing the plate size for a “small” central excitation ($n_c = 1$) may seems to be considered as a necessary and sufficient condition for the convergence between the microstructured plate and the relaxed micromorphic model. This configuration is presented in Figure 3.25. From the default $n_1 = 11, n_2 = 9$ configuration that, due to the limitations of the manufacturing process, has actually been done (see Chapter 3 for a detailed explanation of the design of the experimental set-up), has

been considered the following sizes:

$$\left\{ \begin{array}{l} n_1 = 11, n_2 = 9 \\ n_1 = 21, n_2 = 19 \\ n_1 = 31, n_2 = 29 \\ n_1 = 41, n_2 = 39 \\ n_1 = 51, n_2 = 49 \end{array} \right. \quad \begin{array}{l} \text{(experimental case)} \\ \\ \\ \\ \end{array} \quad (3.233)$$

If the $(n_1 = 11, n_2 = 9)$ configuration was simulated to have a first impression of the response of the experimental structure, choosing $n_1 \neq n_2$, $n_1 \equiv 1 \pmod{2}$ and $n_2 \equiv 1 \pmod{2}$ (respectively breaking the first bisector symmetry and creating symmetry boundary conditions on discontinuous surfaces) allows to consider the most unfavorable conditions for the study of convergence of our models. We will see that, even in such conditions, the relaxed micromorphic model successively described the equivalent microstructured plate.

Figure 3.26 presents the plotting of p_B and m_B for these configurations. One can observe the perfect matching, even for the experimental plate ($n_1 = 11, n_2 = 9$ and $n_c = 1$), between the relaxed micromorphic and the equivalent macroscopic Cauchy model. The progressive increase of the size of the plate, at first, seems to allow the convergence of the considered model. For the largest plate considered ($n_1 = 51, n_2 = 49$), the difference between, on one hand, the microstructured plate and on the other hand the relaxed micromorphic and the homogenized model increases. This behaviour can be interpreted as an expansion load on such a “small” zone is seen, from the perspective of the “large plate” considered, as a punctual load, and therefore, the characteristic lengths of the cell being neglected, the relaxed micromorphic model nor the homogenized model manage to describe properly the response of the microstructured plate.

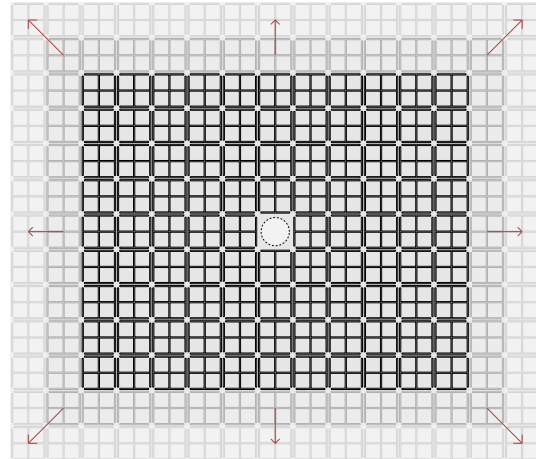


Figure 3.25: Increasing the size of the microstructured plate for $n_c = 1$.

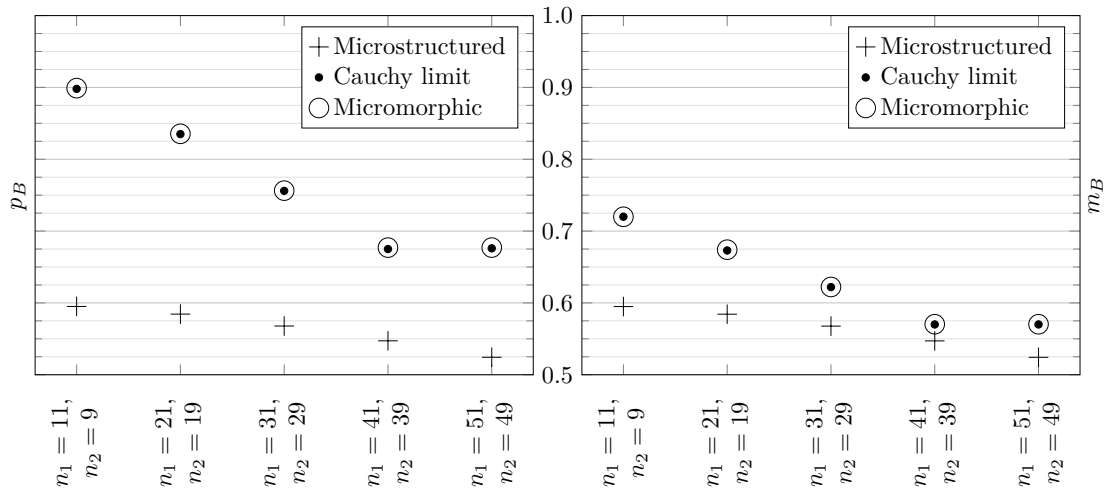


Figure 3.26: Pointwise (*left*) and mean (*right*) displacement for the static responses of the microstructured, the homogenized and the relaxed micromorphic models at point B for $(n_1 = 11, n_2 = 9)$.

One can also notice that, as it will be seen in Figure 3.28, the difference between the three models is always smaller for the mean displacement m_X than for the pointwise p_X : once again, the homogenization techniques can be considered valid for average quantities such as energy (in the case of KUBC methods) or dispersion diagrams (used for the calibration of the parameters of the relaxed micromorphic model), where the use of the Bloch-Floquet theorem allows to compute the response of an infinite periodic structure to the study of a unit cell of the considered system. Given this, a second parametric study is considered, where the size of the central excitation varies through the modification of n_c , as presented in Figure 3.27: given the small size of considered plate ($n_1 = 11, n_2 = 9$), only three values of n_c are considered:

$$\begin{cases} n_c = 1 & \text{(experimental case)} \\ n_c = 3 \\ n_c = 5 \end{cases} \quad (3.234)$$

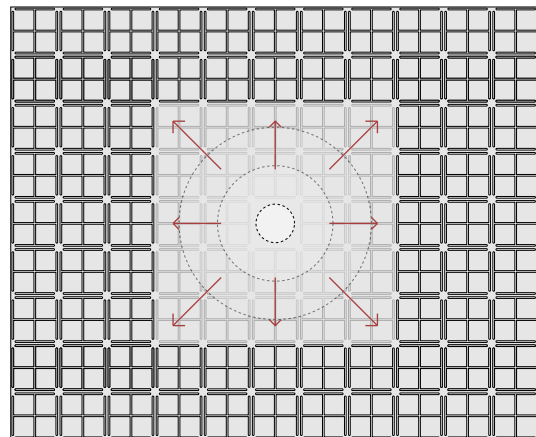


Figure 3.27: Increasing the size of the central excitation ($n_c = 1, 3$ and 5) for $n_1 = 11$ and $n_2 = 9$.

The corresponding plot of m_B and p_B is given in Figure 3.28. The decreasing of the difference between the microstructured plate and the relaxed micromorphic model may not be only due to the influence of the enlarging of the central zone: the imposed displacement on $\partial\Omega_e$ being closer to the measured point A and area Ω_A , one has natu-

rally

$$p_B \xrightarrow[n_c \rightarrow n_1]{} 1 \quad \text{and} \quad m_B \xrightarrow[n_c \rightarrow n_1]{} 1 \quad (3.235)$$

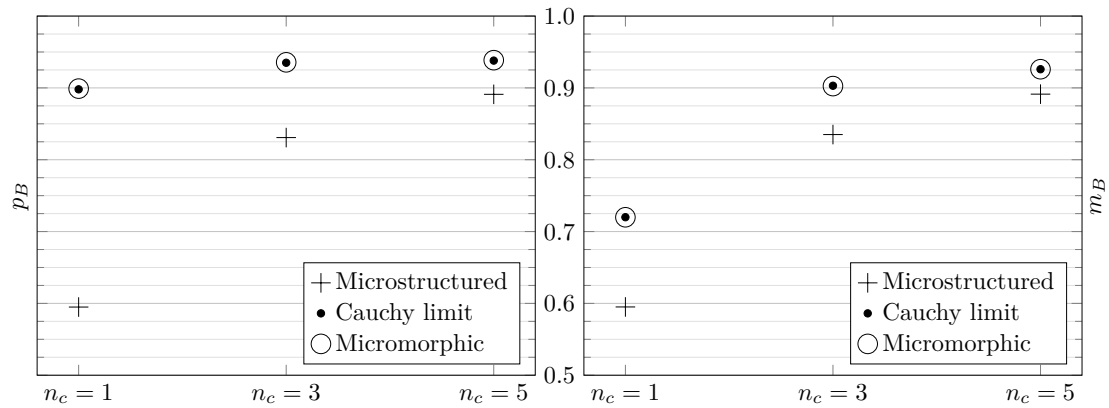


Figure 3.28: Pointwise (left) and mean (right) displacement for the static responses of the microstructured, the homogenized and the relaxed micromorphic models at point B for $(n_1 = 11, n_2 = 9)$.

To remove this ambiguity, Let us consider a last case, where both the size of the plate of the size of the central zone, as represented in 3.29. Given the results of Figure 3.26, we consider a $n_1 = 51 \times n_2 = 49$ cells plate. Such a plate size allows:

- to observe the singularity identified for $n_c = 1$
- to be “large enough” to verify Saint Venant’s hypothesis, *i.e.* to be “far enough” from the excitation not to be influenced by the nature of load considered.

Given this, the following cases have been considered for n_c :

$$\left\{ \begin{array}{l} n_c = 1 \\ n_c = 3 \\ n_c = 5 \\ n_c = 7 \\ n_c = 9 \\ n_c = 11 \end{array} \right. \quad (3.236)$$

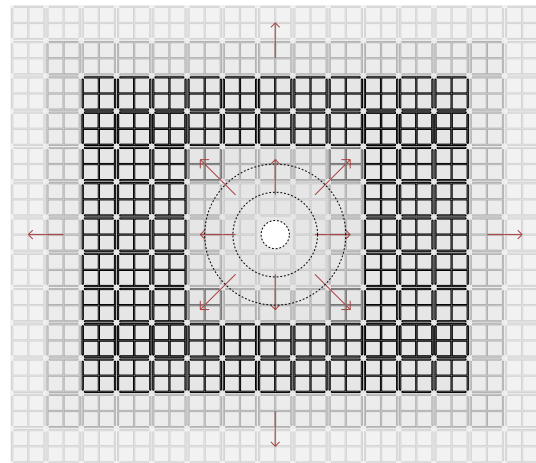


Figure 3.29: Increasing both the size of the microstructured plate and the central excitation.

Figure 3.30 gives the plot of p_B and m_B for these configurations. As soon as a n_c reaches 9, one can see that the responses of the three models converge, while its lowest values underline the

Chapter 3. From Cauchy to micromorphic modelling

singularity observed for $n_c = 1$.

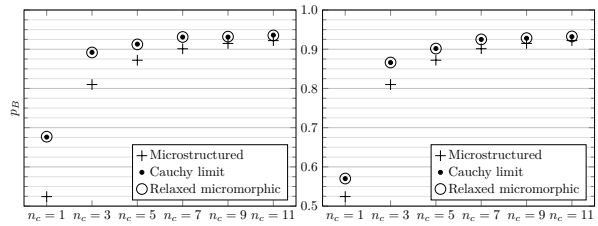


Figure 3.30: Pointwise (*left*) and mean (*right*) displacement for the static responses of the microstructured, the homogenized and the relaxed micromorphic models at point B for $(n_1 = 51, n_2 = 49)$.

Given this, one can formulate, in the same spirit of the slenderness hypothesis for beams (requiring, for an Euler beam, a slenderness of 10 or more), the homogenization conditions of the relaxed micromorphic medium in the bidimensional case:

The convergence between the microstructured plate and its equivalent relaxed micromorphic model requires both

- a “sufficiently large” size of the plate
- a “sufficiently large” size of the load areas

In practice, one shall consider at least a 50×50 cells plate and each prescribed load/displacement to be applied on 10 cells or more.

In addition, as theoretically expected, the convergence between the relaxed micromorphic model and the homogenized Cauchy plate is always verified (in the static regime only, for obvious reasons), regardless of the two conditions previously stated.

We will show in the next section that these assertions made in the static regime are also valid, in the dynamic regime, for frequencies going beyond the band gap.

The same study could be made for a metamaterial beam, considering an appropriate displacement field (and more particularly in terms of micro-distortion) and generalized stress with respect to the boundary conditions, eventually leading to new homogenization conditions in terms of beam length and parameters of section. However, the use of metamaterials in beams being more adapted to unidirectional metamaterials, such a study has not been considered.

Figure 3.31 presents the static responses of the three models for the $(n_1 = 51, n_2 = 49, n_c = 11)$ converged case.

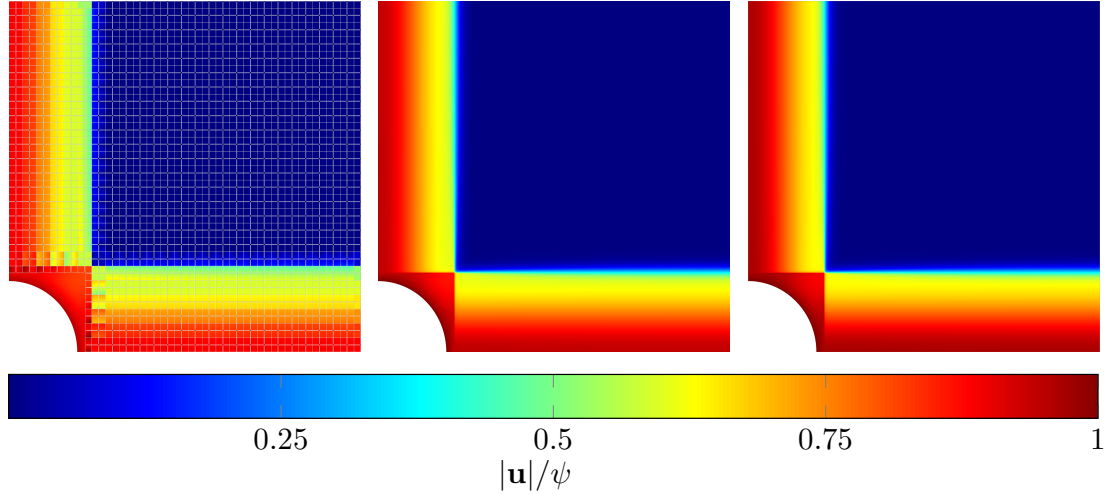


Figure 3.31: (from *left to right*) Normalized displacement for the static responses of the microstructured, the relaxed micromorphic and the homogenized Cauchy model.

3.8.2 Broadband dynamics of the metamaterial's plate

We present here the broadband response for both the microstructured and relaxed micromorphic plate when considering a size of 51×49 cells and a load applied on a square whose side is 11 unit cells. We will show that the values of n_1 , n_2 and n_c necessary to the static convergence also allows the relaxed micromorphic model to correctly reproduce the dynamical response of the considered metamaterial for a wide set of frequencies (from zero to beyond the first band-gap).

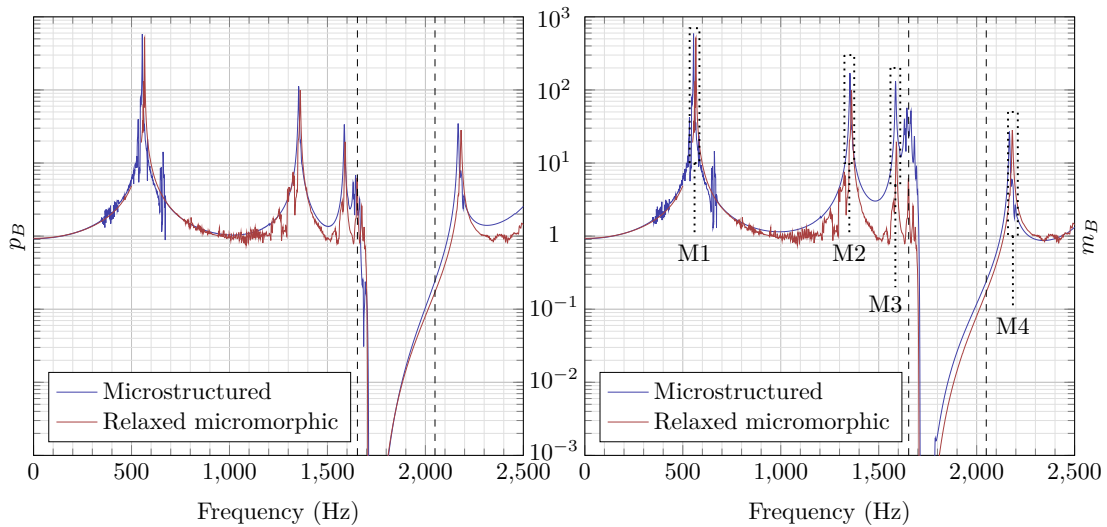


Figure 3.32: (*left*) Pointwise displacement p_B of the microstructured and relaxed micromorphic models with the theoretical band-gap (dashed) for $n_1 = 51$, $n_2 = 49$ and $n_c = 11$. (*right*) Mean displacement m_B of the microstructured and relaxed micromorphic models with the theoretical band-gap (dashed) for $n_1 = 51$, $n_2 = 49$ and $n_c = 11$.

Chapter 3. From Cauchy to micromorphic modelling

Figure 3.32 shows this broadband response for the considered metamaterial plate: it is apparent that the relaxed micromorphic model describes well the plate's behavior for the whole considered frequency range. The size of the considered plate ($n_1 = 51, n_2 = 49$) was still allowing a direct comparison of the relaxed micromorphic model the microstructured simulations. However, the computational time was considerably higher for the microstructured plate. An explicit comparison for larger plates would be out of reach with standard computational tools. This calls for the importance of our model in view of its use for the design of larger-scale engineering metastructures.

To give an outlook of the efficiency of the relaxed micromorphic model, we plot in Figs. 3.33-3.36 the solution for the displacement field at frequencies M_1, M_2, M_3 as defined in Fig. 3.32 (right). For each point M_i , we actually consider two adjacent values of the frequency to compute the solution (see Fig. 3.32 right). It can be clearly inferred that the relaxed micromorphic model encodes all the main features of the metamaterial's response at a fraction of the computational cost.

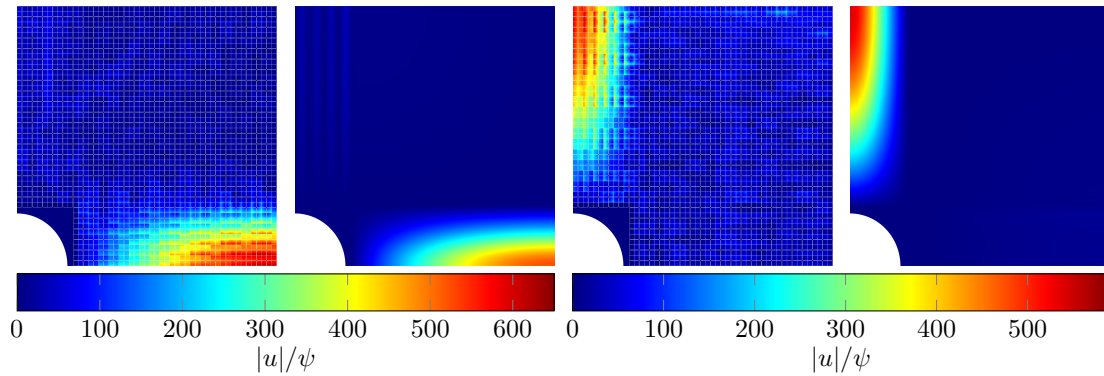


Figure 3.33: $|u|/\psi$ at frequency M_1 for the microstructured model and the relaxed micromorphic model, the first two figures correspond to M_1 (left) and the last two figures to M_1 (right) (see Fig. 3.32 for the definition of these points).

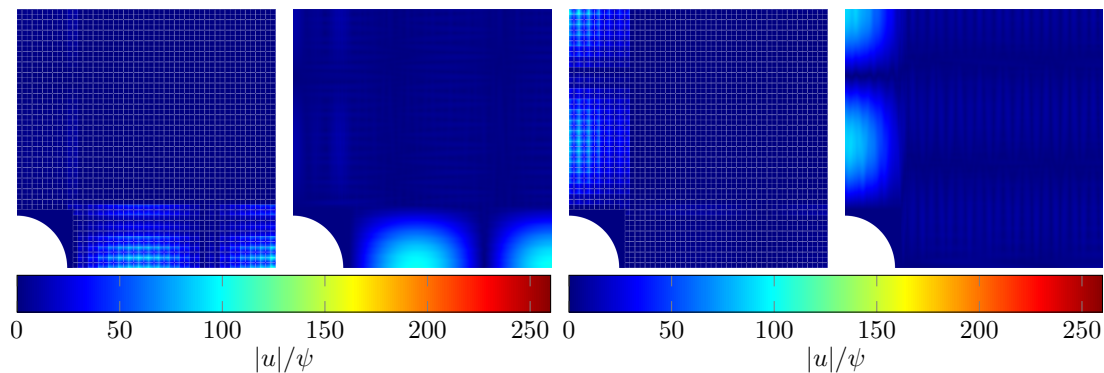


Figure 3.34: $|u|/\psi$ at frequency M_2 for the microstructured model and the relaxed micromorphic model, the first two figures correspond to M_2 (left) and the last two figures to M_2 (right) (see Fig. 3.32 for the definition of these points).

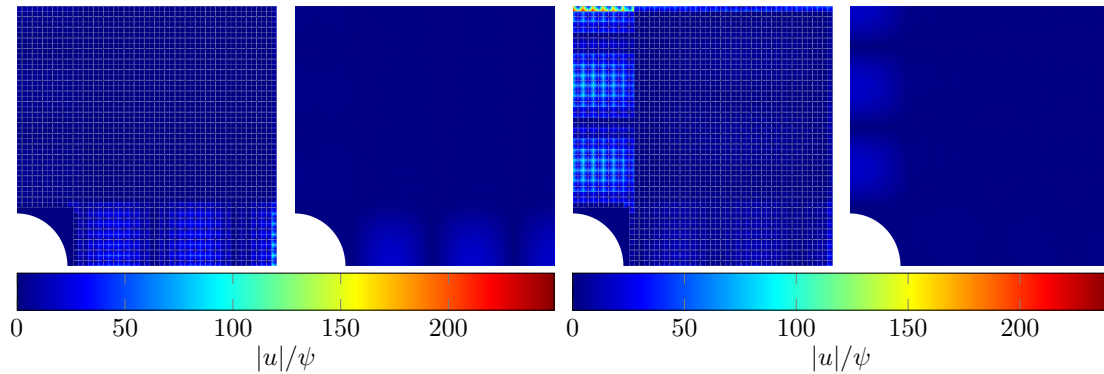


Figure 3.35: $|u|/\psi$ at frequency M_3 for the microstructured model and the relaxed micromorphic model, the first two figures correspond to M_3 (left) and the last two figures to M_3 (right) (see Fig. 3.32 for the definition of these points).

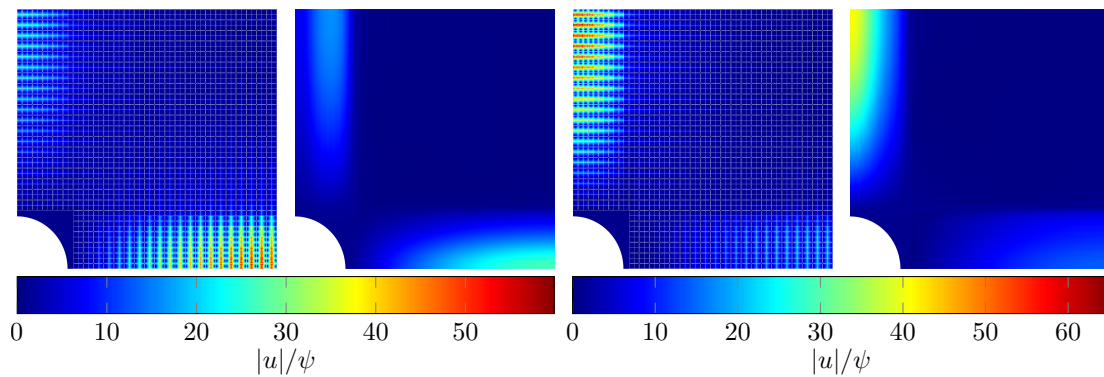


Figure 3.36: $|u|/\psi$ at frequency M_4 for the microstructured model and the relaxed micromorphic model, the first two figures correspond to M_4 (left) and the last two figures to M_1 (right) (see Fig. 3.32 for the definition of these points).

Figure 3.37 presents the response of the microstructured and the relaxed micromorphic models in the band gap. In this figure we chose to use a different scale for the two pictures so as to show the load concentration around the Cauchy region that occurs for both the relaxed micromorphic and the microstructured model. Indeed, due to the lack of higher space derivatives of the microdistortion P , the relaxed micromorphic medium cannot catch the highly concentrated peaks of displacement occurring in few isolated cells. However, apart from these pointwise difference the solution is well reproduced and, above all, the band-gap behavior is correctly described.

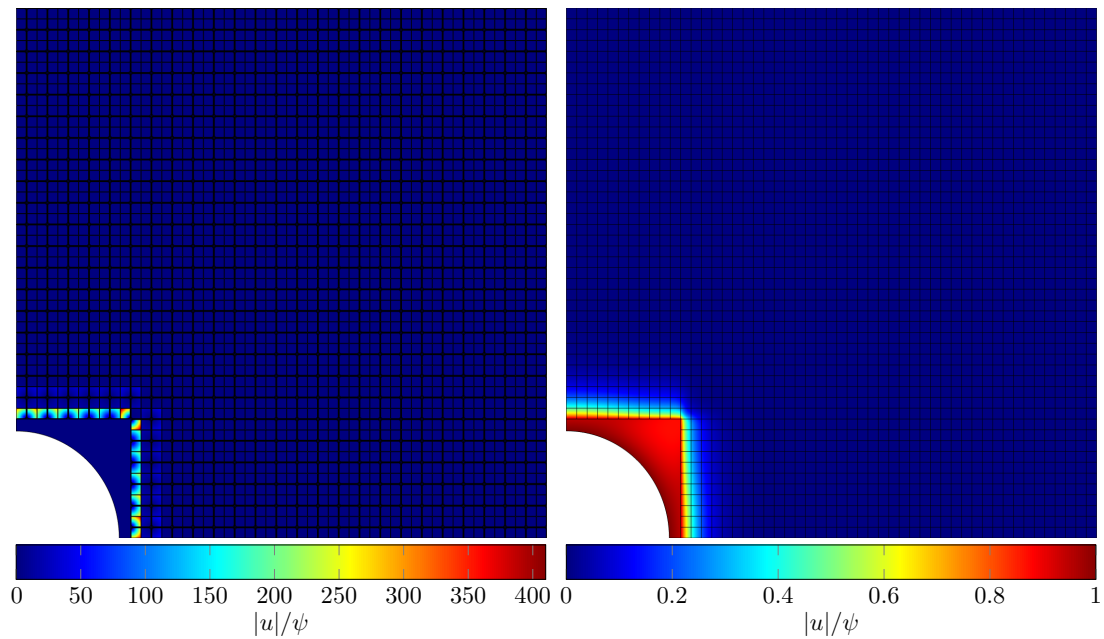


Figure 3.37: $|u|/\psi$ in the band-gap for the microstructured model and the relaxed micromorphic model at 1717 Hz.

By introducing a new kinematic field and an appropriate Lagrangian density, eventually leading to new equilibrium equations for our media, we managed to model the band-gap effect in an enriched continuum, sharing with a given metamaterial the same dispersion curves, *i.e.* its **spectral signature**, completely characterizing its mechanical behaviour. The coincidence of these spectral signatures (obtained through the calibration of the dispersion curves *via* a Bloch-Floquet analysis), combined with the adequate boundary conditions and, as we just presented, size of both the structure and the excitation, allow such an enriched continuum to successfully describe the response of our systems on a large frequency range.

Confronting our models to the experiment

Contents

4.1	Writing of the 3D model	95
4.1.1	For the classical Cauchy model	95
4.1.2	For the relaxed micromorphic model	98
4.2	Recalibrating the model	101
4.2.1	For the microstructured system	102
4.2.2	For the micromorphic system	107
4.3	Perturbating the model	114
4.4	Comparison with the experiment	122
4.4.1	Point-to-point displacement comparison	123
4.4.2	2D response of the plate	126
4.5	Enabling meta-structural engineering design	128

Chapter 4. Confronting our models to the experiment

For the subsequent purposes of comparison with the experiment presented in Chapter 2, we introduce four points C_i $i \in \llbracket 1, 4 \rrbracket$ far from the excitation. As these points are only considered in comparison with the experimental setup, their coordinates are directly given for $n_1 = 11$, $n_2 = 9$ and $n_c = 1$ in Table 4.1 and Figure 4.1.

Point	C_1	C_2	C_3	C_4
x_1 coordinate [mm]	105	105	5	15
x_2 coordinate [mm]	5	15	85	85

Table 4.1: Coordinates of the measurement points.

We will show that, to take into account the inappropriateness of the plane strain hypothesis in our plate, the presence of defects in the fabrication process, and, to a smaller extent, to measurement inaccuracy, a recalibration and perturbation of our models has to be considered. Given the change of nature of the excitation of the system, we redefine p and m presented in Chapter 3 by:

$$p_B = \sqrt{\langle \mathbf{u}(B), \bar{\mathbf{u}}(B) \rangle} \quad \text{and} \quad m_B = \frac{4}{a^2} \int_{\Omega_B} \sqrt{\langle \mathbf{u}(\mathbf{x}), \bar{\mathbf{u}}(\mathbf{x}) \rangle} dx_1 dx_2 \quad (4.1)$$

For

$$B = (11, 0)^T \quad \text{and} \quad \Omega_B = [10, 11] \times [0, 1] \quad [\text{cm}] \quad (4.2)$$

Figure 4.1 presents the position of the points C_i , B and Ω_B on the microstructured plate and the relaxed micromorphic model. Annex C presents the rest of results of the points along the symmetry planes.

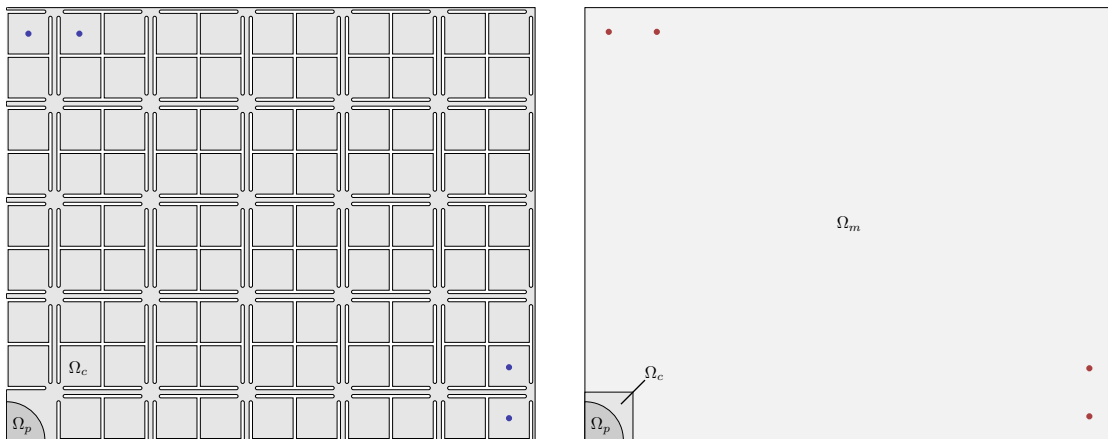


Figure 4.1: (left) Microstructured symmetrized model with the selected points (blue) for the comparison with the experimental system. (right) Relaxed micromorphic symmetrized model with the selected points (red) for the comparison with the experimental system.

4.1 Writing of the 3D model

In Chapter 3, we presented the relaxed micromorphic model, given the complexity of such medium, in the bidimensional case : such simplified modelling was sufficient for the first model we present : in particular, it was only associated with a classical Cauchy medium with boundary conditions that could easily be implemented in the bidimensional case. As it has been presented in Chapter 2, we now have to model piezoelectric patches used as actuators, where the three directions of space have to be considered.

As we did in Chapter 3, the introduction of a suitable action functional will allow to make our different continua coexist, eventually facilitating the implementation for the resolution of our problems *via* the Finite-Element Method under *Comsol Multiphysics*[®].

4.1.1 For the classical Cauchy model

From the structure presented in Figure 3.23 in Chapter 1, the central hole can be replaced by the piezoelectric patches. Given the symmetries of the considered system along the three main symmetry planes of space, only one 1/8 of the microstructured plate (1/4 from the top view, its thickness being divided by 2) can be considered and one patch of the two used for the excitation of the plate. These two configurations are presented in Figure 4.2.

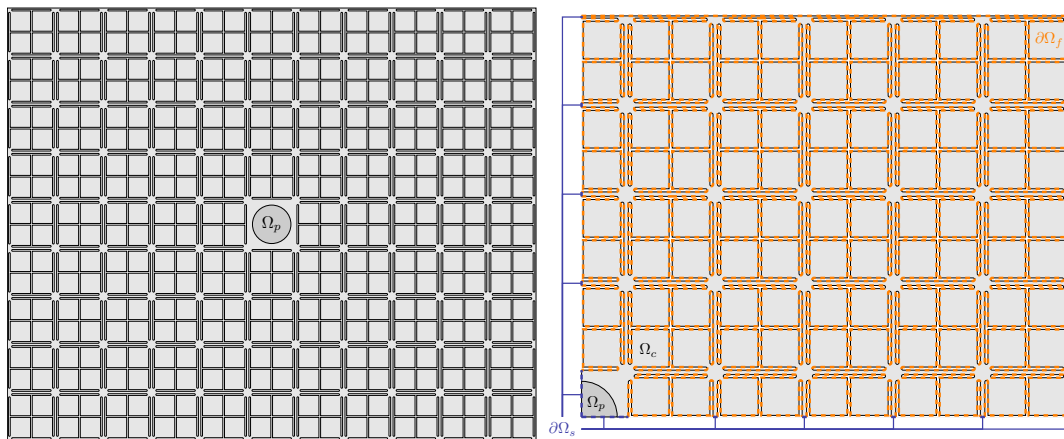


Figure 4.2: (left) Top view of the unsymmetrized microstructured plate with the upper piezoelectric patch Ω_p . (right) Top view of the symmetrized microstructured plate with the traction free boundaries $\partial\Omega_f$ and the symmetry planes $\partial\Omega_s$.

Figure 4.3 represents the section of the full system, which will help us to implement properly the plane strain condition necessary to the relaxed micromorphic modelling.

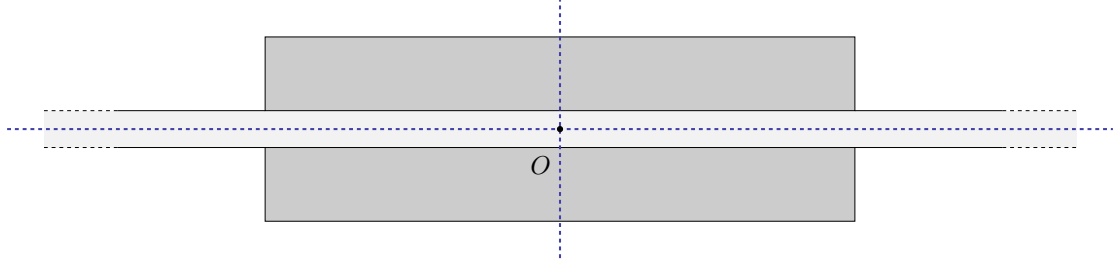


Figure 4.3: Section at $x_2 = 0$ of the (light grey) full microstructured plate with the (dark grey) two piezoelectric patches and, in dashed blue lines, the symmetry planes $x_1 = 0$ and $x_3 = 0$, the origin O being set at the center of the plate.

As it has been proved in Chapter 3, we have in the symmetry plane $\partial\Omega_s^3$ ($x_3 = 0$)

$$\mathbf{u}(\mathbf{x}) = \begin{pmatrix} \star \\ \star \\ 0 \end{pmatrix} \quad \text{and} \quad (\nabla\mathbf{u})(\mathbf{x}) = \begin{pmatrix} \star & \star & 0 \\ \star & \star & 0 \\ 0 & 0 & \star \end{pmatrix} \quad \text{in } \partial\Omega_s^3 \quad (4.3)$$

Given this, the necessary plane strain hypothesis can be interpreted as considering the displacement on $\partial\Omega_s^3$ in the plate. Nevertheless, the plane strain hypothesis still has to be made for the symmetrized structure, *i.e.*

$$\begin{cases} u_1(x_1\mathbf{x}_1 + x_2\mathbf{x}_2 + x_3\mathbf{x}_3) = u_1(x_1\mathbf{x}_1 + x_2\mathbf{x}_2) \\ u_2(x_1\mathbf{x}_1 + x_2\mathbf{x}_2 + x_3\mathbf{x}_3) = u_2(x_1\mathbf{x}_1 + x_2\mathbf{x}_2) \\ u_3(x_1\mathbf{x}_1 + x_2\mathbf{x}_2 + x_3\mathbf{x}_3) = 0 \end{cases} \quad \forall \mathbf{x} \in \left[0, \frac{n_1a}{2}\right] \times \left[0, \frac{n_2a}{2}\right] \times \left[0, \frac{e}{2}\right] \quad (4.4)$$

We can now detail the boundary conditions for the piezoelectric patch and the microstructured plate. The section of the symmetrized structure is presented in Figure 4.4: the plate's thickness is represented while we consider the displacement only at $x_3 = 0$.

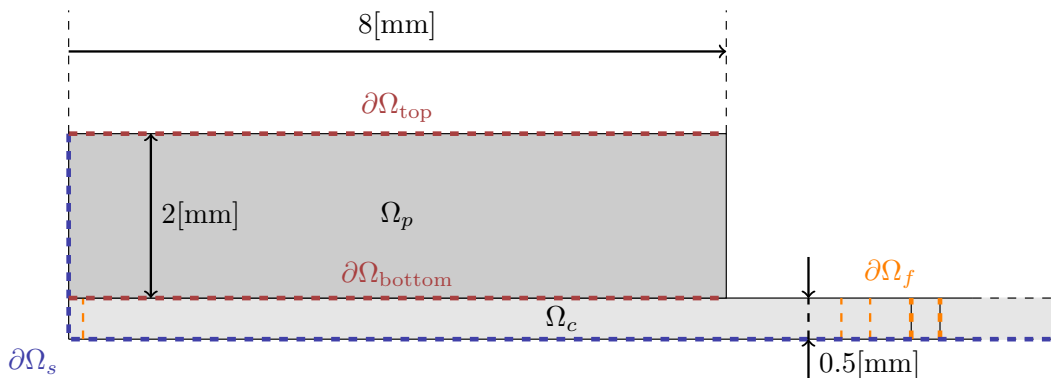


Figure 4.4: Section of the symmetrized microstructured plate with the piezoelectric patch (one eighth on the whole system) and the boundaries' denomination $\partial\Omega_{\text{top}}$ and $\partial\Omega_{\text{bottom}}$ where the electric potential is imposed.

From these considerations, we propose the following action functional for the reduced structure, mixing 3D formulation for the upper piezoelectric patch and 2D formulation for the microstructured plate:

$$\mathcal{A}_{\text{int}}[\mathbf{u}, V] = \int_{t_1}^{t_2} \left[\int_{\Omega_p} (k_p - w_p - q) dx_1 dx_2 dx_3 + \frac{e}{2} \int_{\Omega_c} (k_c - w_c) dx_1 dx_2 \right] dt \quad (4.5)$$

where $e = 10^{-3}$ [m] is the thickness of the full plate. The hypothesis of plane strain in the plate leads to

$$\mathbf{u} = \begin{pmatrix} u_1 \\ u_2 \\ 0 \end{pmatrix} \quad \text{in } \Omega_c \quad \text{and} \quad \mathbf{u} = \begin{pmatrix} u_1 \\ u_2 \\ u_3 \end{pmatrix} \quad \text{in } \Omega_p \quad (4.6)$$

In particular, we have

$$u_3 = 0 \quad \text{on } \partial\Omega_{\text{bottom}} \quad (4.7)$$

allowing to delete vertical rigid body modes for the piezoelectric patch. Let us study the continuity of displacement between the piezoelectric patch and the microstructured plate. The displacement in Ω_p and Ω_c being respectively written \mathbf{u}_p and \mathbf{u}_c , the action functional introduced in Equation 4.5 becomes

$$\mathcal{A}'_{\text{int}}[\mathbf{u}, V, \boldsymbol{\lambda}] = \mathcal{A}_{\text{int}}[\mathbf{u}, V] - \int_{t_1}^{t_2} \int_{\partial\Omega_{\text{bottom}}} \langle \boldsymbol{\lambda}, \mathbf{u}_c - \mathbf{u}_p \rangle dx_1 dx_2 dt \quad (4.8)$$

The Lagrange equation $\mathcal{L}_{\mathbf{u}_p}$ associated with \mathbf{u}_p has already been computed and studied in Chapter 1, and allows to conclude that :

- $\lambda_n = \langle \boldsymbol{\lambda}, \mathbf{x}_3 \rangle$ is the reaction force guaranteeing the nullity of u_3 on $\partial\Omega_{\text{bottom}}$, *i.e.* the symmetry condition derived from the plane strain hypothesis.
- $\lambda_t = \boldsymbol{\lambda} - \lambda_n \mathbf{x}_3$ in the tangential force at the interface guaranteeing the continuity of displacement between the two media.

Let us write the Lagrange equation associated to $\mathcal{L}_{\mathbf{u}_c}$, we have

$$\rho_c \ddot{\mathbf{u}}_c = \nabla \cdot \boldsymbol{\sigma} + \frac{2\lambda_t}{e} \quad \text{in } \partial\Omega_{\text{bottom}} \quad (4.9)$$

Making $\frac{2\lambda_t}{e}$ correspond to the surface density of force guaranteeing the continuity of displacement at the interface and therefore, for Ω_c , shall not be treated as a boundary condition. λ_t corresponding to the tangential forces for the upper piezoelectric patch, the contribution of the lower patch is "reintroduced" through the division by 2 of the microstructured plate, hence $\frac{2\lambda_t}{e}$. We can now detail the boundary conditions of the upper piezoelectric patch. The first interface conditions represent the imposition of the electric potential while the second are associated to the symmetry conditions of the reduced problem, in formulas:

$$\begin{cases} V = 0 & \text{on } \partial\Omega_{\text{bottom}} \\ V = V_0 & \text{on } \partial\Omega_{\text{top}} \end{cases} \quad \text{and} \quad \begin{cases} \langle \mathbf{u}, \mathbf{n} \rangle = 0 \\ \langle \mathbf{D}, \mathbf{n} \rangle = 0 \end{cases} \quad \text{on } \partial\Omega_s \quad (4.10)$$

Chapter 4. Confronting our models to the experiment

where $V_0 = 100[\text{V}]$. The free of charges vertical cylinder surface is characterized by $\langle \mathbf{D}, \mathbf{n} \rangle = 0$, such boundary condition being naturally verified as proven in Chapter 3. For the microstructured plate Ω_c , we have:

$$\boldsymbol{\sigma} \cdot \mathbf{n} = \mathbf{0} \quad \text{on } \partial\Omega_f \quad \text{and} \quad \langle \mathbf{u}, \mathbf{n} \rangle = 0 \quad \text{on } \partial\Omega_s \quad (4.11)$$

The response of this structure will be given after the presentation of the relaxed micromorphic model.

4.1.2 For the relaxed micromorphic model

The experimental plate, corresponding to a $n_1 = 11$, $n_2 = 9$ and $n_c = 1$ plate is, considering the conclusions of Chapter 1, has both a too small outer size and inner "excitation size". Nevertheless, we will show that, although such plate not satisfying the homogenization conditions, the relaxed micromorphic model still manage to describe the non-propagation of the waves in the band-gap regime and more generally the response of the microstructured plate in a large frequency range, whose equivalent full and symmetrized plate is presented in Figure 4.5.

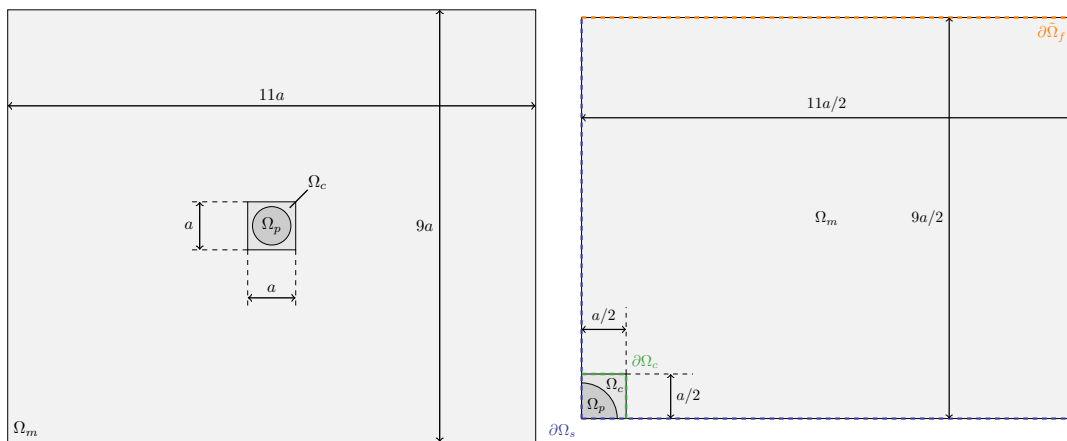


Figure 4.5: (left) Top view of the full relaxed micromorphic model with the upper piezoelectric patch Ω_p , the central Cauchy bulk cell Ω_c and the relaxed micromorphic medium Ω_m . (right) Top view of the symmetrized relaxed micromorphic model with the (generalized) traction free boundaries $\partial\tilde{\Omega}_f$, the symmetry planes $\partial\Omega_s$ and the interface $\partial\Omega_c$.

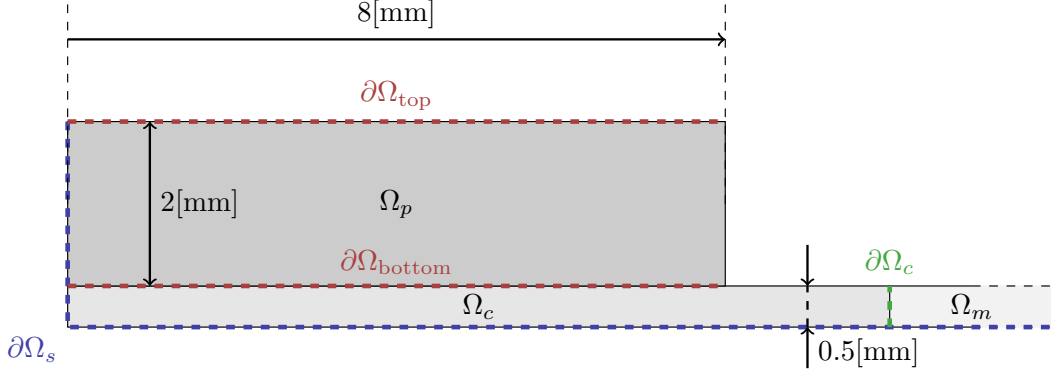


Figure 4.6: Section of the symmetrized relaxed micromorphic plate with the piezoelectric patch (one eight on the whole system) and the boundaries' denomination $\partial\Omega_{\text{top}}$ and $\partial\Omega_{\text{bottom}}$ where the electric potential is imposed.

As the plane strain hypothesis has already been presented for the microstructured plate and that the central zone under the piezoelectric patch remain untouched, we directly present the symmetrized model in Figure 4.6. As the microstructured part of the plate is replaced by relaxed micromorphic model, we introduce the action functional of this equivalent model as

$$\mathcal{A}_{\text{int}}[\mathbf{u}, \mathbf{P}, V] = \int_{t_1}^{t_2} \left[\int_{\Omega_p} (k_p - w_p - q) d\Omega + \frac{e}{2} \left[\int_{\Omega_c} (k_c - w_c) d\Gamma + \int_{\Omega_m} (k_m - w_m) d\Gamma \right] \right] dt \quad (4.12)$$

The hypothesis of plane strain in the plate leads to

$$\mathbf{u} = \begin{pmatrix} u_1 \\ u_2 \\ u_3 \end{pmatrix} \text{ in } \Omega_p, \quad \mathbf{u} = \begin{pmatrix} u_1 \\ u_2 \\ 0 \end{pmatrix} \text{ in } \Omega_c, \quad \mathbf{u} = \begin{pmatrix} u_1 \\ u_2 \\ 0 \end{pmatrix} \text{ and } \mathbf{P} = \begin{pmatrix} P_{11} & P_{12} & 0 \\ P_{21} & P_{22} & 0 \\ 0 & 0 & 0 \end{pmatrix} \text{ in } \Omega_m \quad (4.13)$$

In particular, we have

$$u_3 = 0 \quad \text{on } \partial\Omega_{\text{bottom}} \quad (4.14)$$

The boundary conditions for the piezoelectric patch have already been presented in subsection 3.1.1. For the central square $\partial\Omega_c$ modeled, in absence of an architected geometry, by a classical Cauchy medium, we just have to set the symmetry condition

$$\langle \mathbf{u}, \mathbf{n} \rangle = 0 \quad \text{on } \partial\Omega_s \quad (4.15)$$

The boundary conditions for the relaxed micromorphic medium have already been largely discussed. The continuity of generalized stress and its nullity upon traction-free boundaries, being not naturally verified, we have to set, in addition to the symmetry boundary conditions:

$$\begin{cases} (\hat{\sigma}_{ij} + \tilde{\sigma}_{ij})n_j = 0 & \text{on } \partial\tilde{\Omega}_f \\ (\hat{\sigma}_{ij} + \tilde{\sigma}_{ij})n_j = \sigma_{ij}^c n_j & \text{on } \partial\Omega_c \end{cases} \text{ and } \begin{cases} u_i n_i = 0 \\ (\delta_{ki} - n_k n_i)(P_{ij} n_j) = 0 \end{cases} \text{ on } \partial\Omega_s \quad (4.16)$$

Chapter 4. Confronting our models to the experiment

This model and the microstructured plate one have been implemented and solved in *Comsol Multiphysics*[®]. We saw in Chapter 3 that the Finite Element method gave us the displacement in the microstructured plate / relaxed micromorphic model through its discretization, in formula:

$$\mathbf{u}(\mathbf{x}) = \mathbf{e}_u^T(\mathbf{x})\mathbf{q}_u \quad (4.17)$$

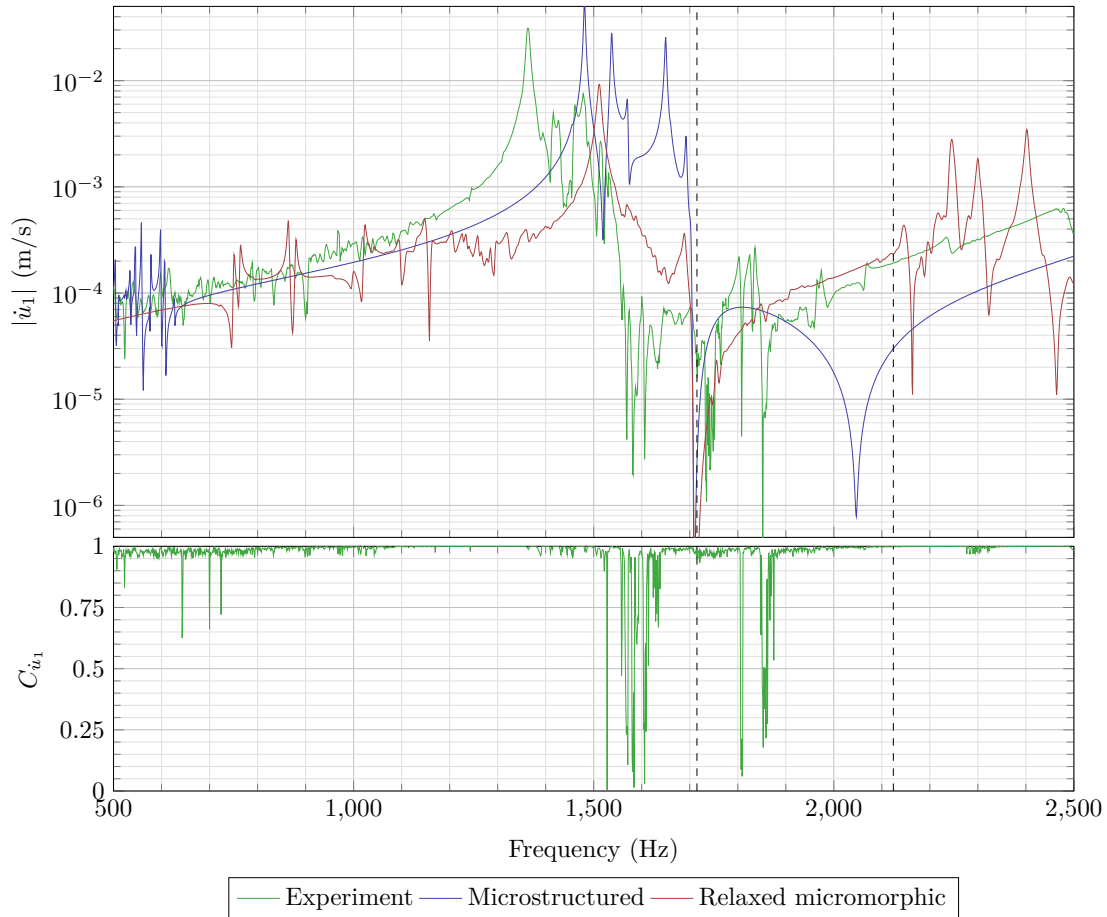


Figure 4.7: Amplitude of $|\dot{u}_1|$ at C_1 (see Figure 4.1 for the definition of this point) for the experiment, the microstructured and relaxed micromorphic models with the theoretical limits of the band-gap obtained *via* the Bloch-Floquet analysis (dashed lines).

On the other hand, the experiment giving the measured speed of the center of the resonators while the finite elements resolution computes the displacement of the discretized plate, it is mandatory to derivate the theoretical displacement. A linear model being considered for the microstructured and the relaxed micromorphic models and given the small displacement and deformations in the system, one can compute the theoretical speed across the system in the frequency domain by assuming the hypothesis of harmonic form for the time-component of the solution:

$$\dot{\mathbf{u}}(\mathbf{x}) = 2\pi i f \mathbf{u}(\mathbf{x}) \quad (4.18)$$

where f is the frequency (in Hz) considered. As the theoretical speed tends to 0 at low frequency and is therefore of no interest, the chosen frequency range becomes [500, 2500] Hz. The response of the experimental set-up, the microstructured plate and the relaxed micromorphic model are plotted in Figure 4.7. Despite the overall good description of the observed response in the considered frequency range, one can observe a shift between the experiment and the two theoretical models, in particular for the first structural mode and at the first anti-resonance in the band-gap. If this difference can be partially explained, for the relaxed micromorphic model, to the unfulfilling of the homogenization conditions, a recalibration procedure for both models have to be considered.

4.2 Recalibrating the model

To account for the presence of defects and get closer to the experimental results, the system can be modified, taking into account several potential differences between the analytical models and experimental system. In a first time, we can list the hypotheses made in the framework of our modelling:

- the plane strain hypothesis in the plate
- small displacement and small deformation hypotheses
- linear hypothesis more generally
- idealized geometry
- idealized constitutive laws (including dissipation)
- idealized boundary conditions (at the interfaces and at the traction-free boundaries)

The first hypothesis is the more criticizable, indeed, we theoretically have, for a traction-free surface like the horizontal surfaces of our microstructured plate

$$\boldsymbol{\sigma} \cdot (\pm \mathbf{x}_3) = \mathbf{0} \quad \Rightarrow \quad \sigma_{13} = 0 = \sigma_{23} = \sigma_{33} \quad \forall \mathbf{x} \in \left\{ x_1^2 + x_2^2 > r_{\text{piezo}}^2 \right\} \times \left\{ -\frac{e}{2}, \frac{e}{2} \right\} \quad (4.19)$$

Supposing moreover that, in the considered frequency range, σ_{13} , σ_{23} and σ_{33} vary little through $x_3 \in [-e/2, e/2]$, we should rather have considered

$$\boldsymbol{\sigma} = \begin{pmatrix} * & * & 0 \\ * & * & 0 \\ 0 & 0 & 0 \end{pmatrix} \quad \forall \mathbf{x} \in \left\{ x_1^2 + x_2^2 > r_{\text{piezo}}^2 \right\} \times \left[-\frac{e}{2}, \frac{e}{2} \right] \quad (4.20)$$

The linearity of our system has been proved to be a very reasonable hypothesis, given the coherences of the measured signal given in Chapter 2: the small amplitude of applied loads of the structure strong predicted such observations. The idealization of geometry will be treated in the ‘‘perturbation’’ Section: we will show that taking them into account allows to describe precisely the response of the structure in the band-gap. The idealization of the constitutive laws, with respect to the

relaxed micromorphic model, is precisely discussed in this manuscript: we will show that, despite the smallness of both the plate and the excitation compared to the homogenization conditions detailed in Chapter 3, such model is able to describe the overall response of the microstructured plate for a large frequency range including the band-gap. We saw that the difficulty to introduce damping in the relaxed micromorphic material let us little choice when it comes to the model to choose: the material considered, weakly damped, having little influence on the plate's response, allow us not to pay particular attention of its modelling (*e.g.*, the Basile hypothesis allow us to neglect modal coupling).

4.2.1 For the microstructured system

Very classically, as the Poisson ratio is not influenced by the defects nor the manufacturing process, we chose to modify the Young modulus and the mass density, in formulas:

$$E^{\text{recalibration}} = (1 + \kappa_E)E_{\text{Ti}} \quad \text{and} \quad \rho_c^{\text{recalibration}} = (1 + \kappa_\rho)\rho_{\text{Ti}} \quad (4.21)$$

where κ_E and κ_ρ are the respective recalibration for the Young modulus and the mass density ($\kappa_E = 0 = \kappa_\rho$ corresponding to the default values of these two parameters E_{Ti} and ρ_{Ti}). Leading, for the local energy densities, to

$$w_c^{\text{recalibration}} = (1 + \kappa_E)w_c \quad \text{and} \quad k_c^{\text{recalibration}} = (1 + \kappa_\rho)k_c \quad (4.22)$$

Such consideration allows to modify the action functional of the structure presented in Figure 4.2 by

$$\mathcal{A}_{\text{int}}[\mathbf{u}, V] = \int_{t_1}^{t_2} \left[\int_{\Omega_p} (k_p - w_p - q) d\Omega + \frac{e}{2} \int_{\Omega_c} [(1 + \kappa_\rho)k_c - (1 + \kappa_E)w_c] d\Gamma \right] dt \quad (4.23)$$

the coefficients of the piezoelectric patch remaining untouched: this medium has not undergone any manufacturing process and therefore its mechanical characteristics may have not been as altered as the microstructured plate may have, in addition of the plane strain hypothesis. Moreover, the modification of its mass density and strain energy density would have had more complex repercussions on the responses of both models, eventually leading to "unreasonable" values of κ_E and κ_ρ to fit the experimental curves. The procedure to find κ_w and κ_k is present through an algorithm given in Figure 4.8.

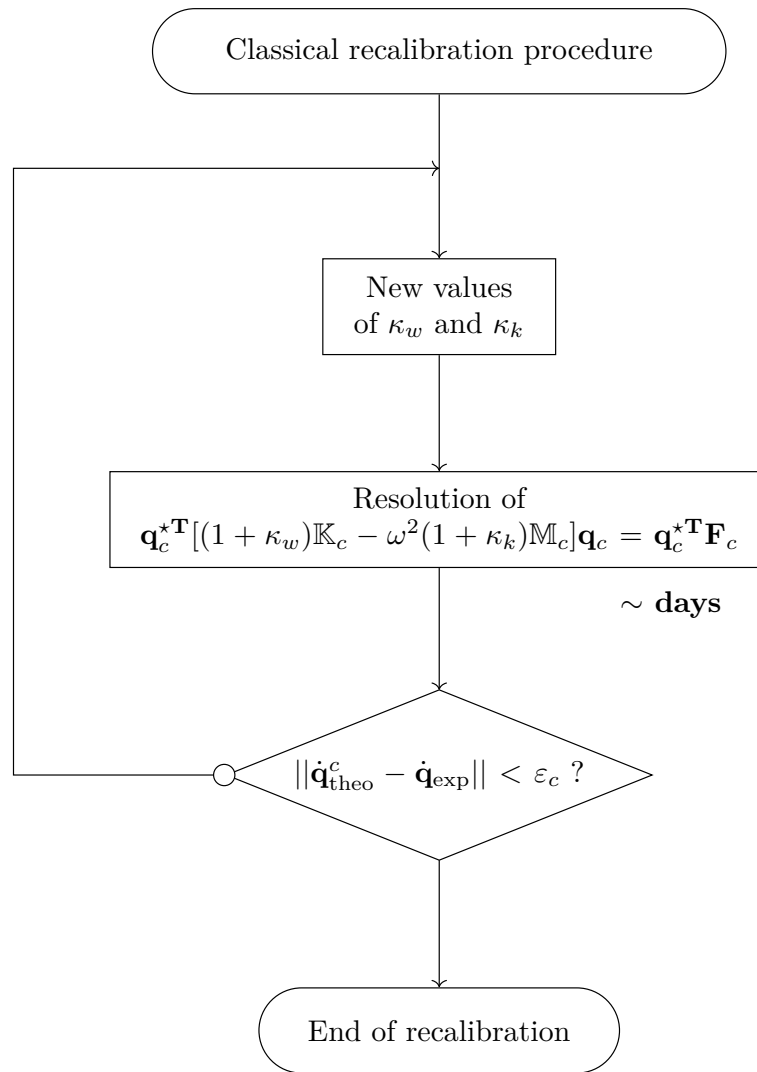


Figure 4.8: Recalibration procedure for the classical Cauchy model given in Figure 4.2

The influence of κ_k and κ_w on the frequency response can easily be inferred as given in Figure 4.9. Classically, the recalibration of the static and dynamic response of the plate could have been driven by:

- a static test to determine the value of κ_w
- the computation of the eigenfrequency of a structural mode, for a κ_w given, the value of κ_k

In formulas:

$$\frac{u_0^{\text{recalibration}}}{u_0} \approx 1 + \kappa_E \quad \text{and} \quad \frac{\omega_0^{\text{recalibration}}}{\omega_0} \approx \sqrt{\frac{1 + \kappa_E}{1 + \kappa_\rho}} \quad (4.24)$$

where u_0 is the static response of the plate and w the eigenfrequency of the first structural mode of the plate (in the absence of recalibration for the piezoelectric patches, we won't dare to write equal signs here).

Chapter 4. Confronting our models to the experiment

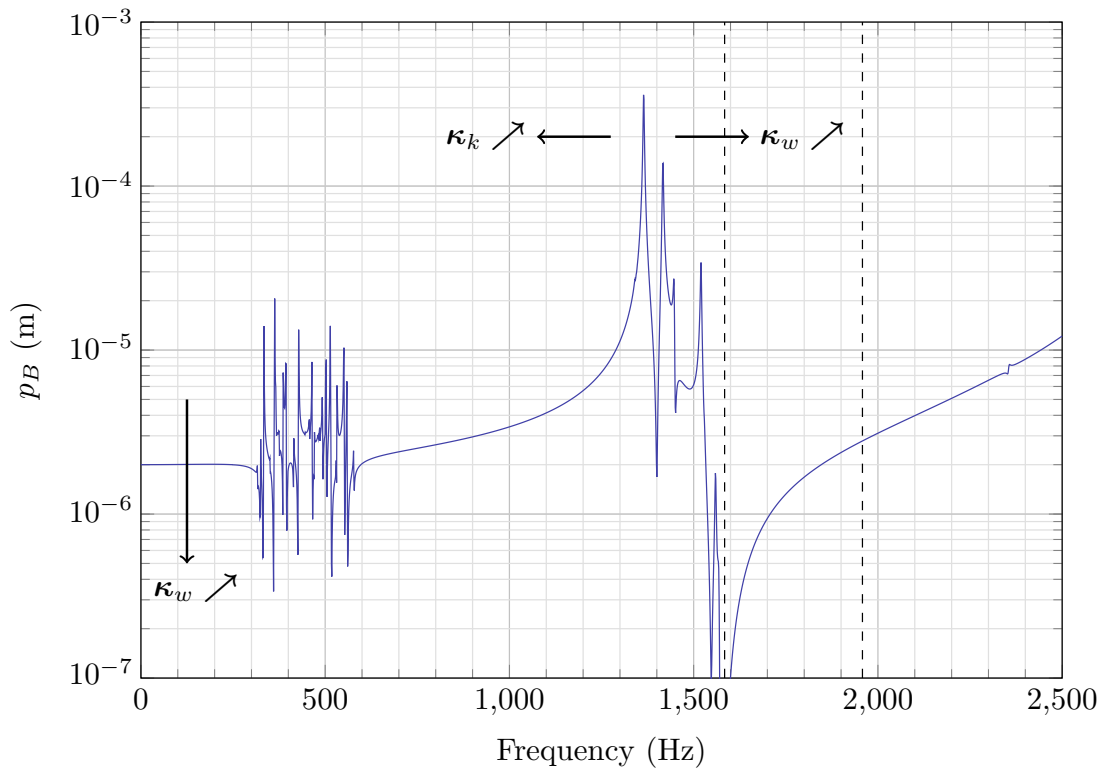


Figure 4.9: Effects of the recalibration procedure on the response of the plate for p_B according to Equations 4.24.

To consider point-to-point displacement or average displacement or eigenfrequency could be questioned, we will show that our “simple” procedure gives good results on the whole the plate. Unfortunately, having only access to speed measurements, we did not have access to the static response of the experimental set-up: this difficulty can easily be overcome by considering the slope, supposed to be constant, of the speed between 0 Hz and the first structural mode of the plate. We then have

$$\frac{\omega_4 - \omega_3}{\omega_2 - \omega_1} \cdot \frac{\int_{\omega_1}^{\omega_2} \dot{u}_0^{\text{recalibration}}(\omega) d\omega}{\int_{\omega_3}^{\omega_4} \dot{u}_0(\omega) d\omega} \approx 1 + \kappa_E \quad (4.25)$$

Confronting the theoretical results to the experiments eventually led to

$$\boxed{\kappa_\rho = +0.05 \quad \text{and} \quad \kappa_E = -0.10875} \quad (4.26)$$

We just saw that the most suitable hypothesis here was

$$\sigma = \begin{pmatrix} * & * & 0 \\ * & * & 0 \\ 0 & 0 & 0 \end{pmatrix} \quad \text{instead of} \quad \nabla \mathbf{u} = \begin{pmatrix} * & * & 0 \\ * & * & 0 \\ 0 & 0 & 0 \end{pmatrix} \quad \forall \mathbf{x} \in \left\{ x_1^2 + x_2^2 > r_{\text{piezo}}^2 \right\} \times \left[-\frac{e}{2}, \frac{e}{2} \right] \quad (4.27)$$

via the stress-strain and strain-stress relations (3.50) and (3.50) in Chapter 1, one can get

$$\begin{cases} u_{3,3} = \frac{\lambda}{\lambda + 2\mu}(u_{1,1} + u_{2,2}) & \text{(for the plane stress hypothesis)} \\ \sigma_{33} = \nu(\sigma_{11} + \sigma_{22}) & \text{(for the plane strain hypothesis)} \end{cases} \quad (4.28)$$

The strain-stress relations are, in the plane stress hypothesis,

$$\begin{cases} u_{1,1} = \frac{\sigma_{11} - \nu\sigma_{22}}{E} \\ u_{2,2} = \frac{\sigma_{22} - \nu\sigma_{11}}{E} \\ \frac{1}{2}(u_{1,2} + u_{2,1}) = \frac{(1 + \nu)\sigma_{12}}{E} \end{cases} \quad (4.29)$$

Having $u_{2,3} = 0 = u_{3,2} = u_{1,3} = u_{3,1}$ (resp. $\sigma_{13} = 0 = \sigma_{13}$) for the plane stress hypothesis (resp. plane strain hypothesis), the plane strain and plane stress hypothesis may be seen as equivalent, provided that the mechanical parameters for the plane stress model are modified by the following rule:

$$E_{\text{Plane Stress}} = E_{\text{Plane Strain}}(1 + \nu)(1 - \nu) = E_{\text{Plane Strain}}(1 - \nu^2) \quad (4.30)$$

without developing the rules for λ and ν , we can notice that

$$E_{\text{recalibration}} = (1 + \kappa_E)E_{\text{Ti}} \quad \text{and} \quad E_{\text{Plane Stress}} = (1 - \nu^2)E_{\text{Plane Strain}} \quad (4.31)$$

look pretty much the same. Having $\nu = 0.34$, we have

$$- \nu^2 = -0.1156 \quad \text{while we had} \quad \kappa_E = -0.10875 \quad (4.32)$$

Given this, we can argue that the recalibration for the Young modulus takes into account, to some extent, the inaccuracy of the plane strain hypothesis. Once again, to consider the plane stress hypothesis for the relaxed micromorphic model would have considerably complexified the identification of the mechanical parameters. Figure 4.10 gives the FRFs of p_B and m_B for the recalibrated and the original microstructured plate.

Chapter 4. Confronting our models to the experiment

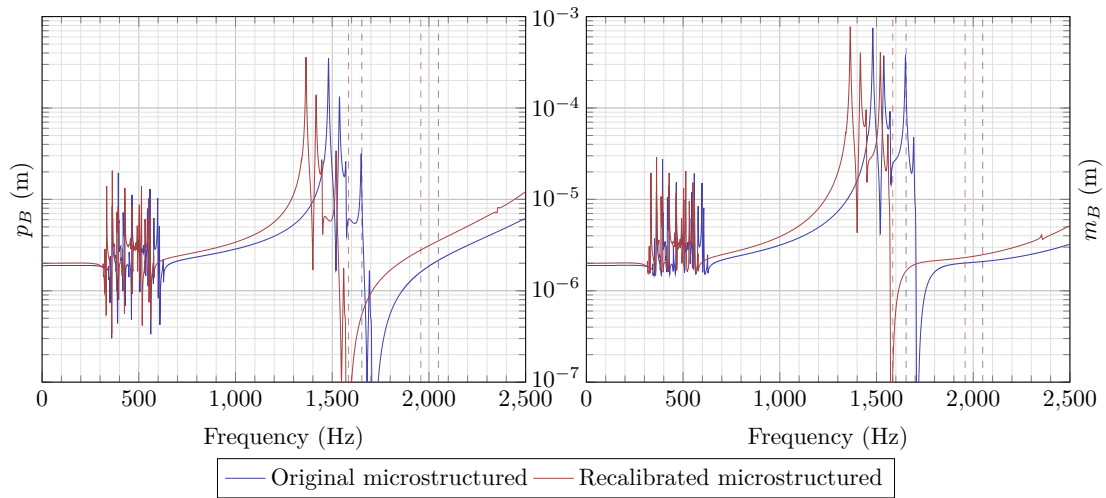


Figure 4.10: (*left*) Pointwise displacement p_B for the original and recalibrated microstructured models at point B . (*right*) Mean displacement m_B for the original and recalibrated microstructured models. The theoretical limits of the band-gap obtained via the Bloch-Floquet analysis for the original and recalibrated architected unit cell are given in dashed lines.

Figure 4.11 presents the FRFs of the recalibrated microstructured plate and the experimental one: one can notice the dramatic decrease of the difference between them, specifically in:

- the static behaviour till the first structural mode
- the description of the pre-band-gap resonance
- the collapse of the response at the beginning of the band-gap

The theoretical position of the band gap has also been updated: the recalibrated values of the Young modulus and the mass density has been used to compute the dispersion curves of the microstructured unit cell. As it appears in Figure 4.11, the lower bound of the band gap perfectly matches with the first antiresonance of the system.

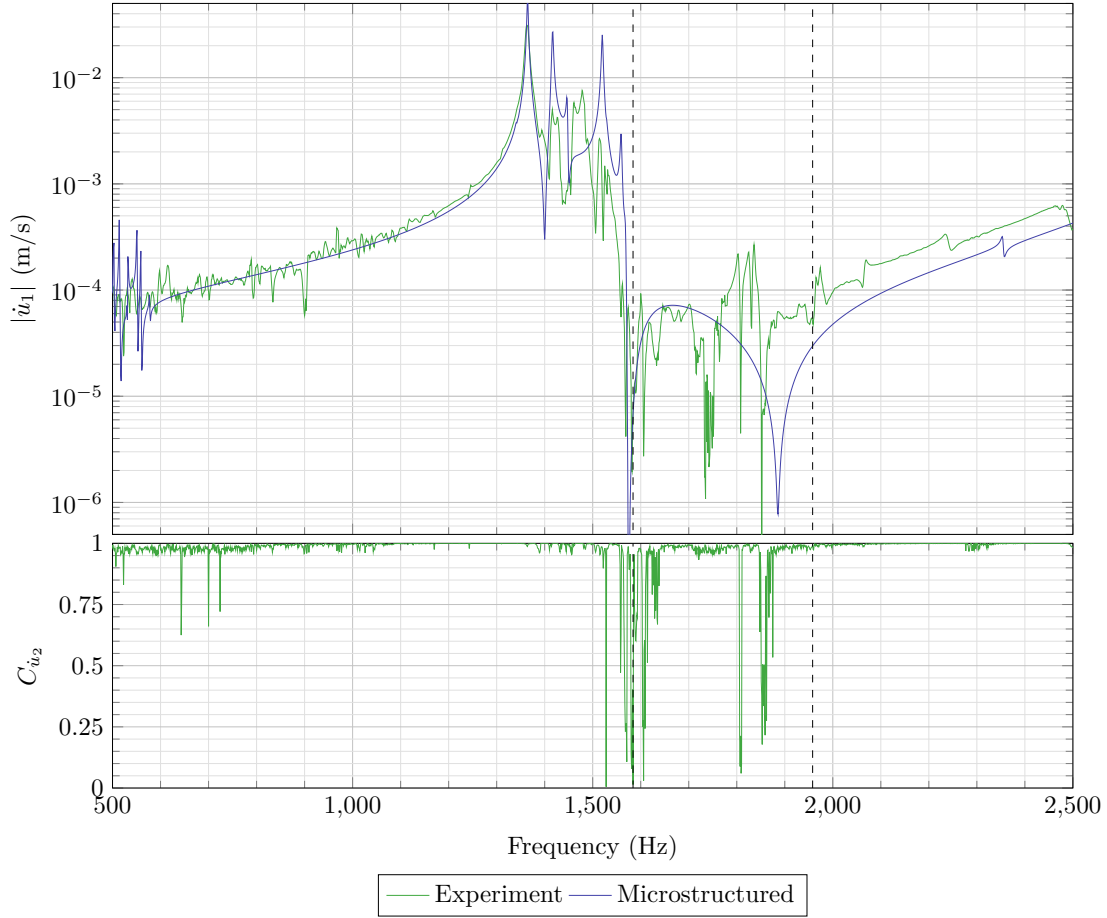


Figure 4.11: (top) $|u_1|$ for C_1 for the experiment (green) and the recalibrated microstructured plate (blue). (bottom) Coherence of $|u_1|$ for the experiment. The dashed lines represent the theoretical lower and upper limit of the band-gap on the recalibrated unit cell.

4.2.2 For the micromorphic system

The recalibration for the relaxed micromorphic model, due to the relatively large number of independent coefficients (16 in our case), to our knowledge, has not been considered yet. We present here a simple yet powerful procedure allowing, as we will show, to facilitate considerably the determination of the recalibration parameters κ_i introduced in the previous section. We saw that our modification of the Young modulus and the mass density corresponded to an affine modification of its kinetic and strain energy densities. In the same way, the kinetic and potential density of energy for the relaxed micromorphic model are modified as

$$k_m^{\text{recalibration}} = (1 + \kappa_k)k_m \quad \text{and} \quad w_m^{\text{recalibration}} = (1 + \kappa_w)w_m \quad (4.33)$$

where k_m and w_m are respectively the initial kinetic and strain energy densities of the relaxed micromorphic model. To recalibrate the relaxed micromorphic model

Chapter 4. Confronting our models to the experiment

on the microstructured model, we set

$$\boxed{\kappa_k = \kappa_\rho \quad \text{and} \quad \kappa_w = \kappa_E} \quad (4.34)$$

The equivalence between κ_E and κ_w derives from the equivalence of the strain energy of the architected cell Ω_c and the relaxed micromorphic model. We saw that

$$E^{\text{recalibration}} = (1 + \kappa_E)E_{\text{Ti}} \quad \Rightarrow \quad w_c^{\text{recalibration}} = (1 + \kappa_E)w_c \quad (4.35)$$

Having by hypothesis (calibration procedure used to determine the relaxed micromorphic static parameters):

$$\begin{cases} w_m = \frac{1}{a^2} \int_{\Omega_c} w_c d\Omega \\ w_m^{\text{recalibration}} = \frac{1}{a^2} \int_{\Omega_c} w_c^{\text{recalibration}} d\Omega \end{cases} \quad (4.36)$$

Then

$$w_m^{\text{recalibration}} = \frac{1 + \kappa_E}{a^2} \int_{\Omega_c} w_c^{\text{recalibration}} d\Omega = (1 + \kappa_E)w_m \quad (4.37)$$

The proof for the kinetic energy is a bit more tricky. The computation of the values of the coefficients of the generalized kinetic energy is made by the correspondence of the dispersion curves along ΓX and ΓM . In the hypothesis of a perfect matching of the dispersion curves between the microstructured cell and the relaxed micromorphic medium, one can write

$$\omega_c^i(\mathbf{k}) = \omega_m^i(\mathbf{k}) \quad (4.38)$$

ω_c^i (resp. ω_m^i) being the eigenfrequency of the i -th mode of propagation of the microstructured cell (resp. the relaxed micromorphic medium). Once again, one can notice that

$$\rho_c^{\text{recalibration}} = (1 + \kappa_\rho)\rho_{\text{Ti}} \quad \Rightarrow \quad k_c^{\text{recalibration}} = (1 + \kappa_\rho)k_c \quad (4.39)$$

Let us write the Rayleigh quotient \mathcal{R}_c for the microstructured cell ($\Omega_c =$ architected unit cell given in Figure 3.6). For the sake of simplicity, Let us write

$$k_i = -\omega^2 \bar{k}_i \quad \text{for} \quad i = \{c, m\} \quad (4.40)$$

Then

$$\mathcal{R}_c(\mathbf{u}) = \frac{\int_{\Omega_c} w_c(\mathbf{u}) d\Omega}{\int_{\Omega_c} \bar{k}_c(\mathbf{u}) d\Omega} = \frac{\int_{\Omega_c} \langle \text{sym} \nabla \mathbf{u}, \mathbb{C} \text{sym} \nabla \mathbf{u} \rangle d\Omega}{\int_{\Omega_c} \langle \mathbf{u}, \rho_c \mathbf{u} \rangle d\Omega} \quad (4.41)$$

For the recalibrated microstructured cell, we have

$$\begin{aligned} \mathcal{R}_c^{\text{recalibrated}}(\mathbf{u}) &= \frac{\int_{\Omega_c} w_c^{\text{recalibrated}}(\mathbf{u}) d\Omega}{\int_{\Omega_c} \bar{k}_c^{\text{recalibrated}}(\mathbf{u}) d\Omega} \\ &= \frac{1 + \kappa_E}{1 + \kappa_\rho} \mathcal{R}_c(\mathbf{u}) \end{aligned} \quad (4.42)$$

In the same way, Let us define the Rayleigh ratio \mathcal{R}_m for the relaxed micromorphic model (as the dispersion curves are computed analytically straight through the local equilibrium equations, there's no need to integrate over the unit cell):

$$\begin{aligned} \mathcal{R}_m(\mathbf{u}, \mathbf{P}) &= \frac{w_m(\nabla \mathbf{u}, \mathbf{P})}{\bar{k}_m(\mathbf{u}, \nabla \mathbf{u}, \mathbf{P})} \\ &= \frac{\langle \text{sym}(\nabla \mathbf{u} - \mathbf{P}), \mathbb{C}_e \text{sym}(\nabla \mathbf{u} - \mathbf{P}) \rangle + \langle \text{sym} \mathbf{P}, \mathbb{C}_m \text{sym} \mathbf{P} \rangle + \langle \text{skew}(\nabla \mathbf{u} - \mathbf{P}), \mathbb{C}_c \text{skew}(\nabla \mathbf{u} - \mathbf{P}) \rangle}{\langle \mathbf{u}, \rho_m \mathbf{u} \rangle + \langle \text{sym} \mathbf{P}, \mathbb{J}_m \text{sym} \mathbf{P} \rangle + \langle \text{skew} \mathbf{P}, \mathbb{J}_c \text{skew} \mathbf{P} \rangle + \langle \text{sym} \nabla \mathbf{u}, \mathbb{T}_e \text{sym} \nabla \mathbf{u} \rangle + \langle \text{skew} \nabla \mathbf{u}, \mathbb{T}_c \text{skew} \nabla \mathbf{u} \rangle} \end{aligned} \quad (4.43)$$

We also have

$$\begin{aligned} \mathcal{R}_m^{\text{recalibrated}}(\mathbf{u}, \mathbf{P}) &= \frac{w_m^{\text{recalibrated}}(\mathbf{u}, \mathbf{P})}{\bar{k}_m^{\text{recalibrated}}(\mathbf{u}, \mathbf{P})} \\ &= \frac{1 + \kappa_E}{1 + \kappa_\rho} \mathcal{R}_m(\mathbf{u}, \mathbf{P}) \end{aligned} \quad (4.44)$$

For the i -th eigenvector ϕ_c^i of the microstructured cell (resp. ϕ_m^i and Φ_m^i for the relaxed micromorphic medium), one has

$$\begin{cases} \mathcal{R}_c(\phi_c^i, \mathbf{k}) = [\omega_c^i(\mathbf{k})]^2 \\ \mathcal{R}_m(\mathbf{u} = \phi_m^i, \mathbf{P} = \Phi_m^i, \mathbf{k}) = [\omega_m^i(\mathbf{k})]^2 \end{cases} \quad (4.45)$$

Having $\omega_c^i(\mathbf{k}) = \omega_m^i(\mathbf{k})$, the perfect matching of the dispersion curves between the microstructured cell and the relaxed micromorphic medium gives

$$\mathcal{R}_m(\phi_m^i, \Phi_m^i, \mathbf{k}) = \mathcal{R}_c(\phi_c^i, \mathbf{k}) \quad (4.46)$$

We can write

$$\begin{aligned} \mathcal{R}_m^{\text{recalibrated}}(\phi_m^i, \Phi_m^i, \mathbf{k}) &= \frac{1 + \kappa_E}{1 + \kappa_\rho} \mathcal{R}_m(\phi_m^i, \Phi_m^i, \mathbf{k}) \\ &= \frac{1 + \kappa_E}{1 + \kappa_\rho} \mathcal{R}_c(\phi_c^i, \mathbf{k}) \\ &= \mathcal{R}_c^{\text{recalibrated}}(\phi_c^i, \mathbf{k}) \end{aligned} \quad (4.47)$$

which gives

$$\omega_m^{\text{recalibrated}}(\mathbf{k}) = \omega_c^{\text{recalibrated}}(\mathbf{k}) \quad (4.48)$$

if the equality of the mode shapes of dispersion was verified, which is the case given the recalibration procedure considered here. Such assumption can be proven considering the eigenvalue problem solved by the Finite Element Method presented in Chapter 3.

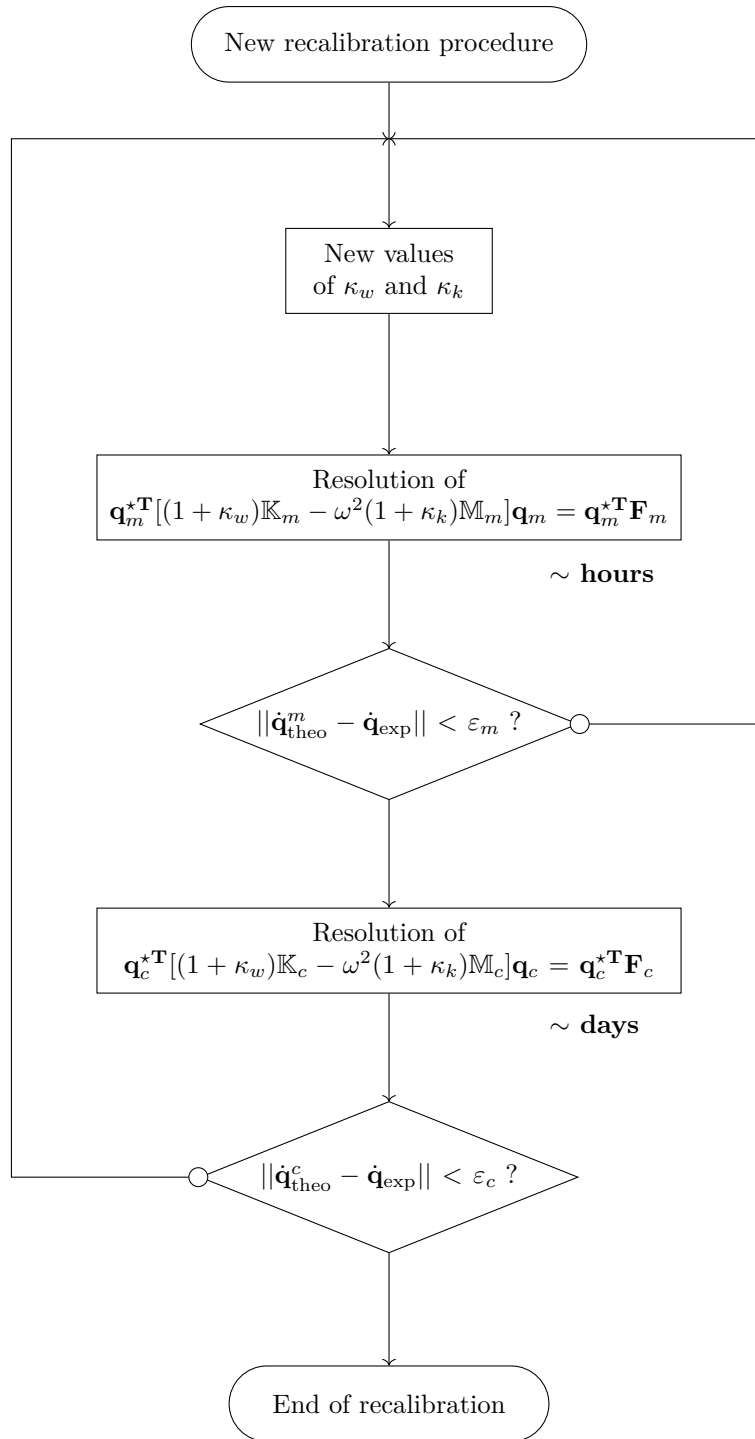


Figure 4.12: New recalibration algorithm using the relaxed micromorphic model to compute faster the fitting of the response of the microstructured plate. Two different stopping criteria associated to two maximum admissible differences ε_m and ε_c as, failing to respect the homogenization conditions given in Chapter 3, the relaxed micromorphic model will not, outside the band-gap, get as close as the microstructured model to the experimental response.

The relaxed micromorphic model was recalibrated on the experiment and the parameters of the microstructured model were then updated by the following rule:

$$\left\{ \begin{array}{l} \rho_c^{\text{recalibration}} = (1 + \kappa_k) \rho_{Ti} \\ E^{\text{recalibration}} = (1 + \kappa_w) E_{Ti} \end{array} \right. \longleftrightarrow \left\{ \begin{array}{l} \rho_m^{\text{recalibration}} = (1 + \kappa_k) \rho_m \\ \eta_i^{\text{recalibration}} = (1 + \kappa_k) \eta_i, i \in \llbracket 1, 3 \rrbracket \\ \eta_1^* \text{recalibration} = (1 + \kappa_k) \bar{\eta}_1^* \\ \bar{\eta}_i^{\text{recalibration}} = (1 + \kappa_k) \bar{\eta}_i, i \in \llbracket 1, 3 \rrbracket \\ \bar{\eta}_1^* \text{recalibration} = (1 + \kappa_k) \bar{\eta}_1^* \\ \lambda_i^{\text{recalibration}} = (1 + \kappa_w) \lambda_i, i \in \{e, m\} \\ \mu_i^{\text{recalibration}} = (1 + \kappa_w) \mu_i, i \in \{e, m\} \\ \mu_i^* \text{recalibration} = (1 + \kappa_w) \mu_i^*, i \in \{e, m\} \\ \mu_c^{\text{recalibration}} = (1 + \kappa_w) \mu_c \end{array} \right. \quad (4.49)$$

This technique is presented in the algorithm given in Figure 4.12: it allows to recalibrate faster our theoretical models upon the experimental results. Given the small size of the plate and of the excitation of the manufactured plate, such procedure was difficult to apply, making necessary the verification step where the response of the classical Cauchy model is computed (only once). This method would not be applicable if the considered structure was too large to be computed by the classical Cauchy model: fortunately, such case fulfill the requirements of the homogenization, allowing the relaxed micromorphic model to describe more accurately the response. This will be used in the following section of this chapter, where a such structure will be studied. Eventually, the action functional of the system introduced in 4.5 for the microstructured plate becomes

$$\mathcal{A}_{\text{int}}[\mathbf{u}, V] = \int_{t_1}^{t_2} \left[\int_{\Omega_p} (k_p - w_p - q) d\Omega + \frac{e}{2} \int_{\Omega_c} ((1 + \kappa_k) k_c - (1 + \kappa_w) w_c) d\Gamma \right] dt \quad (4.50)$$

For the relaxed micromorphic model, we have

$$\begin{aligned} \mathcal{A}_{\text{int}}[\mathbf{u}, \mathbf{P}, V] &= \int_{t_1}^{t_2} \int_{\Omega_p} (k_p - w_p - q) d\Omega dt \\ &+ \frac{e}{2} \int_{t_1}^{t_2} \left[\int_{\Omega_c} ((1 + \kappa_k) k_c - (1 + \kappa_w) w_c) d\Gamma + \int_{\Omega_m} ((1 + \kappa_k) k_m - (1 + \kappa_w) w_m) d\Gamma \right] dt \end{aligned} \quad (4.51)$$

Figure 4.13 present p_B and m_B for the original and recalibrated relaxed micromorphic model. We remark that, once calibrated, both the pointwise and the mean displacement describe well the local resonance occurring at the lower band-gap limit. As expected, the mean displacements for the relaxed micromorphic and microstructured model show better agreement than the pointwise displacement

Chapter 4. Confronting our models to the experiment

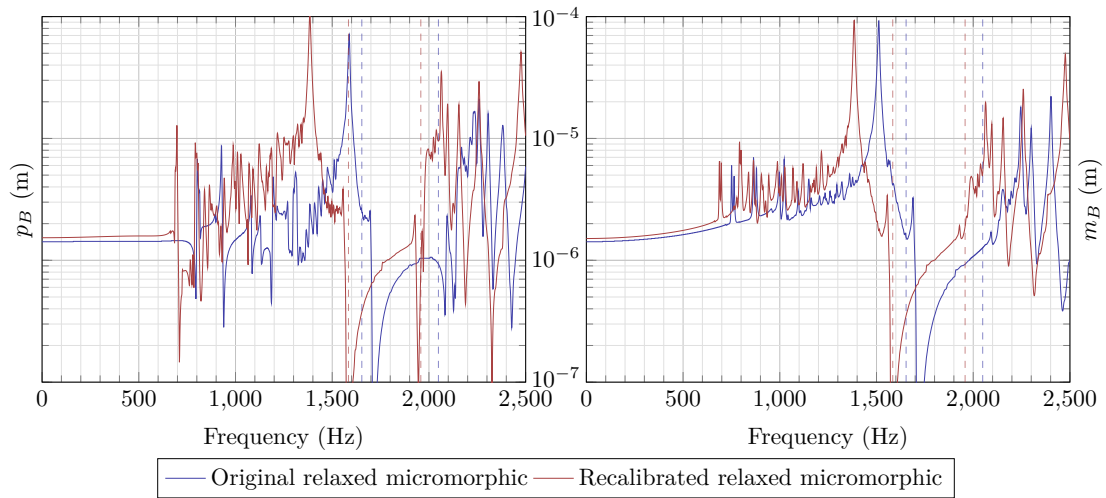


Figure 4.13: (*left*) Pointwise displacement p_B for the original and recalibrated relaxed micromorphic models at point B . (*right*) Mean displacement m_B for the original and recalibrated relaxed micromorphic models. The theoretical limits of the band-gap obtained via the Bloch-Floquet analysis for the original and recalibrated architected unit cell are given in dashed lines.

The perfect coincidence of the antiresonances at the beginning of the band gap between the microstructured plate and the relaxed micromorphic model, *i.e.* the accuracy of the recalibration procedure, is presented in Figure 4.14.

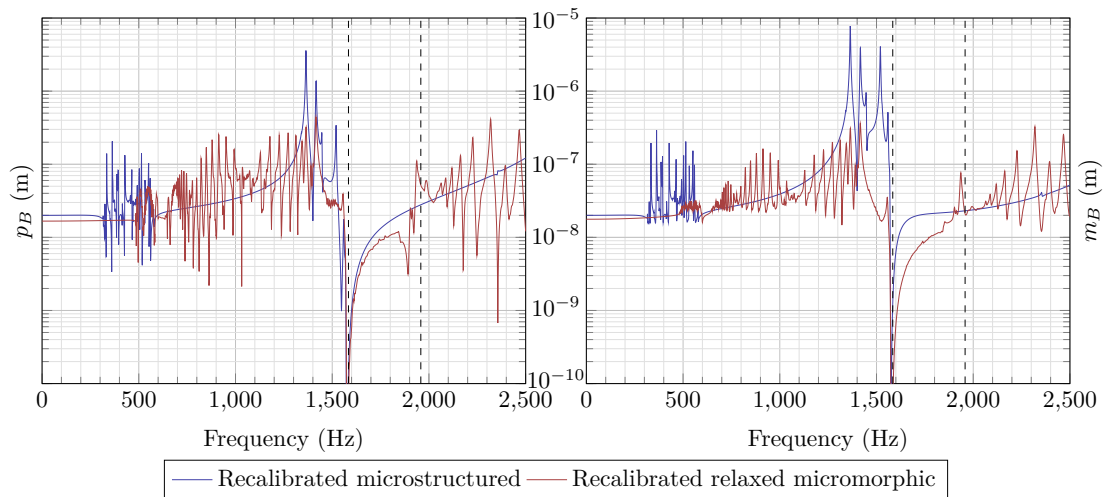


Figure 4.14: (*left*) Pointwise displacement p_B for the recalibrated microstructured and relaxed micromorphic models at point B . (*right*) Mean displacement m_B for the recalibrated microstructured and relaxed micromorphic models. The theoretical limits of the band-gap obtained via the Bloch-Floquet analysis for the original and recalibrated architected unit cell are given in dashed lines.

	Original unit cell	Recalibrated unit cell
Lower limit of the band gap	1715	1584
Upper limit of the band gap	2124	1958
Center of the band gap	1919	1771
Width of the band gap	409	374

Table 4.2: Characteristics of the theoretical limits of the band-gap obtained via the Bloch-Floquet analysis for the original and recalibrated architected unit cell.

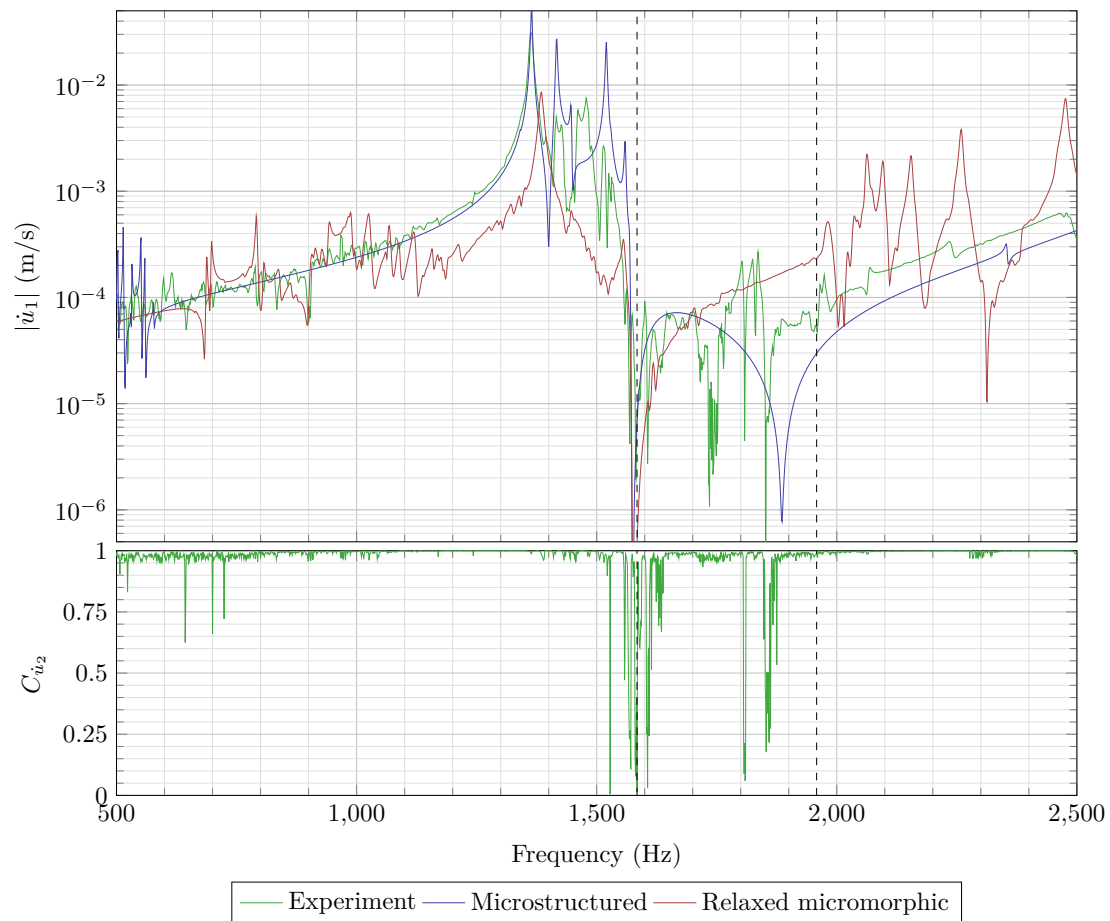


Figure 4.15: (top) $|\dot{u}_1|$ for C_1 for the experiment (green), the relaxed micromorphic (red) and the recalibrated microstructured models (blue). (bottom) Coherence of $|\dot{u}_1|$ for the experiment. The theoretical limits of the band-gap obtained via the Bloch-Floquet analysis for the recalibrated architected unit cell are given in dashed lines.

Figure 4.15 presents the experimental response of the plate and the theoretical response of both the microstructured plate and the relaxed micromorphic model. One can appreciate the efficacy of our recalibration procedure, despite the non-conformity of the plate to the homogenization conditions given in Chapter 3, the

ability of the relaxed micromorphic model to describe the most characteristic aspect of our band gap material, *i.e.* the collapse of the response of the plate at the lower bound of the theoretical band-gap. Nevertheless, one can notice the experimental response not to be as “sharp” as the theoretical ones: if the small damping considered for our simulations may explain, to some extent, this difference, we will show that this phenomenon can be explained by taking into account the manufacturing defects occurring in the plate.

4.3 Perturbating the model

For now, we “corrected” our theoretical systems, taking into account, among others, the inaccuracy of the plane strain hypothesis. However, the following points still has not been investigated:

- the idealization of geometry
- the idealization of constitutive laws

One can remember that the band-gap effect is obtained by the repetition, in one, two or three directions of space, of a microstructured unit cell: in practice, such hypothesis supposing uniform paving is not verified, due to manufacturing defect and the variation of the mechanical properties through the plate. Rather than modifying the geometry, we incorporated the manufacturing defects, *i.e.* the variation of the unit cell geometry through the plate, in the variation of mechanical properties, in formulas:

$$\begin{cases} \rho_c(\mathbf{x}) = (1 + \theta_\rho(\mathbf{x}))\rho_c^{\text{recalibration}} = (1 + \theta_\rho(\mathbf{x}))(1 + \kappa_k)\rho_{Ti} \\ E(\mathbf{x}) = (1 + \theta_E(\mathbf{x}))E^{\text{recalibration}} = (1 + \theta_E(\mathbf{x}))(1 + \kappa_w)E_{Ti} \end{cases} \quad (4.52)$$

Where θ_E et θ_ρ both follow a zero-mean probability law.

More subtly, perfectly generalizing the linear perturbation of the potential and kinetic energy densities of the microstructured system, each of the inertial operators and constitutive laws describing the relaxed micromorphic medium are disturbed:

$$\begin{cases} \rho_m(\mathbf{x}) = (1 + \theta_1(\mathbf{x}))\rho_m^{\text{recalibration}} = (1 + \theta_1(\mathbf{x}))(1 + \kappa_k)\rho_m \\ \mathbb{J}_m(\mathbf{x}) = (1 + \theta_2(\mathbf{x}))\mathbb{J}_m^{\text{recalibration}} = (1 + \theta_2(\mathbf{x}))(1 + \kappa_w)\mathbb{J}_m \\ \mathbb{T}_e(\mathbf{x}) = (1 + \theta_3(\mathbf{x}))\mathbb{T}_e^{\text{recalibration}} = (1 + \theta_3(\mathbf{x}))(1 + \kappa_w)\mathbb{T}_e \\ \mathbb{C}_e(\mathbf{x}) = (1 + \theta_4(\mathbf{x}))\mathbb{C}_e^{\text{recalibration}} = (1 + \theta_4(\mathbf{x}))(1 + \kappa_w)\mathbb{C}_e \\ \mathbb{C}_m(\mathbf{x}) = (1 + \theta_5(\mathbf{x}))\mathbb{C}_m^{\text{recalibration}} = (1 + \theta_5(\mathbf{x}))(1 + \kappa_w)\mathbb{C}_m \\ \mathbb{J}_c(\mathbf{x}) = (1 + \theta_6(\mathbf{x}))\mathbb{J}_c^{\text{recalibration}} = (1 + \theta_6(\mathbf{x}))(1 + \kappa_w)\mathbb{J}_c \\ \mathbb{T}_c(\mathbf{x}) = (1 + \theta_7(\mathbf{x}))\mathbb{T}_c^{\text{recalibration}} = (1 + \theta_7(\mathbf{x}))(1 + \kappa_w)\mathbb{T}_c \\ \mathbb{C}_c(\mathbf{x}) = (1 + \theta_8(\mathbf{x}))\mathbb{C}_c^{\text{recalibration}} = (1 + \theta_8(\mathbf{x}))(1 + \kappa_w)\mathbb{C}_c \end{cases} \quad (4.53)$$

Each θ_i , $i \in \llbracket 1, 8 \rrbracket$ follows an uniform law corresponding to a variation of $\pm 5\%$ around the deterministic value. Figure 4.16 presents the continuous uniform distributions used for our models, making the mechanical parameters vary of $\pm 5\%$ around their deterministic value.

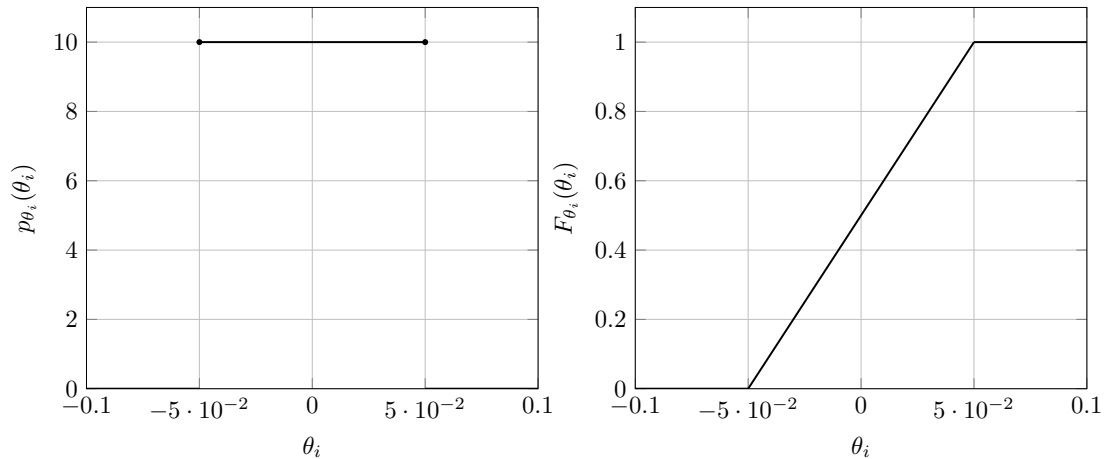


Figure 4.16: (left) Probability density function used for the θ_i and (right) its distribution function used for the cauchy and the relaxed micromorphic model.

Several strategies of perturbation may have been considered to take into account the manufacturing process of the microstructured plate. Since no strategy has been yet, to our knowledge, being developed for the relaxed micromorphic model, we chose to use “simple” probability laws to facilitate its comparison with the classical Cauchy model.

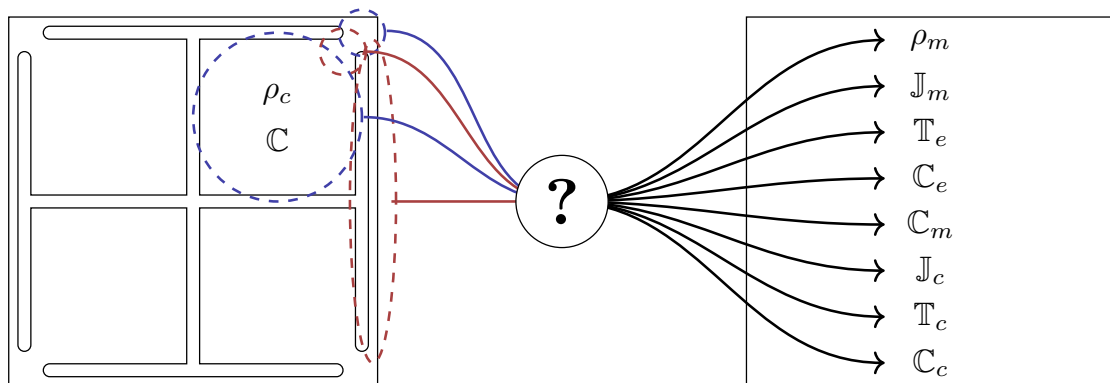


Figure 4.17: Equivalence between the (left) microstructured unit cell and the (right) relaxed micromorphic parameters, *red* corresponding to spring-like elements and *blue* to mass-like elements.

By perturbing one by one each of the constitutive tensors of the relaxed micromorphic model, one could investigate how each parameter of the relaxed micromorphic model correspond to the geometrical parameters of the microstructured

Chapter 4. Confronting our models to the experiment

unit cell.

Let us go back to our theoretical models: as the static and dynamic parameters randomly varying through the plate, the former x_1 and x_2 symmetries cannot be used anymore to reduce the size of the system. The considered structures are presented in Figures 4.18.

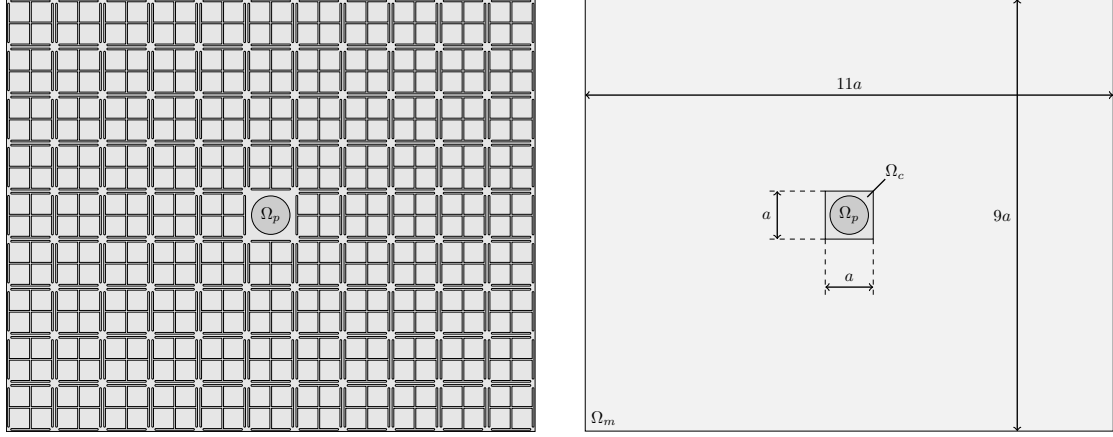


Figure 4.18: (left) Top view of the microstructured plate. (right) Top view of the relaxed micromorphic plate.

To eliminate rigid body moves of these two structures, homogeneous Dirichlet boundary conditions have to be applied to the system to u_1 and u_2 . At first, translations are prevented by immobilizing the plate's central point:

$$\mathbf{u}(\mathbf{x} = \mathbf{0}) = \mathbf{0} \quad (4.54)$$

"Residual rotations" around the center are suppressed by imposing the additional constrain

$$u_2(x_1 = a/2, x_2 = 0) = 0 \quad (4.55)$$

No additional boundary conditions needs to be prescribed upon \mathbf{P} for the relaxed micromorphic medium. The action functional for the microstructured plate presented in 4.18 is

$$\begin{aligned} \mathcal{A}_{\text{int}}[\mathbf{u}, V] = & \int_{t_1}^{t_2} \int_{\Omega_p} \left[\frac{1}{2} \langle \dot{\mathbf{u}}, \rho \dot{\mathbf{u}} \rangle - \frac{1}{2} \langle \text{sym } \nabla \mathbf{u}, \mathbb{C} \text{sym } \nabla \mathbf{u} + \xi^T \mathbf{E} \rangle - \frac{1}{2} \langle \mathbf{E}, \varepsilon_0 \varepsilon \mathbf{E} + \xi \text{sym } \nabla \mathbf{u} \rangle \right] d\Omega dt \\ & + \frac{e}{2} \int_{t_1}^{t_2} \int_{\Omega_c} \left[\frac{1}{2} (1 + \theta_\rho)(1 + \kappa_k) \langle \dot{\mathbf{u}}, \rho_c \dot{\mathbf{u}} \rangle - \frac{1}{2} (1 + \theta_E)(1 + \kappa_w) \langle \text{sym } \mathbf{u}, \mathbb{C} \text{sym } \mathbf{u} \rangle \right] d\Gamma dt \end{aligned} \quad (4.56)$$

For the relaxed micromorphic plate, the action functional corresponding to the

model implemented in *Comsol Multiphysics*[®] is:

$$\begin{aligned}
\mathcal{A}_{\text{int}}[\mathbf{u}, \mathbf{P}, V] = & \int_{t_1}^{t_2} \int_{\Omega_p} \left[\frac{1}{2} \langle \dot{\mathbf{u}}, \rho \dot{\mathbf{u}} \rangle - \frac{1}{2} \langle \text{sym } \nabla \mathbf{u}, \mathbb{C} \text{sym } \nabla \mathbf{u} + \xi^T \mathbf{E} \rangle - \frac{1}{2} \langle \mathbf{E}, \varepsilon_0 \boldsymbol{\varepsilon} \mathbf{E} + \xi \text{sym } \nabla \mathbf{u} \rangle \right] d\Omega dt \\
& + \frac{e}{2} \int_{t_1}^{t_2} \int_{\Omega_c} \left[\frac{1}{2} (1 + \theta_\rho)(1 + \kappa_k) \langle \dot{\mathbf{u}}, \rho_c \dot{\mathbf{u}} \rangle - \frac{1}{2} (1 + \theta_E)(1 + \kappa_w) \langle \text{sym } \mathbf{u}, \mathbb{C} \text{sym } \mathbf{u} \rangle \right] d\Gamma dt \\
& + \frac{e}{2} \int_{t_1}^{t_2} \int_{\Omega_m} \frac{1}{2} (1 + \theta_1)(1 + \kappa_k) \langle \dot{\mathbf{u}}, \rho_m \dot{\mathbf{u}} \rangle d\Gamma dt \\
& + \frac{e}{2} \int_{t_1}^{t_2} \int_{\Omega_m} \left[\frac{1}{2} (1 + \theta_2)(1 + \kappa_k) \langle \text{sym } \dot{\mathbf{P}}, \mathbb{J}_m \text{sym } \dot{\mathbf{P}} \rangle + \frac{1}{2} (1 + \theta_3)(1 + \kappa_k) \langle \text{skew } \dot{\mathbf{P}}, \mathbb{J}_c \text{skew } \dot{\mathbf{P}} \rangle \right] d\Gamma dt \\
& + \frac{e}{2} \int_{t_1}^{t_2} \int_{\Omega_m} \left[\frac{1}{2} (1 + \theta_4)(1 + \kappa_k) \langle \text{sym } \nabla \dot{\mathbf{u}}, \mathbb{T}_e \text{sym } \nabla \dot{\mathbf{u}} \rangle + \frac{1}{2} (1 + \theta_5)(1 + \kappa_k) \langle \text{skew } \nabla \dot{\mathbf{u}}, \mathbb{T}_c \text{skew } \nabla \dot{\mathbf{u}} \rangle \right] d\Gamma dt \\
& - \frac{e}{2} \int_{t_1}^{t_2} \int_{\Omega_m} \frac{1}{2} (1 + \theta_6)(1 + \kappa_w) \langle \text{sym}(\nabla \mathbf{u} - \mathbf{P}), \mathbb{C}_e \text{sym}(\nabla \mathbf{u} - \mathbf{P}) \rangle d\Gamma dt \\
& - \frac{e}{2} \int_{t_1}^{t_2} \int_{\Omega_m} \frac{1}{2} (1 + \theta_7)(1 + \kappa_w) \langle \text{sym } \mathbf{P}, \mathbb{C}_m \text{sym } \mathbf{P} \rangle d\Gamma dt \\
& - \frac{e}{2} \int_{t_1}^{t_2} \int_{\Omega_m} \frac{1}{2} (1 + \theta_8)(1 + \kappa_w) \langle \text{skew}(\nabla \mathbf{u} - \mathbf{P}), \mathbb{C}_c \text{skew}(\nabla \mathbf{u} - \mathbf{P}) \rangle d\Gamma dt
\end{aligned} \tag{4.57}$$

Figures 4.19, 4.20 and 4.21 present the comparison between the deterministic and stochastic microstructured plate and relaxed micromorphic model.

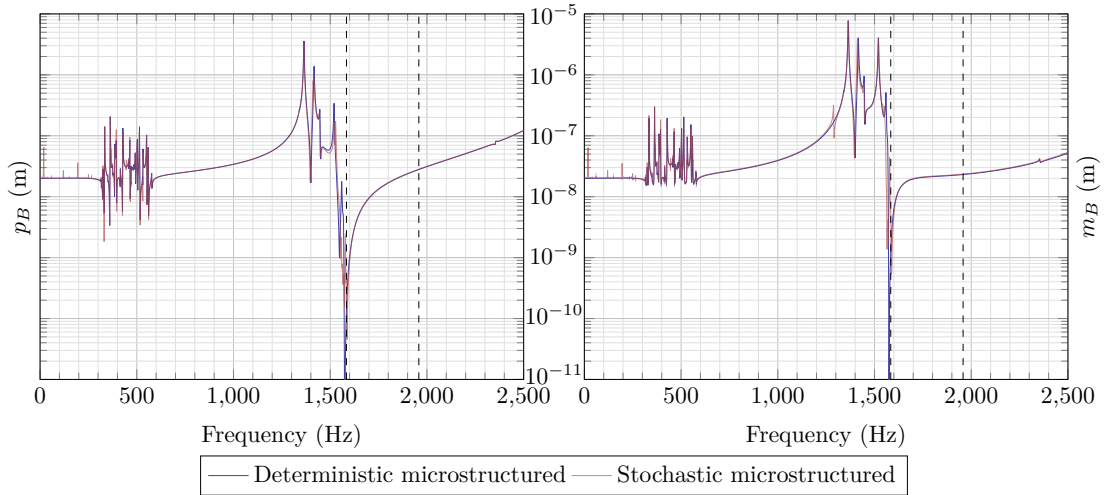


Figure 4.19: (*left*) Pointwise displacement p_B for the recalibrated deterministic (*blue*) and stochastic (*red*) microstructured models. (*right*) Mean displacement m_B for the recalibrated deterministic (*blue*) and stochastic (*red*) microstructured models. The theoretical limits of the band-gap obtained via the Bloch-Floquet analysis for the recalibrated architected unit cell are given in dashed lines.

Chapter 4. Confronting our models to the experiment

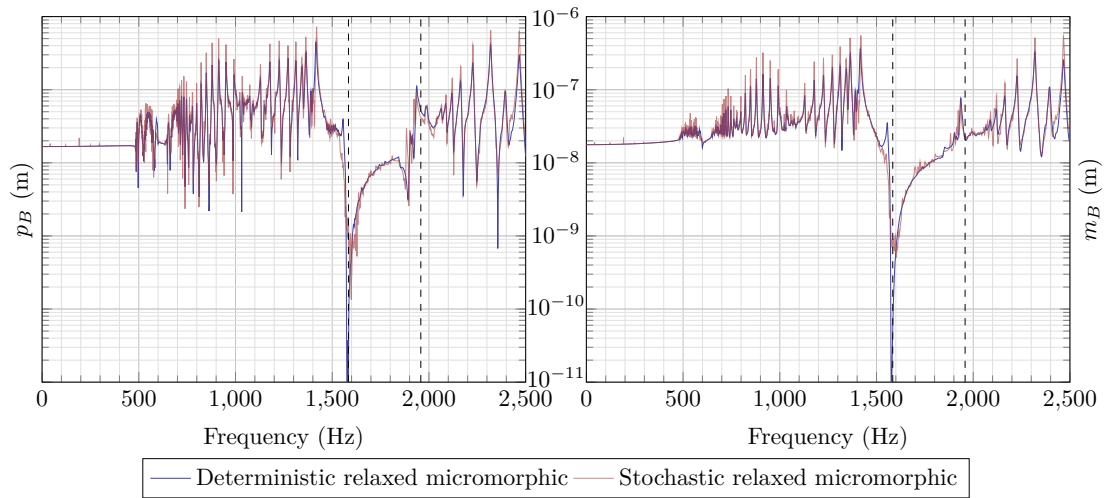


Figure 4.20: (*left*) Pointwise displacement p_B for the recalibrated deterministic (*blue*) and stochastic (*red*) relaxed micromorphic models. (*right*) Mean displacement m_B for the recalibrated deterministic (*blue*) and stochastic (*red*) relaxed micromorphic models. The theoretical limits of the band-gap obtained via the Bloch-Floquet analysis for the recalibrated architected unit cell are given in dashed lines.

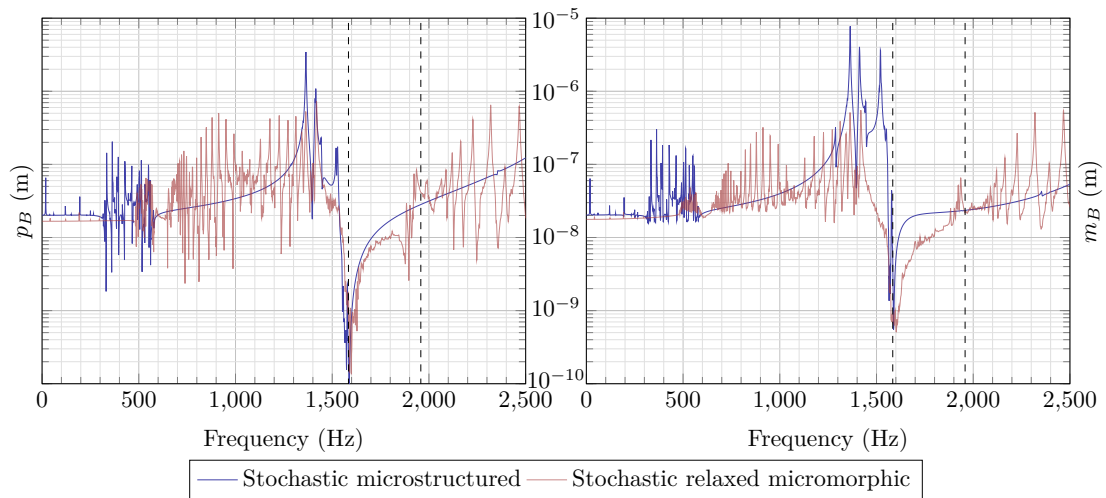


Figure 4.21: (*left*) Pointwise displacement p_B for the recalibrated deterministic stochastic microstructured (*blue*) and relaxed micromorphic (*blue*) models. (*right*) Mean displacement m_B for the recalibrated stochastic microstructured (*blue*) and relaxed micromorphic (*red*) models. The theoretical limits of the band-gap obtained via the Bloch-Floquet analysis for the recalibrated architected unit cell are given in dashed lines.

Outside the band-gap, perturbation of the structures have two main consequences:

- the appearance of parasitic modes due (for some of them) to the loss of symmetry,

- the “erosion” of the pre-existing structural modes.

These observations can be made for both the microstructured and the relaxed micromorphic models. The “depth” of the band gap is considerably reduced by the introduction of perturbation, may be explained saying that, each cell, for the microstructured model, having lightly different resonance frequency, only a few of those frequencies are close enough from the considered frequency for the cell to fully resonate, *i.e.* concentrating locally the energy. Inversely, the set of resonance frequencies no longer being reduced to a singleton widen the band-gap: Figure 4.22 present this effect observed through the FRF of, once again, the FRF of an microstructured beam under a traction/compression load. To understand clearly, one can define H_n^t and H_n^r for the n^{th} cell of the beam:

$$\begin{aligned} H_n^t &= \frac{\sqrt{\langle \bar{\mathbf{u}}, \mathbf{u} \rangle(x_1 = na, x_2 = 0)}}{\sqrt{\langle \bar{\mathbf{u}}, \mathbf{u} \rangle(x_1 = (n-1)a, x_2 = 0)}} \\ H_n^r &= \frac{\sqrt{\langle \bar{\mathbf{u}}, \mathbf{u} \rangle(x_1 = (n-1/4)a, x_2 = a/2)}}{\sqrt{\langle \bar{\mathbf{u}}, \mathbf{u} \rangle(x_1 = (n-1)a, x_2 = 0)}} \end{aligned} \quad (4.58)$$

We can also define the width Δf_r and depth ΔH of the band-gap, respectively characterizing the frequency range where the attenuation of the response of our structure exceeds a given ratio r (*e.g.* $\sqrt{2}$, corresponding to a division by 2 of the transmitted energy) and the maximum collapse of the response of the plate in this considered frequency range, in formulas:

$$\begin{cases} \Delta f_r &= \omega_2 - \omega_1 & \text{where} & (w_1, w_2) = \left\{ \omega \in [\omega_1, \omega_2] : \frac{H(\omega = 0)}{H(\omega)} \leq r \right\} \\ \Delta H &= \frac{H(\omega = 0)}{\min_{\omega \in [\omega_1, \omega_2]} H(\omega)} \end{cases} \quad (4.59)$$

How $H : \omega \mapsto H(\omega)$ should be chosen depends on the structure: we chose, through this manuscript, alternatively pointwise or average transfert functions. For this section, we set

$$H = p_B \quad \text{and} \quad r = \sqrt{2} \quad (4.60)$$

Chapter 4. Confronting our models to the experiment

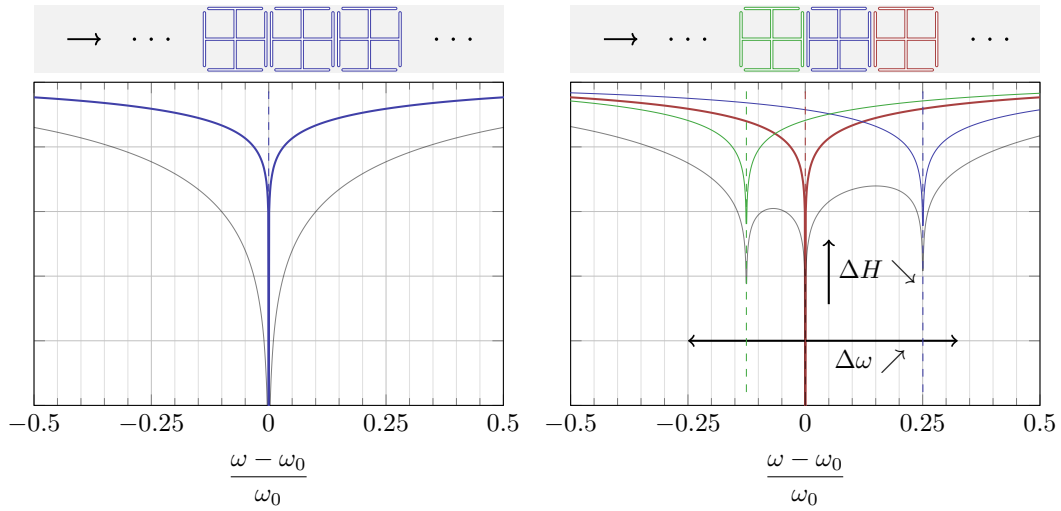


Figure 4.22: (*left, top*) Beam composed of three non-disturbed architected cells (*i.e.* identical) under a axial load with (*left, bottom*) their frequency response function $H_1^t = H_t = H_2^t = H_3^t$ (green, blue and red) and the global response $H_1^t H_2^t H_3^t = H_t^3$ (black). (*right, top*) Beam composed of three different architected cells under a axial load with (*right, bottom*) their respective frequency response function H_1^t, H_2^t and H_3^t (green, blue and red) and the global response $H_1^t H_2^t H_3^t$ (black).

The influence of the introduced perturbation in our structures is presented in Table 4.3.

		$\frac{\Delta\omega}{\sqrt{2}}$	ΔH
		[Hz]	-
Microstructured	Deterministic structure	206	$\geq 10^6$
	Stochastic structure	219	50
Relaxed micromorphic	Deterministic structure	262	$\geq 1.6 \cdot 10^5$
	Stochastic structure	282	33.2

Table 4.3: Band gap characteristics of the structures presented in Figures 4.5 and 4.18.

Due to the small size of the considered system ($n_1 = 11, n_2 = 9$), this widening is only visible in the core of the band-gap. One can also notice, for the microstructured model, a parasitic resonance in the band-gap, corresponding to the local resonance of the cell whose frequency now differs from those near close to the excitation: cells “far” from the center of the plate, previously “in the shadow” of the central

cells resonances, are now distinct in the perturbed system. This phenomenon is presented in Figure 4.23. It also explains how the band gap can be experimentally measured despite the local resonance of each square of the unit cells. Such effect do not appear for larger structures, where the large number of cells and the increasing density of resonance frequency as the probability to find several cells (between the excitation and the considered one) who resonances are close enough to the latter one erase such local resonance far from the excitation. This is visible on the relaxed micromorphic model where, if the band gap width's and depth are necessarily limited by the small size of the system, the homogenized medium mimics a considerable number of cells.

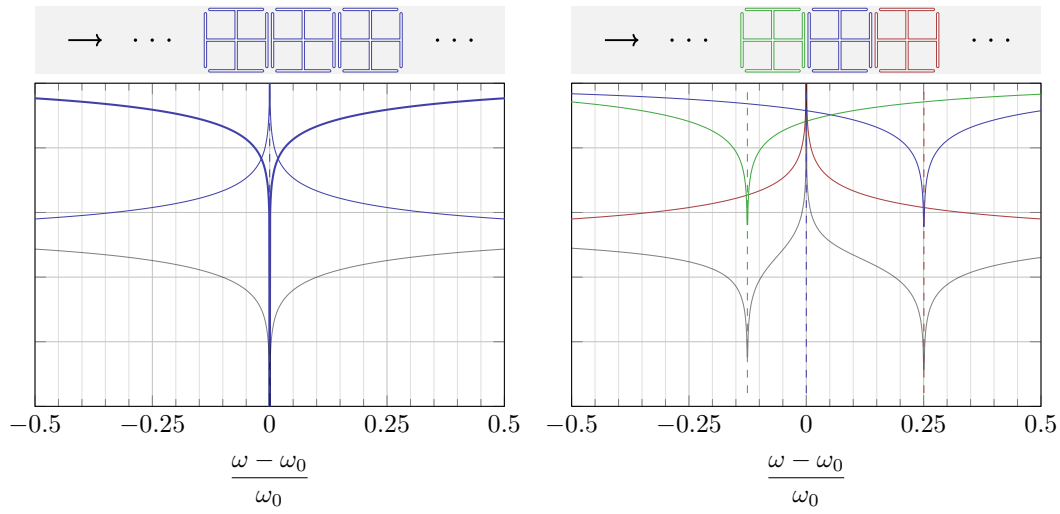


Figure 4.23: (left, top) Beam composed of three non-disturbed architectural cells (*i.e.* identical) under a axial load with (left, bottom) their frequency response function $H_1^t = H_t = H_2^t$ and H_3^r (green, blue and red) and $H_1^t H_2^t H_3^r = H_t^2 H_r$ (black). (right, top) Beam composed of three disturbed architectural cells under a axial load with (right, bottom) their respective frequency response function H_1^t, H_2^t and H_3^r (green, blue and red) and $H_1^t H_2^t H_3^r$ (black).

For once, one has to take into account the discretization of the system done by the Finite Element method: if the theoretical eigenfrequency is the same for each of the 396 of the 11×9 cells plate, an irregular meshing of the microstructured plate would lead to introduce some “artificial” perturbation in the plate, different meshes generating slightly different resonators and, consequently, different eigenfrequencies in the plate. A special attention has been brought to the mesh of the microstructured plate, where the same mesh has been used for every resonator in the plate. From Figure 4.1 and section 4.1, one can focus on four particular points which response in the two directions of the plane are presented in Figures 4.25, 4.26, 4.27 and 4.28. The position of those points have been presented in Figure 4.1.

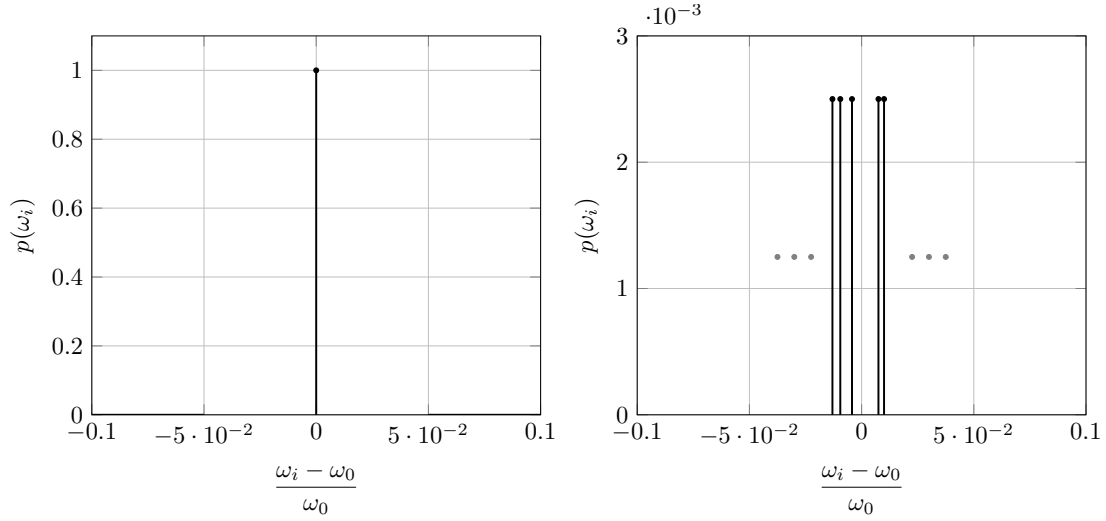


Figure 4.24: (left) Distribution of the normalized eigenfrequency of each resonator for the deterministic system (for the analytical model). (right) Distribution of the normalized eigenfrequency for some of the 396 resonators of the disturbed plate. w_i is the eigenfrequency of the i^{th} resonator and w_0 the theoretical eigenfrequency of the deterministic unit cell.

4.4 Comparison with the experiment

Given the strong directivity of our structure, we switch the plotting of $\langle \bar{\mathbf{u}}, \mathbf{u} \rangle$ for the plotting of its components, *i.e.*

- \dot{u}_1 for C_1 and C_2
- \dot{u}_2 for C_3 and C_4

Moreover, given the small size of both the plate and the excitation, degrading the results for the relaxed micromorphic model, the theoretical displacement orthogonal to the main direction of displacement would present a slightly difference from the experiment, as the displacement along x_2 for C_1 and C_2 (respectively x_1 for C_3 and C_4) for the relaxed micromorphic model is mostly due to the Poisson effect, while it is, for the microstructured model, due to the rotation of the considered resonator. As $\mathbf{u} \in \mathbb{C}^2$, we define

$$\begin{cases} |\dot{u}_k| = 2\pi f \sqrt{u_k \bar{u}_k} \\ \phi_{\dot{u}_k} = \arg(\dot{u}_k) \end{cases} \quad (4.61)$$

which, as we introduced in Chapter 2, are the amplitude and the phase of \dot{u}_k . We still present the coherence of the experimental signal: if it cannot be compared to the theoretical responses of the microstructured plate nor the relaxed micromorphic model (where we would have $C_{\dot{u}_k} = 1, \forall f \in [0, 2500]$ Hz, in the hypothesis of linearity), it can still be superposed of the theoretical position of the recalibrated band-gap of the architected unit cell.

4.4.1 Point-to-point displacement comparison

Figure 4.25 shows a really good correspondence between the two theoretical models and the experimental measures both on the amplitudes and on the general appearance: the first structural mode around 1300 Hz and the amplitude drop characteristic of the band gap at 1600 Hz being correctly described. One can notice the fall of coherence around 1600 and 1850 Hz, corresponding to the considerable decrease of the amplitude, characteristic of the band-gap. The phase switch between the first structural mode of the system at 1300 Hz and the second anti-resonance in the band-gap (1850 Hz) is observable for the experiment and the microstructured model, while the relaxed micromorphic, due to the small size of the plate and excitation size, can only predict this phase switch till the first anti-resonance in the band-gap.

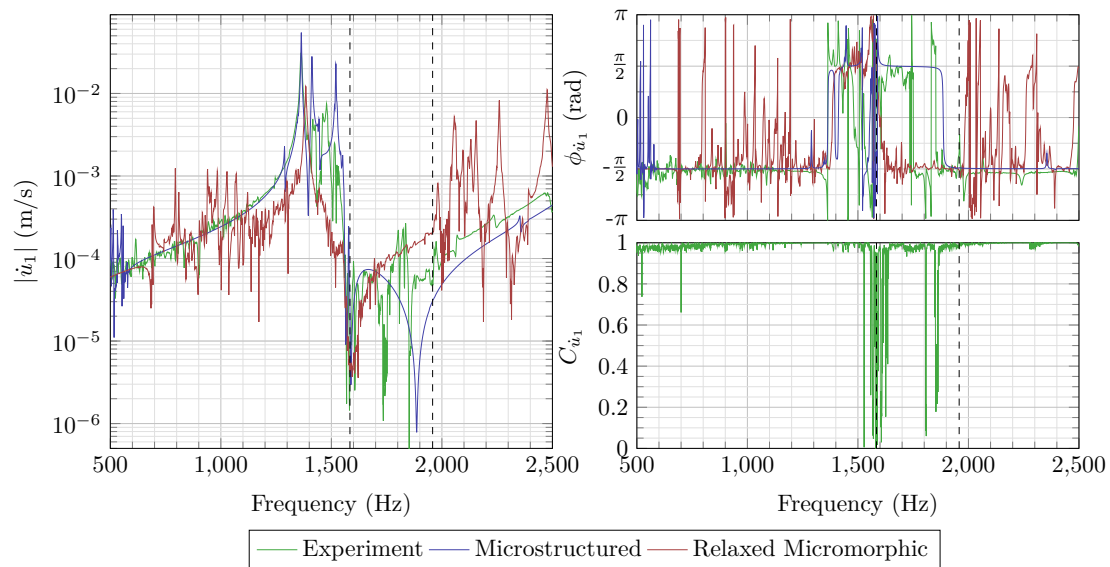


Figure 4.25: (left) Amplitude of \dot{u}_1 at C_1 (see Fig. 4.1 for the definition of this point) for the experiment, the microstructured and relaxed micromorphic models. (right, top) Phase of \dot{u}_1 at C_1 for the experiment, the microstructured and relaxed micromorphic model. (right, bottom) Coherence of \dot{u}_1 at C_1 for the experiment.

The coherence decrease around 1600 Hz is the signature of the band-gap: this fall is not due to the antiresonance, the sine swipe being slow enough not to decrease the coherence at the passage of the modes of the system, the coherence staying at its maximal value while crossing the first structural mode at 1364 Hz, but to the non-correlation of the measure with the excitation at the considered frequency. A resonance can also be observed for the experiment and the microstructured model at the beginning of the band-gap around 1600 Hz. The collapse of the response of the points far from the piezoelectric excitation, being due to the band-gap effect, *i.e.* the resonance of the inner squares of the cells composing the plate. Due to the perturbation added to the microstructured model, the resonance of every square

Chapter 4. Confronting our models to the experiment

of the structure do not occur anymore at the same frequency, having two effects:

- the widening of the anti-resonance at the beginning of the band-gap
- the shallower depth of this anti-resonance

This second effect mimicks an artificial additional damping for this mode. C_1 being at the center of a resonator, one can observe the resonance of this square, whose frequency is not, due to the perturbation on the system, is not aligned anymore with the other resonators, and can therefore be measured. The same phenomenon can be observed for the experiment, where the perturbation is given, in addition to spatial variations of the Young modulus and density, of the imperfection of geometry and boundary conditions across the plate.

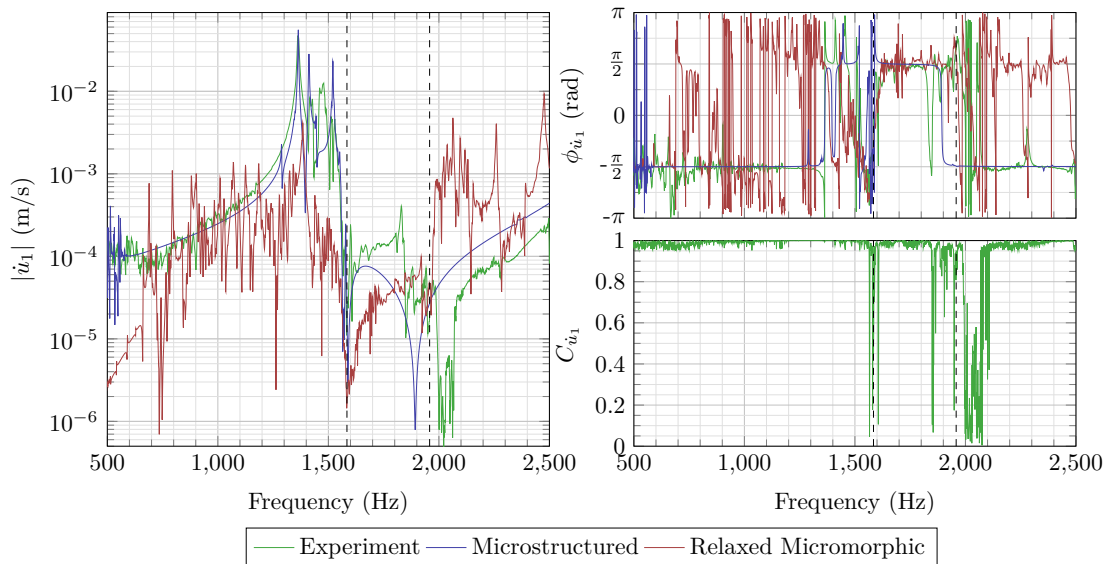


Figure 4.26: (left) Amplitude of \dot{u}_1 at C_2 (see Fig. 4.1 for the definition of this point) for the experiment, the microstructured and relaxed micromorphic models. (right, top) Phase of \dot{u}_1 at C_2 for the experiment, the microstructured and relaxed micromorphic models. (right, bottom) Coherence of \dot{u}_1 at C_2 for the experiment.

Getting away from the x_1 symmetry plane, the relaxed micromorphic model, despite its difficulties to predict the right amplitudes of the experimental system, successfully describes the first structural mode and the first anti-resonance at the beginning of the band-gap. The microstructured model predicts almost perfectly the experiment as shown in Figure 4.27, proving the interest of the recalibration. The perturbation of the system is once again visible in the band-gap, where the decrease of the depth of the band-gap and the resonance of the measured square can be observed.

For C_3 and C_4 , the main direction of displacement became x_2 : u_1 and u_2 having close to symmetrical roles compared to C_1 and C_2 , which would be the case (with

small phase sign change) if $m = n$. For that reason, we present the responses at C_3 and C_4 only in the x_2 direction.

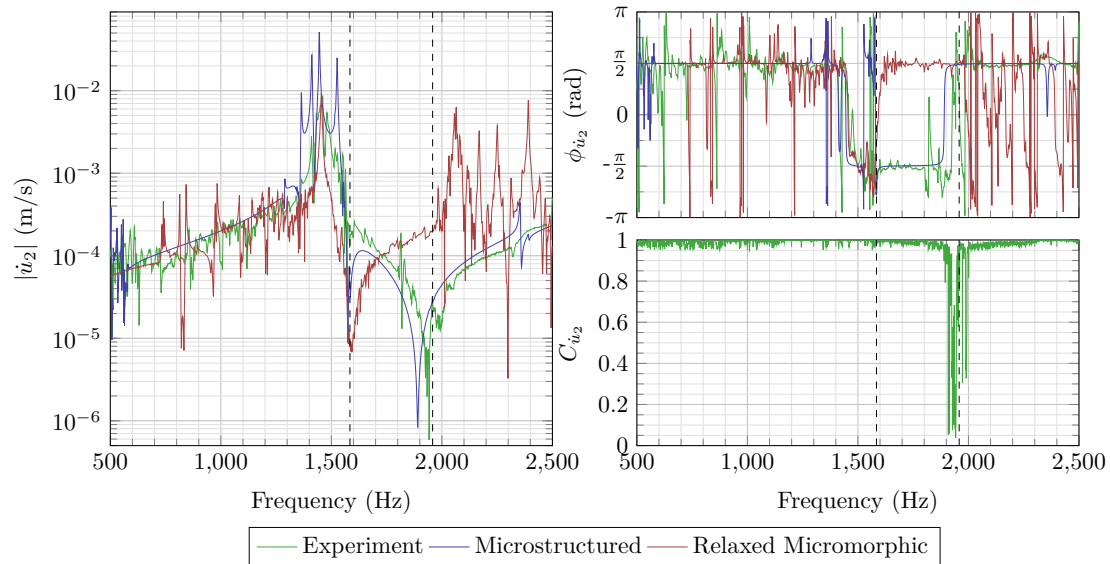


Figure 4.27: (*left*) Amplitude of \dot{u}_2 at C_3 (see Fig. 4.1 for the definition of this point) for the experiment, the microstructured and relaxed micromorphic models. (*right, top*) Phase of \dot{u}_2 at C_3 for the experiment, the microstructured and relaxed micromorphic models. (*right, bottom*) Coherence of \dot{u}_2 at C_3 for the experiment.

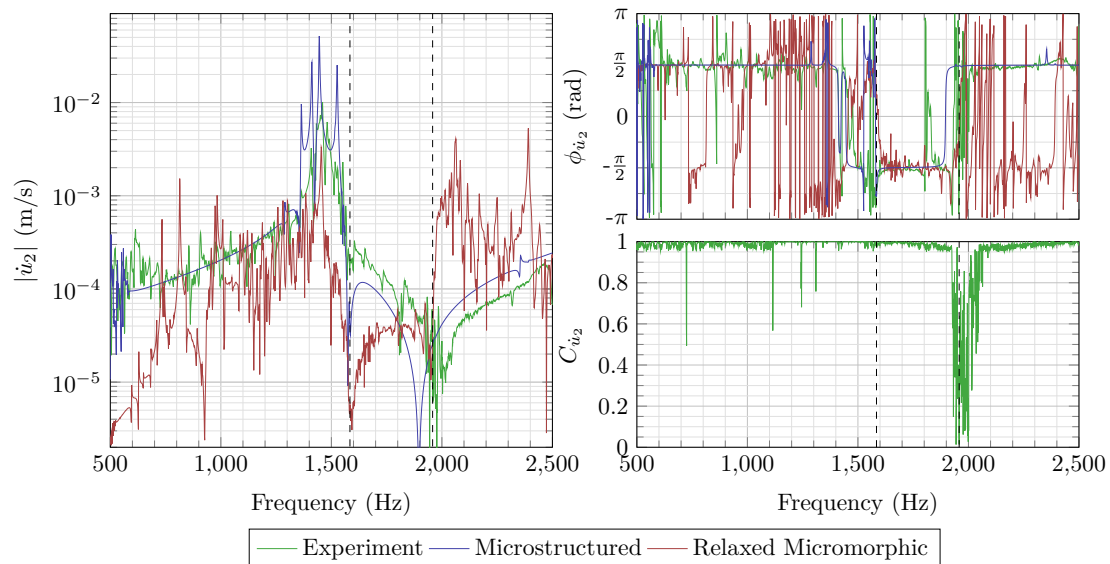


Figure 4.28: (*left*) Amplitude of \dot{u}_2 at C_4 (see Fig. 4.1 for the definition of this point) for the experiment, the microstructured and relaxed micromorphic models. (*right, top*) Phase of \dot{u}_2 at C_4 for the experiment, the microstructured and relaxed micromorphic models. (*right, bottom*) Coherence of \dot{u}_2 at C_4 for the experiment.

Chapter 4. Confronting our models to the experiment

Figures 4.27 and 4.28 show clearly the phase sign change between the first structural mode of the system and the second anti-resonance at the end of the band-gap (from 1350 to 1900 Hz) for both theoretical models and the experiment even if, as said previously, the small dimensions at the experimental set do not allow to predict the second anti-resonance of the system at the end of the band-gap. The recalibration of the deterministic model also shows its efficiency by the prediction of the second anti-resonance at the end of the band-gap (from 1900 to 2000 Hz).

4.4.2 2D response of the plate

Figures 4.29, 4.30 and 4.31 present the speed field across the plate for the experiment with the microstructured model. The structural mode at 1364 Hz along the x_1 axis is shown in Figure 4.29, where the effects of the recalibration of the theoretical system can be appreciated.

As only a quarter of the plate has been instrumented (by the imposition of reflector patches), corresponding to approximately 200 points measured one by one, the displacement has been symmetrized to represent the whole system. For that reason, the experimental response may appear as falsely symmetrical, especially in the heart of the band gap where the influence of the defects breaks significantly the symmetries of the plate.

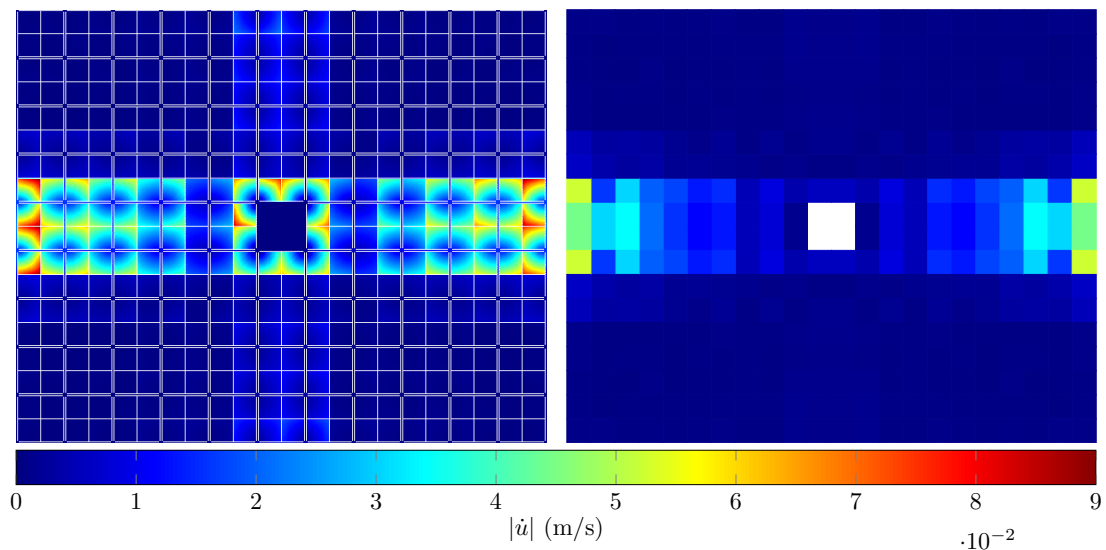


Figure 4.29: $|\dot{u}|$ (in m/s) at 1365 Hz for the microstructured model (*left*) and for the symmetrized experimental system (*right*), each square representing the speed at the center of the resonator of the 1/4 of cell considered.

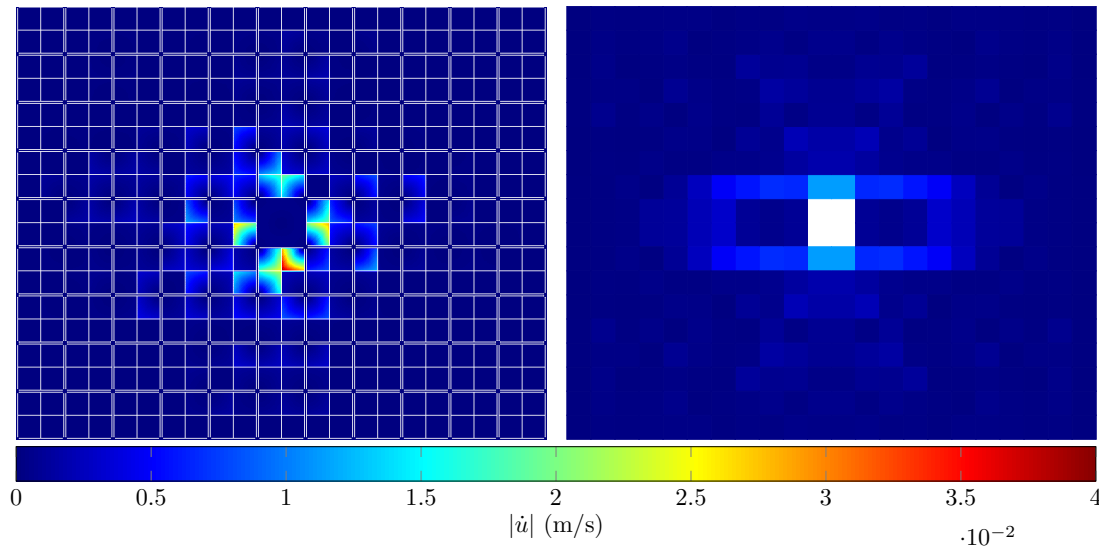


Figure 4.30: $|\dot{\mathbf{u}}|$ (in m/s) at 1589 Hz for the microstructured model (*left*) and for the symmetrized experimental system (*right*), each square representing the speed at the center of the resonator of the $1/4$ of cell considered.

Figure 4.30 presents the speed field of the structure in the heart of the band-gap. This band-gap being omnidirectionnal, the strong directivity of the system disappears, the cells closer to the central excitation while resonating while speed response along the rest of the plate vanishes. Given the small size of the experimental plate (*i.e.* the small number of cells) and the speed measured on the resonators, the measured values remain non-negligible, even if the band-gap effect can be clearly observed. The microstructured model presents a strongly asymmetric response, with an important resonance of a square close to the piezoelectric patches, and the resonance of some squares, yet further from the excitation than some others, greater than the latter. Such effect is due to the combination of:

- the perturbation of the Young modulus and density across the plate
- the small damping used for the simulations

The perturbation of the plate's mechanical parameters induces the resonance of each square of the plate at different frequencies: the resonator with the closest resonant frequency to the considered one (here, 1589 Hz) consequently have a considerable greater amplitude, due to the small damping introduced, than the other ones. For the same reason, a square further from the piezoelectric patches than another one, having his resonant frequency closer to the excitation one may, despite the (small, again, due to the small damping) attenuation of the in-plane expansion wave, from an wave point of view, may have a greater amplitude than the square closer to the excitation. Such phenomenon is also visible for the experiment, the resonance of the square at $(x_1 = 5 \text{ [mm]}, x_2 = 15 \text{ [mm]})$ has to be compared to the one at $(x_1 = 15 \text{ [mm]}, x_2 = 5 \text{ [mm]})$, while the artificial symmetry presented gives a false impression of an uniform resonance around the excitation. Figure 4.31

presents the response on the system for higher frequencies of the theoretical band-gap. One can observe the resonance of the closest resonators to the piezoelectric excitation and the decreasing displacement along the two main axis of the plate.

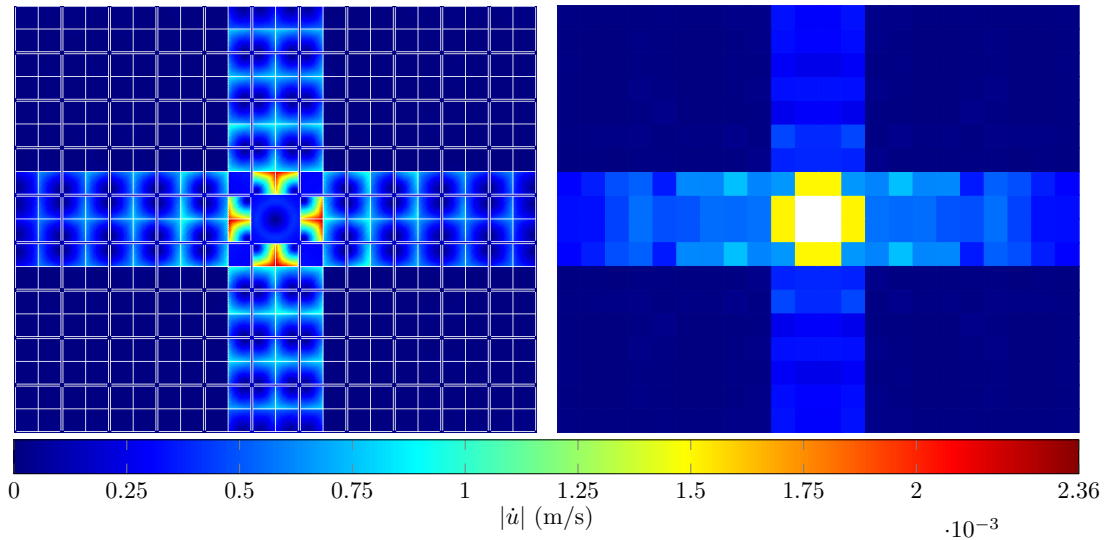


Figure 4.31: $|\dot{\mathbf{u}}|$ (in m/s) at 1742 Hz for the microstructured model (*left*) and for the symmetrized experimental system (*right*), each square representing the speed at the center of the resonator of the 1/4 of cell considered.

4.5 Enabling meta-structural engineering design

As we pointed in Chapter 3, the relaxed micromorphic model successfully describes the mechanical response of our microstructured metamaterials as soon as a *sufficiently large* plate, both in terms of number of cells and excitation. Our experimental *proof of concept* did not meet these requirements, mostly because of the design constraints, to know:

- n_1 and $n_2 \geq 30$ cells
- $n_c \geq 9$ cells

In this section, we propose a new complex metastructure verifying such criteria able to concentrate energy for an eventual re-use through conversion, *e.g.*, of mechanical energy into heat or electricity. Such bidimensionnal structure is presented in Figure 4.32: the central domain Ω_m^1 is made up of our usual unit cell while the outer domain Ω_m^2 is made of a metamaterial with the same geometry whose unit cell is doubled. Both metamaterials' domains are very large (101×51 unit cells in Ω_m^1 and 51×51 unit cells in Ω_m^2 for the symmetrized structure): such large-scale structure points towards realistic structural engineering design (think, for example, that the domain Ω_m^1 is located around a railway truck and that the domain Ω_m^2 are the lateral banks).

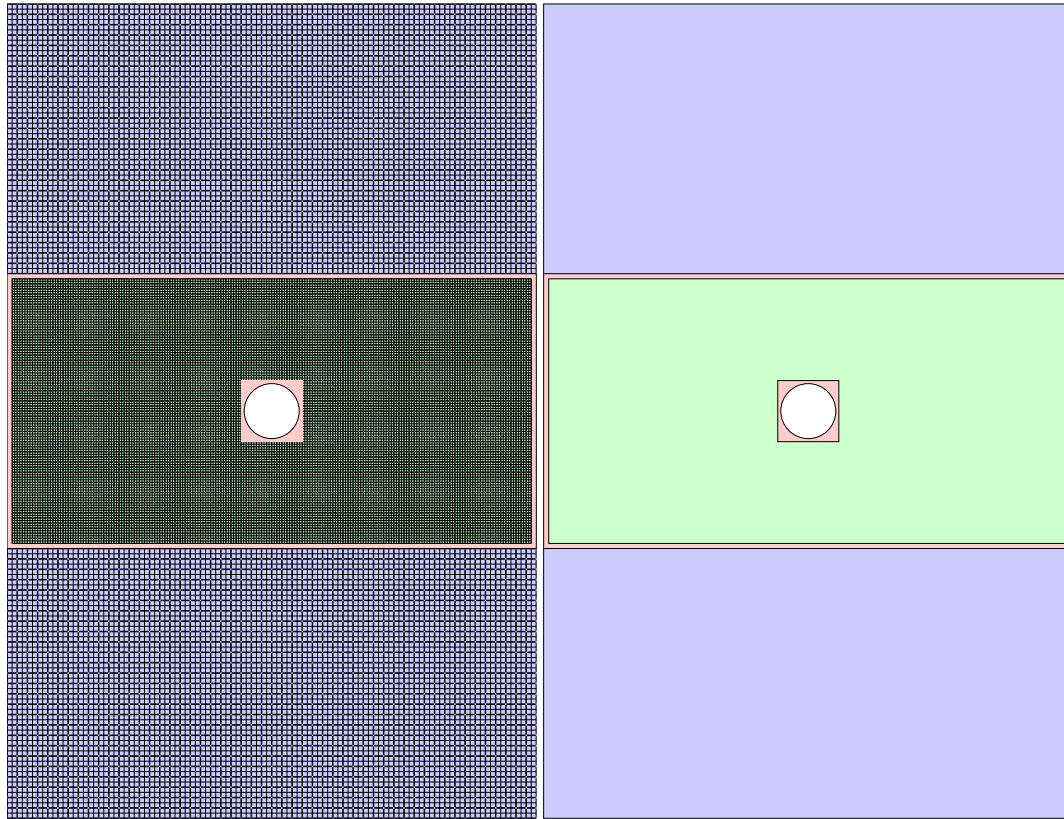


Figure 4.32: (left) Top view of the full microstructured plate with the two different cells. (right) Top view of the full equivalent relaxed micromorphic plate.

If the resolution of the microstructured structure *via* the Finite Element Method would not be feasible, it can reasonably be undertaken only for the relaxed micromorphic model: as we placed ourselves in the conditions of convergence for the relaxed micromorphic plate, we can fully rely on the homogenized plate's result. As we did for our previous models, the symmetries of this structure can be exploited to reduce its size, as presented in Figure 4.33. The two metamaterials' domains are separated by a classical Cauchy material occupying the annular domain Ω_c . The elastic properties of such soft Cauchy material are given in Table 4.4 and a detail of this annular Cauchy region is given in Figure 4.34.

ρ_2	λ_2	μ_2
[kg.m ⁻³]	[Pa]	[Pa]
3000	$9.74 \cdot 10^8$	$5.88 \cdot 10^5$

Table 4.4: Mechanical parameters of the second isotropic Cauchy medium between the two relaxed micromorphic mediums.

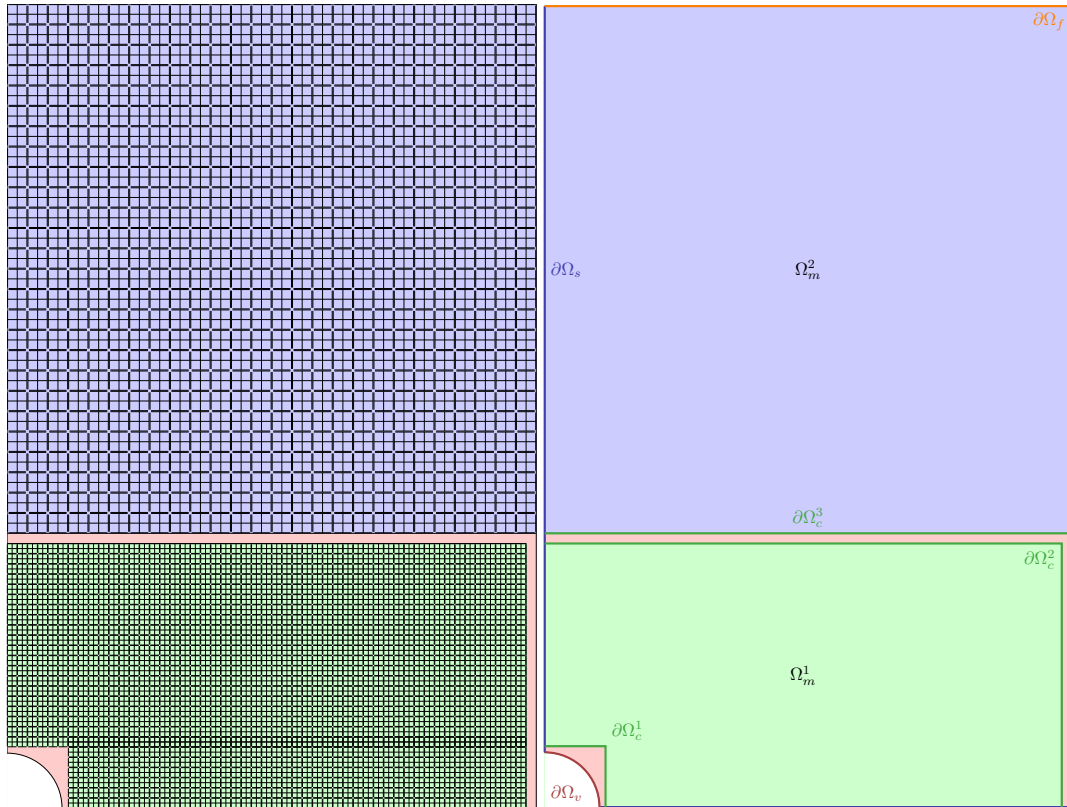


Figure 4.33: (left) Top view of the symmetrized microstructured plate with the two different cells. (right) Top view of the symmetrized equivalent micromorphic plate with the boundaries and medium denominations.

As a new architected unit cell is introduced, its relaxed micromorphic parameters have to be computed, *i.e.* the dispersion curves used for the calibration procedure. Introducing the ratio r between the ratio of the original cell \mathcal{C}_1 parameter χ^1 and the parameter χ^2 of the “double” cell \mathcal{C}_2 :

$$r = \frac{a^2}{a^1} = \frac{e_p^2}{e_p^1} = \frac{e_g^2}{e_g^1} = 2 \quad (4.62)$$

we have, by duality,

$$(f, \mathbf{k}) \in \mathcal{D}_{\mathcal{C}_1} \quad \Rightarrow \quad \left(\frac{f}{r}, \frac{\mathbf{k}}{r}\right) \in \mathcal{D}_{\mathcal{C}_2} \quad (4.63)$$

where $\mathcal{D}_{\mathcal{C}_i}$ is the dispersion curve of the architected unit cell \mathcal{C}_i . Given this, the dispersion curves for both cells can be plotted in Figure 4.35 without additional computations.

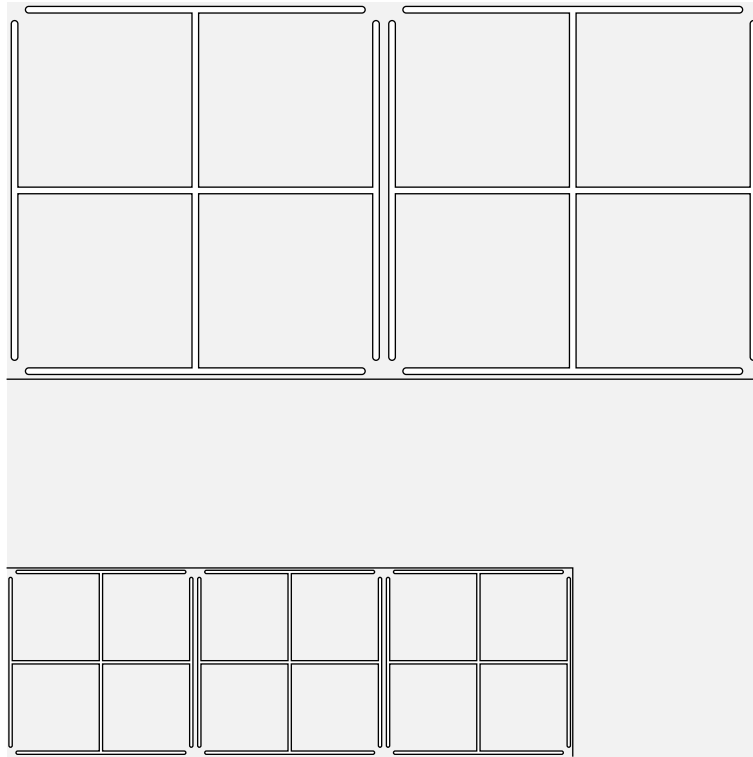


Figure 4.34: Detail of the annular Cauchy domain Ω_c , the central domain Ω_m^1 with the “usual” unit cell and the outer domain Ω_m^2 paved with double unit cells.

These two microstructured unit cells’ band gap being positioned at two different frequency range, a traction-compression pulse signal emitted in the center of the plate at a suitable frequency could propagate through Ω_m^1 to fall into the band-gap of the double microstructured unit cell paving Ω_m^2 . Given the position of the respective band gaps of the two unit cells,

$$f_0 = 857.5 \text{ [Hz]} \quad (4.64)$$

is a good candidate.

Chapter 4. Confronting our models to the experiment

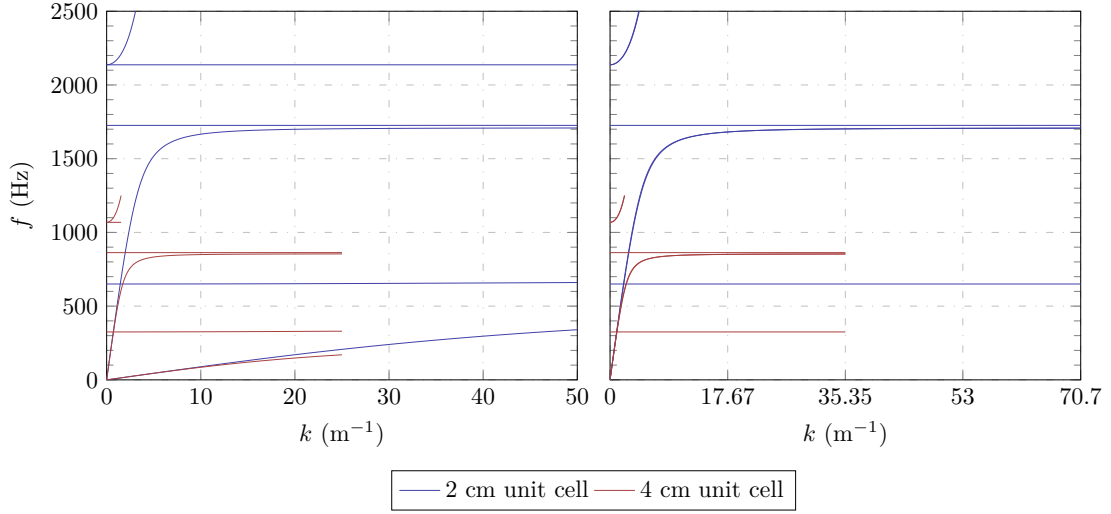


Figure 4.35: (*left*) Dispersion curves for the 4cm unit cell (red) and the 2 cm unit cell (blue) along ΓX (propagation at 0°) and (*right*) along ΓM (propagation at 45°).

The relaxed micromorphic parameters of the double unit cell can be computed from the standard unit cell without an additional calibration upon the dispersion curves obtained via the Bloch-Floquet analysis by setting

$$\begin{cases} \rho_m^2 = \rho_m^1 \\ \mathbb{C}_e^2 = \mathbb{C}_e^1 \\ \mathbb{C}_m^2 = \mathbb{C}_m^1 \\ \mathbb{C}_c^2 = \mathbb{C}_c^1 \\ \mathbb{J}_m^2 = r_c^2 \mathbb{J}_m^1 \\ \mathbb{T}_e^2 = r_c^2 \mathbb{T}_e^1 \\ \mathbb{J}_c^2 = r_c^2 \mathbb{J}_m^1 \\ \mathbb{T}_c^2 = r_c^2 \mathbb{T}_c^1 \end{cases} \quad i.e. \quad \begin{cases} \rho_m^2 = \rho_m^1 \\ \lambda_i^2 = \lambda_i^1, i \in \{e, m\} \\ \mu_i^2 = \mu_i^1, i \in \{e, m\} \\ \mu_i^2 = \mu_i^{*1}, i \in \{e, m\} \\ \mu_c^2 = \mu_c \\ \eta_i^2 = r^2 \eta_i^1, i \in \llbracket 1, 3 \rrbracket \\ \bar{\eta}_1^{*2} = r^2 \bar{\eta}_1^{*1} \\ \bar{\eta}_i^2 = r^2 \bar{\eta}_i^1, i \in \llbracket 1, 3 \rrbracket \\ \bar{\eta}_1^{*2} = r^2 \bar{\eta}_1^{*1} \end{cases} \quad (4.65)$$

where \mathbb{K}^i is the tensor associated with the \mathcal{C}_i cell and χ^i its parameters. Given the calibration procedure for the static parameters, based on the equivalence of strain energy densities, and the physical meaning of ρ_m , these parameters logically remain untouched. The dispersion curves for the double microstructured cell and its equivalent relaxed micromorphic modelling are given in Figure 4.36.

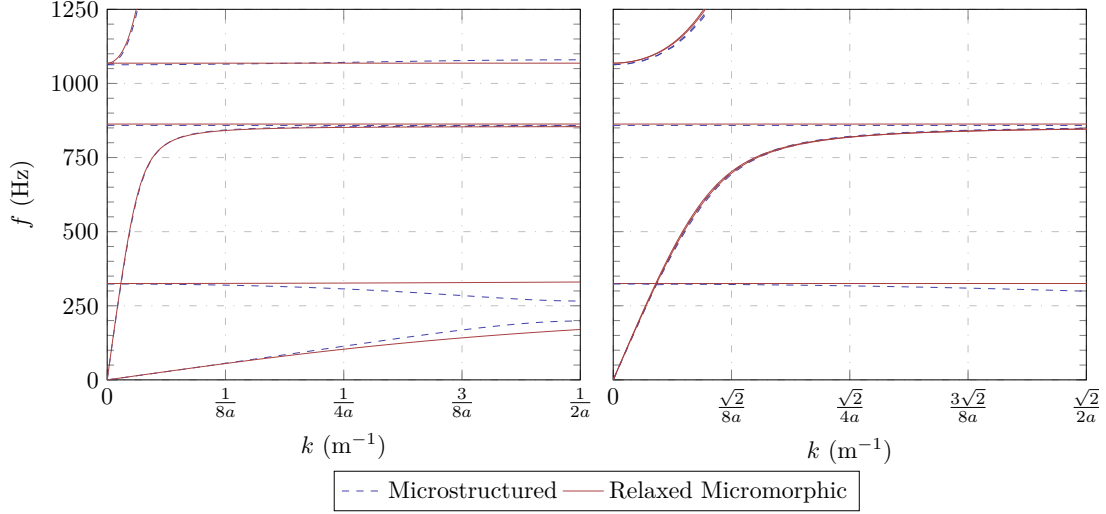


Figure 4.36: (*left*) Dispersion curves of the microstructured and the relaxed micromorphic “double cell” along ΓX (propagation at 0°). (*right*) Dispersion curves of the microstructured and the relaxed micromorphic “double cell” along ΓM (propagation at 45°).

The action functional of the reduced relaxed micromorphic model is

$$\mathcal{A}_{\text{int}}[\mathbf{u}, \mathbf{P}] = \int_{t_1}^{t_2} \left[\int_{\Omega_c^1} (k_c^1 - w_c^1) d\Omega + \int_{\Omega_m^1} (k_m^1 - w_m^1) d\Omega + \int_{\Omega_c^2} (k_c^2 - w_c^2) d\Omega + \int_{\Omega_m^2} (k_m^2 - w_m^2) d\Omega \right] dt \quad (4.66)$$

The boundary conditions are a bit trickier. We have

$$\begin{cases} (\hat{\boldsymbol{\sigma}}_1 + \tilde{\boldsymbol{\sigma}}_1) \cdot \mathbf{n} = \boldsymbol{\sigma}_1 \cdot \mathbf{n} & \text{on } \partial\tilde{\Omega}_c^1 \\ \boldsymbol{\sigma}_2 \cdot \mathbf{n} = (\hat{\boldsymbol{\sigma}}_1 + \tilde{\boldsymbol{\sigma}}_1) \cdot \mathbf{n} & \text{on } \partial\tilde{\Omega}_c^2 \\ \boldsymbol{\sigma}_2 \cdot \mathbf{n} = \mathbf{0} & \text{on } \partial\tilde{\Omega}_f \\ (\hat{\boldsymbol{\sigma}}_1 + \tilde{\boldsymbol{\sigma}}_1) \cdot \mathbf{n} = \boldsymbol{\sigma}_2 \cdot \mathbf{n} & \text{on } \partial\tilde{\Omega}_c^3 \\ (\hat{\boldsymbol{\sigma}}_1 + \tilde{\boldsymbol{\sigma}}_1) \cdot \mathbf{n} = \mathbf{0} & \text{on } \partial\tilde{\Omega}_f \end{cases} \quad \text{and} \quad \begin{cases} u_i = \psi n_i & \text{on } \partial\Omega_e \\ u_i n_i = 0 & \text{on } \partial\Omega_s \\ (\delta_{ki} - n_k n_i)(P_{ij} n_j) = 0 & \text{on } \partial\Omega_s \end{cases} \quad (4.67)$$

The annular Cauchy material is chosen so that a filtering effect is triggered (the wave coming from Ω_m^1 can pass, but cannot go back) [Rizzi 2021]. Thanks to this design, the proposed meta-structure can focus an important part of the elastic energy in the annular Cauchy region (see Table 6). It can be noted that the energy concentration in the annular Cauchy material is evident, also due to the restricted area in which it occurs (see Figure 4.37). A structure of this type could be used to locate energy converters in the annular Cauchy region for subsequent energy conversion and re-use.

Chapter 4. Confronting our models to the experiment

857.5 Hz	Ω_c^1 [J.m ⁻³]	Ω_m^1 [J.m ⁻³]	Ω_c^2 [J.m ⁻³]	Ω_m^2 [J.m ⁻³]
W	$55.1 \cdot 10^3$	$45.5 \cdot 10^3$	$29.5 \cdot 10^3$	$7.74 \cdot 10^3$
K	$3.42 \cdot 10^6$	$43.6 \cdot 10^3$	$26.3 \cdot 10^3$	$7.84 \cdot 10^3$

Table 4.5: Values of the average total energy for each domain of the structure at 857.5 Hz.

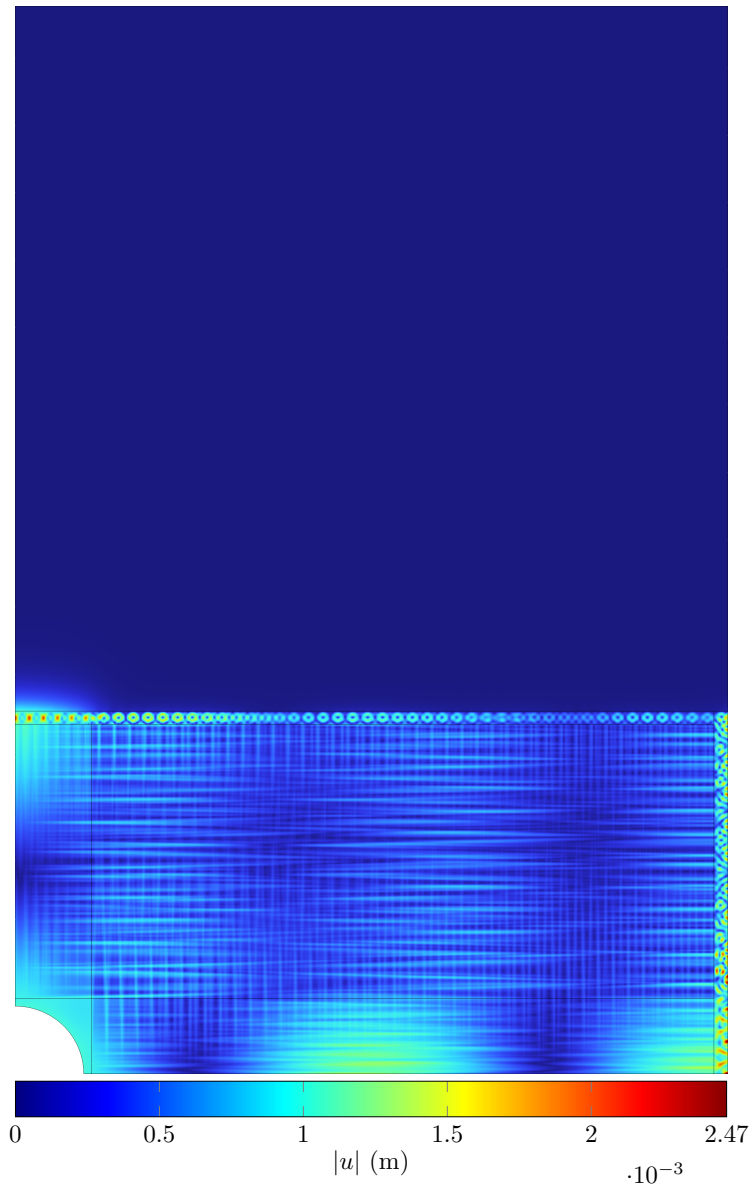


Figure 4.37: Displacement field in the structure at 857.5 Hz.

Conclusion and perspectives

Metamaterials with frequency band-gap, *i.e.* able to inhibit wave propagation for a large frequency range, can be achieved either by Bragg scattering or local resonance. By investigating the latter technical solution, we eventually designed a new microstructured unit cell having a band-gap in the low acoustic frequency range of only 2 centimeters size, up to ten times smaller than “classical” microstructured unit cells with similar characteristics. The characterization of such unorthodox performances requires the use of specific mathematical tools, *e.g.* Bloch-Floquet analysis, allowing to compute the dispersion curves of the designed cell.

Dispersion curves of a (meta-)material may be seen as its spectral signature, fully characterizing its wave behaviour. With the relaxed micromorphic model, we produced a continuum able to mimic the same wave behaviour and, in particular, the non-propagation of mechanical waves in a large frequency range. This has been made possible by the enriching the kinematic description of our medium: where higher-order theories, introducing a considerable number of additional mechanical parameters and requires a stronger regularity of the displacement, can describe some dispersive behaviours, only the introduction of a second-order tensor – *i.e.* micro-distortion – and a few mechanical parameters, is able to describe the localization of energy at microscopic level in our structures.

If the response of an infinite periodic structure, through Bloch theorem, can be reduced to the computation of a generalized eigenvalue problem over the unit cell, their numerical simulation, due to their microstructural complexity, turn out to be particularly tricky when considering large-scale finite-sized structures. Finite Element Method, heavily used in Engineering Sciences, turns out to be poorly adapted to metamaterial modelling *via* the classical Cauchy continuum: the meshing of the complex geometry at microscopic scale necessitates a consequent number of degrees of freedom, in practice incompatible to conciliate with a reasonable calculation time. The homogenization provided by the relaxed micromorphic continuum allows, under the right conditions, to reduce considerably the computation time of microstructured systems, eventually making possible the computation of even larger structures that would not have been possible otherwise.

The *proof of concept* we designed, manufactured, instrumented and characterized showed the reliability of our theories, from the prediction of the band gap to the mechanical behaviour over a large frequency range through the performance degradation due to manufacturing defects. Despite these more successful conclusions, several difficulties arised:

Chapter 5. Conclusion and perspectives

- the slight error introduced by using the plane strain hypothesis for a thin microstructured plates
- the non-perfect convergence of the relaxed micromorphic model due to insufficient dimensions of the experimental plate

If we managed to “rectify” the first hypothesis by tuning the mechanical parameters of the Cauchy continuum and, through our recalibration procedure, reflect these changes on the relaxed micromorphic model, a new calibration procedure to determine its mechanical parameters has to be considered. Let us try to draw the main axes of this study:

- Compute the dispersion curves of the architected cell with the plane stress hypothesis
- Write the dual formulation of the relaxed micromorphic equilibrium equations
- Calibrate the parameters of the generalized compliance tensors

The SUBC method (Static Uniform Boundary Conditions), given the hypothesis made, shall be preferred to the KUBC one, that corresponded to the plain strain hypothesis used previously. One can write the expression of the generalized strain-stress relations for the relaxed micromorphic model:

$$\begin{cases} \nabla \mathbf{u} - \mathbf{P} = \mathbb{S}_e \text{sym } \tilde{\boldsymbol{\sigma}} + \mathbb{S}_c \text{skew } \tilde{\boldsymbol{\sigma}} \\ \text{sym } \mathbf{P} = \mathbb{S}_m \mathbf{s} \end{cases} \quad (5.1)$$

where \mathbb{S}_e , \mathbb{S}_c and \mathbb{S}_m are respectively the generalized elastic, the local rotational elastic and the micro self compliance tensors. One can then compute the generalized complementary strain energy \bar{w}_m for the relaxed micromorphic continuum:

$$\bar{w}_m(\mathbf{s}, \tilde{\boldsymbol{\sigma}}) = \frac{1}{2} \langle \text{sym } \tilde{\boldsymbol{\sigma}}, \mathbb{S}_e \text{sym } \tilde{\boldsymbol{\sigma}} \rangle + \frac{1}{2} \langle \text{sym } \mathbf{s}, \mathbb{S}_m \text{sym } \mathbf{s} \rangle + \frac{1}{2} \langle \text{skew } \tilde{\boldsymbol{\sigma}}, \mathbb{S}_c \text{skew } \tilde{\boldsymbol{\sigma}} \rangle \quad (5.2)$$

with the (generalized) plane stress hypothesis

$$\mathbf{s} = \begin{pmatrix} * & * & 0 \\ * & * & 0 \\ 0 & 0 & 0 \end{pmatrix} \quad \text{and} \quad \tilde{\boldsymbol{\sigma}} = \begin{pmatrix} * & * & 0 \\ * & * & 0 \\ 0 & 0 & 0 \end{pmatrix} \quad (5.3)$$

Unlike the classical Cauchy medium, the gradient micro-inertia will have to be treated in the same way, in formulas:

$$\nabla \ddot{\mathbf{u}} = \mathbb{B}_e \text{sym } \hat{\boldsymbol{\sigma}} + \mathbb{B}_c \text{skew } \hat{\boldsymbol{\sigma}} \quad (5.4)$$

with

$$\hat{\boldsymbol{\sigma}} = \begin{pmatrix} * & * & 0 \\ * & * & 0 \\ 0 & 0 & 0 \end{pmatrix} \quad (5.5)$$

Due to manufacturing constrains, the microstructured plate designed in this thesis did not meet the homogenization conditions established in Chapter 3. For an even brighter proof of the relaxed micromorphic model's capability, a new plate respecting those criteria should be manufactured. To do so, different manufacturing processes should be considered to build such "large" structures, *e.g.*

- Additive manufacturing
- Laser / waterjet cutting

As we already mentioned in Chapter 2, the manufacturing process has to be considered jointly with the material used, raising new issues we briefly evoked in Chapter 3. If the metallic alloys considered in this manuscript allowed us to consider "simple" dissipative laws in our media, *i.e.* loss factor damping, some materials (*e.g.* polymers) may require more complex damping in our structures. The study of wave propagation in damped metamaterials requires specific mathematical tools. Thanks to the homogenization, methods like the Shift Cell Operator do not have to be developed, but dissipation laws can be directly implemented in the local equilibrium laws. A procedure to study propagation in damped relaxed micromorphic continuum could be:

1. Compute the dispersion curves of the unit cell *via* the Bloch-Floquet analysis
2. Calibrate the conservative parameters of the relaxed micromorphic medium
3. Choose a damping for the metamaterial described by the classical Cauchy model
4. Compute the dispersion curves of the damped unit cell *via* the Shift Cell Operator
5. Choose a damping for the relaxed micromorphic model describing the metamaterial
6. Calibrate the damping parameters of the relaxed micromorphic medium

Due to the complexity of the introduction of viscous damping in relaxed micromorphic continuum and the important number of damping coefficients, one could in a first attempt verify the relevance of the hypothesis of correspondence of loss factor damping, *i.e.* that

$$w_c = (1 + i\eta)w_c \quad \text{and} \quad w_m = (1 + i\eta)w_m \quad (5.6)$$

produces the same dispersion curves for both models, *e.g.* for real and imaginary parts of k_1 or k_2 at $\omega = \omega_0 \in \mathbb{R}$ given. Such comparison may also allow to study the influence of each elastic tensor of the relaxed micromorphic model in the description of the band-gap.

If we focused, in this manuscript, on bi-dimensional metamaterials, we saw that it implied some difficulties in terms of, among others, static resistance, design of the band-gap position and width, which may not fit into every mechanical structures. The tridimensional metamaterial, based on the generalization of the unit cell considered here is presented in Figure 5.1. In the absence of strain strain hypothesis for such media, the computation of dispersion curves for the relaxed micromorphic model as well as the calibration procedure, implying a greater number of coefficients will be considerably complexified.

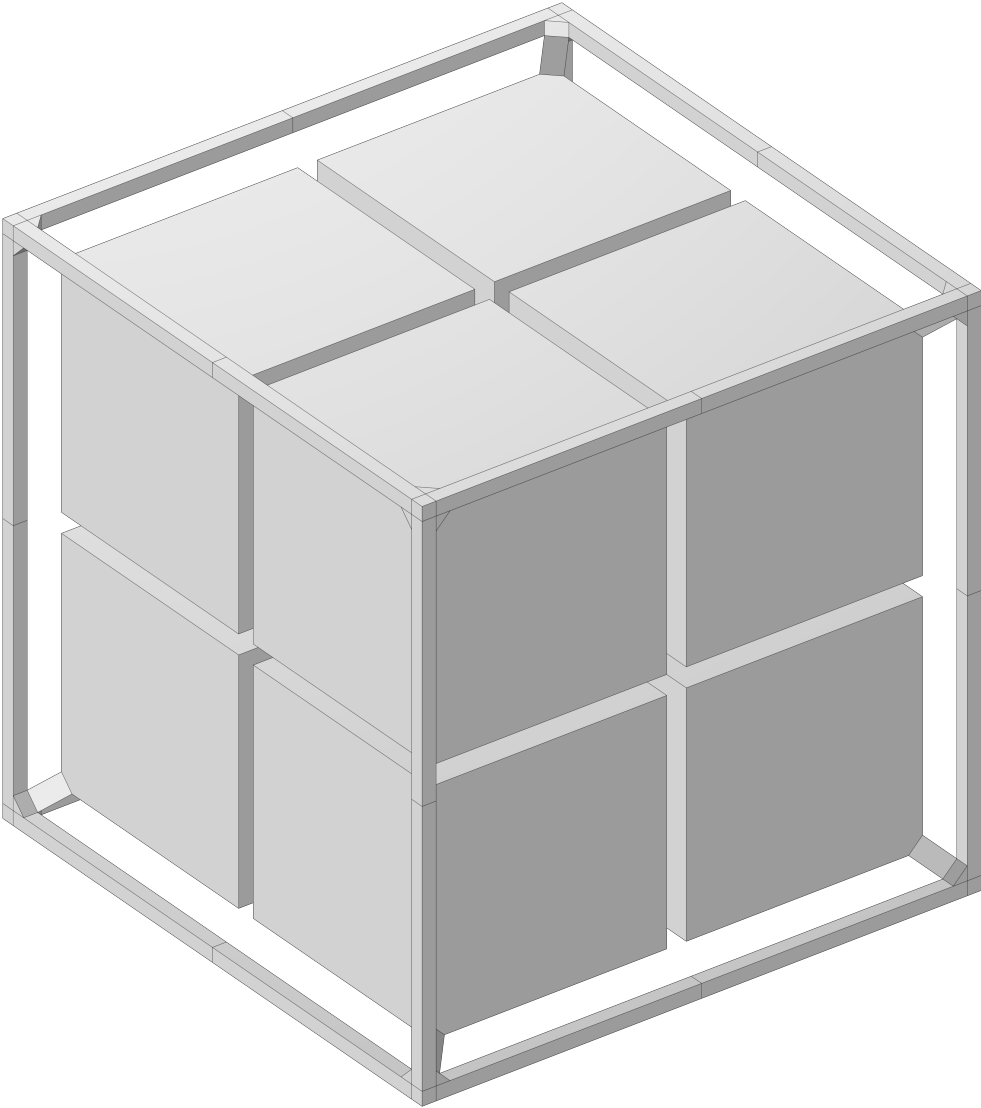


Figure 5.1: Equivalent tridimensional cell, consisting of beams on its edges and of cubes for the resonators linked to the unit cell's corners by small beams.

Annexes

Variation of the action of the relaxed micromorphic medium

We have for the first term of the gradient micro-inertia:

$$\begin{aligned}
\delta \int_{t_1}^{t_2} \int_{\Omega} \frac{1}{2} \langle \text{sym } \nabla \dot{\mathbf{u}}, \mathbb{T}_e \text{sym } \nabla \dot{\mathbf{u}} \rangle d\Omega dt &= \int_{t_1}^{t_2} \left[\int_{\partial\Omega} \langle \delta \dot{\mathbf{u}}, (\mathbb{T}_e \text{sym } \nabla \dot{\mathbf{u}}) \cdot \mathbf{n} \rangle d\Gamma dt - \int_{\Omega} \langle \delta \dot{\mathbf{u}}, \nabla \cdot (\mathbb{T}_e \text{sym } \nabla \dot{\mathbf{u}}) \rangle d\Omega \right] dt \\
\int_{t_1}^{t_2} \int_{\partial\Omega} \langle \delta \dot{\mathbf{u}}, (\mathbb{T}_e \text{sym } \nabla \dot{\mathbf{u}}) \cdot \mathbf{n} \rangle d\Gamma dt &= - \int_{t_1}^{t_2} \int_{\partial\Omega} \langle \delta \mathbf{u}, (\mathbb{T}_e \text{sym } \nabla \ddot{\mathbf{u}}) \cdot \mathbf{n} \rangle d\Gamma dt \\
- \int_{t_1}^{t_2} \int_{\Omega} \langle \delta \dot{\mathbf{u}}, \nabla \cdot (\mathbb{T}_e \text{sym } \nabla \dot{\mathbf{u}}) \rangle d\Omega dt &= + \int_{t_1}^{t_2} \int_{\Omega} \langle \delta \mathbf{u}, \nabla \cdot (\mathbb{T}_e \text{sym } \nabla \ddot{\mathbf{u}}) \rangle d\Omega dt \\
\delta \int_{t_1}^{t_2} \int_{\Omega} \frac{1}{2} \langle \text{sym } \nabla \dot{\mathbf{u}}, \mathbb{T}_e \text{sym } \nabla \dot{\mathbf{u}} \rangle d\Omega dt &= \int_{t_1}^{t_2} \left[- \int_{\partial\Omega} \langle \delta \mathbf{u}, (\mathbb{T}_e \text{sym } \nabla \ddot{\mathbf{u}}) \cdot \mathbf{n} \rangle d\Gamma + \int_{\Omega} \langle \delta \mathbf{u}, \nabla \cdot (\mathbb{T}_e \text{sym } \nabla \ddot{\mathbf{u}}) \rangle d\Omega \right] dt
\end{aligned} \tag{A.1}$$

In the same way, we have for the second term of the gradient micro-inertia term:

$$\begin{aligned}
\delta \int_{t_1}^{t_2} \int_{\Omega} \frac{1}{2} \langle \text{skew } \nabla \dot{\mathbf{u}}, \mathbb{T}_c \text{skew } \nabla \dot{\mathbf{u}} \rangle d\Omega dt &= \int_{t_1}^{t_2} \left[\int_{\partial\Omega} \langle \delta \dot{\mathbf{u}}, (\mathbb{T}_c \text{skew } \nabla \dot{\mathbf{u}}) \cdot \mathbf{n} \rangle d\Gamma dt - \int_{\Omega} \langle \delta \dot{\mathbf{u}}, \nabla \cdot (\mathbb{T}_c \text{skew } \nabla \dot{\mathbf{u}}) \rangle d\Omega \right] dt \\
\int_{t_1}^{t_2} \int_{\partial\Omega} \langle \delta \dot{\mathbf{u}}, (\mathbb{T}_c \text{skew } \nabla \dot{\mathbf{u}}) \cdot \mathbf{n} \rangle d\Gamma dt &= - \int_{t_1}^{t_2} \int_{\partial\Omega} \langle \delta \mathbf{u}, (\mathbb{T}_c \text{skew } \nabla \ddot{\mathbf{u}}) \cdot \mathbf{n} \rangle d\Gamma dt \\
- \int_{t_1}^{t_2} \int_{\Omega} \langle \delta \dot{\mathbf{u}}, \nabla \cdot (\mathbb{T}_c \text{skew } \nabla \dot{\mathbf{u}}) \rangle d\Omega dt &= + \int_{t_1}^{t_2} \int_{\Omega} \langle \delta \mathbf{u}, \nabla \cdot (\mathbb{T}_c \text{skew } \nabla \ddot{\mathbf{u}}) \rangle d\Omega dt \\
\delta \int_{t_1}^{t_2} \int_{\Omega} \frac{1}{2} \langle \text{skew } \nabla \dot{\mathbf{u}}, \mathbb{T}_c \text{skew } \nabla \dot{\mathbf{u}} \rangle d\Omega dt &= \int_{t_1}^{t_2} \left[- \int_{\partial\Omega} \langle \delta \mathbf{u}, (\mathbb{T}_c \text{skew } \nabla \ddot{\mathbf{u}}) \cdot \mathbf{n} \rangle d\Gamma + \int_{\Omega} \langle \delta \mathbf{u}, \nabla \cdot (\mathbb{T}_c \text{skew } \nabla \ddot{\mathbf{u}}) \rangle d\Omega \right] dt
\end{aligned} \tag{A.2}$$

For the classical elastic energy, we have

$$\begin{aligned}
\delta \int_{t_1}^{t_2} \int_{\Omega} \frac{1}{2} \langle \text{sym}(\nabla \mathbf{u} - \mathbf{P}), \mathbb{C}_e \text{sym}(\nabla \mathbf{u} - \mathbf{P}) \rangle d\Omega dt &= \int_{t_1}^{t_2} \int_{\Omega} [\langle \nabla \delta \mathbf{u}, \mathbb{C}_e \text{sym}(\nabla \mathbf{u} - \mathbf{P}) \rangle - \langle \delta \mathbf{P}, \mathbb{C}_e \text{sym}(\nabla \mathbf{u} - \mathbf{P}) \rangle] d\Omega dt \\
&= \int_{t_1}^{t_2} \left[\int_{\partial\Omega} \langle \delta \mathbf{u}, (\mathbb{C}_e \text{sym}(\nabla \mathbf{u} - \mathbf{P})) \cdot \mathbf{n} \rangle d\Gamma - \int_{\Omega} [\langle \delta \mathbf{u}, \nabla \cdot (\mathbb{C}_e \text{sym}(\nabla \mathbf{u} - \mathbf{P})) \rangle + \langle \delta \mathbf{P}, \mathbb{C}_e \text{sym}(\nabla \mathbf{u} - \mathbf{P}) \rangle] d\Omega \right] dt
\end{aligned} \tag{A.3}$$

For the micro self energy, we have directly

$$\delta \int_{t_1}^{t_2} \int_{\Omega} \frac{1}{2} \langle \text{sym } \mathbf{P}, \mathbb{C}_m \text{sym } \mathbf{P} \rangle d\Omega dt = \int_{t_1}^{t_2} \int_{\Omega} \langle \delta \mathbf{P}, \mathbb{C}_m \text{sym } \mathbf{P} \rangle d\Omega dt \tag{A.4}$$

A. Variation of the action of the relaxed micromorphic medium

We eventually have, for the local rotational elastic coupling,

$$\begin{aligned} \delta \int_{t_1}^{t_2} \int_{\Omega} \frac{1}{2} \langle \text{skew}(\nabla \mathbf{u} - \mathbf{P}), \mathbb{C}_c \text{skew}(\nabla \mathbf{u} - \mathbf{P}) \rangle d\Omega dt &= \int_{t_1}^{t_2} \int_{\Omega} [\langle \nabla \delta \mathbf{u}, \mathbb{C}_c \text{skew}(\nabla \mathbf{u} - \mathbf{P}) \rangle - \langle \delta \mathbf{P}, \mathbb{C}_c \text{skew}(\nabla \mathbf{u} - \mathbf{P}) \rangle] d\Omega dt \\ &= \int_{t_1}^{t_2} \left[\int_{\partial\Omega} \langle \delta \mathbf{u}, (\mathbb{C}_c \text{skew}(\nabla \mathbf{u} - \mathbf{P})) \cdot \mathbf{n} \rangle d\Gamma - \int_{\Omega} [\langle \delta \mathbf{u}, \nabla \cdot (\mathbb{C}_c \text{skew}(\nabla \mathbf{u} - \mathbf{P})) \rangle] d\Omega + \langle \delta \mathbf{P}, \mathbb{C}_c \text{skew}(\nabla \mathbf{u} - \mathbf{P}) \rangle] d\Omega \right] dt \end{aligned} \quad (\text{A.5})$$

One can eventually compute the the expressions of kinetic and strain densities of energy

$$\begin{aligned} k_m &= \frac{1}{2} \rho_m (\dot{u}_1^2 + \dot{u}_2^2) \\ &+ \frac{1}{2} \left[2\eta_1 (\dot{P}_{11}^2 + \dot{P}_{22}^2) + \eta_3 (\dot{P}_{11} + \dot{P}_{22})^2 + \eta_1^* (\dot{P}_{12} + \dot{P}_{21})^2 + \eta_2 (\dot{P}_{12} - \dot{P}_{21})^2 \right] \\ &+ \frac{1}{2} \left[2\bar{\eta}_1 (\dot{u}_{1,1}^2 + \dot{u}_{2,2}^2) + \bar{\eta}_3 (\dot{u}_{1,1} + \dot{u}_{2,2})^2 + \bar{\eta}_1^* (\dot{u}_{1,2} + \dot{u}_{2,1})^2 + \bar{\eta}_2 (\dot{u}_{1,2} - \dot{u}_{2,1})^2 \right] \\ w_m &= \frac{1}{2} \left[2\mu_e ((P_{11} - u_{1,1})^2 + (P_{22} - u_{2,2})^2) + \lambda_e (P_{11} + P_{22} - u_{1,1} - u_{2,2})^2 + \mu_e^* (P_{12} - u_{1,2} + P_{21} - u_{2,1})^2 \right] \\ &+ \frac{1}{2} \left[2\mu_m (P_{11}^2 + P_{22}^2) + \lambda_m (P_{11} + P_{22})^2 + \mu_m^* (P_{12} + P_{21})^2 \right] \\ &+ \frac{1}{2} \left[\mu_c (P_{12} + P_{21} - u_{1,2} - u_{2,1})^2 \right] \end{aligned} \quad (\text{A.6})$$

Comparison of the FRFs

We present here the experimental FRFs measured along the symmetry planes: given the strong directivity of the microstructured plate due to the slenderness of the “beams” constituting the unit cell, the response of points “far” from the symmetry planes can be considered, outside of the structural modes of the plate, as negligible in comparison of the points formerly mentioned. We also present the corresponding responses of the perturbed recalibrated microstructured and relaxed micromorphic models given in Chapter 4.

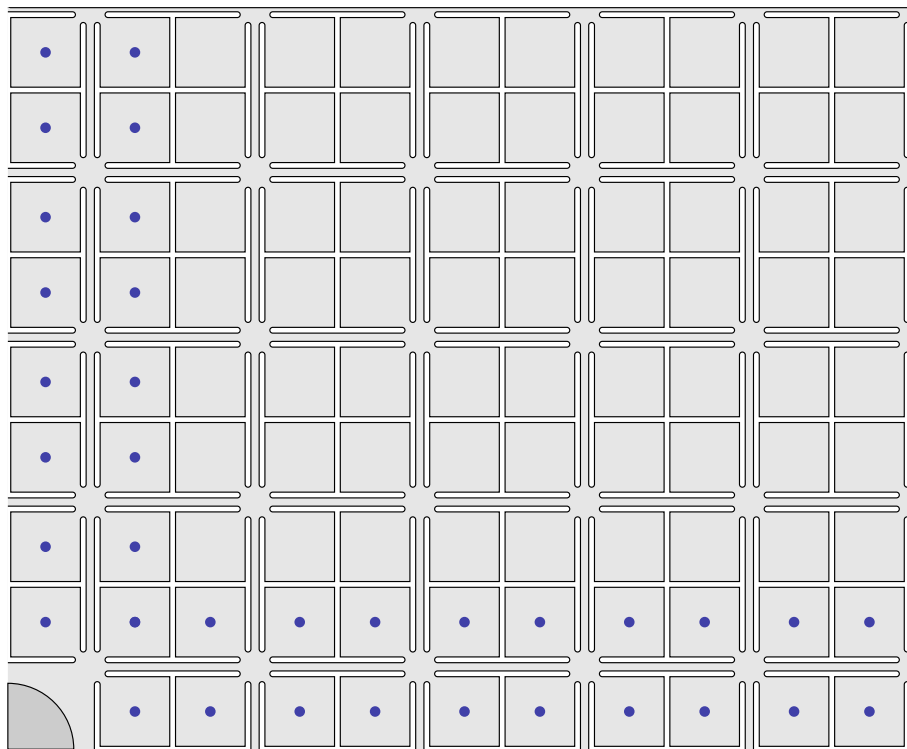


Figure B.1: Top view of the full microstructured plate with the most remarkable points along the symmetry planes of the system. Given the strong directivity of the plate we do not consider other points outside the dashed domain.

Appendix B. Comparison of the FRFs

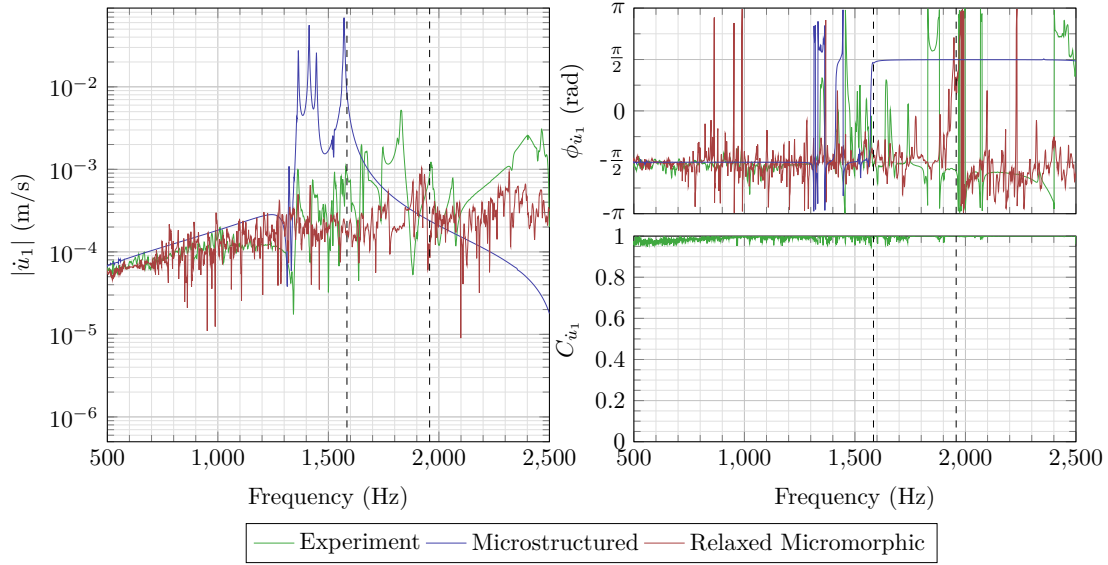


Figure B.2: (*left*) Amplitude of \dot{u}_1 at $(x_1, x_2) = (1.5, 0.5)$ [cm] for the experiment, the microstructured and relaxed micromorphic models. (*right, top*) Phase of \dot{u}_1 at $(x_1, x_2) = (1.5, 0.5)$ [cm] for the experiment, the microstructured and relaxed micromorphic models. (*right, bottom*) Coherence of \dot{u}_1 at $(x_1, x_2) = (1.5, 0.5)$ [cm] for the experiment. Dashed lines correspond to the theoretical bounds of the band gap.

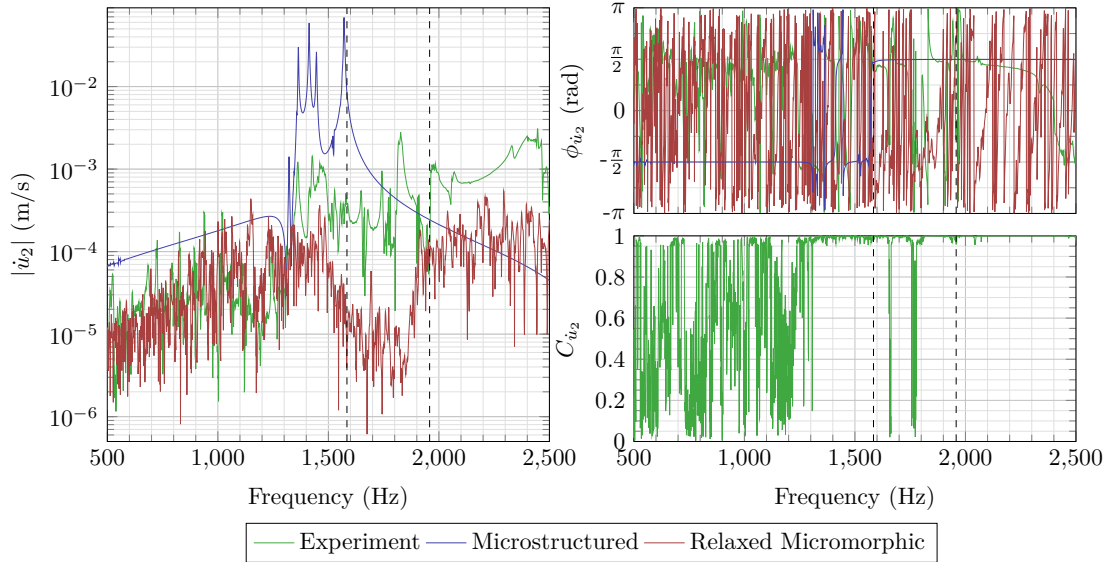


Figure B.3: (*left*) Amplitude of \dot{u}_2 at $(x_1, x_2) = (1.5, 0.5)$ [cm] for the experiment, the microstructured and relaxed micromorphic models. (*right, top*) Phase of \dot{u}_2 at $(x_1, x_2) = (1.5, 0.5)$ [cm] for the experiment, the microstructured and relaxed micromorphic models. (*right, bottom*) Coherence of \dot{u}_2 at $(x_1, x_2) = (1.5, 0.5)$ [cm] for the experiment. Dashed lines correspond to the theoretical bounds of the band gap.

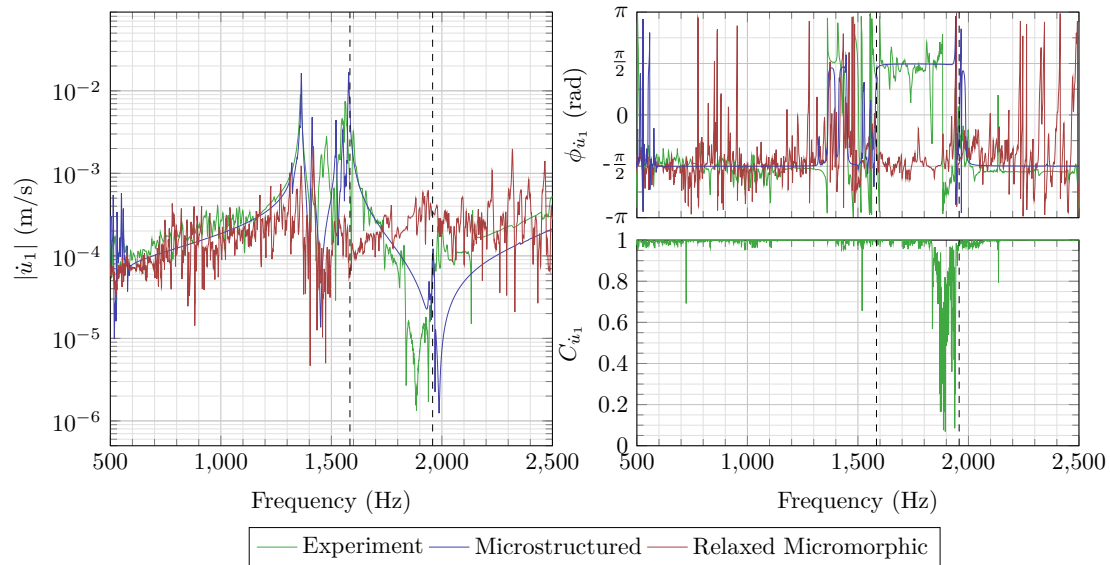


Figure B.4: (*left*) Amplitude of \dot{u}_1 at $(x_1, x_2) = (2.5, 0.5)$ [cm] for the experiment, the microstructured and relaxed micromorphic models. (*right, top*) Phase of \dot{u}_1 at $(x_1, x_2) = (2.5, 0.5)$ [cm] for the experiment, the microstructured and relaxed micromorphic models. (*right, bottom*) Coherence of \dot{u}_1 at $(x_1, x_2) = (2.5, 0.5)$ [cm] for the experiment. Dashed lines correspond to the theoretical bounds of the band gap.

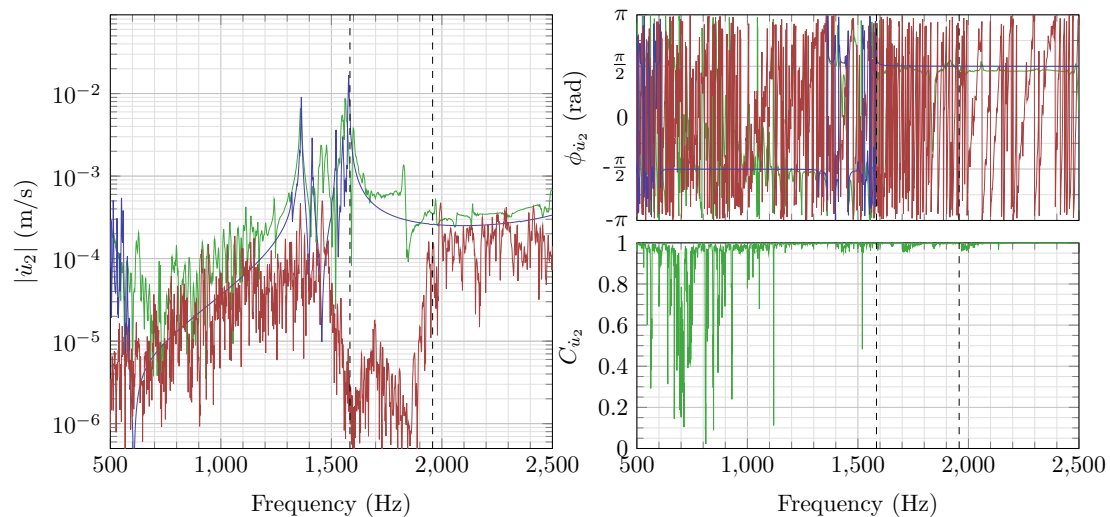


Figure B.5: (*left*) Amplitude of \dot{u}_2 at $(x_1, x_2) = (2.5, 0.5)$ [cm] for the experiment, the microstructured and relaxed micromorphic models. (*right, top*) Phase of \dot{u}_2 at $(x_1, x_2) = (2.5, 0.5)$ [cm] for the experiment, the microstructured and relaxed micromorphic models. (*right, bottom*) Coherence of \dot{u}_2 at $(x_1, x_2) = (2.5, 0.5)$ [cm] for the experiment. Dashed lines correspond to the theoretical bounds of the band gap.

Appendix B. Comparison of the FRFs

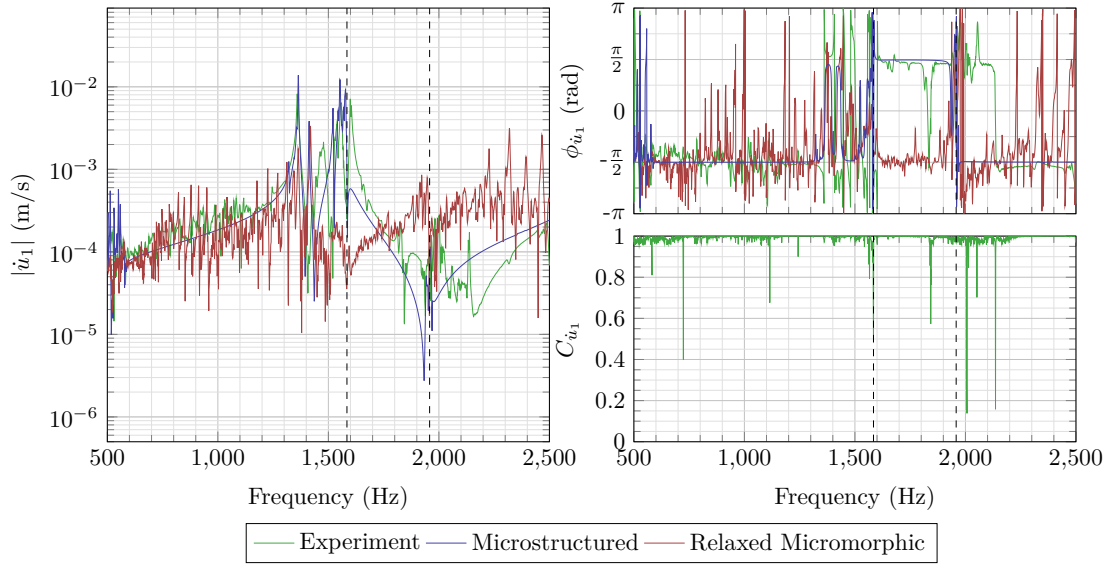


Figure B.6: (*left*) Amplitude of \dot{u}_1 at $(x_1, x_2) = (2.5, 0.5)$ [cm] for the experiment, the microstructured and relaxed micromorphic models. (*right, top*) Phase of \dot{u}_1 at $(x_1, x_2) = (2.5, 0.5)$ [cm] for the experiment, the microstructured and relaxed micromorphic models. (*right, bottom*) Coherence of \dot{u}_1 at $(x_1, x_2) = (2.5, 0.5)$ [cm] for the experiment. Dashed lines correspond to the theoretical bounds of the band gap.

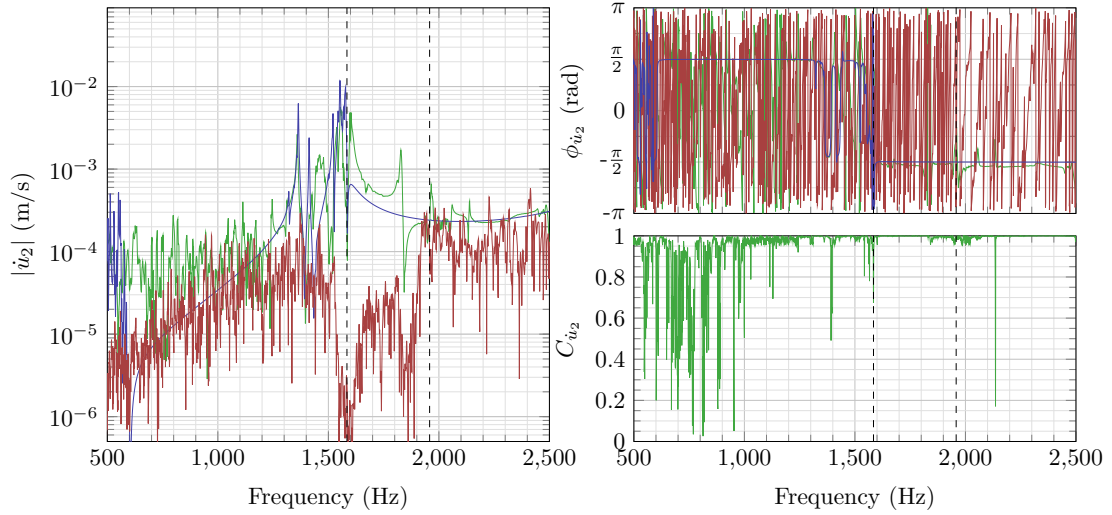


Figure B.7: (*left*) Amplitude of \dot{u}_2 at $(x_1, x_2) = (2.5, 0.5)$ [cm] for the experiment, the microstructured and relaxed micromorphic models. (*right, top*) Phase of \dot{u}_2 at $(x_1, x_2) = (2.5, 0.5)$ [cm] for the experiment, the microstructured and relaxed micromorphic models. (*right, bottom*) Coherence of \dot{u}_2 at $(x_1, x_2) = (2.5, 0.5)$ [cm] for the experiment. Dashed lines correspond to the theoretical bounds of the band gap.

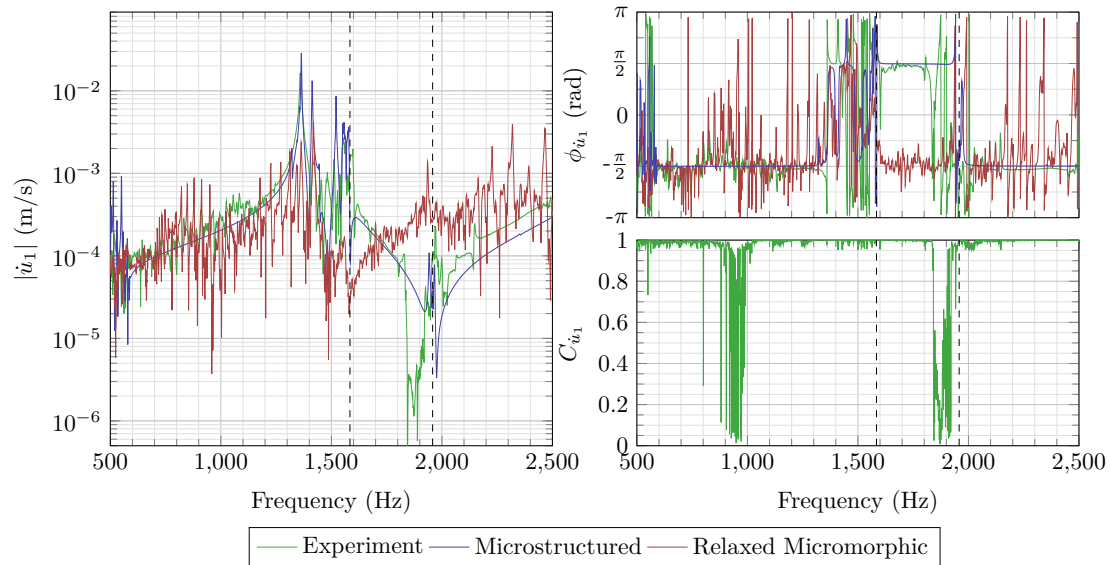


Figure B.8: (left) Amplitude of \dot{u}_1 at $(x_1, x_2) = (2.5, 0.5)$ [cm] for the experiment, the microstructured and relaxed micromorphic models. (right, top) Phase of \dot{u}_1 at $(x_1, x_2) = (2.5, 0.5)$ [cm] for the experiment, the microstructured and relaxed micromorphic models. (right, bottom) Coherence of \dot{u}_1 at $(x_1, x_2) = (2.5, 0.5)$ [cm] for the experiment. Dashed lines correspond to the theoretical bounds of the band gap.

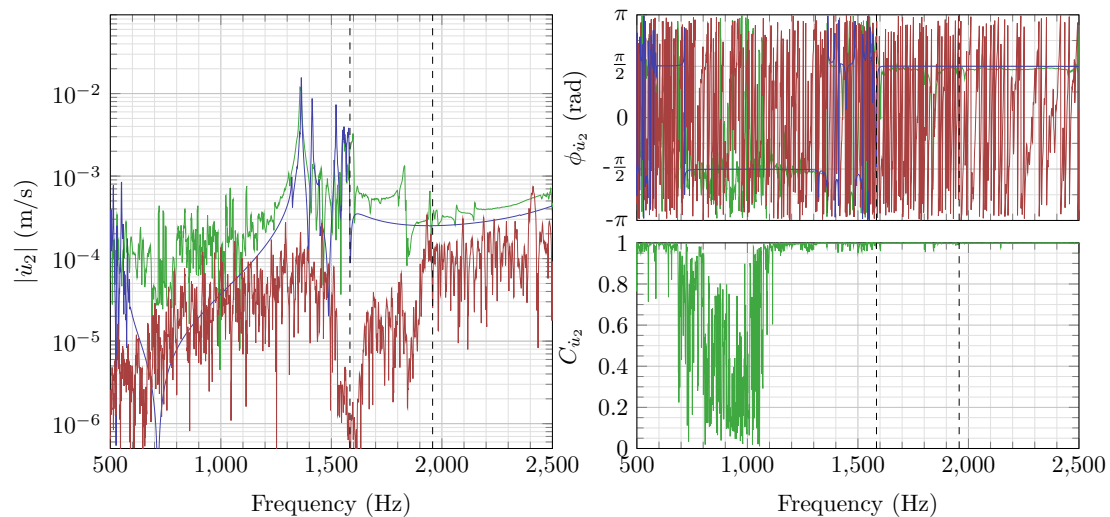


Figure B.9: (left) Amplitude of \dot{u}_2 at $(x_1, x_2) = (2.5, 0.5)$ [cm] for the experiment, the microstructured and relaxed micromorphic models. (right, top) Phase of \dot{u}_2 at $(x_1, x_2) = (2.5, 0.5)$ [cm] for the experiment, the microstructured and relaxed micromorphic models. (right, bottom) Coherence of \dot{u}_2 at $(x_1, x_2) = (2.5, 0.5)$ [cm] for the experiment. Dashed lines correspond to the theoretical bounds of the band gap.

Appendix B. Comparison of the FRFs

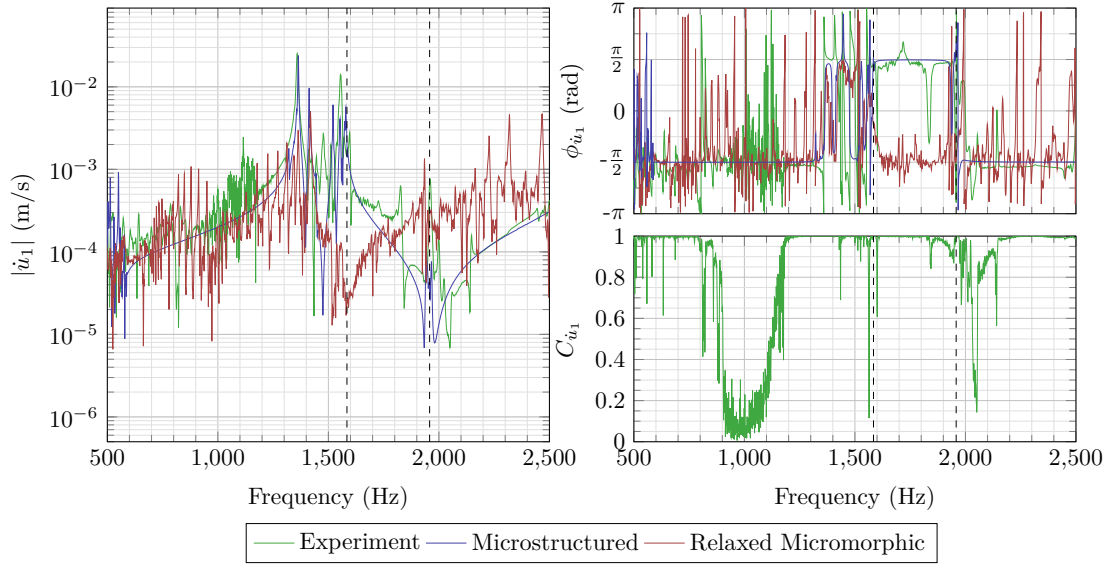


Figure B.10: (*left*) Amplitude of \dot{u}_1 at $(x_1, x_2) = (2.5, 0.5)$ [cm] for the experiment, the microstructured and relaxed micromorphic models. (*right, top*) Phase of \dot{u}_1 at $(x_1, x_2) = (2.5, 0.5)$ [cm] for the experiment, the microstructured and relaxed micromorphic models. (*right, bottom*) Coherence of \dot{u}_1 at $(x_1, x_2) = (2.5, 0.5)$ [cm] for the experiment. Dashed lines correspond to the theoretical bounds of the band gap.

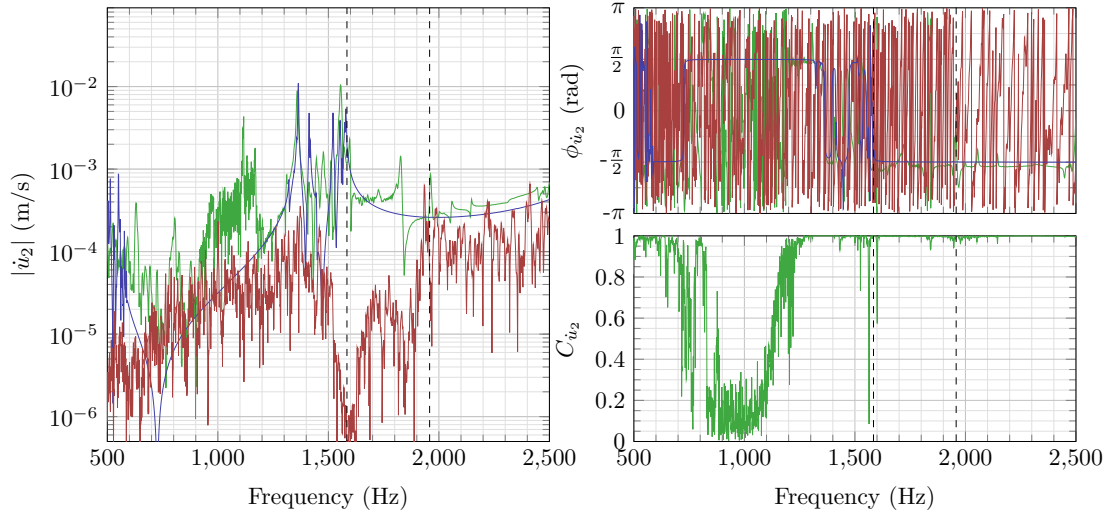


Figure B.11: (*left*) Amplitude of \dot{u}_2 at $(x_1, x_2) = (2.5, 0.5)$ [cm] for the experiment, the microstructured and relaxed micromorphic models. (*right, top*) Phase of \dot{u}_2 at $(x_1, x_2) = (2.5, 0.5)$ [cm] for the experiment, the microstructured and relaxed micromorphic models. (*right, bottom*) Coherence of \dot{u}_2 at $(x_1, x_2) = (2.5, 0.5)$ [cm] for the experiment. Dashed lines correspond to the theoretical bounds of the band gap.

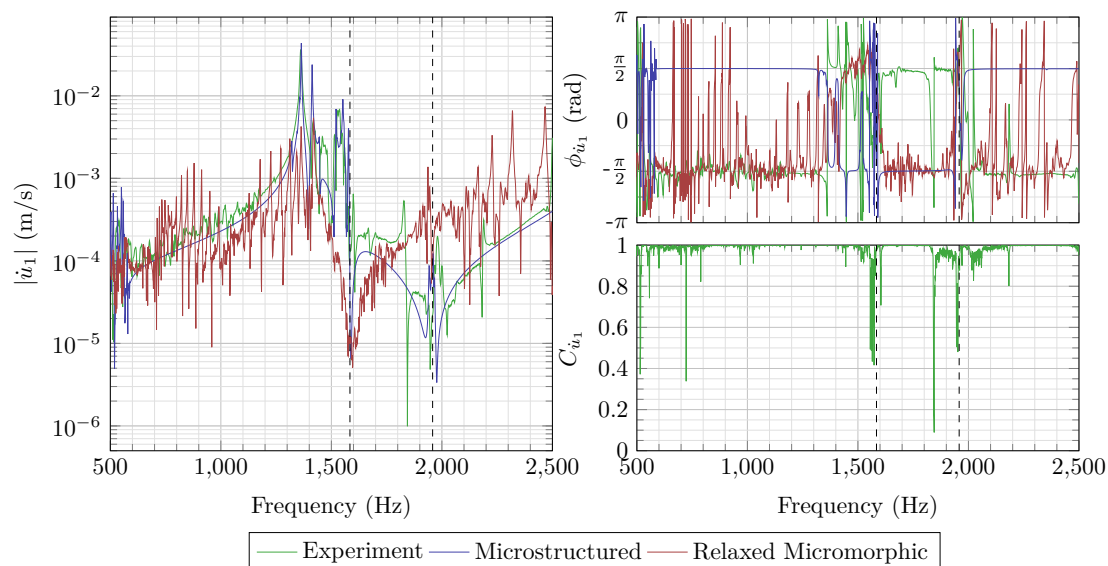


Figure B.12: (left) Amplitude of \dot{u}_1 at $(x_1, x_2) = (2.5, 0.5)$ [cm] for the experiment, the microstructured and relaxed micromorphic models. (right, top) Phase of \dot{u}_1 at $(x_1, x_2) = (2.5, 0.5)$ [cm] for the experiment, the microstructured and relaxed micromorphic models. (right, bottom) Coherence of \dot{u}_1 at $(x_1, x_2) = (2.5, 0.5)$ [cm] for the experiment. Dashed lines correspond to the theoretical bounds of the band gap.

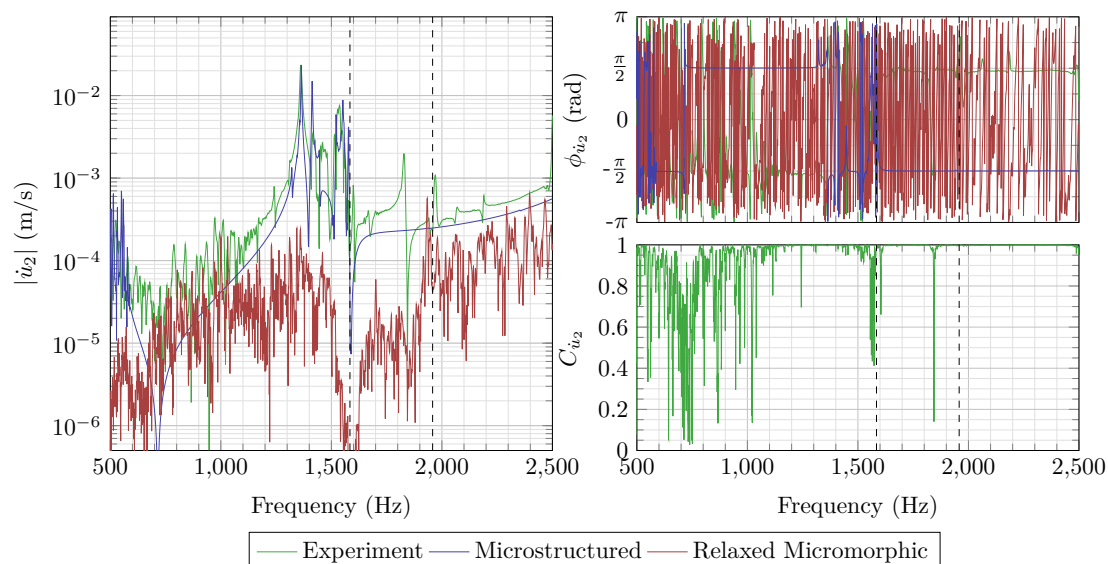


Figure B.13: (left) Amplitude of \dot{u}_2 at $(x_1, x_2) = (2.5, 0.5)$ [cm] for the experiment, the microstructured and relaxed micromorphic models. (right, top) Phase of \dot{u}_2 at $(x_1, x_2) = (2.5, 0.5)$ [cm] for the experiment, the microstructured and relaxed micromorphic models. (right, bottom) Coherence of \dot{u}_2 at $(x_1, x_2) = (2.5, 0.5)$ [cm] for the experiment. Dashed lines correspond to the theoretical bounds of the band gap.

Appendix B. Comparison of the FRFs

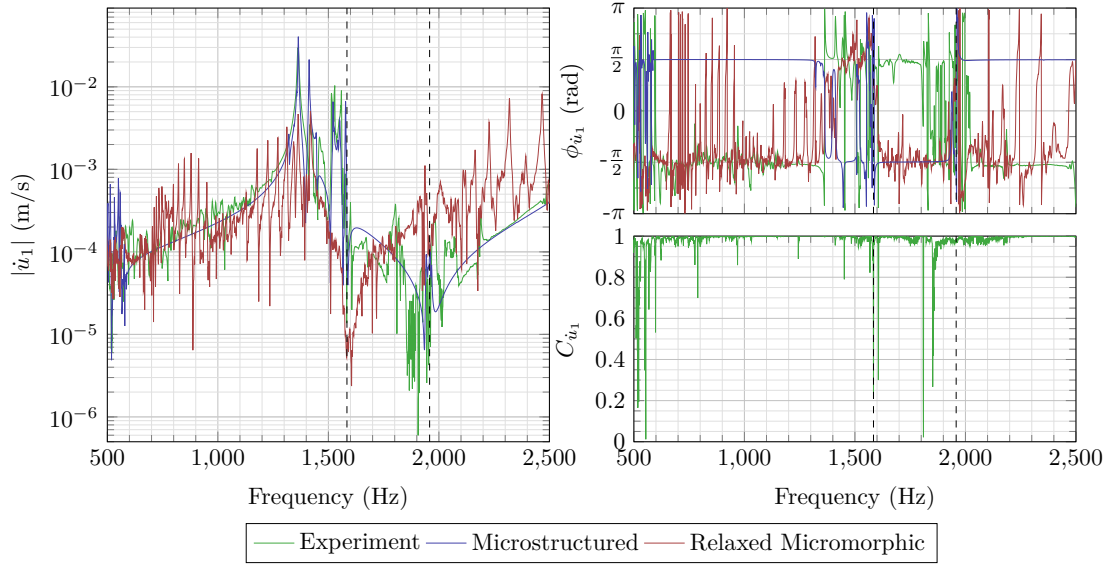


Figure B.14: (left) Amplitude of \dot{u}_1 at $(x_1, x_2) = (2.5, 0.5)$ [cm] for the experiment, the microstructured and relaxed micromorphic models. (right, top) Phase of \dot{u}_1 at $(x_1, x_2) = (2.5, 0.5)$ [cm] for the experiment, the microstructured and relaxed micromorphic models. (right, bottom) Coherence of \dot{u}_1 at $(x_1, x_2) = (2.5, 0.5)$ [cm] for the experiment. Dashed lines correspond to the theoretical bounds of the band gap.

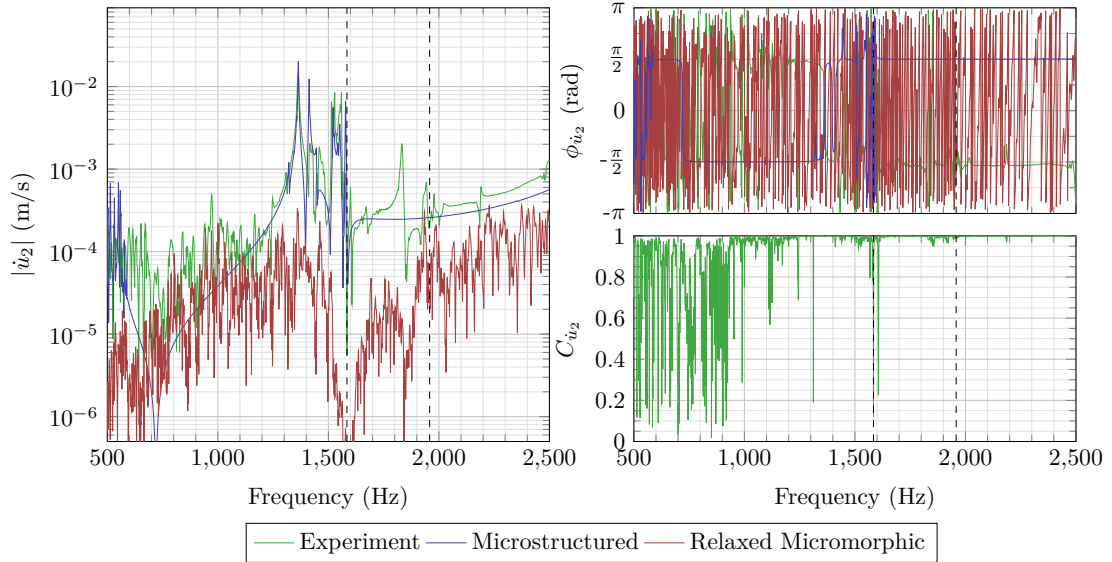


Figure B.15: (left) Amplitude of \dot{u}_2 at $(x_1, x_2) = (2.5, 0.5)$ [cm] for the experiment, the microstructured and relaxed micromorphic models. (right, top) Phase of \dot{u}_2 at $(x_1, x_2) = (2.5, 0.5)$ [cm] for the experiment, the microstructured and relaxed micromorphic models. (right, bottom) Coherence of \dot{u}_2 at $(x_1, x_2) = (2.5, 0.5)$ [cm] for the experiment. Dashed lines correspond to the theoretical bounds of the band gap.

Discrete model

Due to the specific geometry of the cell and the range of frequency studied, the displacement field along the whole system can be modeled using only 16 degrees of freedom for each cell and still be able to describe the band-gap effect.

Like the FE method, the plane displacement field along the structure is defined piecewise using two different models:

- an Euler-Bernoulli beam coupled with the Guyan static reduction
- the rigid body model

An additional spring will also be introduced between the resonator and the “corner” to model the resonance inside the cell, which causes the band-gap effect. To know a mechanical system is to know its kinetic and potential energy. To do so, every element composing the system will be presented through its associated energies.

C.1 The rigid body model

A rigid body under no conservative forces doesn't have any potential energy, and it can be shown that its kinetic energy can be computed by

$$K = \frac{1}{2} \langle \dot{\mathbf{u}}_{M \in S/R}, m \dot{\mathbf{u}}_{S/R} \rangle + \frac{1}{2} \langle \boldsymbol{\sigma}_{M \in S/R}, \boldsymbol{\Omega}_{S/R} \rangle \quad (\text{C.1})$$

It is usually calculated at the center of gravity of the solid G , where it takes the following expression

$$K = \frac{1}{2} \langle \dot{\mathbf{u}}_{G \in S/R}, m \dot{\mathbf{u}}_{G \in S/R} \rangle + \frac{1}{2} \langle \boldsymbol{\Omega}_{S/R}, \mathbf{I}_{G,S/R} \boldsymbol{\Omega}_{S/R} \rangle \quad (\text{C.2})$$

The virtual power P^* of the external forces of resultant \mathbf{F} and torque \mathbf{C} is

$$P^* = \langle \mathbf{F}_{\bar{S} \rightarrow S}, \dot{\mathbf{u}}_{M \in S/R}^* \rangle + \langle \mathbf{C}_{M, \bar{S} \rightarrow S}, \boldsymbol{\Omega}_{S/R}^* \rangle \quad (\text{C.3})$$

C.2 The Euler-Bernoulli beam

Let's consider a beam of neutral axis $\Gamma : x \in [0, L] \mapsto \Gamma(x)$, $L > 0$ of cross section S of curvilinear abscissa x . Under Navier's hypothesis, the cross-section stays

Appendix C. Discrete model

plane after deformation, when Bernoulli assumes that even stay perpendicular to the neutral axis, which is

$$\forall x \in [0, L], \forall (A, B) \in S_x^2, \langle \mathbf{AB}, \mathbf{\Gamma}(x), x \rangle = 0 \quad (\text{C.4})$$

$\Gamma \in C^1([0, L], \mathbb{R}^3)$. These assumptions allows to describe the displacement field in the whole structure through the study of the neutral axis with the equilibrium equations

$$\begin{cases} ESu_{1,1} = N & (\text{Hooke's law}) \\ EI_G u_{2,22} = M_f \end{cases} \quad (\text{C.5})$$

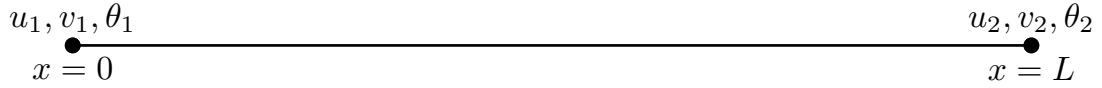
where E is the Young's modulus, S the cross section, N the normal effort, I_G the area moment of inertia and M_f the bending moment.

C.3 The Guyan static reduction

In the Guyan reduction, the displacement field is the one of the static response of a beam, which is of the form

$$u(x) = Ax + B \quad (\text{C.6})$$

$$v(x) = Cx^3 + Dx^2 + Ex + F \quad (\text{C.7})$$



It can be fully determined by displacements and rotations of the extremities. Bernoulli's hypothesis gives

$$u_{2,1}(x_1 = 0) = \theta_1 \quad \text{and} \quad u_{2,1}(x = L) = \theta_2 \quad (\text{C.8})$$

Allowing to set the values of A, B, C, D, E and F . Kinetic and potential energy of the beam are then given by

$$K = \frac{1}{2} \int_0^L \rho S (\dot{u}^2 + \dot{v}^2) dx_1 \quad (\text{C.9})$$

$$W = \frac{1}{2} \int_0^L [ESu_{1,1}^2 + EI_G u_{2,22}^2] dx_1 \quad (\text{C.10})$$

C.4 Parametrization

All the dexterity of the mechanician lies in the choice of the parametrization. The non-redundant parametrization has been made:

- 3 degrees of freedom for each corner of the cells, two corresponding to the position of the point M and one for the rotation of \mathcal{C} .
- One additional degree of freedom by resonator, representing the rotation of \mathcal{R} .

The figure below presents the discretization of a quarter of cell.

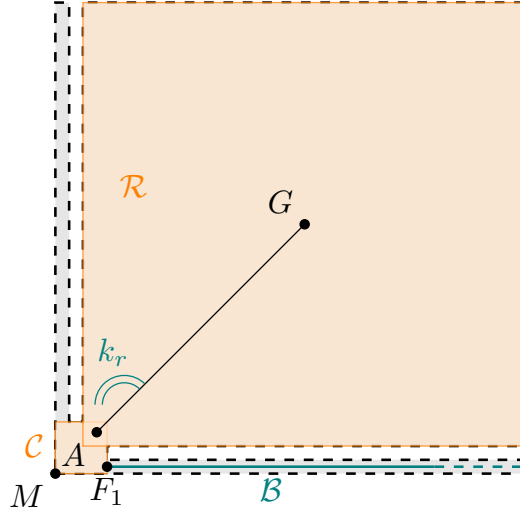


Figure C.1: Parametrization of the model

Such choice allows to easily connect cells between them and to apply forces on the cell. The pendulum configuration consisting in $\{\mathcal{C} + \mathcal{R}\}$ strongly suggests to parametrize this system by adding just one degree of freedom in rotation, which allows to naturally satisfy the holonomical constrains

$$\begin{cases} \|\mathbf{AG}\| = l \text{ (constant length of the pendulum)} \\ \forall M \in \mathcal{R}, \langle \mathbf{GA}, \mathbf{GM} \rangle_{,t} = 0 \text{ (no rotation of } \mathcal{R} \text{ around } G) \end{cases} \quad (\text{C.11})$$

The resonance can be very simply mimicked by adding to the pendulum a linear torsion spring of potential energy

$$W = \frac{1}{2} k_r (\theta_r - \pi/4 - \theta_c)^2 \quad (\text{C.12})$$

where k_r is the rotational stiffness of the spring. \mathcal{C} and \mathcal{R} are considered to be squares of respective sides a_c and a_r and of areal density $e\rho_t$. The points F_1 and A , the attachment points on \mathcal{C} respectively of the beam and the pendulum, require to introduce additional geometrical parameters defined through

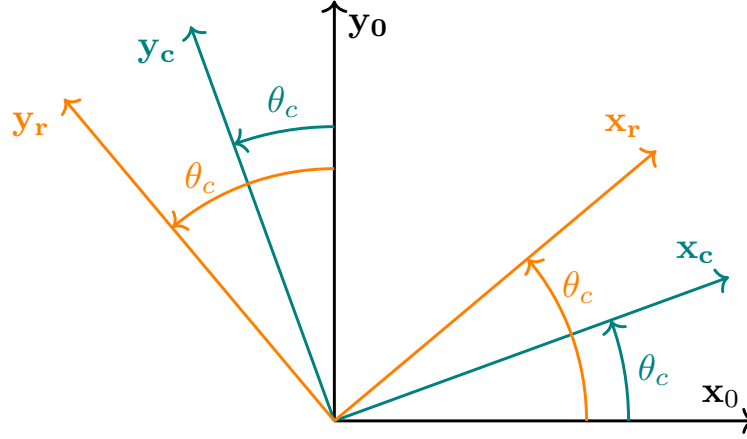


Figure C.2: Angular parametrization of the discrete system

$$\begin{cases} \text{MF}_1 = d_x \mathbf{x}_1^c + d_y \mathbf{x}_2^c \\ \text{MA} = e_x \frac{\mathbf{x}_1^c + \mathbf{x}_2^c}{\sqrt{2}} \end{cases} \quad (\text{C.13})$$

C.5 Parameters identification

To sum up, the discrete model, consisting in rigid squares and rectangular beams, is fully determined through

- A_c and A_r , the respective side lengths of the corner and resonator squares
- L , b and h , the dimensions of the “side” beams
- l , the length of the pendulum
- k_r , the pendulum’s stiffness
- d_x and d_y , beam’s attachment point coordinates for \mathcal{C}
- e_x , defined previously

As we obviously take the titanium alloy’s density to compute kinetic energy. Some parameters, through simple geometrical considerations, can easily and certainly determined. Let’s assume

$$A_r = \frac{a}{2} - e_p - e_g - \frac{e_g}{2} \text{ and } A_c = \frac{a - l_p - e_g}{2} \quad (\text{C.14})$$

$$d_y = \frac{e_p}{2} \quad (\text{C.15})$$

$$b = e_p \text{ (beam’s width) and } h = e \text{ (beam’s height)} \quad (\text{C.16})$$

The remaining parameters L , d_x , e_x and k_r will be determined through mechanical, *via* both static or modal approaches.

Beam's geometry

Let's consider the beam under the bending load F , one can easily get the extremal displacement δu

$$\delta u = \frac{4l^3}{b^3 h E} F \quad (\text{C.17})$$

so

$$l = \sqrt[3]{\frac{\delta u h E}{4F}} b, \text{ N.A. : } l = 9,2 \cdot 10^{-3} \text{ m} \quad (\text{C.18})$$

Geometric considerations give

$$d_x = a/2 - l \quad (\text{C.19})$$

C.6 Pendulum's parameters

A being \mathcal{R} 's center of rotation, we have

$$\forall M \in \mathcal{R}, \langle \mathbf{A}\mathbf{M}, \dot{\mathbf{u}}_{M \in \mathcal{R}/\mathcal{C}} \rangle = 0 \quad (\text{C.20})$$

Considering symmetries, A belongs to $[MG]$. Given any other point outside $[MG]$ and its speed's direction, one can eventually get

$$e_x \approx 1,0587 \cdot 10^{-3} \text{ m} \quad (\text{C.21})$$

Geometric considerations allow to determine l through

$$l = \sqrt{2}(e_p + e_g + A_r/2) - e_x \quad (\text{C.22})$$

Pendulum's stiffness k_r and mass m_r

The stiffness k_r can be easily found by a static equilibrium of the pendulum under a load F compatible with the system, *e.g.* one orthogonal to the pendulum. We have then

$$FL = k_r \delta \theta_r \quad (\text{C.23})$$

At the first order, we have

$$\delta \theta_r \approx \frac{\delta u}{L} \quad (\text{C.24})$$

An FE model gives, for $F = 1 \text{ N}$ (small enough to have a "small" angle)

$$k_r = 1.52 \text{ N.m} \quad (\text{C.25})$$

Assuming $\theta_c = 0$, Lagrange's equation for θ_r is

$$m_r L^2 \ddot{\theta}_r + k_r (\theta_r - \pi/4) = 0 \quad (\text{C.26})$$

Appendix C. Discrete model

Its first mode (and the only one that can describe the model) lies at

$$\omega_r = \frac{\sqrt{k_r}}{L\sqrt{m_r}} \quad (\text{C.27})$$

The theoretical ω_r has been computed by a classical finite-element approach *via Comsol Multiphysics*[®].

$$m_r = \frac{k_r}{L^2\omega_r^2} = 3.1648 \cdot 10^{-4} \text{ kg} \quad (\text{C.28})$$

It is interesting to compare it to theoretical mass of the resonator

$$m_r^{\text{th}} = \rho_t A_r^2 e = 3,74 \cdot 10^{-4} \text{ kg} > m_r \quad (\text{C.29})$$

Which seems perfectly normal, as the kinetic energy of the discrete model should be great that the one of the real system. Accordingly, we modify A_r by

$$A_r = \sqrt{\frac{m_r}{\rho_t e}} = 8,48 \cdot 10^{-3} \text{ m} \quad (\text{C.30})$$

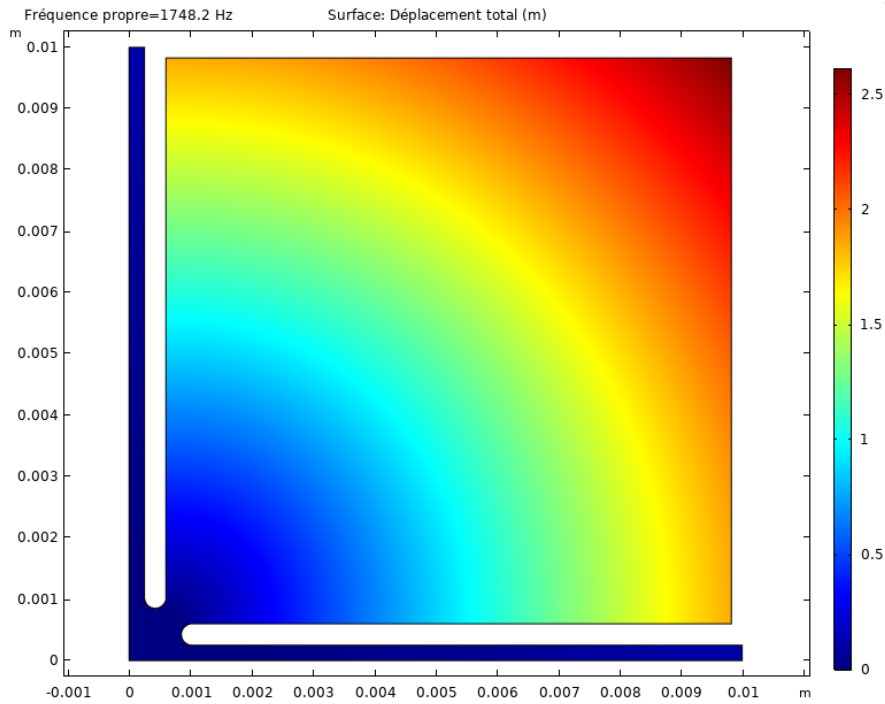


Figure C.3: Resonance mode of the pendulum

C.7 Writing the equations

By scalability, the Lagrangian of the whole system is

$$L = \sum_i L_i \text{ where } L_i = T_i - W_i - P_i \text{ for each element of the system} \quad (\text{C.31})$$

The generalized coordinates are $q = (x_1, y_1, \theta_{c1}, \dots, x_n, y_n, \theta_{cn}, \theta_{r1}, \dots, \theta_{rm})^T$ where (x_i, y_i) is the displacement around its equilibrium position of $M_i \in \mathcal{C}_i$ of the i -th of the n corners and θ_{ci} its rotation, θ_{ri} the rotation of the i -th of the m resonators \mathcal{R}_i . The system respects the Principle of Least Action, which means that q minimise the action

$$\int_{t_1}^{t_2} L(q, \dot{q}) dt \quad (\text{C.32})$$

Leading to the $n + m$ Lagrange's equations

$$\frac{d}{dt} \frac{\partial L}{\partial \dot{q}_i} - \frac{\partial L}{\partial q_i} = Q_i, i \in \llbracket 1, n + m \rrbracket \quad (\text{C.33})$$

Where Q_i is the generalized force defined by

$$Q_i = \frac{\partial P^*}{\partial q_i^*} \quad \text{where} \quad P^* = \{F\} \otimes \{V^*\} \quad (\text{C.34})$$

C.8 Linearization

As the previous system is a set of non-linear second order ordinary differential equations, its is not possible, in the usual sense, to compute the frequency response function of the system (FRF) in order to compare it to the other simulations. As the displacement field induced by the piezoelectric patches remains very low, we can legitimately linearize the system around its equilibrium position. Two approaches are possible, both leading to the same linear system:

- manipulate the Lagrange's equations
- build the mass and stiffness from K and W

While the first technique expects some dexterity, by

- make a first order Taylor's development on non-linear q_i -depending terms
- neglect quadratic and higher orders terms (like q_i^2 or $q_i \dot{q}_j$)

For every \mathcal{L}_i equation, the second directly gives

$$\mathbb{M} \ddot{\mathbf{q}} + \mathbb{K} \mathbf{q} = \mathbf{F} \quad (\text{C.35})$$

with

$$\mathbb{M}_{ij} = \frac{\partial^2 K}{\partial \dot{q}_i \partial \dot{q}_j} \Big|_{\mathbf{q}=\mathbf{q}_0}, \mathbb{K}_{ij} = \frac{\partial^2 W}{\partial q_i \partial q_j} \Big|_{\mathbf{q}=\mathbf{q}_0} \quad \text{and} \quad \mathbf{F}_i = \frac{\partial P}{\partial q_i} \Big|_{\mathbf{q}=\mathbf{q}_0} \quad (\text{C.36})$$

List of Figures

1.1	(left to right) (a) <i>Lamprocyphus augustus</i> , whose iridescent scales contain a photonic crystal structure with directional band-gaps [Galusha 2008]. (b) Frequency response in a temperature-dependent band-gap phononic crystal slab based on the combination of metallic parts and highly dissipative polymers [Billon 2019]. (c) Resonances in trees may result in forests acting as a natural seismic metamaterial for Rayleigh surface waves [Colombi 2016].	1
1.2	Plan of the manuscript seen by the engineer's approach.	4
2.1	Definitive geometry of the architected cell with its parametrization.	10
2.2	Geometry of the architected plate consisting in a bidimensionnal paving of the unit cell given in 2.1, with, in the center, the excitation zone.	11
2.3	(left) Geometry of the cell in the physical space (right) Dual space, the first zone of Brillouin and the irreducible zone.	12
2.4	Dispersion curves along ΓX for the considered microstructured cell and their respective modeshapes.	14
2.5	Dispersion curves along ΓM for the considered microstructured cell .	15
2.6	Dispersion curves along XM for the considered microstructured cell	16
2.7	Top view of the full microstructured plate with (blue) the boundary conditions consisting of 4 flat supports at the corners of the plate and (red) the load (10g).	17
2.8	Top view of the symmetrized microstructured plate with (blue) the boundary conditions consisting of a flat support at the corner of the plate and (red) the load (10g).	18
2.9	(left) classical architected cell and (right) novel geometry.	19
2.10	Configurations available for the positioning of the resonator. (center) side of the cell and resonator, whose position generates two different unit cell geometry.	20
2.11	Manufacturing of the microstructured plate.	23

List of Figures

2.12	Considered power supplies with the piezoelectric patches. Elements in dashed lines represent the non-powered piezoelectric patches and undistorted center of the plate while elements in continuous lines represent the powered piezoelectric patches deforming the microstructured plate. In particular, blues lines represent the side of the piezoelectric patches connected to the ground while red lines represent the powered side of the piezoelectric patches, the red arrows the polarization. For the sake of simplicity and symmetry reasons, the same electric potential is applied on both red areas.	24
2.13	Chosen electric supply of the piezoelectric patches	24
2.14	Upper piezoelectric patch <i>in situ</i> with its electric supply, glued to the architected plate.	25
2.15	Energy and acquisition chain for the experimental set-up.	27
2.16	Experimental set-up: glued in the center of the metamaterial's plate there is the top piezoelectric patch (another one being placed on the other side of the plate) that has been used as an actuator for the external excitation. The tapes placed on the top-right quarter of the plate can reflect a laser's beam for speed measurements.	28
2.17	Overview of the interface developed under MATLAB. (<i>left</i>) Parameters of the acquisition/reading. (<i>right, top to bottom</i>) Temporal response in the three directions of space with their respective coherence and spectrogram.	29
2.18	Energy and information chain of the instrumented microstructured plate.	29
2.19	Comparison in the frequency domain between the experimental system and the theoretical models as presented in Figure 1.2.	30
3.1	Transformation of a Cauchy medium	32
3.2	Evolution of the system in the space of configurations \mathcal{Q} : two admissible trajectories (dashed lines) and the actual trajectory (thick line) verifying the Principle of Least Action.	35
3.3	Dispersion curves for the Cauchy continuum for longitudinal (<i>red</i>) and shear waves (<i>blue</i>), of respective equations $\omega = c_l \mathbf{k} $ and $\omega = c_s \mathbf{k} $ in an isotropic plate.	42
3.4	Classical and generalized continuum mechanics.	44
3.5	Transformation for an enriched micromorphic medium	45
3.6	Definitive geometry of the architected cell with its parametrization.	48
3.7	(<i>red</i>) Different identifications of the unit cell from a microstructured plate.	50

3.8	(left) Dispersion curves of the microstructured and the relaxed micromorphic systems along ΓX (propagation at 0°). (right) Dispersion curves of the microstructured and the relaxed micromorphic systems along ΓM (propagation at 45°).	51
3.9	Respective domains and constitutive laws of the classical Cauchy and the relaxed micromorphic medium.	52
3.10	Between mechanic and electrostatic: the piezoelectric effect.	54
3.11	(left) Unsymmetrized system with its load and symmetry planes. (right) Reduced system with the created symmetry boundary $\partial\Omega_s$	57
3.12	Interface between two Cauchy media	61
3.13	(left) Interface between a Cauchy and a relaxed micromorphic medium. (right) Fictive split between a Cauchy and a relaxed micromorphic medium.	62
3.14	(left) Shape function e_3^u chosen for \mathbf{u} . The black dots represents the nodes where \mathbf{u} is interpolated. (right) Shape function e_3^P chosen for \mathbf{P} . The black dots represents the nodes where \mathbf{P} is interpolated.	67
3.15	Unrefined mesh for the corner of the microstructured cell, the exact geometry of the cell is represented in gray, one can notice the difference between the mesh and the geometry at the bottom of the holes.	68
3.16	(left) Mesh for a quarter unit cell of the microstructured model: the portions of domain with coarse mesh allows a reduction of the total number of degrees of freedom, while a finer mesh is needed in the slender portions of the domain in order to be able to properly describe the behaviour of the microstructure in the band-gap frequency range. (right) Mesh for the equivalent relaxed micromorphic model.	69
3.17	Element K of a Finite Element model with its greatest dimension $h(K)$	70
3.18	(top) Scaled displacement for the first (left) and 5 th (right) tensile mode of the beam with their respective (bottom) mesh necessary for convergence.	70
3.19	Elementary unit of the relaxed micromorphic model	71
3.20	Integration of linear systems using modal synthesis or homogenization techniques.	78
3.21	(left) First mode of a beam under a axial tensile load with the divergence of its response in the absence of damping. (right) First mode of a damped beam under a axial tensile load with the emitted and reflected waves eventually converging to its stationary response as $t \rightarrow +\infty$	79
3.22	(left) Co-localized response of the beam for the undamped system. (right) Co-localized response of the beam for the damped system.	79

List of Figures

3.23	(left) Top view of the full microstructured plate and identification of points A and B. (right) Top view of the full relaxed micromorphic plate and identification of the corresponding volumes Ω_A and Ω_B . Given the strong directivity of the plate we do not consider other points outside the dashed domain to show the simulation's results. .	82
3.24	(left) Top view of the symmetrized microstructured plate, denomination of the traction-free boundaries $\partial\Omega_f$ and the symmetry boundaries $\partial\Omega_s$. (right) Top view of the symmetrized relaxed micromorphic plate, denomination of the traction-free boundaries $\partial\Omega_f$ and the symmetry boundaries $\partial\Omega_s$	83
3.25	Increasing the size of the microstructured plate for $n_c = 1$	85
3.26	Pointwise (left) and mean (right) displacement for the static responses of the microstructured, the homogenized and the relaxed micromorphic models at point B for $(n_1 = 11, n_2 = 9)$	86
3.27	Increasing the size of the central excitation ($n_c = 1, 3$ and 5) for $n_1 = 11$ and $n_2 = 9$	86
3.28	Pointwise (left) and mean (right) displacement for the static responses of the microstructured, the homogenized and the relaxed micromorphic models at point B for $(n_1 = 11, n_2 = 9)$	87
3.29	Increasing both the size of the microstructured plate and the central excitation.	87
3.30	Pointwise (left) and mean (right) displacement for the static responses of the microstructured, the homogenized and the relaxed micromorphic models at point B for $(n_1 = 51, n_2 = 49)$	88
3.31	(from left to right) Normalized displacement for the static responses of the microstructured, the relaxed micromorphic and the homogenized Cauchy model.	89
3.32	(left) Pointwise displacement p_B of the microstructured and relaxed micromorphic models with the theoretical band-gap (dashed) for $n_1 = 51, n_2 = 49$ and $n_c = 11$. (right) Mean displacement m_B of the microstructured and relaxed micromorphic models with the theoretical band-gap (dashed) for $n_1 = 51, n_2 = 49$ and $n_c = 11$	89
3.33	$ \mathbf{u} /\psi$ at frequency M_1 for the microstructured model and the relaxed micromorphic model, the first two figures correspond to M_1 (left) and the last two figures to M_1 (right) (see Fig. 3.32 for the definition of these points).	90
3.34	$ \mathbf{u} /\psi$ at frequency M_2 for the microstructured model and the relaxed micromorphic model, the first two figures correspond to M_2 (left) and the last two figures to M_2 (right) (see Fig. 3.32 for the definition of these points).	90

3.35	$ \mathbf{u} /\psi$ at frequency M_3 for the microstructured model and the relaxed micromorphic model, the first two figures correspond to M_3 (left) and the last two figures to M_3 (right) (see Fig. 3.32 for the definition of these points).	91
3.36	$ \mathbf{u} /\psi$ at frequency M_4 for the microstructured model and the relaxed micromorphic model, the first two figures correspond to M_4 (left) and the last two figures to M_1 (right) (see Fig. 3.32 for the definition of these points).	91
3.37	$ \mathbf{u} /\psi$ in the band-gap for the microstructured model and the relaxed micromorphic model at 1717 Hz.	92
4.1	(left) Microstructured symmetrized model with the selected points (blue) for the comparison with the experimental system. (right) Relaxed micromorphic symmetrized model with the selected points (red) for the comparison with the experimental system.	94
4.2	(left) Top view of the unsymmetrized microstructured plate with the upper piezoelectric patch Ω_p . (right) Top view of the symmetrized microstructured plate with the traction free boundaries $\partial\Omega_f$ and the symmetry planes $\partial\Omega_s$	95
4.3	Section at $x_2 = 0$ of the (light grey) full microstructured plate with the (dark grey) two piezoelectric patches and, in dashed blue lines, the symmetry planes $x_1 = 0$ and $x_3 = 0$, the origin O being set at the center of the plate.	96
4.4	Section of the symmetrized microstructured plate with the piezoelectric patch (one eighth on the whole system) and the boundaries' denomination $\partial\Omega_{\text{top}}$ and $\partial\Omega_{\text{bottom}}$ where the electric potential is imposed.	96
4.5	(left) Top view of the full relaxed micromorphic model with the upper piezoelectric patch Ω_p , the central Cauchy bulk cell Ω_c and the relaxed micromorphic medium Ω_m . (right) Top view of the symmetrized relaxed micromorphic model with the (generalized) traction free boundaries $\partial\tilde{\Omega}_f$, the symmetry planes $\partial\Omega_s$ and the interface $\partial\Omega_c$	98
4.6	Section of the symmetrized relaxed micromorphic plate with the piezoelectric patch (one eighth on the whole system) and the boundaries' denomination $\partial\Omega_{\text{top}}$ and $\partial\Omega_{\text{bottom}}$ where the electric potential is imposed.	99
4.7	Amplitude of $ \dot{u}_1 $ at C_1 (see Figure 4.1 for the definition of this point) for the experiment, the microstructured and relaxed micromorphic models with the theoretical limits of the band-gap obtained <i>via</i> the Bloch-Floquet analysis (dashed lines).	100

List of Figures

4.8	Recalibration procedure for the classical Cauchy model given in Figure 4.2	103
4.9	Effects of the recalibration procedure on the response of the plate for p_B according to Equations 4.24.	104
4.10	<i>(left)</i> Pointwise displacement p_B for the original and recalibrated microstructured models at point B . <i>(right)</i> Mean displacement m_B for the original and recalibrated microstructured models. The theoretical limits of the band-gap obtained via the Bloch-Floquet analysis for the original and recalibrated architected unit cell are given in dashed lines.	106
4.11	<i>(top)</i> $ \dot{u}_1 $ for C_1 for the experiment (<i>green</i>) and the recalibrated microstructured plate (<i>blue</i>). <i>(bottom)</i> Coherence of $ \dot{u}_1 $ for the experiment. The dashed lines represent the theoretical lower and upper limit of the band-gap on the recalibrated unit cell.	107
4.12	New recalibration algorithm using the relaxed micromorphic model to compute faster the fitting of the response of the microstructured plate. Two different stopping criteria associated to two maximum admissible differences ε_m and ε_c as, failing to respect the homogenization conditions given in Chapter 3, the relaxed micromorphic model will not, outside the band-gap, get as close as the microstructured model to the experimental response.	110
4.13	<i>(left)</i> Pointwise displacement p_B for the original and recalibrated relaxed micromorphic models at point B . <i>(right)</i> Mean displacement m_B for the original and recalibrated relaxed micromorphic models. The theoretical limits of the band-gap obtained via the Bloch-Floquet analysis for the original and recalibrated architected unit cell are given in dashed lines.	112
4.14	<i>(left)</i> Pointwise displacement p_B for the recalibrated microstructured and relaxed micromorphic models at point B . <i>(right)</i> Mean displacement m_B for the recalibrated microstructured and relaxed micromorphic models. The theoretical limits of the band-gap obtained via the Bloch-Floquet analysis for the original and recalibrated architected unit cell are given in dashed lines.	112
4.15	<i>(top)</i> $ \dot{u}_1 $ for C_1 for the experiment (<i>green</i>), the relaxed micromorphic (<i>red</i>) and the recalibrated microstructured models (<i>blue</i>). <i>(bottom)</i> Coherence of $ \dot{u}_1 $ for the experiment. The theoretical limits of the band-gap obtained via the Bloch-Floquet analysis for the recalibrated architected unit cell are given in dashed lines.	113
4.16	<i>(left)</i> Probability density function used for the θ_i and <i>(right)</i> its distribution function used for the cauchy and the relaxed micromorphic model.	115

- 4.17 Equivalence between the (*left*) microstructured unit cell and the (*right*) relaxed micromorphic parameters, *red* corresponding to spring-like elements and *blue* to mass-like elements. 115
- 4.18 (*left*) Top view of the microstructured plate. (*right*) Top view of the relaxed relaxed micromorphic plate. 116
- 4.19 (*left*) Pointwise displacement p_B for the recalibrated deterministic (*blue*) and stochastic (*red*) microstructured models. (*right*) Mean displacement m_B for the recalibrated deterministic (*blue*) and stochastic (*red*) microstructured models. The theoretical limits of the band-gap obtained via the Bloch-Floquet analysis for the recalibrated architected unit cell are given in dashed lines. 117
- 4.20 (*left*) Pointwise displacement p_B for the recalibrated deterministic (*blue*) and stochastic (*red*) relaxed micromorphic models. (*right*) Mean displacement m_B for the recalibrated deterministic (*blue*) and stochastic (*red*) relaxed micromorphic models. The theoretical limits of the band-gap obtained via the Bloch-Floquet analysis for the recalibrated architected unit cell are given in dashed lines. 118
- 4.21 (*left*) Pointwise displacement p_B for the recalibrated deterministic stochastic microstructured (*blue*) and relaxed micromorphic (*blue*) models. (*right*) Mean displacement m_B for the recalibrated stochastic microstructured (*blue*) and relaxed micromorphic (*red*) models. The theoretical limits of the band-gap obtained via the Bloch-Floquet analysis for the recalibrated architected unit cell are given in dashed lines. 118
- 4.22 (*left, top*) Beam composed of three non-disturbed architected cells (*i.e.* identical) under a axial load with (*left, bottom*) their frequency response function $H_1^t = H_t = H_2^t = H_3^t$ (*green, blue* and *red*) and the global response $H_1^t H_2^t H_3^t = H_t^3$ (*black*). (*right, top*) Beam composed of three different architected cells under a axial load with (*right, bottom*) their respective frequency response function H_1^t, H_2^t and H_3^t (*green, blue* and *red*) and the global response $H_1^t H_2^t H_3^t$ (*black*). 120
- 4.23 (*left, top*) Beam composed of three non-disturbed architected cells (*i.e.* identical) under a axial load with (*left, bottom*) their frequency response function $H_1^t = H_t = H_2^t$ and H_3^r (*green, blue* and *red*) and $H_1^t H_2^t H_3^r = H_t^2 H_r$ (*black*). (*right, top*) Beam composed of three disturbed architected cells under a axial load with (*right, bottom*) their respective frequency response function H_1^t, H_2^t and H_3^r (*green, blue* and *red*) and $H_1^t H_2^t H_3^r$ (*black*). 121

List of Figures

4.24	<i>(left)</i> Distribution of the normalized eigenfrequency of each resonator for the deterministic system (for the analytical model). <i>(right)</i> Distribution of the normalized eigenfrequency for some of the 396 resonators of the disturbed plate. w_i is the eigenfrequency of the i^{th} resonator and w_0 the theoretical eigenfrequency of the deterministic unit cell.	122
4.25	<i>(left)</i> Amplitude of \dot{u}_1 at C_1 (see Fig. 4.1 for the definition of this point) for the experiment, the microstructured and relaxed micromorphic models. <i>(right, top)</i> Phase of \dot{u}_1 at C_1 for the experiment, the microstructured and relaxed micromorphic model. <i>(right, bottom)</i> Coherence of \dot{u}_1 at C_1 for the experiment.	123
4.26	<i>(left)</i> Amplitude of \dot{u}_1 at C_2 (see Fig. 4.1 for the definition of this point) for the experiment, the microstructured and relaxed micromorphic models. <i>(right, top)</i> Phase of \dot{u}_1 at C_2 for the experiment, the microstructured and relaxed micromorphic models. <i>(right, bottom)</i> Coherence of \dot{u}_1 at C_2 for the experiment.	124
4.27	<i>(left)</i> Amplitude of \dot{u}_2 at C_3 (see Fig. 4.1 for the definition of this point) for the experiment, the microstructured and relaxed micromorphic models. <i>(right, top)</i> Phase of \dot{u}_2 at C_3 for the experiment, the microstructured and relaxed micromorphic models. <i>(right, bottom)</i> Coherence of \dot{u}_2 at C_3 for the experiment.	125
4.28	<i>(left)</i> Amplitude of \dot{u}_2 at C_4 (see Fig. 4.1 for the definition of this point) for the experiment, the microstructured and relaxed micromorphic models. <i>(right, top)</i> Phase of \dot{u}_2 at C_4 for the experiment, the microstructured and relaxed micromorphic models. <i>(right, bottom)</i> Coherence of \dot{u}_2 at C_4 for the experiment.	125
4.29	$ \dot{\mathbf{u}} $ (in m/s) at 1365 Hz for the microstructured model <i>(left)</i> and for the symmetrized experimental system <i>(right)</i> , each square representing the speed at the center of the resonator of the 1/4 of cell considered.	126
4.30	$ \dot{\mathbf{u}} $ (in m/s) at 1589 Hz for the microstructured model <i>(left)</i> and for the symmetrized experimental system <i>(right)</i> , each square representing the speed at the center of the resonator of the 1/4 of cell considered.	127
4.31	$ \dot{\mathbf{u}} $ (in m/s) at 1742 Hz for the microstructured model <i>(left)</i> and for the symmetrized experimental system <i>(right)</i> , each square representing the speed at the center of the resonator of the 1/4 of cell considered.	128
4.32	<i>(left)</i> Top view of the full microstructured plate with the two different cells. <i>(right)</i> Top view of the full equivalent relaxed micromorphic plate.	129

- 4.33 (*left*) Top view of the symmetrized microstructured plate with the two different cells. (*right*) Top view of the symmetrized equivalent micromorphic plate with the boundaries and medium denominations. 130
- 4.34 Detail of the annular Cauchy domain Ω_c , the central domain Ω_m^1 with the “usual” unit cell and the outer domain Ω_m^2 paved with double unit cells. 131
- 4.35 (*left*) Dispersion curves for the 4cm unit cell (red) and the 2 cm unit cell (blue) along ΓX (propagation at 0°) and (*right*) along ΓM (propagation at 45°). 132
- 4.36 (*left*) Dispersion curves of the microstructured and the relaxed micromorphic “double cell” along ΓX (propagation at 0°). (*right*) Dispersion curves of the microstructured and the relaxed micromorphic “double cell” along ΓM (propagation at 45°). 133
- 4.37 Displacement field in the structure at 857.5 Hz. 134
- 5.1 Equivalent tridimensional cell, consisting of beams on its edges and of cubes for the resonators linked to the unit cell’s corners by small beams. 138
- B.1 Top view of the full microstructured plate with the most remarkable points along the symmetry planes of the system. Given the strong directivity of the plate we do not consider other points outside the dashed domain. 143
- B.2 (*left*) Amplitude of \dot{u}_1 at $(x_1, x_2) = (1.5, 0.5)$ [cm] for the experiment, the microstructured and relaxed micromorphic models. (*right, top*) Phase of \dot{u}_1 at $(x_1, x_2) = (1.5, 0.5)$ [cm] for the experiment, the microstructured and relaxed micromorphic models. (*right, bottom*) Coherence of \dot{u}_1 at $(x_1, x_2) = (1.5, 0.5)$ [cm] for the experiment. Dashed lines correspond to the theoretical bounds of the band gap. 144
- B.3 (*left*) Amplitude of \dot{u}_2 at $(x_1, x_2) = (1.5, 0.5)$ [cm] for the experiment, the microstructured and relaxed micromorphic models. (*right, top*) Phase of \dot{u}_2 at $(x_1, x_2) = (1.5, 0.5)$ [cm] for the experiment, the microstructured and relaxed micromorphic models. (*right, bottom*) Coherence of \dot{u}_2 at $(x_1, x_2) = (1.5, 0.5)$ [cm] for the experiment. Dashed lines correspond to the theoretical bounds of the band gap. 144

List of Figures

<p>B.4 (left) Amplitude of \dot{u}_1 at $(x_1, x_2) = (2.5, 0.5)$ [cm] for the experiment, the microstructured and relaxed micromorphic models. (right, top) Phase of \dot{u}_1 at $(x_1, x_2) = (2.5, 0.5)$ [cm] for the experiment, the microstructured and relaxed micromorphic models. (right, bottom) Coherence of \dot{u}_1 at $(x_1, x_2) = (2.5, 0.5)$ [cm] for the experiment. Dashed lines correspond to the theoretical bounds of the band gap.</p>	145
<p>B.5 (left) Amplitude of \dot{u}_2 at $(x_1, x_2) = (2.5, 0.5)$ [cm] for the experiment, the microstructured and relaxed micromorphic models. (right, top) Phase of \dot{u}_2 at $(x_1, x_2) = (2.5, 0.5)$ [cm] for the experiment, the microstructured and relaxed micromorphic models. (right, bottom) Coherence of \dot{u}_2 at $(x_1, x_2) = (2.5, 0.5)$ [cm] for the experiment. Dashed lines correspond to the theoretical bounds of the band gap.</p>	145
<p>B.6 (left) Amplitude of \dot{u}_1 at $(x_1, x_2) = (2.5, 0.5)$ [cm] for the experiment, the microstructured and relaxed micromorphic models. (right, top) Phase of \dot{u}_1 at $(x_1, x_2) = (2.5, 0.5)$ [cm] for the experiment, the microstructured and relaxed micromorphic models. (right, bottom) Coherence of \dot{u}_1 at $(x_1, x_2) = (2.5, 0.5)$ [cm] for the experiment. Dashed lines correspond to the theoretical bounds of the band gap.</p>	146
<p>B.7 (left) Amplitude of \dot{u}_2 at $(x_1, x_2) = (2.5, 0.5)$ [cm] for the experiment, the microstructured and relaxed micromorphic models. (right, top) Phase of \dot{u}_2 at $(x_1, x_2) = (2.5, 0.5)$ [cm] for the experiment, the microstructured and relaxed micromorphic models. (right, bottom) Coherence of \dot{u}_2 at $(x_1, x_2) = (2.5, 0.5)$ [cm] for the experiment. Dashed lines correspond to the theoretical bounds of the band gap.</p>	146
<p>B.8 (left) Amplitude of \dot{u}_1 at $(x_1, x_2) = (2.5, 0.5)$ [cm] for the experiment, the microstructured and relaxed micromorphic models. (right, top) Phase of \dot{u}_1 at $(x_1, x_2) = (2.5, 0.5)$ [cm] for the experiment, the microstructured and relaxed micromorphic models. (right, bottom) Coherence of \dot{u}_1 at $(x_1, x_2) = (2.5, 0.5)$ [cm] for the experiment. Dashed lines correspond to the theoretical bounds of the band gap.</p>	147
<p>B.9 (left) Amplitude of \dot{u}_2 at $(x_1, x_2) = (2.5, 0.5)$ [cm] for the experiment, the microstructured and relaxed micromorphic models. (right, top) Phase of \dot{u}_2 at $(x_1, x_2) = (2.5, 0.5)$ [cm] for the experiment, the microstructured and relaxed micromorphic models. (right, bottom) Coherence of \dot{u}_2 at $(x_1, x_2) = (2.5, 0.5)$ [cm] for the experiment. Dashed lines correspond to the theoretical bounds of the band gap.</p>	147

- B.10 (*left*) Amplitude of \dot{u}_1 at $(x_1, x_2) = (2.5, 0.5)$ [cm] for the experiment, the microstructured and relaxed micromorphic models. (*right, top*) Phase of \dot{u}_1 at $(x_1, x_2) = (2.5, 0.5)$ [cm] for the experiment, the microstructured and relaxed micromorphic models. (*right, bottom*) Coherence of \dot{u}_1 at $(x_1, x_2) = (2.5, 0.5)$ [cm] for the experiment. Dashed lines correspond to the theoretical bounds of the band gap. 148
- B.11 (*left*) Amplitude of \dot{u}_2 at $(x_1, x_2) = (2.5, 0.5)$ [cm] for the experiment, the microstructured and relaxed micromorphic models. (*right, top*) Phase of \dot{u}_2 at $(x_1, x_2) = (2.5, 0.5)$ [cm] for the experiment, the microstructured and relaxed micromorphic models. (*right, bottom*) Coherence of \dot{u}_2 at $(x_1, x_2) = (2.5, 0.5)$ [cm] for the experiment. Dashed lines correspond to the theoretical bounds of the band gap. 148
- B.12 (*left*) Amplitude of \dot{u}_1 at $(x_1, x_2) = (2.5, 0.5)$ [cm] for the experiment, the microstructured and relaxed micromorphic models. (*right, top*) Phase of \dot{u}_1 at $(x_1, x_2) = (2.5, 0.5)$ [cm] for the experiment, the microstructured and relaxed micromorphic models. (*right, bottom*) Coherence of \dot{u}_1 at $(x_1, x_2) = (2.5, 0.5)$ [cm] for the experiment. Dashed lines correspond to the theoretical bounds of the band gap. 149
- B.13 (*left*) Amplitude of \dot{u}_2 at $(x_1, x_2) = (2.5, 0.5)$ [cm] for the experiment, the microstructured and relaxed micromorphic models. (*right, top*) Phase of \dot{u}_2 at $(x_1, x_2) = (2.5, 0.5)$ [cm] for the experiment, the microstructured and relaxed micromorphic models. (*right, bottom*) Coherence of \dot{u}_2 at $(x_1, x_2) = (2.5, 0.5)$ [cm] for the experiment. Dashed lines correspond to the theoretical bounds of the band gap. 149
- B.14 (*left*) Amplitude of \dot{u}_1 at $(x_1, x_2) = (2.5, 0.5)$ [cm] for the experiment, the microstructured and relaxed micromorphic models. (*right, top*) Phase of \dot{u}_1 at $(x_1, x_2) = (2.5, 0.5)$ [cm] for the experiment, the microstructured and relaxed micromorphic models. (*right, bottom*) Coherence of \dot{u}_1 at $(x_1, x_2) = (2.5, 0.5)$ [cm] for the experiment. Dashed lines correspond to the theoretical bounds of the band gap. 150
- B.15 (*left*) Amplitude of \dot{u}_2 at $(x_1, x_2) = (2.5, 0.5)$ [cm] for the experiment, the microstructured and relaxed micromorphic models. (*right, top*) Phase of \dot{u}_2 at $(x_1, x_2) = (2.5, 0.5)$ [cm] for the experiment, the microstructured and relaxed micromorphic models. (*right, bottom*) Coherence of \dot{u}_2 at $(x_1, x_2) = (2.5, 0.5)$ [cm] for the experiment. Dashed lines correspond to the theoretical bounds of the band gap. 150

List of Figures

C.1	Parametrization of the model	153
C.2	Angular parametrization of the discrete system	154
C.3	Resonance mode of the pendulum	156

List of Tables

2.1	Main functions performed by the metamaterial cell	8
2.2	Manufacturing constraints for the microstructured plate	9
2.3	Static design constraints for the microstructured plate	9
2.4	Mechanical parameters used for the computation of dispersion curves of our unit cell.	13
2.5	Characteristics of the final cell	22
3.1	Geometrical and mechanical properties of the unit cell given in Figure 3.6.	49
3.2	Values of the elastic and micro-inertia relaxed micromorphic parameters calibrated on the metamaterial whose unit cell is reported in Figure 3.6.	51
3.3	Values of the elastic the corresponding long-wave limit Cauchy material parameters calibrated on the metamaterial whose unit cell is reported in Figure 3.6.	53
3.4	Mechanical, coupling and electrical parameters parameters of the piezoelectric patches.	57
4.1	Coordinates of the measurement points.	94
4.2	Characteristics of the theoretical limits of the band-gap obtained via the Bloch-Floquet analysis for the original and recalibrated architected unit cell.	113
4.3	Band gap characteristics of the structures presented in Figures 4.5 and 4.18.	120
4.4	Mechanical parameters of the second isotropic Cauchy medium between the two relaxed micromorphic mediums.	129
4.5	Values of the average total energy for each domain of the structure at 857.5 Hz.	134

Bibliography

- [Aivaliotis 2020] Alexios Aivaliotis, Domenico Tallarico, Marco-Valerio d'Agostino, Ali Daouadji, Patrizio Neff et Angela Madeo. *Frequency- and angle-dependent scattering of a finite-sized meta-structure via the relaxed micromorphic model*. *Archive of Applied Mechanics*, vol. 90, no. 5, pages 1073–1096, 2020.
- [Bacigalupo 2014] A. Bacigalupo et L. Gambarotta. *Second-gradient homogenized model for wave propagation in heterogeneous periodic media*. *International Journal of Solids and Structures*, vol. 51, no. 5, pages 1052–1065, Mars 2014.
- [Barbagallo 2017] Gabriele Barbagallo, Angela Madeo, Marco Valerio d'Agostino, Rafael Abreu, Ionel-Dumitrel Ghiba et Patrizio Neff. *Transparent anisotropy for the relaxed micromorphic model: Macroscopic consistency conditions and long wave length asymptotics*. *International Journal of Solids and Structures*, vol. 120, pages 7–30, 2017.
- [Barbagallo 2019a] Gabriele Barbagallo, Domenico Tallarico, Marco Valerio d'Agostino, Alexios Aivaliotis, Patrizio Neff et Angela Madeo. *Relaxed micromorphic model of transient wave propagation in anisotropic band-gap metastructures*. *International Journal of Solids and Structures*, vol. 162, pages 148–163, 2019.
- [Barbagallo 2019b] Gabriele Barbagallo, Domenico Tallarico, Marco Valerio d'Agostino, Alexios Aivaliotis, Patrizio Neff et Angela Madeo. *Relaxed micromorphic model of transient wave propagation in anisotropic band-gap metastructures*. *International Journal of Solids and Structures*, vol. 162, pages 148–163, 2019.
- [Barchiesi 2019] Emilio Barchiesi, Mario Spagnuolo et Luca Placidi. *Mechanical metamaterials: a state of the art*. *Mathematics and Mechanics of Solids*, vol. 24, no. 1, pages 212–234, 2019.
- [Billon 2019] Kévin Billon, Morvan Ouisse, Emeline Sadoulet, Manuel Collet, Pauline Butaud, Gael Chevallier et Abdelkrim Khelif. *Design and experimental validation of a temperature-driven adaptive phononic crystal slab*. *Smart Materials and Structures*, vol. 28, no. 3, 2019.
- [Bloch 1929] F. Bloch. *Über die Quantenmechanik der Elektronen in Kristallgittern*. *Zeitschrift für Physik*, vol. 52, pages 555–600, 1929.
- [Boltzmann 1905] L. Boltzmann. *Populäre Schriften*. Barth, 1905.
- [Bordiga 2019] Giovanni Bordiga, Luigi Cabras, Andrea Piccolroaz et Davide Bigoni. *Prestress tuning of negative refraction and wave channeling from flexural sources*. *Applied Physics Letters*, vol. 114, no. 4, 2019.
- [Bragg 1915] W. Bragg. *Bakerian lecture : X-rays and crystal structure*. *Philosophical Transactions of the Royal Society of London*, vol. 215, page 253–274, 1915.

Bibliography

- [Brillouin 1953] L. Brillouin. *Wave propagation in periodic structures*. Dover Publication, 1953.
- [Bückmann 2015] Tiemo Bückmann, Muamer Kadic, Robert Schittny et Martin Wegener. *Mechanical cloak design by direct lattice transformation*. Proceedings of the National Academy of Sciences, vol. 112, no. 16, pages 4930–4934, 2015.
- [Cauchy 1828a] A.L. Cauchy. *De la pression ou tension dans un corps solide*. Ex. de Math., 1828.
- [Cauchy 1828b] A.L. Cauchy. *Sur les équations qui expriment les conditions d'équilibre, ou les lois du mouvement intérieur d'un corps solide, élastique ou non élastique*. Oeuvres complètes, 1828.
- [Celli 2019] Paolo Celli, Behrooz Yousefzadeh, Chiara Daraio et Stefano Gonella. *Bandgap widening by disorder in rainbow metamaterials*. Applied Physics Letters, vol. 114, no. 9, page 091903, 2019.
- [Collet 2011] M. Collet, M. Ouisse, M. Ruzzene et M.N. Ichchou. *Floquet–Bloch decomposition for the computation of dispersion of two-dimensional periodic, damped mechanical systems*. International Journal of Solids and Structures, vol. 48, no. 20, pages 2837–2848, 2011.
- [Colombi 2016] A. Colombi, Roux P., Guenneau S., Gueguen P. et Craster R.V. *Forests as a natural seismic metamaterial: Rayleigh wave bandgaps induced by local resonances*. Scientific Reports, 2016.
- [Cosserat 1909] E. Cosserat et F. Cosserat. *Théorie des corps déformables*. Hermann, 1909.
- [Cross 2001] N. Cross. *Designerly Ways of Knowing: Design Discipline Versus Design Science*. Design Issues, vol. 17, page 49-55, 2001.
- [Curie 1881] P. Curie et J. Curie. *Contractions et dilatations produites par des tensions électriques dans les cristaux hémihédres à faces inclinées*. Comptes rendus de l'Académie des Sciences, vol. XCIII, page 1137, 1881.
- [Dell'Isola 2016a] Francesco Dell'Isola, A. Corte, Raffaele Esposito et Lucio Russo. *Some cases of unrecognized transmission of scientific knowledge: From antiquity to gabrio piola's peridynamics and generalized continuum theories*, pages 77–128. Springer, 2016.
- [Dell'Isola 2016b] Francesco Dell'Isola, David Steigmann et Alessandro Della Corte. *Synthesis of Fibrous Complex Structures: Designing Microstructure to Deliver Targeted Macroscale Response*. Applied Mechanics Reviews, vol. 67, no. 6, 2016.
- [Dell'Isola 2012a] Francesco Dell'Isola, Angela Madeo et Luca Placidi. *Linear plane wave propagation and normal transmission and reflection at discontinuity surfaces in second gradient 3D continua*. Zeitschrift für Angewandte Mathematik und Mechanik, vol. 9, page 52–71, 2012.

- [Dell'Isola 2012b] Francesco Dell'Isola et Luca Placidi. *Variational principles are a powerful tool also for formulating field theories*. Variational Models and Methods in Solid and Fluid Mechanics, Volume 535 of the series CISM Courses and Lectures, pages 1–15, 2012.
- [Dell'Isola 2016] F. Dell'Isola, A. Madeo et Pierre Seppecher. *Cauchy Tetrahedron Argument applied to Higher Contact Interactions*. Archive for Rational Mechanics and Analysis, vol. 219, pages 1305–1341, 2016.
- [d'Agostino 2020] M.V. d'Agostino, G. Barbagallo, I.D. Ghiba, B. Eidel, P. Neff et A. Madeo. *Effective description of anisotropic wave dispersion in mechanical band-gap metamaterials via the relaxed micromorphic model*. Journal of Elasticity, vol. 39, pages 299–329, 2020.
- [Eringen 1968] A. C. Eringen. *Mechanics of Micromorphic Continua*. In Ekkehart Kröner, editeur, Mechanics of Generalized Continua, pages 18–35. Springer, 1968.
- [Eringen 1999] A.C. Eringen. Microcontinuum field theories. Springer, 1999.
- [Floquet 1883] G. Floquet. *Sur les équations différentielles à coefficients périodiques*. Annales scientifiques de l'École Normale Supérieure, vol. 12, pages 47–88, 1883.
- [Frenzel 2017] Tobias Frenzel, Muamer Kadic et Martin Wegener. *Three-dimensional mechanical metamaterials with a twist*. Science, vol. 358, no. 6366, pages 1072–1074, 2017.
- [Galusha 2008] Jeremy W. Galusha, Lauren R. Richey, John S. Gardner, Jennifer N. Cha et Michael H. Bartl. *Discovery of a diamond-based photonic crystal structure in beetle scales*. Phys. Rev. E, vol. 77, 2008.
- [Ghiba 2015] Ionel-Dumitrel Ghiba, Patrizio Neff, Angela Madeo, Luca Placidi et Giuseppe Rosi. *The relaxed linear micromorphic continuum: Existence, uniqueness and continuous dependence in dynamics*. Mathematics and Mechanics of Solids, vol. 20, no. 10, pages 1171–1197, 2015.
- [Guenneau 2007] Sébastien Guenneau, Alexander Movchan, Gunnar Pétursson et S Anantha Ramakrishna. *Acoustic metamaterials for sound focusing and confinement*. New Journal of Physics, vol. 9, no. 11, 2007.
- [Hamel 1912] G. Hamel. *Elementare mechanik: ein lehrbuch*. Teubner, 1912.
- [Hill 1963] R. Hill. *Elastic properties of reinforced solids: Some theoretical principles*. Journal of the Mechanics and Physics of Solids, vol. 11, page 357–372, 1963.
- [Hill 1967] R. Hill. *The essential structure of constitutive laws for metal composites and polycrystals*. Journal of the Mechanics and Physics of Solids, pages 79–95, 1967.
- [Joannopoulos 2011] J. Joannopoulos, S. Johnson, J. Winn et R. Meade. *Photonic crystals: molding the flow of light*. Princetown university press, pages 21–29, 2011.

Bibliography

- [Kaina 2015] Nadège Kaina, Fabrice Lemoult, Mathias Fink et Geoffroy Lerosey. *Negative refractive index and acoustic superlens from multiple scattering in single negative metamaterials*. *Nature*, vol. 525, no. 7567, pages 77–81, 2015.
- [Kaina 2017] Nadège Kaina, Alexandre Causier, Yoan Bourlier, Mathias Fink, Thomas Berthelot et Geoffroy Lerosey. *Slow waves in locally resonant metamaterials line defect waveguides*. *Scientific Reports*, vol. 7, no. 1, 2017.
- [Lakes 1987] Roderic Lakes. *Foam structures with a negative Poisson's ratio*. *Science*, vol. 235, no. 4792, pages 1038–1040, 1987.
- [Lamé 1852] G. Lamé. *Leçons sur la théorie mathématique de l'élasticité des corps solides*. École Polytechnique, 1852.
- [Lee 2008] Sam Hyeon Lee, Choon Mahn Park, Yong Mun Seo, Zhi Guo Wang et Chul Koo Kim. *Negative effective density in an acoustic metamaterial*. arXiv, 2008.
- [Lee 2009] Sam Hyeon Lee, Choon Mahn Park, Yong Mun Seo, Zhi Guo Wang et Chul Koo Kim. *Acoustic metamaterial with negative modulus*. *Journal of Physics: Condensed Matter*, 2009.
- [Li 2004] Jensen Li et Che Ting Chan. *Double-negative acoustic metamaterial*. *Physical Review E*, vol. 70, no. 5, 2004.
- [Liu 2018] Chenchen Liu et Celia Reina. *Broadband locally resonant metamaterials with graded hierarchical architecture*. *Journal of Applied Physics*, vol. 123, no. 9, 2018.
- [Mace 2008] Brian Mace et Elisabetta Manconi. *Modelling wave propagation in two-dimensional structures using finite element analysis*. *Journal of Sound and Vibration*, vol. 318, pages 884–902, 2008.
- [Madeo 2014] Angela Madeo, Patrizio Neff, Ionel-Dumitrel Ghiba, Luca Placidi et Giuseppe Rosi. *Band gaps in the relaxed linear micromorphic continuum*. *Zeitschrift für Angewandte Mathematik und Mechanik*, vol. 95, page 880–887, 2014.
- [Madeo 2015] Angela Madeo, Patrizio Neff, Ionel-Dumitrel Ghiba, Luca Placidi et Giuseppe Rosi. *Wave propagation in relaxed micromorphic continua: modeling metamaterials with frequency band-gaps*. *Continuum Mechanics and Thermodynamics*, vol. 27, page 551–570, 2015.
- [Madeo 2016a] Angela Madeo, Patrizio Neff, Marco Valerio d'Agostino et Gabriele Barbagallo. *Complete band gaps including nonlocal effects occur only in the relaxed micromorphic model*. *Comptes Rendus Mécanique*, 2016.
- [Madeo 2016b] Angela Madeo, Neff Patrizio, Ghiba Ionel-Dumitrel et Rosi Giuseppe. *Reflection and transmission of elastic waves in non-local band-gap metamaterials: a comprehensive study via the relaxed micromorphic model*. *Journal of the Mechanics and Physics of Solids*, 2016.
- [Madeo 2017] Angela Madeo, Patrizio Neff, Gabriele Barbagallo, Marco Valerio d'Agostino et Ionel-Dumitrel Ghiba. *A review on wave propagation modeling*

- in band-gap metamaterials via enriched continuum models.* In *Mathematical Modelling in Solid Mechanics. Advanced Structured Materials.* arXiv, 2017.
- [Madeo 2018a] A. Madeo, G. Barbagallo, M. Collet, M.V. D’agostino, M. Miniaci et P. Neff. *Relaxed micromorphic modeling of the interface between a homogeneous solid and a band-gap metamaterial: New perspectives towards metastructural design.* *Mathematics and Mechanics of Solids*, vol. 23, pages 1485—1506, 2018.
- [Madeo 2018b] Angela Madeo, Manuel Collet, M. Miniaci, Kévin Billon, Morvan Ouisse et Patrizio Neff. *Modeling real phononic crystals via the weighted relaxed micromorphic model with free and gradient micro-inertia.* *Journal of Elasticity*, vol. 130, no. 1, pages 59 – 83, 2018.
- [Mandel 1962] J. Mandel. *Plastic waves in an infinite three dimensional medium.* *Journal de Mécanique*, vol. 30, pages 1–3, 1962.
- [Mandel 1972] J. Mandel. *Plasticité classique et viscoplasticité.* *CISM courses and lectures*, vol. 97, 1972.
- [Mauguin 1980] G. A. Maugin. *The method of virtual power in continuum mechanics: application to coupled fields.* *Acta Mech.*, vol. 35, page 1–70, 1980.
- [Maurin 2018] Florian Maurin, Claus Claeys, Elke Deckers et Wim Desmet. *Probability that a band-gap extremum is located on the irreducible Brillouin-zone contour for the 17 different plane crystallographic lattices.* *International Journal of Solids and Structures*, vol. 135, pages 26–36, 2018.
- [Mindlin 1964] R. D. Mindlin. *Micro-structure in linear elasticity.* *Archive for Rational Mechanics and Analysis*, vol. 16, no. 1, pages 51–78, Janvier 1964.
- [Mindlin 1965] R.D Mindlin. *Second gradient of strain and surface tension in linear elasticity.* *International Journal of Solids Structures*, vol. 1, page 417–438, 1965.
- [Misseroni 2016] D. Misseroni, D. J. Colquitt, A. B. Movchan, N. V. Movchan et I. S. Jones. *Cymatics for the cloaking of flexural vibrations in a structured plate.* *Scientific Reports*, vol. 6, no. 1, page 23929, Avril 2016.
- [Nicolaou 2012] Zachary G Nicolaou et Adilson E Motter. *Mechanical metamaterials with negative compressibility transitions.* *Nature materials*, 2012.
- [O.R. Bilal 2018] C. Daraio O.R. Bilal D. Ballagi. *Architected lattices for simultaneous broadband attenuation of airborne sound and mechanical vibrations in all directions.* *Physical Review Applied*, vol. 10.5:054060, 2018.
- [Piola 1825] Gabrio Piola. *Sull’applicazione de’ principj della meccanica analitica del Lagrange ai principali problemi.* *Memoria di Gabrio Piola presentata al concorso del premio e coronata dall’I.R. Istituto di Scienze*, 1825.
- [Placidi 2014] Luca Placidi, Giuseppe Rosi, Ivan Giorgio et Angela Madeo. *Reflection and transmission of plane waves at surfaces carrying material properties and embedded in second-gradient materials.* *Mathematics and Mechanics of Solids*, vol. 19, page 555–578, 2014.

Bibliography

- [Rizzi 2019] G Rizzi, F Dal Corso, D Veber et D Bigoni. *Identification of second-gradient elastic materials from planar hexagonal lattices. Part II: Mechanical characteristics and model validation*. International Journal of Solids and Structures, vol. 176, pages 19–35, 2019.
- [Rizzi 2021] Gianluca Rizzi, Domenico Tallarico, Patrizio Neff et Angela Madeo. *Towards the conception of complex engineering meta-structures: relaxed-micromorphic modelling of mechanical diodes*. (arXiv:2012.11192) to appear in Wave Motion, 2021.
- [Sigmund 2001] O. Sigmund. *A 99 line topology optimization code written in Matlab*. Structural and Multidisciplinary Optimization, vol. 21, page 120–127, 2001.
- [Tallarico 2017] D. Tallarico, A. Trevisan, N.V. Movchan et A.B. Movchan. *Edge waves and localization in lattices containing tilted resonators*. Frontiers in Materials, vol. 4(16), 2017.
- [Toupin 1962] R.A Toupin. *Elastic materials with couple-stresses*. Arch. Rational Mech. Anal., vol. 11, page 385–414, 1962.
- [Truesdell 1960] C Truesdell et R Toupin. *Principles of Classical Mechanics and Field Theory*. Encyclopedia of Physics, 1960.
- [Veselago 1968] V. Veselago. *The electrodynamics of substances with simultaneously negative values of epsilon and mu*. Soviet Physics Uspekhi, vol. 10, page 509, 1968.
- [Veselago 2006] V. Veselago et E. Narimanov. *The left hand of brightness: past, present and future of negative index materials*. Nature Materials, 2006.
- [Voigt 1887] W. Voigt. *Theoretische studien uber die elasticitatsverhaltnisse der krystalle*. Konigliche Gesellschaft der Wissenschaften zu Gottingen, 1887.
- [Voigt 1889] W. Voigt. *Ueber die Beziehung zwischen den beiden Elasticitatskonstanten isotroper Korper.* Annalen der Physik, vol. 274, pages 573–587, 1889.
- [Wang 2014] Pai Wang, Filippo Casadei, Sicong Shan, James C. Weaver et Katia Bertoldi. *Harnessing buckling to design tunable locally resonant acoustic metamaterials*. Physical Review Letters, vol. 113, no. 1, page 014301, 2014.
- [Willis 2016] J. R. Willis. *Negative refraction in a laminate*. Journal of the Mechanics and Physics of Solids, vol. 97, pages 10–18, 2016.
- [Zhu 2014] R. Zhu, X. N. Liu, G. K. Hu, C. T. Sun et G. L. Huang. *Negative refraction of elastic waves at the deep-subwavelength scale in a single-phase metamaterial*. Nature Communications, vol. 5, no. 1, 2014.

AUTORISATION DE SOUTENANCE

Vu les dispositions de l'arrêté du 25 mai 2016,

Vu la demande du directeur de thèse

Monsieur M. COLLET

et les rapports de

M. J-F. DEU

Professeur - CNAM Paris - LMSS, Mécanique - case courrier 2D6R10 - 292 rue Saint-Martin
75141 Paris cedex 03

et de

M. P. SEPPECHER

Professeur - Université de Toulon - IMATH - avenue de l'Université - 83130 La Garde

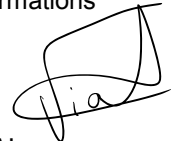
Monsieur DEMORE Félix

est autorisé à soutenir une thèse pour l'obtention du grade de **DOCTEUR**

Ecole doctorale Mécanique, Energétique, Génie civil, Acoustique

Fait à Ecully, le 10 octobre 2022

Pour le directeur de l'Ecole centrale de Lyon
Le directeur des Formations



Grégory VIAL